

STUDY OF HfO₂ BASED STRUCTURES FOR OPTICAL AND THERMOELECTRIC APPLICATIONS

**THESIS SUBMITTED TO
Delhi Technological University
for the award of the degree of
DOCTOR OF PHILOSOPHY
in
PHYSICS**



by

RAJESH KUMAR
(2K18/PHD/AP/511)

Under the supervision of

Dr. MUKHTIYAR SINGH

Supervisor

Department of Applied Physics
Delhi Technological University
Delhi-110 042, India

Dr. ANKUSH VIJ

Co-Supervisor

Department of Physics and Astrophysics
Central University of Haryana
Haryana-123 031, India

**DEPARTMENT OF APPLIED PHYSICS
DELHI TECHNOLOGICAL UNIVERSITY
DELHI-110 042, INDIA**

DECEMBER 2023

©Delhi Technological University-2023

All rights reserved





*This Thesis is
Dedicated to
My Parents
&
Teachers*



Delhi Technological University

(Govt. of National Capital Territory of Delhi)

Shahbad Daultpur, Bawana Road, Delhi-110042

CERTIFICATE

This is to certify that the thesis entitled “*Study of HfO₂ based Structures for Optical and Thermoelectric Applications*” submitted by *Mr. Rajesh Kumar (2K18/PHD/AP/511)* to Delhi Technological University, Delhi, India for the degree of Doctor of Philosophy in Physics, is a bonafide record of the research work carried out by him under our supervision and guidance. The work embodied in this thesis has been carried out in the Department of Applied Physics, Delhi Technological University, Delhi, India. The work of this thesis is original and has not been submitted in parts or fully to any other Institute or University for the award of any other degree or diploma.

Dr. Mukhtiyar Singh

Supervisor

Department of Applied Physics

Delhi Technological University

Delhi-110 042, India

Dr. Ankush Vij

Co-Supervisor

Department of Physics and Astrophysics

Central University of Haryana

Haryana-123 031, India

Prof. A. S. Rao

Head, Department of Applied Physics

Delhi Technological University

Delhi-110 042, India



Delhi Technological University

(Govt. of National Capital Territory of Delhi)

Shahbad Daulatpur, Bawana Road, Delhi-110042

CANDIDATE'S DECLARATION

I, hereby certify that the thesis titled “*Study of HfO₂ based Structures for Optical and Thermoelectric Applications*” submitted in the fulfilment of the requirements for the award of the degree of Doctor of Philosophy is an authentic record of my research work carried out under the supervision of **Dr. Mukhtiyar Singh** and **Dr. Ankush Vij**. Any material borrowed or referred to is duly acknowledged.

Mr. Rajesh Kumar

2K18/PHD/AP/511

Department of Applied Physics

Delhi Technological University

Delhi-110 042, India

ACKNOWLEDGEMENTS

This Ph.D. thesis is the result of challenging journey and it would not have been possible to write this doctoral thesis without the support of kind people around me, to only some of whom it is possible to give particular mention here.

Foremost, I would like to express my gratitude to my supervisor **Dr. Mukhtiyar Singh**, Department of Applied Physics, Delhi Technological University, Delhi, India for his supervision, valuable guidance, and genuine advice from the early stage of this research. Each step in this research work was carried out with his highly coherent suggestions and help. Highly organised discussions, and very healthy and homely atmosphere created by him made my, research working days memorable. His dedication, timely advice, scientific intuition and instinct have exceptionally inspired and enriched my growth as the student and research scholar. I would like to convey sincere gratitude to my co-supervisor **Dr. Ankush Vij**, Department of physics and Astrophysics, Central university of Haryana, Haryana, India. Throughout my research work, I have received highly fruitful suggestions, help in finding promising literature and criticisms, which help to enhance the research work. I am privileged to have a supervisor & Co-supervisor who cared so much about my work and who provided me constant support. Their enthusiasm in research has always motivated me to take challenges for solving the advance and complex problems in my research field. The critical comments rendered by them during the discussions are highly appreciated.

My sincere thanks to **Hon'ble Prof. Prateek Sharma**, Vice Chancellor, DTU and officials of DTU for their precious support and providing ample research facilities to conduct this research.

I would also thank, Head of Department, **Prof. A. S. Rao** for his originality that has triggered and nourished my maturity and benefitted me for long time. Moreover, I would also thank all other faculty and staff members of Department of Applied Physics, DTU for their help and cooperation throughout my research period.

I would also like to express huge and warm thanks to my lab mates; **Mr. Ramesh Kumar, Ms. Sangeeta, Mr. Kulwinder Kumar** for the stimulating discussions, scientific inputs. Their cooperation and understanding are sustaining factors in accomplishing this thesis successfully.

I also explicitly thank my colleagues and friends *Dr. Jyoti, Mr. Rajat Bajaj, Mr. Vikas Sangwan* for all their selfless support and the fun we have had in the last five years.

I am grateful to some of my dear friends *Mr. Ajay Yadav, Mr. Mahesh Yadav, Mr. Amit Sharma, Mr. Krishan, Mr. Manoj, Mr. Praveen Garg, Mr. Sumit Dhaka, Mr. Parvesh, Mr. Hardhyan, Mr. Rahul, Mr. Harish, Dr. Deepak, Dr. Umang Sharma, Mr. Sagar Khanna and Mr. Harender Mor* for influencing me in a positive way and for their moral support and motivation, which drives me to give my best.

I would also like to acknowledge *National Supercomputing Mission (NSM)* for providing computing resources of '*PARAM SEVA*' at IIT Hyderabad and '*PARAM SMRITI*' at NABI Mohali, which are implemented by *C-DAC* and supported by the *Ministry of Electronics and Information Technology (MeitY)* and *Department of Science and Technology (DST), Government of India*. I also want to thank *IUAC Delhi* for providing experimental facilities.

I would like to pay high regards to my grandfather *Sub. Surender Singh* and grandmother *Mrs. Meva Devi*, and my beloved parents *Mr. Vikram Singh* and *Mrs. Mosham Devi* for their unconditional support. I would show my special thanks to my sister *Dr. Rekha Yadav* for constant motivation and her help throughout my academic journey. I would like to extend my gratitude to my relatives, *Mr. Dharamvir Singh, Mrs. Bimla Devi, Mr. Surender, Mrs. Radha Devi, Mr. Kuldeep Yadav* for their support. I want to thank my uncle *Mr. Vijay Singh, Mr. Vinod Singh* and aunty *Mrs. Lalita, Mrs. Sushila*. My cousins, *Ms. Pinki, Mr. Rahul Singh, Mr. Rohit Singh, Mr. Mohit Singh, Mr. Rajat and Mr. Ankit* for adding fun in my life.

Above all, I thank the Almighty God for giving me the strength and patience to work through all these years so that today I can stand proudly with my head held high.

List of publications

Thesis Work:

1. **Rajesh Kumar**, Mukhtiyar Singh, Ankush Vij, “*Unraveling the effect of pressure on structural phase transition, electronic and optical properties of $Hf_{1-x}Si_xO_2$ ($x = 0, 0.03, 0.06, 0.09$): A first-principles investigation*”, **J. Phys. Chem. Solids** 185, 111773 (2024). <https://doi.org/10.1016/j.jpcs.2023.111773>
2. **Rajesh Kumar**, Jitender Kumar, Ramesh Kumar, Akshay Kumar, Aditya Sharma, S.O. Won, K.H. Chae, Mukhtiyar Singh, Ankush Vij, “*Monoclinic to cubic structural transformation, local electronic structure, and luminescence properties of Eu-doped HfO_2* ”, **Appl. Phys. A** 129, 712 (2023). <https://doi.org/10.1007/s00339-023-06997-0>
3. **Rajesh Kumar**, Ramesh Kumar, Mukhtiyar Singh, Deshraj Meena, Ankush Vij, “*Carrier concentration mediated enhancement in thermoelectric performance of various polymorphs of hafnium oxide: a plausible material for high temperature thermoelectric energy harvesting application*”, **J. Phys. D: Appl. Phys.** 55, 495302 (2022). <https://doi.org/10.1088/1361-6463/ac9986>
4. **Rajesh Kumar**, Ramesh Kumar, Mukhtiyar Singh, Ankush Vij, “*A first-principle study of electronic, thermoelectric, and optical properties of sulfur doped c- HfO_2* ”, **Phys. Scr.** 97, 075813 (2022). <https://doi.org/10.1088/1402-4896/ac7678>
5. **Rajesh Kumar**, Mukhtiyar Singh, Ankush Vij, “*Electronic, thermoelectric, and optical studies of cubic $Hf_{1-x}Ti_xO_2$: An attempt to enhance the key parameters*”, **J. Solid State Chem.** 307, 122829 (2022). <https://doi.org/10.1016/j.jssc.2021.122829>.
6. **Rajesh Kumar**, Mukhtiyar Singh, Ankush Vij, “*Defects Assisted Luminescence in m- HfO_2 Nanocrystals: An Experimental and Theoretical Study*”, **Optik** 248, 168121 (2021). <https://doi.org/10.1016/j.ijleo.2021.168121>

Other than thesis work:

1. **Rajesh Kumar**, Sangeeta, Ramesh Kumar, Ramesh Kumar Bibiyan, Mukhtiyar Singh, Ankush Vij, “*An ab-initio study of induced half metallic ferromagnetism in Hf–Nb alloy oxides*”, **Eur. Phys. J. Plus** 138, 561 (2023). <https://doi.org/10.1140/epjp/s13360-023-04179-8>
2. **Rajesh Kumar**, Ramesh Kumar, Sangeeta, Kulwinder Kumar, Mukhtiyar Singh, “*Insights in to structural, electronic and thermoelectric properties of ZnTMN₂ (TM= Zr and Hf)*”, **Indian J. Pure Appl. Phys.** 61, 910-914 (2023). <https://doi.org/10.56042/ijpap.v61i11.3151>
3. Sangeeta, **Rajesh Kumar**, Ramesh Kumar, Kulwinder Kumar, Mukhtiyar Singh, “*Unravelling the Ultralow Thermal Conductivity of Ternary Antimonide Zintl Phase RbGaSb₂: A First-principles Study*”, **Indian J. Pure Appl. Phys** 61, 731-734 (2023). <https://doi.org/10.56042/ijpap.v61i9.3152>
4. Ramesh Kumar, **Rajesh Kumar**, Sangeeta, Mukhtiyar Singh, “*Pressure Induced Surface States and Wannier Charge Centers in Ytterbium Monoarsenide*”, **Indian J. Pure Appl. Phys** 61, 735-738 (2023). <https://doi.org/10.56042/ijpap.v61i9.3148>
5. Jitender Kumar, **Rajesh Kumar**, Mukhtiyar Singh, Shalendra Kumar, Ravi Kumar, Sung Ok Won, Ranjeet Brajpuriya, Sourabh Dwivedi, Ram K. Sharma, Ankush Vij, “*Structural, diffuse reflectance and luminescence study of t-Mg₂BO₅ nanostructures*”. **Appl. Phys. A** 127, 617 (2021). <https://doi.org/10.1007/s00339-021-04761-w>
6. Nimit Jain, **Rajesh Kumar**, Ramesh Kumar, Mukhtiyar Singh, “*Enhancement of thermoelectric performance of ZrO₂ via Titanium doping*”, **materials today: proceedings** 51, 699-702 (2022). <https://doi.org/10.1016/j.matpr.2021.06.211>

Abstract

The quest for clean and sustainable energy sources has prompted significant research interest towards the exploration of efficient energy conversion technologies such as thermoelectric (TE) energy harvesting and solid state lighting. The tailored materials required in these technologies are currently at the center stage of material science research. The TE materials can convert waste heat into usable electrical energy and are useful for a wide span of applications ranging from wearable devices to space applications. On the other hand, the good luminescent properties of a material is the first condition for its use in optoelectronic and light emitting applications. The energy conservation based on the light emitting diodes are viable substitute for incandescent bulbs on account of their high brightness, efficiency, fast response rate, and low energy consumption. The distinctive properties of metal oxides make them potential candidates for high temperature TE application and solid state lighting.

In this thesis, we have carried out a detailed investigation of structural phase transition, electronic, transport, and optical properties of various phases of HfO₂ for enhanced TE performance as well as the optical response using computational and experimental approaches.

We realized that carrier concentration optimization is an effective way to enhance the TE performance of HfO₂. The feasibility of high *p*-type carrier concentration (order of $\sim 10^{22}$ cm⁻³) was experimentally demonstrated in HfO₂. In light of these studies, using the first-principles calculation combined with the semi-classical Boltzmann transport theory, we have reported high TE performance in various polymorphs of HfO₂ in a range of carrier concentrations (order of $\sim 10^{18}$ - 10^{22} cm⁻³) at high temperatures. The highest value of Seebeck coefficient has observed in tetragonal phase at 300 K. The lattice thermal conductivities at room temperature are 5.56, 2.87, 4.32, and 1.75 Wm⁻¹K⁻¹ for cubic (*c*-), monoclinic (*m*-), orthorhombic (*o*-) and tetragonal (*t*-) HfO₂, respectively which decrease to 1.58, 0.92, 1.12, 0.53 Wm⁻¹K⁻¹ at 1200 K for respective phases. The low lattice thermal conductivities lead to the high values of the figure of merit, i.e., 0.97, 0.87, 0.83, and 0.77 at 1200 K for the *m*-, *o*-, *t*-, and *c*- HfO₂, respectively, at the optimized carrier concentrations ($\sim 10^{21}$ cm⁻³). Further to enhance the TE performance of *c*-HfO₂, we have investigated the doping of Ti and S at cationic and anionic sites. The convex hull method has been employed to estimate the stability of various doped structures. Doping leads to create new trap states in the band gap. The band gap with Ti doping decreases more

sharply as compared to S doping. The magnitude of the Seebeck coefficient is high in Ti doping as compared to S doping. The figure of merit of *c*-HfO₂ with doping enhances ~0.82 at 800 K.

We have analyzed the structural phase transition in the HfO₂ under the effect of doping and pressure. We discussed the phase transition from a centrosymmetric *m*-HfO₂ to a non-centrosymmetric *o*-HfO₂ with Si doping. The reported phase transition pressures i.e., 15 GPa, 14 GPa, 8 GPa, and 8 GPa for $x = 0, 0.03, 0.06,$ and $0.09,$ respectively for Hf_{1-x}Si_xO₂ are in excellent agreement with available experimental results. It has observed that with increasing Si concentrations the transition pressures reduce significantly which is understood in terms of bond length and charge transfer. The thermal stability of the obtained *o*-HfO₂ phase has examined via ab initio molecular dynamics up to its synthesis temperature. The density of states indicates the noticeable appearance of Si states in the lower conduction band and an increase in the extent of hybridization.

The effect of Si, along with other dopants such as Ti and S, also examined on the optical properties of HfO₂ by calculating the dielectric function and refractive index. The refractive index slightly enhanced with Ti and S doping. The desired and suitable optical properties can be augmented via the suggested doping mechanism. The effect of Si doping on *o*-HfO₂ also broader the UV absorption range but no significant enhancement in refractive index is observed. Our calculations have revealed that the value of refractive index *o*-HfO₂ at 15 GPa can be readily attained at lower pressure i.e., 8 GPa with 9% of Si doing. The optical response of HfO₂ under different doping makes it a viable candidate in optoelectronic applications.

The structure phase transformation and luminescence properties of undoped and doped HfO₂ have been explored experimentally. The samples were synthesized via chemical co-precipitation method. The crystal structure and phase analysis of the prepared sample have carried out by XRD and Rietveld refinement studies. The UV-visible spectroscopy has used to analyze the band gap of HfO₂. The observed band gap using the TB-mBJ approach is in good agreement with the experimental results. The photoluminescence peaks corresponding to 562 nm, 536 nm, and 450 nm wavelength are attributed to oxygen vacancy. To analyze the vacancy, we have calculated the density of states of O₃ and O₄ vacancy using density functional theory. The peaks correlated with the total density of states of O₄ single vacancy are in close agreement with our experimental observation.

A low temperature synthesis of HfO₂:xEu³⁺ ($x = 0, 3, 5$ and 7 mol%) at 600 °C. The XRD results revealed the monoclinic phase in undoped HfO₂ and showed mixed phase formation at lower

concentrations and a dominant cubic phase achieved at 5 mol% doping of Eu in HfO₂. The phase transition has also been calculated using density function theory which shows transition point at ~5.11% doping concentration. X-ray absorption spectra has used to identify the oxidation state of Eu ions in the HfO₂. Photoluminescence study has demonstrated the emission in the red region with high color purity under different excitation wavelengths from near UV to blue light. The reddish photoluminescence emission with high color purity under different excitation wavelengths from n-UV to blue region may be exploited in solid state lighting-based applications.

We hope that our studies regarding structural phase transition in HfO₂ help to understand how pressure and doping can be used to optimized various properties of interest. The strategies for enhancing optical and TE properties via doping and carrier concentration optimization may open new avenues for exploring HfO₂ for solid state lighting and high temperature TE energy harvesting applications.

LIST OF FIGURES

Fig. No.	Page No.
Chapter: 1	
1.1 A schematic representation of the Jablonski diagram to explain photoluminescence..	8
1.2 Configuration coordinate diagram representing the absorption and emission transitions.....	10
Chapter: 2	
2.1 Flow chart for self-consistent density functional calculations.....	31
2.2 Muffin-Tin approximation.....	34
2.3 A schematic instrumental arrangement for X-ray diffraction technique.....	45
2.4 A schematic illustration of energy level diagram for Raman spectroscopy.....	48
2.5 A schematic representation of X-ray absorption spectra.....	50
2.6 A typical experimental set up of diffuse reflectance spectra.....	52
2.7 A diagram representing the setup for photoluminescence measurements.....	53
Chapter: 3	
3.1 Energy vs Volume optimization curve of all polymorphs of HfO ₂	60
3.2 The phonon band structure diagram for (a) <i>c</i> -HfO ₂ , (b) <i>m</i> -HfO ₂ , (c) <i>o</i> -HfO ₂ , and (d) <i>t</i> -HfO ₂	61
3.3 A schematic convex hull of (a) Hf _{1-x} Ti _x O ₂ and (b) HfO _{2-x} S _x at different composition (in %). ΔE _d is given by the vertical distance in formation energy space between the particular material and the hull line.....	62
3.4 The first Brillouin zone of all polymorphs of HfO ₂ with high symmetry points.....	64
3.5 The band structure diagram of all the polymorphs of HfO ₂ (E _F is shifted to 0 eV) (Inset VBM of <i>o</i> -HfO ₂).....	65
3.6 The partial density of states of all the polymorphs of HfO ₂ (E _F is shifted to 0 eV).....	65
3.7 Band structure of Hf _{1-x} Ti _x O ₂ (a) x = 0.25, (b) x = 0.12, (c) x = 0.06, (d) x = 0.03 (E _F is shifted to 0 eV).....	66
3.8 Density of states of Hf _{1-x} Ti _x O ₂ (a) x = 0.25, (b) x = 0.12, (c) x = 0.06, (d) x = 0.03 (E _F is shifted to 0 eV).....	67
3.9 Band structures of HfO _{2-x} S _x (a) x = 0.03, (b) x = 0.06 using TB-mBJ approach (E _F is shifted to 0 eV).....	68

3.10	Density of states of $\text{HfO}_{2-x}\text{S}_x$ (a) $x = 0.03$, (b) $x = 0.06$ (E_F is shifted to 0 eV).....	68
3.11	The variation in Seebeck Coefficient with carrier concentrations at varying temperatures for all the polymorphs of HfO_2	70
3.12	The variation in electrical conductivity with carrier concentrations at varying temperatures for all the polymorphs of HfO_2	71
3.13	The variation in electronic thermal conductivity with carrier concentrations at varying temperatures for all the polymorphs of HfO_2	72
3.14	The variation in power factor with carrier concentrations at varying temperatures for all the polymorphs of HfO_2	72
3.15	The behaviour of lattice thermal conductivity with varying temperatures for all the polymorphs of HfO_2	73
3.16	The variation in the figure of merit with carrier concentrations at varying temperatures for all the polymorphs of HfO_2	74
3.17	The variation in figure of merit with temperature at the optimized carrier concentrations ($3 \times 10^{20} \text{ cm}^{-3}$, $1 \times 10^{21} \text{ cm}^{-3}$, $2 \times 10^{21} \text{ cm}^{-3}$, $5 \times 10^{20} \text{ cm}^{-3}$ for <i>c</i> -, <i>m</i> -, <i>o</i> - and <i>t</i> - phases, respectively).....	75
3.18	The variation of Seebeck coefficient of (a) $\text{Hf}_{1-x}\text{Ti}_x\text{O}_2$ ($x = 0, 0.03, 0.06, 0.12, 0.25$) and (b) $\text{HfO}_{2-x}\text{S}_x$ ($x = 0, 0.03, 0.06$).....	76
3.19	The variation of electrical conductivity of (a) $\text{Hf}_{1-x}\text{Ti}_x\text{O}_2$ ($x = 0, 0.03, 0.06, 0.12, 0.25$) and (b) $\text{HfO}_{2-x}\text{S}_x$ ($x = 0, 0.03, 0.06$).....	77
3.20	The variation of electronic thermal conductivity of (a) $\text{Hf}_{1-x}\text{Ti}_x\text{O}_2$ ($x = 0, 0.03, 0.06, 0.12, 0.25$) and (b) $\text{HfO}_{2-x}\text{S}_x$ ($x = 0, 0.03, 0.06$).....	78
3.21	The variation of power factor of (a) $\text{Hf}_{1-x}\text{Ti}_x\text{O}_2$ ($x = 0, 0.03, 0.06, 0.12, 0.25$) and (b) $\text{HfO}_{2-x}\text{S}_x$ ($x = 0, 0.03, 0.06$).....	78
3.22	The variation of ZT of (a) $\text{Hf}_{1-x}\text{Ti}_x\text{O}_2$ ($x = 0, 0.03, 0.06, 0.12, 0.25$) and (b) $\text{HfO}_{2-x}\text{S}_x$ ($x = 0, 0.03, 0.06$).....	79

Chapter: 4

4.1	The structural phase transition of <i>m</i> - and <i>o</i> - $\text{Hf}_{1-x}\text{Si}_x\text{O}_2$ for (a) $x = 0$, (b) $x = 0.03$, (c) $x = 0.06$, and (d) $x = 0.09$ (values written in black and red colours represent the enthalpy of monoclinic and orthorhombic phases, respectively).....	89
4.2	Change in volume as a function of pressure in <i>m</i> - to <i>o</i> - HfO_2	89

4.3	(a) Variation in bond length of $o\text{-Hf}_{1-x}\text{Si}_x\text{O}_2$ ($x = 0, 0.03, 0.06,$ and 0.09) at 0 GPa (b) Density of states of isolated and Si-doped HfO_2 at 0 GPa.....	90
4.4	Isosurface plot of partial charge density (a) $o\text{-HfO}_2$ (b) $\text{Hf}_{0.97}\text{Si}_{0.03}\text{O}_2$ (c) $\text{Hf}_{0.94}\text{Si}_{0.06}\text{O}_2$ (d) $\text{Hf}_{0.91}\text{Si}_{0.09}\text{O}_2$. (In the units of $e/\text{\AA}^3$ with isosurface level 0.015).....	91
4.5	The phonon dispersion curve of (a) $m\text{-HfO}_2$ (b) $o\text{-HfO}_2$ at 15 GPa.....	92
4.6	The AIMD simulations of temperature fluctuations versus time of $o\text{-Hf}_{1-x}\text{Si}_x\text{O}_2$ ($x = 0, 0.03, 0.06,$ and 0.09).....	93
4.7	The variation in diffusion coefficient with doping concentration for $o\text{-Hf}_{1-x}\text{Si}_x\text{O}_2$ ($x = 0, 0.03, 0.06,$ and 0.09).....	93
4.8	Band structure of $o\text{-HfO}_2$ (a) 0 GPa (b) 8 GPa (c) 14 GPa (d) 15 GPa at phase transition pressures within TB-mBJ approach (E_F is shifted to 0 eV).....	94
4.9	Band structure of (a) $o\text{-Hf}_{0.97}\text{Si}_{0.03}\text{O}_2$ at 14 GPa, (b) $o\text{-Hf}_{0.94}\text{Si}_{0.06}\text{O}_2$ at 8 GPa (a) $o\text{-Hf}_{0.91}\text{Si}_{0.09}\text{O}_2$ at 8 GPa calculated within TB-mBJ approach (E_F is shifted to 0 eV).....	95
4.10	Band structure of (a) $o\text{-HfO}_2$ and (b) $o\text{-Hf}_{0.91}\text{Si}_{0.09}\text{O}_2$ at transition pressure of 8 GPa (E_F is shifted to 0 eV).....	96
4.11	Density of States of (a) $o\text{-HfO}_2$ (b) $o\text{-Hf}_{0.97}\text{Si}_{0.03}\text{O}_2$ (c) $o\text{-Hf}_{0.94}\text{Si}_{0.06}\text{O}_2$ (d) $o\text{-Hf}_{0.91}\text{Si}_{0.09}\text{O}_2$ (E_F is shifted to 0 eV).....	97

Chapter: 5

5.1	Real part of dielectric function (a) $\text{Hf}_{1-x}\text{Ti}_x\text{O}_2$ ($x = 0, 0.03, 0.06, 0.12$ and 0.25) (b) $\text{HfO}_{2-x}\text{S}_x$ ($x = 0, 0.03,$ and 0.06).....	104
5.2	Imaginary part of dielectric function of (a) $\text{Hf}_{1-x}\text{Ti}_x\text{O}_2$ ($x = 0, 0.03, 0.06, 0.12$ and 0.25) (b) $\text{HfO}_{2-x}\text{S}_x$ ($x = 0, 0.03,$ and 0.06).....	105
5.3	Refractive index of (a) $\text{Hf}_{1-x}\text{Ti}_x\text{O}_2$ ($x = 0, 0.03, 0.06, 0.12$ and 0.25) (b) $\text{HfO}_{2-x}\text{S}_x$ ($x = 0, 0.03,$ and 0.06).....	105
5.4	Extinction coefficient of (a) $\text{Hf}_{1-x}\text{Ti}_x\text{O}_2$ ($x = 0, 0.03, 0.06, 0.12$ and 0.25) (b) $\text{HfO}_{2-x}\text{S}_x$ ($x = 0, 0.03,$ and 0.06).....	106
5.5	Reflectivity of (a) $\text{Hf}_{1-x}\text{Ti}_x\text{O}_2$ ($x = 0, 0.03, 0.06, 0.12$ and 0.25) (b) $\text{HfO}_{2-x}\text{S}_x$ ($x = 0, 0.03,$ and 0.06).....	107
5.6	Optical conductivity of (a) $\text{Hf}_{1-x}\text{Ti}_x\text{O}_2$ ($x = 0, 0.03, 0.06, 0.12$ and 0.25) (b) $\text{HfO}_{2-x}\text{S}_x$ ($x = 0, 0.03,$ and 0.06).....	107
5.7	Absorption Coefficient of (a) $\text{Hf}_{1-x}\text{Ti}_x\text{O}_2$ ($x = 0, 0.03, 0.06, 0.12$ and 0.25) (b) $\text{HfO}_{2-x}\text{S}_x$ ($x = 0, 0.03,$ and 0.06).....	108

5.8	(a) Real part (b) Imaginary part (c) Refractive index (d) Extinction coefficient of $o\text{-Hf}_{1-x}\text{Si}_x\text{O}_2$ ($x = 0, 0.03, 0.06, \text{ and } 0.09$).....	109
5.9	(a) Reflectivity (b) Conductivity of $o\text{-Hf}_{1-x}\text{Si}_x\text{O}_2$ ($x = 0, 0.03, 0.06, \text{ and } 0.09$).....	110
5.10	Absorption Coefficient of $o\text{-Hf}_{1-x}\text{Si}_x\text{O}_2$ ($x = 0, 0.03, 0.06, \text{ and } 0.09$).....	110

Chapter: 6

6.1	XRD and Rietveld refinement of $m\text{-HfO}_2$	118
6.2	XRD patterns of pure and Eu doped HfO_2 (at 3.0, 5.0 and 7.0 mol%).....	121
6.3	Rietveld refinement of pure and Eu doped HfO_2 (at 5.0 and 7.0 mol%).....	121
6.4	The total energy vs doping concentration of $\text{Hf}_{1-x}\text{Eu}_x\text{O}_2$ (at 0, 3%, 6% and 7%)...	123
6.5	Raman spectra of $m\text{-HfO}_2$	124
6.6	O K -edge XANES spectra of HfO_2 and $\text{HfO}_2:7.0 \text{ mol\% Eu}$	125
6.7	Hf L -edge XANES spectra of HfO_2 and $\text{HfO}_2: 3.0, 5.0 \text{ and } 7.0 \text{ mol\% Eu}$	126
6.8	Eu $M_{5,4}$ -edge XANES spectra of 3.0, 5.0 and 7.0 mol% Eu doped HfO_2	127
6.9	(a) Absorbance spectrum and (b) Tauc plot for $m\text{-HfO}_2$	128
6.10	Band structure of $m\text{-HfO}_2$ using (a) GGA and (b) TB-mBJ approach (E_F is shifted to 0 eV).....	129
6.11	Projected density of states of $m\text{-HfO}_2$ using (a) GGA approach and (b) TB-mBJ approach (E_F is shifted to 0 eV).....	130
6.12	PL emission spectrum and CIE plot (inset) of $m\text{-HfO}_2$	131
6.13	Total density of states of $m\text{-HfO}_2$ with (a) three and (b) four-fold single oxygen vacancy using TB-mBJ (E_F is shifted to 0 eV).....	132
6.14	Photoluminescence excitation spectra for HfO_2 doped with varying Eu^{3+} ion concentrations under 611 nm emission wavelength.....	133
6.15	Emission spectra of Eu^{3+} doped HfO_2 samples pumping under excitation wavelength of 275 nm.....	134
6.16	Emission spectra of Eu^{3+} doped HfO_2 samples pumping under various excitation wavelengths, including 361 nm, 383 nm, 394 nm and 465 nm.....	135
6.17	Partial energy level diagram of Eu^{3+} doped HfO_2 samples.....	136
6.18	CIE chromaticity diagram for optimized $\text{HfO}_2:5.0 \text{ mol\% Eu}^{3+}$ sample under various excitation wavelengths, including 361 nm, 383 nm, 394 nm and 465 nm..	136

LIST OF TABLES

Table No.	Page No.
Chapter 1	
1.1	The source of excitation of various luminescence phenomena..... 7
Chapter 3	
3.1	The optimized lattice parameters of all polymorphs of HfO ₂ 61
3.2	The band gaps (with GGA and TB-mBJ approach) and effective mass for all polymorphs of HfO ₂ 63
3.3	The variation of effective mass with Hf _{1-x} Ti _x O ₂ and HfO _{2-x} S _x 76
Chapter 4	
4.1	Lattice constant (in units of Å) of <i>o</i> -Hf _{1-x} Si _x O ₂ (x = 0, 0.03, 0.06, and 0.09) under pressure (in units of GPa) 88
4.2	The Bader charges of <i>o</i> -Hf _{1-x} Si _x O ₂ (x = 0, 0.03, 0.06 and 0.09) 91
4.3	The calculated band gap of <i>o</i> -Hf _{1-x} Si _x O ₂ (x = 0, 0.03, 0.06, and 0.09) (within GGA and TB-mBJ potentials) 95
Chapter 6	
6.1	Refined parameters, convergence indicator (chi square), phase for HfO ₂ at 1100 °C..... 119
6.2	Refined parameters, convergence indicator (chi square) and phase for pure and doped HfO ₂ 122
6.3	Theoretical and experimental lattice parameters of HfO ₂ 123

CONTENTS

	Page No.
Certificate.....	i
Candidate's Declaration.....	ii
Acknowledgement.....	iii
Abstract.....	v
List of Publications.....	vii
List of Figures.....	x
List of Tables.....	xiv
Contents.....	xv
Nomenclature.....	xix
Chapter 1: Introduction.....	1-23
1.1 Overview of the problem.....	1
1.2 Thermoelectricity.....	1
1.2.1 Seebeck Coefficient.....	2
1.2.2 Electrical Conductivity.....	3
1.2.3 Thermal Conductivity.....	4
1.3 Strategies for optimizing thermoelectric properties.....	4
1.3.1 Band structure engineering.....	5
1.3.2 Structural defects.....	5
1.4 Oxides as thermoelectric materials.....	6
1.5 Luminescence.....	6
1.5.1 Photoluminescence.....	7
1.5.2 Basic of photoluminescence.....	8
1.6 Rare earth dopants.....	10
1.6.1 Intraconfigurational transition.....	10
1.6.2 Interconfigurational transition.....	11
1.7 Solid state lightning.....	12
1.8 Importance of present host material: HfO ₂	13
1.9 Objective of present thesis.....	14
1.10 Scope of present thesis.....	15
References.....	16

Chapter 2: Theoretical and experimental methodology.....	24-57
2.1 Introduction to many-body problem.....	24
2.1.1 Born-Oppenheimer approximation.....	25
2.1.2 Hartree approximation.....	25
2.1.3 Hartree-Fock approximation.....	26
2.2 Density functional theory.....	27
2.2.1 Thomas-Fermi theory.....	27
2.2.2 Hohenberg-Kohn theorem.....	28
2.2.3 Kohn-Sham approach.....	29
2.3 Exchange-correlation potential.....	31
2.3.1 Local density approximation.....	31
2.3.2 Generalized gradient approximation.....	32
2.3.3 Tran-Blaha modified Becke Johnson potential.....	32
2.4 Treating solids with DFT.....	33
2.4.1 Electron-ion interactions.....	33
2.4.1.1 Full potential and charge density.....	34
2.4.1.2 Pseudopotential method.....	35
2.4.1.3 Projected augmented wave method.....	35
2.4.2 Numerical and technical factors.....	35
2.4.2.1 Plane wave expansion.....	36
2.4.2.2 Cut-off energy.....	36
2.4.2.3 K-point sampling.....	37
2.5 Transport in a solid.....	37
2.5.1 Boltzmann transport theory.....	38
2.5.2 Thermoelectric properties.....	40
2.6 Computational software.....	40
2.6.1 WIEN2K.....	40
2.6.2 VASP.....	41
2.6.3 BoltzTraP.....	41
2.6.4 Phonopy.....	42
2.6.5 Phono3py.....	42
2.7 Experimental technique.....	43
2.7.1 Material synthesis.....	43

2.7.2	Characterization techniques.....	43
2.7.2.1	X-ray diffraction.....	44
2.7.2.2	Raman spectroscopy.....	46
2.7.2.3	X-ray absorption spectroscopy.....	48
2.7.2.3.1	Theory.....	48
2.7.2.3.2	Data collection and analysis.....	50
2.7.2.4	Diffuse reflectance spectroscopy.....	51
2.7.2.5	Photoluminescence.....	52
2.8	Summary.....	53
	References.....	54
	Chapter 3: Thermoelectric properties of pure and doped HfO₂.....	58-85
3.1	Introduction	58
3.2	Computational details.....	59
3.3	Results and discussion.....	60
3.3.1	Structural properties.....	60
3.3.2	Electronic properties.....	63
3.3.3	Effect of Ti doping on electronic properties	66
3.3.4	Effect of S doping on electronic properties	67
3.3.5	Thermoelectric properties	69
3.3.6	Effect of doping on thermoelectric properties	75
3.4	Conclusions.....	80
	References.....	81
	Chapter 4: Pressure induced structural phase transition in monoclinic-HfO₂.....	86-100
4.1	Introduction	86
4.2	Computational details.....	87
4.3	Results and discussion.....	87
4.3.1	Structural properties.....	87
4.3.2	Stability analysis.....	91
4.3.3	Electronic properties.....	94
4.4	Conclusions.....	97
	References.....	98
	Chapter 5: Effect of various dopants on optical properties of HfO₂.....	101-114
5.1	Introduction	101

5.2	Computational details.....	101
5.3	Results and discussion.....	102
5.3.1	Ti and S doping in <i>c</i> -HfO ₂	103
5.3.2	Si doping in <i>o</i> -HfO ₂	108
5.4	Conclusions.....	111
	References.....	112
	Chapter 6: Photoluminescence and local electronic structure analysis of pure and Eu³⁺ doped HfO₂.....	115-141
6.1	Introduction	115
6.2	Experimental and theoretical details.....	116
6.2.1	Material synthesis.....	116
6.2.2	Characterization.....	117
6.2.3	Theoretical methodology.....	117
6.3	Results and discussion.....	118
6.3.1	Structural analysis.....	118
6.3.2	<i>First-principles</i> study of structural phase transition.....	122
6.3.3	Raman spectroscopy.....	123
6.3.4	X-ray absorption spectroscopy.....	124
6.3.5	Band gap analysis.....	127
6.3.5.1	Theoretical analysis of band gap.....	128
6.3.6	Photoluminescence.....	130
6.3.6.1	Photoluminescence <i>study of pure HfO₂</i>	130
6.3.6.2	Photoluminescence <i>study of Eu³⁺ doped HfO₂</i>	132
6.3.6.3	Estimation of CIE coordinates, correlated color temperature (CCT) and color purity.....	136
6.4	Conclusions.....	137
	References.....	137
	Chapter 7: Summary and Future outlooks.....	142-145
	Curriculum Vitae.....	146-148

Nomenclature

List of symbols

k_B	Boltzmann's constant
h	Planck's constant
E_F	Fermi level
V_{ext}	External potential
m_i	Electronic mass
M_I	Nuclear mass
H	Hamiltonian
E_o	Ground state energy
E_{xc}	Exchange-correlation energy
R_{MT}	Muffin-tin radius
K_{max}	Plane wave cut-off
S_α	Seebeck coefficient

Greek letters

Ψ	Wave function
σ	Electrical conductivity
τ	Relaxation time
κ	Thermal conductivity
κ_e	Electronic thermal conductivity
κ_l	Lattice thermal conductivity
Ω	Ohm

Abbreviations

DFT	Density functional theory
HF	Hartree-Fock
KS	Kohn-Sham
BZ	Brillouin zone
LDA	Local density approximation
GGA	Generalized gradient approximation
TB-mBJ	Tran Blaha-modified Becke-Johnson
FPLAPW	Full potential linearized augmented plane wave
TE	Thermoelectric
PL	Photoluminescence
TMO	Transition metal oxide
RE	Rare earth
DOS	Density of states
ZT	Figure of merit
PF	Power factor

Chapter 1

Introduction

1.1 Overview of the problem

The unprecedented increasing demand for energy worldwide has wrecked the environment irreparably leading to the devastating problem of global warming. This has led to new avenues of research toward green and clean energy alternatives [1, 2]. The effective implementation of green energy sources has the potential to mitigate the adverse impacts of environmental changes. Hence, it is imperative to shift towards sustainable energy sources to safeguard a habitable environment for forthcoming generations. Thermoelectric (TE) materials have the capacity to capture and transform waste heat into usable electricity. The diversity of TE materials makes them useful in addressing energy challenges covering a wide range of applications such as wearable devices, space exploration, the automotive industry, power generation, and coolers [3–5]. On the other hand, Light-emitting diodes (LEDs) are recognized as extremely efficient lighting alternatives that effectively reduce power usage. The increasing need for energy-efficient lighting systems has witnessed tremendous research towards the improvement of luminescent materials. Conventional light source like incandescent and fluorescent bulbs causes an enormous loss of heat and gas discharge due to the heating of filament at a very high temperature which puts a bar on their efficiency. Furthermore, the introduction of new technologies such as white light emitting diode (*w*-LED) has increased demand for high quality luminescent materials for global and societal development [6]. Hence, both technologies i.e., TE energy harvesting and solid state lighting have the potential to play crucial roles in effectively resolving the difficulties associated with the increasing energy crisis.

This chapter discusses the fundamentals of TE energy harvesting and luminescent properties. Moreover, the importance of the chosen host material (HfO_2) and the objective of accomplished research work is also discussed.

1.2 Thermoelectricity

The utilization of waste heat for the generation of useful energy is a potential area of contemporary research. The conventional energy resources such as wind, geothermal, and solar have their own constraints regarding location and weather [7]. The TE energy conversion, on the other hand, has emerged as a potential technique to convert waste heat from automobiles,

factories, etc., to useful electricity [8]. This technique is foreseen as a clean and sustainable future energy source, given that these thermoelectric devices are eco-friendly, silent, reliable, and contain no moving parts [9].

The TE materials have a significant impact on society due to their cooling and power generation use, which are based on some fundamental effects, namely the Peltier, Seebeck, and Thomson effects. In 1821, Seebeck did an experiment with two dissimilar metals kept at different temperatures [10]. He noticed that the potential gradient (ΔV) is generated, which is directly proportional to the temperature gradient (ΔT) across the junction. The proportionality, $\Delta V/\Delta T$, is called the Seebeck coefficient (S_α), and the phenomenon of producing electricity directly from heat is called the Seebeck effect. In 1834, Peltier observed the reverse of the Seebeck effect, whereby a temperature decreases or increase was observed when current flows across a junction of dissimilar metals [11]. The temperature variation as a function of electrical current is expressed by a proportionality constant, the Peltier coefficient (π). In 1855, William Thomson (later Lord Kelvin) related the Seebeck and Peltier effects to understand the TE phenomena. He observed that Peltier heat (Q_p) at a junction was proportional to the junction current (I) via the relationship $Q_p = \pi I$. He discovered that the Peltier and Seebeck effects are directly connected, with $\pi = S_\alpha T$. He also anticipated that the heat power (Q_t) is absorbed or evolved along a material rod having junctions at different temperatures. The absorbed or evolved heat is proportional to the current and temperature gradient along the rod. The proportionality factor is called the Thomson coefficient [12]. Later, Edmund Altenkirch came up with a model based on the discovery of the above-mentioned TE effects [13]. He defined a dimensionless quantity called the figure of merit, $ZT = \frac{S_\alpha^2 \sigma}{\kappa} T$, which is related to a combination of transport coefficients i.e., electrical conductivity (σ), thermal conductivity (κ), Seebeck coefficient (S_α), and temperature (T). The figure of merit for a thermoelectric material must be maximized to achieve high-performance [14]. Therefore, TE materials must have high S_α , a high σ , and a low κ , which are extremely challenging to achieve experimentally in the same material as these parameters are interdependent on each other. This interdependence amongst various transport parameters is discussed in the following subsections.

1.2.1 Seebeck coefficient

The Seebeck coefficient also known as thermopower, is responsible for causing current to flow when there is a temperature gradient [15, 16]. Consider an n -type semiconductor of length L

with the right side being hot compared to the left side. The electrons diffuse away from the hot side towards the cool side, and thus a positive voltage is developed to pull the electrons back and stop the current flow. The zero current under open-circuit conditions gives a negative open-circuit voltage, which is called the Seebeck coefficient. Similarly, the S_α for a p -type semiconductor is positive. This can be understood by the following differential equation:

$$J_x = -\sigma \frac{dV}{dx} - S_\alpha \sigma \frac{dT}{dx} \quad (1.1)$$

where, J_x is current density in positive x -direction, σ is the electrical conductivity, dV is the voltage gradient across the junction, and dT is the temperature gradient across the semiconductors.

Under open-circuit condition, $J_x = 0$, implying that $-\frac{dV}{dx} = S_\alpha \frac{dT}{dx}$ (1.2)

The S_α is thus the measure of the open-circuit voltage across a semiconductor that has a temperature gradient. From Mott's formula [17], the Seebeck coefficient is expressed as:

$$S_\alpha = \frac{8\pi^2 k_B^2}{3eh^2} m^* T \left(\frac{\pi}{3n} \right)^{2/3} \quad (1.3)$$

Here, e is the electronic charge, h is Planck's constant, n is carrier concentration, k_B is the Boltzmann constant, m^* is the effective mass of the charge carriers, and T is the absolute temperature. There is a direct correlation between the S_α and the effective mass of the charge carriers, whereas an inverse proportionality exists between S_α and carrier concentration. Achieving a greater S_α value demands a larger effective mass and low carrier concentrations.

1.2.2 Electrical conductivity

According to Drude's formula [18], the electrical conductivity depends directly on the carrier concentration and is inversely proportional to the m^* of the charge carriers [19]:

$$\sigma = \frac{ne^2\tau}{m^*} \quad (1.4)$$

Here, τ represents the average relaxation time between two consecutive collisions. Thus, the requirement of lower effective mass for higher electrical conductivity would lower the Seebeck

coefficient. Therefore, a quantity called power factor (PF) is defined as the product of the square of the Seebeck coefficient and the electrical conductivity.

1.2.3 Thermal conductivity

The electrons as well as phonons (lattice vibrations) both contribute to the thermal conductivity in a material. Therefore, the thermal conductivity (κ) is the sum of the electronic contribution (κ_e) and the lattice contribution (κ_l). The thermal conductivity due to electrons is expressed by the Wiedemann-Franz law [19], which is:

$$\kappa_e = L\sigma T \quad (1.5)$$

Where L is Lorentz number. It can be seen that the thermal conductivity due to electrons is directly proportional to that of electrical conductivity, which is contrary to the requirement of higher ZT , i.e., higher σ and a lower value of κ_e . Therefore, the value of κ_l becomes vital in optimizing the TE efficiency of a material. In metals, the electronic contribution is dominant over the lattice contribution in the heat transfer, whereas the lattice vibrations dominate over the electronic contribution for the heat transfer in semiconductors and insulators. Lattice thermal conductivity can be expressed as:

$$\kappa_l = \frac{1}{3} v_p \lambda C_v \quad (1.6)$$

Here, λ , v_p , and C_v represents mean free path, phonon velocity, and the specific heat capacity. Higher the scattering; the lesser would be the mean free path value, resulting in a lesser lattice thermal conductivity value. To have maximum TE performance, a material with a lower value of κ_l is desired.

In the present thesis, we have investigated various external factors that enhance the thermoelectric performance of a HfO₂.

1.3 Strategies for optimizing thermoelectric properties

There is a wide range of established and emerging TE materials but challenges often occur regarding their durability, stability, and high figure of merit. The key TE parameters are interdependent so innovative approaches are needed to decouple this interdependence and to improve the electronic properties without impeding the thermal properties and vice-versa. There exist strategies to enhance the figure of merit and minimize the thermal conductivity, some of which are discussed in this section.

1.3.1 Band structure engineering

The band structure engineering can be done by doping, strain, and effect of the external applied field [20–23]. The dopant in the host can influence the band structure due to the effect on the energy levels in the material to align electronic bands to increase valley degeneracy at the conduction band minimum or the valance band maximum [24]. This leads to an increase in the effective mass of the electron or hole and leads to an increase in available states around the Fermi level, which increases the S_α corresponding increase in the ZT . The influence of dopant also increases the charge carrier type (n -type and p -type) and carrier concentration in the material [25]. Doping increases phonon scattering through the additional disorder in the crystal structure [14]. Isovalent elemental doping induces mass disorder in the structure which reduces the lattice thermal conductivity without significant altering the electrical properties [26]. Lattice strain can arise from the difference in the atomic size of dopants which affects the electronic band structure and phonon scattering [20, 24].

1.3.2 Structural defects

In the oxide-based materials, there exist various point defects. A thorough investigation of the nature of defects, presence of defects, type of defects, and their effect on the various properties has been a hot topic for experimentalists and theorists. Native defects refer to the structural irregularities inside a crystal lattice that are directly associated with the constituent atoms. It may be vacancy, interstitial, and antisite defects. The presence of such imperfections may significantly impact the electrical and optical characteristics of a material. Understanding these effects is crucial for the purpose of designing and manipulating the properties of the material. The aforementioned defects may be classified as either p -type donors or n -type acceptors. The presence of defects inside a material gives rise to trap states located within the band gap, hence serving as a main determinant for altering the material's characteristics. These defect states can be classified as shallow or deep, depending on their proximity to the conduction band and valence band edges, which results in variation of S_α [14]. Therefore, researchers have shown great interest in examining these defect states using *first-principles* calculations [27]. Theoretical calculations are consistently used to interpret experimental findings. The presence of extra atoms at the interstitial locations within the crystal lattice may generate charge carriers and introduce additional scattering of phonons, leading to a decrease in thermal conductivity

[28]. The presence of vacancies inside the crystal lattice induces the formation of charge carriers [29–31].

1.4 Oxides as thermoelectric materials

Metal oxides are significant materials used in several domains of chemistry, physics, and materials science. These materials can possess many structural geometries, resulting in an electronic structure that may display different electronic properties. In comparison to the widely used TE materials such as BiTe, PbTe, and chalcogenides [32–34], oxides offer some compelling features like non-toxicity, high thermal stability, unique electronic and transport properties, and compatibility with the harsh environment [35–37]. Intense research has been carried out on the layered complex oxides, doped zinc oxide, and perovskite type oxides [38–42]. The morphology, stoichiometry, and doping in the transition metal oxides (TMOs) can tune their band gap, effective mass, and conductivity. The TMOs have a wide band gap and the effect of doping and vacancy formation can enhance the carrier concentration which further improves their transport properties [30, 37, 43]. So, to enhance their overall TE performance, a thorough investigation has been conducted by examining the impact of synthesis parameters and doping [44]. Experimental results have demonstrated high carrier concentration due to the existence of oxygen vacancy in HfO₂ [45]. Therefore, optimizing the carrier concentration in HfO₂ can boost its figure of merit.

1.5 Luminescence

Another aspect of this thesis is to explore the luminescent properties of HfO₂. The emission of light by a material when it is excited by an external energy source is called luminescence and such materials are known as luminescent materials or phosphor [46]. These materials are extensively utilized in various fields such as photocatalysis, sensors, drug delivery, and anti-counterfeiting applications. Luminescence is a common phenomenon in our daily life which can be seen in television screens, fluorescent lamps, scintillators, X-ray monitoring, and imaging [47]. Unlike conventional lighting, this phenomenon follows a cold process so the material that undergoes this process offers better efficiency. Based on the source of the excitation, luminescent materials are classified as discussed in Table 1:

Table 1: The source of excitation of various luminescence phenomena

Phenomena	Excitation Source	Application
Photoluminescence	Photon	Sensor Laser Light source Display Devices Highlighting Paints
Thermoluminescence	Any energy (Heat as stimulator)	Archaeological dating Geological Dating Dosimetry
Radioluminescence	X-rays	X-ray screen x-ray Scintillators
Electroluminescence	Electric field	LED Laser Diodes TFEL Display
Cathodoluminescence	Electron beam	CRO TV screen
Chemiluminescence	Chemical reaction	Chemical analysis

1.5.1 Photoluminescence

The photoluminescence (PL) process includes the absorption of energy in the form of photons by trap states and the subsequent emission of light [48]. When the electron returns to the lower energy or ground state the excess energy is released in the form of visible light leading to a radiative process or non-radiative process. To understand the PL process, we have schematically represented the Jablonski diagram as shown in Fig. 1.1. The ground state (S_0) and single excited states (S_1 and S_2) having paired electrons, whereas triplet state (T_1) have unpaired electrons. Further, based on the energy difference between the two electronic states this can be categorized into fluorescence and phosphorescence:

Fluorescence:

It is the absorption of electromagnetic radiation by atoms followed by immediate emission of light. It is a fast process of the order of 10^{-15} s or smaller. Excited electron undergoes electronic transition from singlet state to ground state radiatively. Since it is a spin-allowed transition, thus has a high probability of occurrence [48]. The emission of light halts as soon as the

excitation source is switched off. If the emitted radiation is of the same wavelength as of absorbed radiation, then the phenomenon is termed resonance fluorescence.

Phosphorescence:

It is a delayed emission process as compared to fluorescence. The emission process does not proceed immediately after absorption process, with the time difference being greater than 10^{-8} s. Light can be obtained even after the excitation source is switched off. Intersystem-crossing transfers the electron from a singlet state to a triplet state accompanied by a spin reversal [48]. The emission occurs from the triplet state to ground state and is a spin-forbidden transition, although occurs with a small probability due to spin-orbit coupling. Due to this, a transition from triplet state to ground state is delayed and late emission is observed.

1.5.2 Basic of Photoluminescence process:

Generally, the PL process occurs in the following sequential manner.

- The activators undergo energy absorption, resulting in their transition to an excited state.
- The activator undergoes relaxation to transition into the particular emission state.
- The emission of radiation occurs as a result of the de-excitation process of the activator, leading to its transition to the ground state.

The absorption and emission of the photons might proceed with the intrinsic defect states, vacancies, activator, and sensitizer. The activators (lanthanide ions or transition metal ions) are the dopants in a host, leading to create the trap centers which are responsible for luminescence. Whereas the sensitizers are other impurities added to the host, these impurities absorb the incident energy and transfer it to activators by sensitizing it. The sensitizers are used in the host material when the optical absorption of the activator is weak [47]. The absorption of the energy is basically done by the host or by the activator. The host material can absorb the energy of a particular wavelength from the different excitation sources which excite the electron. After the excitation, it can release the energy by the radiative and non-radiative processes.

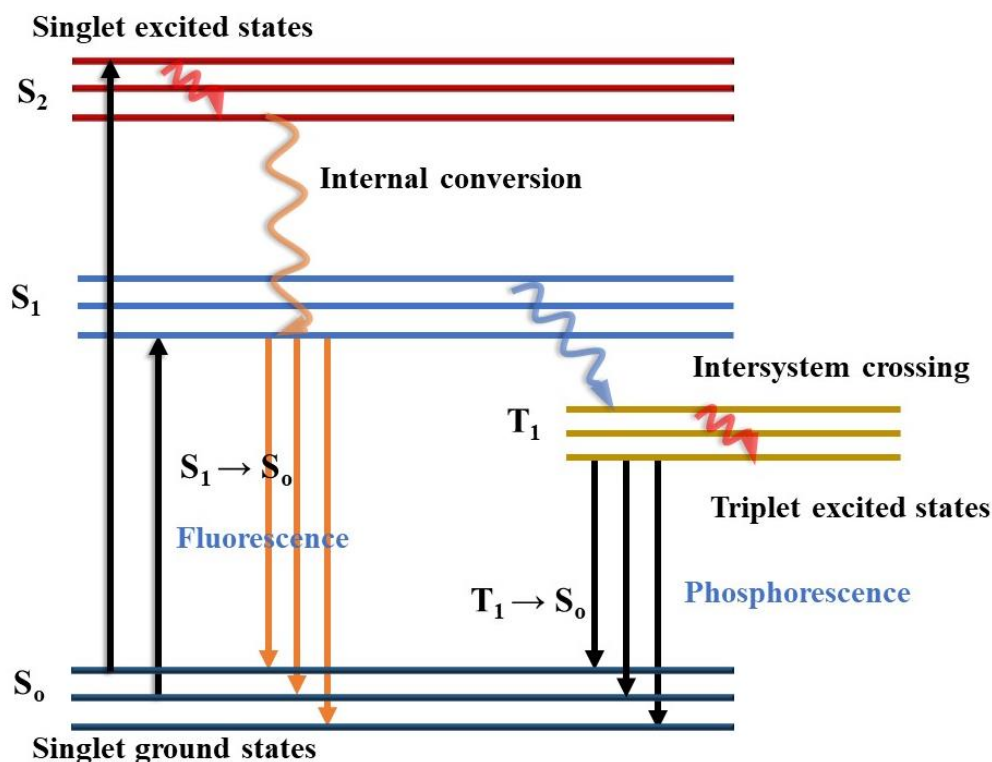


Fig. 1.1: A schematic representation of Jablonski diagram to explain photoluminescence.

The configuration coordinate diagram is used to explain the optical transitions as depicted in Fig 1.2. The ground and excited states of the atom are shown as parabola, which are due to harmonic assumptions of the vibrational motion of atoms. In the configuration coordinate diagram, the horizontal lines represent the vibrational energy levels, and X_0 represents the ground state equilibrium distance. The allowed transitions of the absorbing atom are within the energy states having the same spin and opposite parity are considered as the allowed transitions [49]. The electronic transitions are represented by the vertical lines. The diagram shows the shift in lowest point of the ground state and excited state which measure the interaction of excitation energy and absorbing center. The transition took place from the ground state parabola to the highest vibrational level of the excited state parabola. When the absorbing atom absorbs the excitation energy, there is a slight expansion in the vicinity of the absorber, resulting in a shift in energy to the right side. This shift (ΔX) measures the width of the absorption band. The emission takes place from the lowest point of the excited state parabola, giving out the balance of energy in the form of luminescence. The difference between the excitation and emission energy is referred to as Stokes shift.

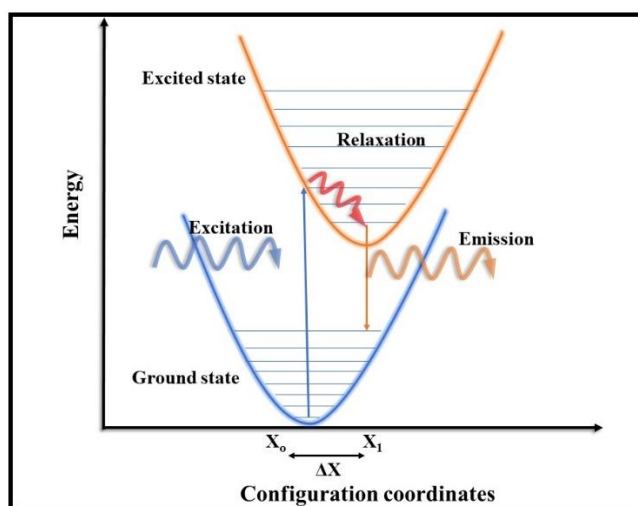


Fig. 1.2: Configuration coordinate diagram representing the absorption and emission transitions.

1.6 Rare earth dopants

The splendid performance of the rare earth (RE) dopants in the electronic display, solar cell, solid state lighting has attracted the attention of scientific society. The interesting luminescence features are due to intraconfigurational $4f \rightarrow 4f$ or interconfigurational $4f \rightarrow 5d$ transitions [46, 50]. In the RE elements, the progressive filling of $4f$ shells takes place and the $5s$ and $5p$ orbitals are strongly shielded by the $4f$ shells. The shielding effect of $4f$ is responsible for their unique optical properties [49]. In some RE ions, electron transfer takes place from $4f$ to $5d$ orbital and charge transfer state in which an electron in the neighbouring anion is transferred to $4f$ orbital. This charge transfer is also affected by the local crystal field symmetry around these RE dopants. Therefore, most of the RE ions show +3 oxidation state, and a few show a +2 oxidation state. The intraconfigurational $4f \rightarrow 4f$ transitions are parity forbidden. Moreover, these RE ions exhibit large Stokes shift, sharp emission band, long lifetime which is a prerequisite for designing a phosphor. The color of emitted light largely depends on the RE ion. The doping of RE ions in the host creates the energy level within the optical band gap of the host. The RE ions can exhibit three types of optical transitions i.e., intraconfigurational $4f^n$ transitions, $4f^n \rightarrow 4f^{n-1}5d^1$ transitions, and charge transfer which are discussed in detail.

1.6.1 Intraconfigurational transitions: The line like emission from RE ions provides high color purity to the emitted light. The emission color is the specific for the various dopants which are attributes to their characteristics $f \rightarrow f$ transitions. The selection rule state that the electronic transitions are only allowed between energy state of the same spin and opposite

parity. In the RE the sharp $4f^n$ transitions indicate the parity violation. The lack of inversion symmetry results in mixing of small fraction of $5d \rightarrow 4f$ wavefunctions this helps $4f^n$ transitions in gaining sharp and intense peaks. Three different interactions mechanism leads to different type of transitions among the RE ions [47, 49]. The interaction of the electric dipole of the RE^{3+} ion with the electric field vector of electromagnetic radiation result in electric dipole transition. The electric dipole moment has an odd parity and is forbidden as per Laporte selection rule. However, electric dipole transitions between $4f$ and $5d$ are parity allowed and therefore has oscillator strengths much more than that of $f - f$ transitions. The selection rules governing induced electric dipole transitions are $|\Delta l| = 1$; $|\Delta s| = 0$; $|\Delta L| \leq 6$; $|\Delta J| \leq 6$. The forbidden $f \rightarrow f$ electric dipole transitions come into to picture due to the admixing of $4f^n$ configuration with the excited configuration of the opposite parity (e.g., $4f^{n-1} \rightarrow 5d$) [46]. The mixing of the electronic states of opposite parity is allowed due to non-centro symmetric interactions. These transitions are relatively much weaker than the ordinary electric dipole transitions with intensities of the order 10^{-6} and are called induced/forbidden electric dipole transition.

When a spectroscopically active ion (RE ion) interacts with the magnetic field vector of the electromagnetic radiation through a magnetic dipole, it induces magnetic dipole transition. A magnetic dipole is created due to the movement of a charge over a curved path. The intensity of magnetic dipole transition is weak and it is also considered as a rotational displacement of charge. The magnetic dipole transition has even parity and selection rules governing induced electric dipole transitions are $|\Delta l| = \pm 1$; $|\Delta s| = 0$; $|\Delta L| \leq 0$; $|\Delta J| \leq 0$; $J = 0 \leftrightarrow 0$ is a forbidden transition [46]. This transition has even parity due to the fact that rotation is not reversed under inversion through a point. Hence a magnetic dipole operator exhibits even transformation properties under inversion and followed between the transitions with equal parity. If a charge is having quadrupole nature i.e., group of four point charges with total zero charge or zero dipole moment, then it shows electric quadrupole nature. An electric quadrupole transitions are followed by even parity and are much weaker than induced electric dipole and magnetic dipole transitions [46].

1.6.2 Interconfigurational transitions:

The transport of $4f$ electrons into the $5d$ subshell is permitted under the principle of parity. The influence of the ligand field effect on d orbitals results in a significant impact on the intensity of transitions. This susceptibility is particularly pronounced in the case of RE ions,

leading to the high intensity of these transitions [49]. The transitions occurring between the $4f^{n-1} \rightarrow 5d^1$ and $4f^n \rightarrow 5d^0$ energy levels exhibit a much wider range of excitation and emission wavelengths in comparison to the much narrower peaks seen in transitions between $4f \rightarrow 4f$ energy levels. The many $f \rightarrow d$ transitions may be explained by two fundamental phenomena: the Franck-Condon principle and the disruption of the degeneracy in the $4f$ ground state [48]. Moreover, the degeneracy of the $4f$ orbitals is disrupted as a result of the interaction between the electron's spin and its orbital motion, known as spin-orbit coupling, leading to the formation of many energy levels. Furthermore, it is worth noting that the activator ion inside a host crystal has the potential to experience both centroid shift and crystal field splitting. The concept of centroid shift refers to the displacement of energy levels in a five-dimensional system towards lower values, which occurs as a result of a reduction in inter-electronic repulsion. The phenomenon known as crystal field splitting refers to the division of $5d$ energy levels resulting from the influence of the host environment on the activator ion that has been doped into it. The amplitude of the crystal field effect is contingent upon many factors, including the bond length between the activator ion and the ligand, the degree of overlap between molecular orbitals, the type of the bond (whether it is ionic or covalent), the characteristics of the surrounding environment, and the site symmetry of the activator ion.

1.7 Solid state lighting

Artificial lighting has created versatile potential in indoor and outdoor systems for extending the productive day into non-sunlit hours of the night, significantly increasing human life production. Globally, the manufacturing of artificial lighting consumes enormous amounts of energy. Previously, traditional lighting sources such as fire lamps (first generation), incandescent bulbs (second generation), and fluorescent lamps (third generation) were utilized for artificial illumination that relied on either heat or gas discharge [51]. These lighting systems generate high temperatures, resulting in significant energy losses. In recent years, the increasing need for yearly energy consumption, as well as other environmental concerns, have compelled the population to migrate towards energy-saving and environmentally friendly alternatives to traditional lighting sources [51]. Solid state lighting (SSL) sources, which have significantly lowered yearly energy consumption, are presently operating as a fourth generation lighting technology in this respect. SSL refers to the light emitted by a solid, which might be a semiconductor or an insulator. The visible light in this revolutionary lighting system originates from solid-state light-emitting diodes, which effectively and immediately convert power to

light. LEDs have reduced the use of incandescent and fluorescent lights because they outperform them in terms of energy efficiency, affordability, proficiency, cost effectiveness, and color-balanced white light [51]. There are primarily two ways available for fabricating *w*-LEDs. The first is to use phosphor-free RGB-LEDs, which combine monochromatic light from red, green, and blue LEDs to produce white light [52]. These integrated LEDs need separate driving currents for each LED to provide consistent white light, which is difficult to acquire and makes it less accessible. Furthermore, differing driving currents cause deterioration of different color LEDs and color temperature instability [53]. Another strategy is to achieve white light emission by combining a blue light emitting InGaN chip with a yellow phosphor (YAG: Ce³⁺), which is currently employed in the majority of commercial *w*-LEDs [54, 55]. Despite having several advantages over RGB-LEDs, such as low cost, ease of fabrication, and high brightness, such *w*-LEDs have some drawbacks, such as a low color rendering index, a high correlated color temperature (CCT >7765 K), and low efficiency due to the lack of the red component [56]. As a result, researchers all across the world presented other solutions to this vexing issue, such as "blue LED coated with green and red phosphors" and "*n*-UV LED coated with an appropriate mixture of RGB phosphors." Both of the aforementioned techniques seem to need the manufacture of a viable red emitting phosphor. A multiphase phosphor method, on the other hand, results in decreased efficiency due to the re-absorption of blue emission by RG phosphors [46, 49]. All of these problems may be addressed by using a more advanced way of coating a co-activated single-phase phosphor that emits warm white light. As-prepared co-activated single-phase phosphors may provide outstanding color reproducibility, adequate CCT, spectrum tunability, and eye-soothing perception.

1.8 Importance of present host material: HfO₂

HfO₂, an IV-B oxide and a member of the transition metal oxide family, is widely recognized as a highly promising and technologically significant material. This is primarily due to its notable characteristics, including a substantial band gap ranging from 5.5 to 6.0 eV, a high dielectric constant, high thermal and chemical stability, and an impressively high melting point exceeding 2700 °C [57–60]. HfO₂ occurs in three distinct polymorphic forms within the natural environment. The monoclinic baddeleyite phase (*m*, space group $P2_1/c$) exhibits stability at low temperatures, undergoing a transformation to a tetragonal structure (*t*, space group $P4_2/nmc$) at around 2000 °C [61, 62]. At elevated temperatures, a transformation occurs wherein the material adopts the cubic fluorite structure (*c*, space group $Fm\bar{3}m$) [63]. The pressure induced orthorhombic phase (*o*, space group $Pbca, Pnma, P2_1c$) [64]. The effect of external parameters

such as pressure, temperature, and doping have been explored for phase transition in HfO_2 which makes it a promising candidate in the field of ferroelectric, piezoelectric, and optical applications [65–68]. HfO_2 is applicable in several fields such as high temperature thermal barrier coatings, as well as in high mechanical resistance applications [69–72]. Considerable effort has been devoted to making HfO_2 as a viable substitute for SiO_2 as a gate dielectric which can minimize leakage current [73]. HfO_2 is presently being recognized as a promising candidate for use as a heavy scintillator with excellent gamma- and X-ray stopping power [74], [75]. Recently, there has been an observation of a wide blue emission band in the undoped HfO_2 lattice when it is in the form of a thin film [76]. The wide band gap and low phonon frequency make it a promising host for doping of rare earth (RE) activator ions [77]. Several investigations have been conducted to investigate the luminescence characteristics of RE doped HfO_2 [78–81]. These studies have shown the potential to adjust the emission color of the material by combining the inherent wide emission with that of the optically active doping ions. Moreover, significant advancements have been made in manipulating the size and structural characteristics of nanocrystals, to produce HfO_2 -based ceramics and nanocomposites that exhibit a broad band gap and transparency [82]. The thin film of HfO_2 has a low thermal conductivity which is a desirable condition for a TE material [83, 84]. The naturally occurring oxygen vacancy defect and doping lead to the enhancement of the carrier concentration of HfO_2 [85]. It has been found in various experimental and theoretical studies that doping, which creates the trap states within the forbidden gap causes a reduction in the band gap of HfO_2 [45, 86, 87].

In light of the aforementioned characteristics of HfO_2 , we have investigated the possibilities of high TE performance and enhanced optical properties with doping, pressure, and varying carrier concentration.

1.9 Objective of present thesis

During the past few years, the oxide-based materials have significantly contributed to the field of TE and LED applications. Several attempts have been made to enhance the luminescent properties and tuning the transport parameters. The altering of the band gap and the stability remains the prime challenge for the practical applicability of the material. This thesis contains a detailed study of structural and electronic properties of HfO_2 based materials. The effect of doping, temperature and pressure on the structural and optical properties are discussed in detail. The tuning of band structure under the doping of various elements at anionic and cationic sites

in HfO₂ was explored for the TE and optical response. The main objectives of the present thesis work are:

- **To unravel the thermoelectric properties of pure and doped HfO₂**
- **To ascertain the pressure induced structure phase transition in *m*-HfO₂**
- **To analyze the effects of various dopants (Ti, S, and Si) on optical properties of HfO₂**
- **To explore the structural and luminescent properties of pure and Eu³⁺ doped HfO₂**

The present thesis embraces seven chapters to accomplish the research objectives.

1.10 Scope of present thesis

The HfO₂ polymorphs show phase dependent properties such as wide band gap, high transmittance, and mechanical hardness making it suitable for optical coatings, bandpass filters, UV mirrors, efficient absorbers for gamma, optical devices, gate oxides, and ferroelectric. We studied the optical and TE properties for future green energy applications. We examined the structural phase transition and electronic and optical properties utilizing experimental and theoretical approaches. A low temperature synthesis route and effect of rare earth dopant was implemented to enhance its luminescent properties.

Secondly, we explored the TE performance of the various existing phases of HfO₂. Enhancing the TE performance of HfO₂ is a daunting task given its wide band gap. However, carrier concentration optimization is an effective strategy to enhance the figure of merit. The experimental reports have shown the possibility of high carrier concentration and low thermal conductivity in HfO₂. We obtained encouraging results regarding TE performance of various polymorphs of HfO₂. Due to a lack of experimental resources currently, we could not verify our predictions of transport properties experimentally. But we hope that this study will pave the way for experimentalists to harness the material's unique characteristics in designing the future TE and optical materials.

Reference

- [1] A. Qazi *et al.*, “Towards Sustainable Energy: A Systematic Review of Renewable Energy Sources, Technologies, and Public Opinions,” *IEEE Access*, 7, 63837–63851, 2019, doi: 10.1109/ACCESS.2019.2906402.
- [2] R. M. Elavarasan *et al.*, “A Comprehensive Review on Renewable Energy Development, Challenges, and Policies of Leading Indian States with an International Perspective,” *IEEE Access*, 8, 74432–74457, 2020, doi: 10.1109/ACCESS.2020.2988011.
- [3] Y. Jia *et al.*, “Wearable Thermoelectric Materials and Devices for Self-Powered Electronic Systems,” *Adv. Mater.*, 33, 2102990, 2021, doi: 10.1002/adma.202102990.
- [4] X.-L. Shi, J. Zou, and Z.-G. Chen, “Advanced Thermoelectric Design: From Materials and Structures to Devices,” *Chem. Rev.*, 120, 7399–7515, 2020, doi: 10.1021/acs.chemrev.0c00026.
- [5] T. M. Tritt, “Thermoelectric Phenomena, Materials, and Applications,” *Annu. Rev. Mater. Res.*, 41, 433–448, 2011, doi: 10.1146/annurev-matsci-062910-100453.
- [6] H. Xiang, R. Wang, J. Chen, F. Li, and H. Zeng, “Research progress of full electroluminescent white light-emitting diodes based on a single emissive layer,” *Light Sci. Appl.*, 10, 206, 2021, doi: 10.1038/s41377-021-00640-4.
- [7] P. A. Østergaard, N. Duic, Y. Noorollahi, H. Mikulcic, and S. Kalogirou, “Sustainable development using renewable energy technology,” *Renew. Energy*, 146, 2430–2437, 2020, doi: 10.1016/j.renene.2019.08.094.
- [8] D. Enescu, “Thermoelectric Energy Harvesting: Basic Principles and Applications,” in *Green Energy Advances*, D. Enescu, Ed., IntechOpen, 2019. doi: 10.5772/intechopen.83495.
- [9] P. K. Sharma, T. D. Senguttuvan, V. K. Sharma, and S. Chaudhary, “Revisiting the thermoelectric properties of lead telluride,” *Mater. Today Energy*, 21, 100713, 2021, doi: 10.1016/j.mtener.2021.100713.
- [10] T. J. Seebeck, “Magnetische polarisation der metalle und erze durch temperaturdifferenz,” 10, 260–373, 1825.
- [11] J. C. A. Peltier, “Nouvelles exp’eriences sur la caloricit’e des courants ’electrique, [new experiments on the heat effects of electric currents],” 56, 371–386, 1834.
- [12] D. M. Rowe, *CRC handbook of thermoelectrics*. Boca Raton New York London: CRC press, 1994.
- [13] E. Altenkirch., “Physikalische zeitschrift,” 10, 560–580, 1909.

- [14] G. J. Snyder and E. S. Toberer, “Complex thermoelectric materials,” *Nat. Mater.*, 7, 105–114, 2008, doi: 10.1038/nmat2090.
- [15] H. J. Goldsmid, *Introduction to Thermoelectricity*, Springer Series in Materials Science, Berlin, Heidelberg: Springer Berlin Heidelberg, 121, 2016. doi: 10.1007/978-3-662-49256-7.
- [16] J. R. Sootsman, D. Y. Chung, and M. G. Kanatzidis, “New and Old Concepts in Thermoelectric Materials,” *Angew. Chem. Int. Ed.*, 48, 8616–8639, 2009, doi: 10.1002/anie.200900598.
- [17] M. Jonson and G. D. Mahan, “Mott’s formula for the thermopower and the Wiedemann-Franz law,” *Phys. Rev. B*, 21, 4223–4229, 1980, doi: 10.1103/PhysRevB.21.4223.
- [18] P. Drude, “Zur Elektronentheorie der Metalle; II. Teil. Galvanomagnetische und thermomagnetische Effecte,” *Ann. Phys.*, 308, 369–402, 1900, doi: 10.1002/andp.19003081102.
- [19] C. Kittel, *Introduction to solid state physics*, 8. ed., [Repr.]. Hoboken, NJ: Wiley, 20.
- [20] Y. Li, K. Ma, X. Fan, F. Liu, J. Li, and H. Xie, “Enhancing thermoelectric properties of monolayer GeSe via strain-engineering: A first principles study,” *Appl. Surf. Sci.*, vol. 521, 146256, 2020, doi: 10.1016/j.apsusc.2020.146256.
- [21] K. H. Lee, S. Kim, H.-S. Kim, and S. W. Kim, “Band Convergence in Thermoelectric Materials: Theoretical Background and Consideration on Bi–Sb–Te Alloys,” *ACS Appl. Energy Mater.*, 3, 2214–2223, 2020, doi: 10.1021/acsaem.9b02131.
- [22] J. L. Baker *et al.*, “Pressure-Induced Enhancement of Thermoelectric Figure of Merit and Structural Phase Transition in TiNiSn,” *J. Phys. Chem. Lett.*, 12, 1046–1051, 2021, doi: 10.1021/acs.jpcclett.0c03609.
- [23] M. Chen *et al.*, “Magnetic-field-enhanced high thermoelectric performance in narrow-band-gap polycrystalline semiconductor $\text{Ag}_{2+\delta}\text{Te}$,” *Mater. Today Phys.*, 36, 101161, 2023, doi: 10.1016/j.mtphys.2023.101161.
- [24] Y. Pei, H. Wang, and G. J. Snyder, “Band Engineering of Thermoelectric Materials,” *Adv. Mater.*, 24, 6125–6135, 2012, doi: 10.1002/adma.201202919.
- [25] Sangeeta and M. Singh, “Augmented thermoelectric performance of LiCaX (X = As, Sb) Half Heusler compounds via carrier concentration optimization,” *J. Phys. Chem. Solids*, 174, 111182, 2023, doi: 10.1016/j.jpcs.2022.111182.
- [26] J. Palraj, M. Moorthy, S. Katlakunta, and S. Perumal, “Isovalent Bi substitution induced low thermal conductivity and high thermoelectric performance in n-type InSb,” *Ceram. Int.*, 48, 29284–29290, 2022, doi: 10.1016/j.ceramint.2022.05.282.

- [27] S. Pandey, A. Shukla, and A. Tripathi, “Elucidating the influence of native defects on electrical and optical properties in semiconducting oxides: An experimental and theoretical investigation,” *Comput. Mater. Sci.*, 210, 111037, 2022, doi: 10.1016/j.commatsci.2021.111037.
- [28] L. Kush, S. Srivastava, Y. Jaiswal, and Y. Srivastava, “Thermoelectric behaviour with high lattice thermal conductivity of Nickel base $\text{Ni}_2\text{CuCrFeAl}_x$ ($x = 0.5, 1.0, 1.5$ and 2.5) high entropy alloys,” *Mater. Res. Express*, 7, 035704, 2020, doi: 10.1088/2053-1591/ab7d5a.
- [29] H. Lee, R. Chidambaram Seshadri, S. J. Han, and S. Sampath, “ TiO_{2-x} based thermoelectric generators enabled by additive and layered manufacturing,” *Appl. Energy*, 192, 24–32, 2017, doi: 10.1016/j.apenergy.2017.02.001.
- [30] A. T. T. Pham *et al.*, “Oxygen vacancy-activated thermoelectric properties of ZnO ceramics,” *Ceram. Int.*, S0272884223035319, Nov. 2023, doi: 10.1016/j.ceramint.2023.11.099.
- [31] Z. Yuan, J. Gong, S. Xu, Z. Li, and G. Tang, “Investigation of the thermoelectric properties of reduced Nb-doped TiO_2 - ceramics,” *J. Alloys Compd.*, 710, 778–783, Jul. 2017, doi: 10.1016/j.jallcom.2017.03.336.
- [32] K. A. Morgan, I. Zeimpekis, Z. Feng, and D. Hewak, “Enhancing thermoelectric properties of bismuth telluride and germanium telluride thin films for wearable energy harvesting,” *Thin Solid Films*, 741, 139015, 2022, doi: 10.1016/j.tsf.2021.139015.
- [33] Y. Xiao and L.-D. Zhao, “Charge and phonon transport in PbTe-based thermoelectric materials,” *Npj Quantum Mater.*, 3, 55, 2018, doi: 10.1038/s41535-018-0127-y.
- [34] Y. Shi, C. Sturm, and H. Kleinke, “Chalcogenides as thermoelectric materials,” *J. Solid State Chem.*, 270, 273–279, 2019, doi: 10.1016/j.jssc.2018.10.049.
- [35] T. Watanabe, S. Takawane, Y. Baba, J. Akaiwa, A. Kondo, and T. Ohba, “Superior Thermal Stability and High Photocatalytic Activity of Titanium Dioxide Nanocatalysts in Carbon Nanotubes,” *J. Phys. Chem. C*, 127, 16861–16869, 2023, doi: 10.1021/acs.jpcc.3c03619.
- [36] W. Chen *et al.*, “Synthesis, Thermal Stability and Properties of ZnO_2 Nanoparticles,” *J. Phys. Chem. C*, 113, 1320–1324, 2009, doi: 10.1021/jp808714v.
- [37] A. I. Romanenko, G. E. Chebanova, T. Chen, W. Su, and H. Wang, “Review of the thermoelectric properties of layered oxides and chalcogenides,” *J. Phys. Appl. Phys.*, 55, 143001, 2022, doi: 10.1088/1361-6463/ac3ce6.

- [38] Z. Zhao, X. Zhang, and L.-D. Zhao, “Strategies for manipulating thermoelectric properties of layered oxides,” *Matter*, 6, 3274–3295, 2023, doi: 10.1016/j.matt.2023.07.014.
- [39] F. Delorme, C. F. Martin, P. Marudhachalam, D. Ovono Ovono, and G. Guzman, “Effect of Ca substitution by Sr on the thermoelectric properties of $\text{Ca}_3\text{Co}_4\text{O}_9$ ceramics,” *J. Alloys Compd.*, 509, 2311–2315, 2011, doi: 10.1016/j.jallcom.2010.10.209.
- [40] B. Sabir, G. Murtaza, Q. Mahmood, R. Ahmad, and K. C. Bhamu, “First principles investigations of electronics, magnetic, and thermoelectric properties of rare earth based PrYO_3 (Y=Cr, V) perovskites,” *Curr. Appl. Phys.*, 17, 1539–1546, 2017, doi: 10.1016/j.cap.2017.07.010.
- [41] M. Saxena and T. Maiti, “Effect of Ba-doping on high temperature thermoelectric properties of $\text{Sr}_2\text{TiMoO}_6$ double perovskites,” *J. Alloys Compd.*, 710, 472–478, 2017, doi: 10.1016/j.jallcom.2017.03.264.
- [42] B. Feng and W. Mao, “The mechanism of the effect of V doping on the thermoelectric properties of ZnO ceramics,” *J. Solid State Chem.*, 305, 122645, 2022, doi: 10.1016/j.jssc.2021.122645.
- [43] X. Liu *et al.*, “High Power Factor Nb-Doped TiO_2 Thermoelectric Thick Films: Toward Atomic Scale Defect Engineering of Crystallographic Shear Structures,” *ACS Appl. Mater. Interfaces*, 15, 5071–5085, 2023, doi: 10.1021/acsami.2c16587.
- [44] P. Zhang *et al.*, “Development and Applications of Thermoelectric Oxide Ceramics and Devices,” *Energies*, 16, 4475, 2023, doi: 10.3390/en16114475.
- [45] E. Hildebrandt, J. Kurian, M. M. Müller, T. Schroeder, H.-J. Kleebe, and L. Alff, “Controlled oxygen vacancy induced *p*-type conductivity in HfO_{2-x} thin films,” *Appl. Phys. Lett.*, 99, 112902, 2011, doi: 10.1063/1.3637603.
- [46] D. R. Viji, Ed., *Luminescence of Solids*. Boston, MA: Springer US, 1998. doi: 10.1007/978-1-4615-5361-8.
- [47] C. Ronda, Ed., *Luminescence: From Theory to Applications*, 1st ed. Wiley, 2007. doi: 10.1002/9783527621064.
- [48] C. N. Banwell, *Fundamentals of molecular spectroscopy*, 2nd ed. London, New York: McGraw-Hill, 1972.
- [49] G. Blasse and B. C. Grabmaier, *Luminescent Materials*. Berlin, Heidelberg: Springer Berlin Heidelberg, 1994. doi: 10.1007/978-3-642-79017-1.

- [50] X. Song, R. Fu, S. Agathopoulos, H. He, X. Zhao, and R. Li, “Luminescence and Energy-Transfer Mechanism in $\text{SrSi}_2\text{O}_2\text{N}_2:\text{Ce}^{3+}$, Eu^{2+} Phosphors for White LEDs,” *J. Electrochem. Soc.*, 157, J34, 2010, doi: 10.1149/1.3270491.
- [51] P. Morgan Pattison, M. Hansen, and J. Y. Tsao, “LED lighting efficacy: Status and directions,” *Comptes Rendus Phys.*, 19, 134–145, 2018, doi: 10.1016/j.crhy.2017.10.013.
- [52] P. Alstone and A. Jacobson, “LED advances accelerate universal access to electric lighting,” *Comptes Rendus Phys.*, 19, 146–158, 2018, doi: 10.1016/j.crhy.2017.10.015.
- [53] S. C. Allen and A. J. Steckl, “A nearly ideal phosphor-converted white light-emitting diode,” *Appl. Phys. Lett.*, 92, 143309, 2008, doi: 10.1063/1.2901378.
- [54] A. J. Fernández-Carrión, M. Ocaña, J. García-Sevillano, E. Cantelar, and A. I. Becerro, “New Single-Phase, White-Light-Emitting Phosphors Based on $\delta\text{-Gd}_2\text{Si}_2\text{O}_7$ for Solid-State Lighting,” *J. Phys. Chem. C*, 118, 18035–18043, 2014, doi: 10.1021/jp505524g.
- [55] Q. Tang, T. Yang, H. Huang, J. Ao, B. Peng, and B. Guo, “A novel near-ultraviolet-light excitable Eu^{3+} -doped $\text{Sr}_2\text{LaTaO}_6$ red phosphor for white-light-emitting diodes,” *Optik*, 240, 166908, 2021, doi: 10.1016/j.ijleo.2021.166908.
- [56] X. Yang, J. Chen, C. Chai, S. Zheng, and C. Chen, “Near ultraviolet excited white light emitting diode (WLED) based on the blue $\text{LiCaPO}_4:\text{Eu}^{2+}$ phosphor,” *Optik*, 198, 163238, 2019, doi: 10.1016/j.ijleo.2019.163238.
- [57] S. Bengi and M. M. Bülbül, “Electrical and dielectric properties of $\text{Al}/\text{HfO}_2/\text{p-Si}$ MOS device at high temperatures,” *Curr. Appl. Phys.*, 13, 1819–1825, 2013, doi: 10.1016/j.cap.2013.07.004.
- [58] K. Yamamoto, S. Hayashi, M. Niwa, M. Asai, S. Horii, and H. Miya, “Electrical and physical properties of HfO_2 films prepared by remote plasma oxidation of Hf metal,” *Appl. Phys. Lett.*, 83, 2229–2231, 2003, doi: 10.1063/1.1609246.
- [59] J. Wang, H. P. Li, and R. Stevens, “Hafnia and hafnia-toughened ceramics,” *J. Mater. Sci.*, 27, 5397–5430, 1992, doi: 10.1007/BF00541601.
- [60] K. Matsumoto, Y. Itoh, and T. Kameda, “EB-PVD process and thermal properties of hafnia-based thermal barrier coating,” *Sci. Technol. Adv. Mater.*, 4, 153–158, 2003, doi: 10.1016/S1468-6996(03)00009-3.
- [61] H. Padma Kumar, S. Vidya, S. Saravana Kumar, C. Vijayakumar, S. Solomon, and J. K. Thomas, “Optical properties of nanocrystalline HfO_2 synthesized by an auto-igniting combustion synthesis,” *J. Asian Ceram. Soc.*, 3, 64–69, 2015, doi: 10.1016/j.jascer.2014.10.009.

- [62] T. Tobase *et al.*, “Pre-Transitional Behavior in Tetragonal to Cubic Phase Transition in HfO₂ Revealed by High Temperature Diffraction Experiments,” *Phys. Status Solidi B*, 255, 1800090, 2018, doi: 10.1002/pssb.201800090.
- [63] N. Kumar, B. P. A. George, H. Abrahamse, V. Parashar, S. S. Ray, and J. C. Ngila, “A novel approach to low-temperature synthesis of cubic HfO₂ nanostructures and their cytotoxicity,” *Sci. Rep.*, 7, 9351, 2017, doi: 10.1038/s41598-017-07753-0.
- [64] D. Banerjee, R. Sewak, C. C. Dey, D. Toprek, and P. K. Pujari, “Orthorhombic phases in bulk pure HfO₂: Experimental observation from perturbed angular correlation spectroscopy,” *Mater. Today Commun.*, 26, 101827, 2021, doi: 10.1016/j.mtcomm.2020.101827.
- [65] O. Ohtaka *et al.*, “Phase Relations and Volume Changes of Hafnia under High Pressure and High Temperature,” *J. Am. Ceram. Soc.*, 84, 1369–1373, 2004, doi: 10.1111/j.1151-2916.2001.tb00843.x.
- [66] W. Zhang *et al.*, “Pressure-Induced Phase Transition and Compression Properties of HfO₂ Nanocrystals,” *Inorg. Chem.*, 61, 3498–3507, 2022, doi: 10.1021/acs.inorgchem.1c03450.
- [67] B. Lai *et al.*, “Study on the phase transition dynamics of HfO₂ -based ferroelectric films under ultrafast electric pulse,” *J. Phys. Condens. Matter*, 33, 405402, 2021, doi: 10.1088/1361-648X/ac14f9.
- [68] Q.-J. Hong *et al.*, “Combined computational and experimental investigation of high temperature thermodynamics and structure of cubic ZrO₂ and HfO₂,” *Sci. Rep.*, 8, 14962, 2018, doi: 10.1038/s41598-018-32848-7.
- [69] M. Berdova *et al.*, “Hardness, elastic modulus, and wear resistance of hafnium oxide-based films grown by atomic layer deposition,” *J. Vac. Sci. Technol. Vac. Surf. Films*, 34, 051510, 2016, doi: 10.1116/1.4961113.
- [70] N.-W. Pi *et al.*, “Microstructure of hard and optically transparent HfO₂ films prepared by high-power impulse magnetron sputtering with a pulsed oxygen flow control,” *Thin Solid Films*, 619, 239–249, 2016, doi: 10.1016/j.tsf.2016.10.059.
- [71] P. Piluso, M. Ferrier, C. Chaput, J. Claus, and J.-P. Bonnet, “Hafnium dioxide for porous and dense high-temperature refractories (2600°C),” *J. Eur. Ceram. Soc.*, 29, 961–968, 2009, doi: 10.1016/j.jeurceramsoc.2008.07.036.
- [72] E. Mańkowska, M. Mazur, M. Kalisz, M. Grobelny, J. Domaradzki, and D. Wojcieszak, “Characterization of Structural, Optical, Corrosion, and Mechanical Properties of HfO₂

- Thin Films Deposited Using Pulsed DC Magnetron Sputtering,” *Materials*, 16, 5005, 2023, doi: 10.3390/ma16145005.
- [73] M. Bohr, R. Chau, T. Ghani, and K. Mistry, “The High-k Solution,” *IEEE Spectr.*, 44, 29–35, 2007, doi: 10.1109/MSPEC.2007.4337663.
- [74] H. Fukushima, D. Nakauchi, T. Kato, N. Kawaguchi, and T. Yanagida, “Investigation of scintillation properties of Hf-based oxide materials,” *Jpn. J. Appl. Phys.*, 62, 010506, 2023, doi: 10.35848/1347-4065/ac9105.
- [75] S. Kurosawa *et al.*, “Investigation of a Tb-Doped HfO₂ Single Crystal Grown by a Skull Melting Method,” *Key Eng. Mater.*, 508, 81–86, 2012, doi: 10.4028/www.scientific.net/KEM.508.81.
- [76] R.-T. Wen *et al.*, “Blue-luminescent hafnia nanoclusters synthesized by plasma gas-phase method,” *Mater. Chem. Phys.*, 130, 823–826, 2011, doi: 10.1016/j.matchemphys.2011.08.006.
- [77] S. Stojadinović, N. Tadić, and R. Vasilic, “Photoluminescence properties of Er³⁺/Yb³⁺ doped ZrO₂ coatings formed by plasma electrolytic oxidation,” *J. Lumin.*, 208, 296–301, 2019, doi: 10.1016/j.jlumin.2018.12.067.
- [78] S. Kumar, T. Dehury, and C. Rath, “Stabilization of Cubic Phase at Room Temperature and Photoluminescence Properties of Dy and Sm Co-Doped HfO₂ Nanoparticles,” *ECS J. Solid State Sci. Technol.*, 10, 081009, 2021, doi: 10.1149/2162-8777/ac1c54.
- [79] N. Sekar, B. Ganesan, H. R. A. S. Khilafath, P. Aruna, and S. Ganesan, “Synthesis and Characterization of Gd³⁺ Doped HfO₂ Nanoparticles for Radiotherapy Applications,” *J. Nanosci. Nanotechnol.*, 20, 819–827, 2020, doi: 10.1166/jnn.2020.16901.
- [80] T. Dehury, S. Kumar, and C. Rath, “Structural transformation and bandgap engineering by doping Pr in HfO₂ nanoparticles,” *Mater. Lett.*, 302, 130413, 2021, doi: 10.1016/j.matlet.2021.130413.
- [81] C. L. Ordóñez-Romero *et al.*, “Effects of the HfO₂ sinterization temperature on the erbium luminescence,” *J. Lumin.*, 145, 713–716, 2014, doi: 10.1016/j.jlumin.2013.08.050.
- [82] I. Villa *et al.*, “Size-Dependent Luminescence in HfO₂ Nanocrystals: Toward White Emission from Intrinsic Surface Defects,” *Chem. Mater.*, 28, 3245–3253, 2016, doi: 10.1021/acs.chemmater.5b03811.
- [83] L. Momenzadeh, I. V. Belova, and G. E. Murch, “Molecular Dynamics Determination of the Lattice Thermal Conductivity of the Cubic Phase of Hafnium Dioxide,” *Diffus. Found.*, 27, 177–185, 2020, doi: 10.4028/www.scientific.net/DF.27.177.

- [84] M. A. Panzer *et al.*, “Thermal Properties of Ultrathin Hafnium Oxide Gate Dielectric Films,” *IEEE Electron Device Lett.*, 30, 1269–1271, 2009, doi: 10.1109/LED.2009.2032937.
- [85] N. Kaiser *et al.*, “Defect-Stabilized Substoichiometric Polymorphs of Hafnium Oxide with Semiconducting Properties,” *ACS Appl. Mater. Interfaces*, 14, 1290–1303, 2022, doi: 10.1021/acsami.1c09451.
- [86] N. Hadacek, A. Nosov, L. Ranno, P. Strobel, and R.-M. Galéra, “Magnetic properties of HfO₂ thin films,” *J. Phys. Condens. Matter*, 19, 486206, 2007, doi: 10.1088/0953-8984/19/48/486206.
- [87] T. V. Perevalov *et al.*, “The atomic and electronic structure of Hf_{0.5}Zr_{0.5}O₂ and Hf_{0.5}Zr_{0.5}O₂:La films,” *J. Sci. Adv. Mater. Devices*, 6, 595–600, 2021, doi: 10.1016/j.jsamd.2021.08.001.

Theoretical and experimental methodology

This chapter briefly discusses the theoretical methods and experimental techniques used for the presented work. The discussion starts with the physical interpretation of many-body problem. Subsequently, we discuss the emergence of Density Functional Theory (DFT), one of the prominent methods for solving many-particle system. In addition to that, the necessary discussion on exchange correlation functionals are included. The semi-classical Boltzmann transport theory, which was used to obtain transport properties, is also discussed. Later part of this chapter discusses the experimental details for fabrication and characterization of the material.

2.1 Introduction to Many-electron System

Schrödinger equation describes the behavior of single electron system nicely [1, 2]. However, the many-electron system has never been solved precisely using this equation. So, what is the problem with the many-electron systems? How to study the dynamics of electrons in solids? To answer these questions, let us begin with the Schrödinger equation for such systems:

$$\hat{H}\Psi(\vec{R}, \vec{r}) = E\Psi(\vec{R}, \vec{r}) \quad (2.1)$$

where \hat{H} and $\Psi(\vec{R}, \vec{r})$ are the Hamiltonian operator and wave function of the system, respectively. \vec{R} and \vec{r} are the position coordinates of the nucleus and electrons, respectively. E is the corresponding eigen energy value of the system. On ignoring relativity, gravity, and time, the Hamiltonian operator can be written as:

$$\hat{H} = -\frac{\hbar^2}{2} \sum_I \frac{\nabla_I^2}{m_I} - \frac{\hbar^2}{2m_e} \sum_i \nabla_i^2 + \sum_I \frac{Z_I Z_J e^2}{|\vec{R}_I - \vec{R}_J|} - \sum_I \sum_i \frac{Z_I Z_J e^2}{|\vec{r}_i - \vec{R}_I|} + \sum_j \sum_{i>j} \frac{e^2}{|\vec{r}_i - \vec{r}_j|} \quad (2.2)$$

The kinetic energy of nuclei and electrons are represented by 1st and 2nd terms, respectively. 3rd, 4th, and 5th terms represent the potential energies from the interactions by nuclei-nuclei, electrons-nuclei, and electrons-electrons, respectively.

The electrons are quantum particles; therefore, it is impossible to locate their position due to the associated wave nature. Due to the uncertainty in the position of electrons, the distance (\vec{r}_{ij}) between them cannot be determined exactly. That is why the simplification of the Hamiltonian

operator is required. Since, we are dealing with solids having billions of atoms, electrons, and nuclei, the inclusion of all the individual interactions are impossible to consider; therefore, approximations are made for solving the equation.

2.1.1 Born-Oppenheimer approximation

In 1927, Born and Oppenheimer developed an approximate method for separating electronic and nuclear motion [3]. The notion behind this is the huge difference between the masses of nuclei and electrons ($m_i \sim 2000 m_e$), therefore the nuclear motion can be considered fixed in comparison to the electronic motion. So, from the prospect of electronic motion, nuclei are no longer variable, but only fixed parameters. Nucleus appears to be frozen in the background of moving electrons. In this sense, nuclear wave functions may be considered independent of electronic coordinates. The total wave function can be written as the product of electronic and nuclear wave functions; therefore, the Schrödinger equation now reduces to the following equation for describing the electronic motion:

$$(\hat{H}_{el} + V_{NN})\Psi_{el}(\vec{R}, \vec{r}) = E_{el}\Psi_{el}(\vec{R}, \vec{r}) \quad (2.3)$$

where,

$$\hat{H}_{el} = \frac{\hbar^2}{2m_e} \sum_i \nabla_i^2 - \sum_I \sum_i \frac{Z_I Z_j e^2}{|\vec{r}_i - \vec{R}_I|} + \sum_j \sum_{i>j} \frac{e^2}{|\vec{r}_i - \vec{r}_j|} \quad (2.4)$$

and V_{NN} is the potential energy due to the nuclei-nuclei interactions. Despite having been simplified, solving the electronic part of the Hamiltonian is still a challenge. Consequently, more approximations are required to solve the equation, which is discussed in the next section.

2.1.2 Hartree approximation

In order to solve the many-body wave equation, Hartree (1928) proposed a method where each electron is moving independently [4]. He assumed the N-electron system as a set of non-interacting one-electron systems, where each electron feels an average electrostatic potential from the rest of the other electrons. According to the Hartree approximation, the Schrödinger wave equation (in atomic units) can be written as:

$$\left(-\frac{1}{2} \sum_i \nabla_i^2 - V_{ext} + V_H \right) \Psi(\vec{r}) = E\Psi(\vec{r}) \quad (2.5)$$

Here, $V_{ext} = \sum_I \sum_i \frac{Z_I}{|\vec{r}_i - \vec{R}_I|}$ i.e., the attractive potential among the nuclei and the electrons, and

V_H is the Hartree potential due to electron-electron Coulomb interaction and defined as:

$$V_H = \int \frac{\rho(\vec{r}')}{|\vec{r} - \vec{r}'|} d\vec{r}' \quad (2.6)$$

This approximation is an independent electron approximation; therefore, the total energy ‘E’ can be written as a sum of N electrons energies:

$$E = E_1 + E_2 + E_3 + \dots + E_N \quad (2.7)$$

Since it is a mean-field approach, it failed to incorporate actual exchange-correlation interactions among the electrons. It does not take into consideration the fermionic character of the electronic wave function, thus demanding further approximations.

2.1.3 Hartree-Fock approximation

In 1930, V. A. Fock refined the Hartree approximation based on the mean-field approach by taking spin into consideration and writing the one-electron wave function in the determinant form proposed by Slater as given below [5]:

$$\Psi(\vec{r}_1, \vec{r}_2, \vec{r}_3, \dots, \vec{r}_n) = \frac{1}{\sqrt{N!}} \begin{vmatrix} \Psi_1(1) & \Psi_1(2) & \Psi_1(3) & \dots & \Psi_1(N) \\ \Psi_2(1) & \Psi_2(2) & \Psi_2(3) & \dots & \Psi_2(N) \\ \Psi_3(1) & \Psi_3(2) & \Psi_3(3) & \dots & \Psi_3(N) \\ \cdot & \cdot & \cdot & \cdot & \cdot \\ \cdot & \cdot & \cdot & \cdot & \cdot \\ \Psi_N(1) & \Psi_N(2) & \Psi_N(3) & \dots & \Psi_N(N) \end{vmatrix} \quad (2.8)$$

Here, in the Slater determinant, the $\frac{1}{\sqrt{N!}}$ is a normalization factor. The total wave function written in the form of a determinant takes care of the anti-symmetric nature of the fermions, i.e., the sign is changed when any two columns or rows are interchanged which ensures the anti-symmetric nature of the total wave function. Moreover, suppose any two rows or columns are identical. In that case, the determinant is zero, implying that the electronic state having electrons of the same spatial and spin coordinates does not exist, thus satisfying the Pauli exclusion principle.

Now, equation 2.5 is modified as:

$$\left(-\frac{1}{2} \sum_i \nabla_i^2 - V_{ext} + V_{ij} \right) \Psi(\vec{r}) = E \Psi(\vec{r}) \quad (2.9)$$

Essentially, V_{ij} is driven by two interactions: Coulomb interaction between electron coordinates i and j , and an exchange interaction caused by the Slater determinant's anti-symmetrical nature. Since exchange interaction will give negative exchange energy, the total energy in Hartree and Fock (HF) approximation will be much closer to the ground state energy, which is minimized using the variational principle:

$$\delta \left(\int \Psi^*(\vec{r}) \hat{H} \Psi(\vec{r}) d\vec{r} \right) = 0 \quad (2.10)$$

Now, the total energy under HF approximation is written as:

$$E = T + E_{ext} + E_H + E_x \quad (2.11)$$

where first, second, third, and fourth terms are kinetic energy of electrons, external energy due to the interaction between nuclei and electrons, Hartree energy, and the exchange energy. It fails to incorporate correlation interactions between electrons with different spins. The neglected correlation energy was included in the density approach method known as DFT, which is discussed in the next section.

2.2 Density functional theory

Solving many electron systems through the wave function approach is highly tedious and computationally expensive. The self-consistency scheme used in HF approximation makes an initial guess on the wave function, which depends on $3N$ variables for N -electrons and, therefore works fine only for smaller systems. To simplify things, Hohenberg and Kohn introduced a new theory [2–7] taking electron density into account rather than wave functions, thus reducing the $3N$ variables problem to 3 coordinates (x, y, z) only. Since the many-electron problem gets reduced to density-dependent 3-coordinates system, the computational cost is cut down significantly. DFT framework involves Thomas-Fermi theory [8, 9], Hohenberg-Kohn theorems[7], and the Kohn-Sham [10] equations which are discussed in the following sections.

2.2.1 Thomas-Fermi theory

The first density approach was proposed by Thomas [8] and Fermi [9] in 1927, named as Thomas-Fermi theory. It is based on the semi-classical assumption that the many electrons

system containing N-electrons confined in a volume 'V' behave as a homogeneous electron gas. The kinetic energy of the electron in a system is approximated as an explicit functional of density for non-interacting electrons, which is expressed as:

$$T(\rho(\vec{r})) = C_1 \int \rho^{5/3}(\vec{r}) d^3\vec{r} \quad (2.12)$$

Where $\rho(\vec{r})$ is the electron density and can be expressed as:

$$\rho(\vec{r}) = N \int \Psi(\vec{r}_1, \vec{r}_2, \vec{r}_3, \dots, \vec{r}_N) \Psi^*(\vec{r}_1, \vec{r}_2, \vec{r}_3, \dots, \vec{r}_N) d^3\vec{r}_1 d^3\vec{r}_2 d^3\vec{r}_3 \dots d^3\vec{r}_N \quad (2.13)$$

Integration of the electron densities in the whole region will give the total number of electrons, i.e., $\int \rho(\vec{r}) d^3\vec{r} = N$.

The accuracy of this kinetic energy expression is limited because of the approximate kinetic energy functional and the absence of inclusion of exchange and correlation among electrons. This exchange and correlation term considered by Dirac in 1930, for the electrons in the presence of an external potential $V_{ext}(\vec{r})$ the energy can be expressed as:

$$E_{TF}[\rho(\vec{r})] = C_1 \int \rho^{5/3}(\vec{r}) d^3\vec{r} + C_2 \int \rho^{4/3}(\vec{r}) d^3\vec{r} + \int \rho(\vec{r}) V_{ext} d^3\vec{r} + \frac{1}{2} \iint \frac{\rho(\vec{r}) \rho(\vec{r}')}{|\vec{r} - \vec{r}'|} d^3\vec{r} d^3\vec{r}' \quad (2.14)$$

The first and second integral in the above equation is a local approximation to the kinetic energy and the local exchange terms, respectively; and the last integral is the classical electrostatic

Hartree energy. The values of constant multipliers are: $C_1 = \frac{3}{10} (3\pi^2)^{2/3}$ and $C_2 = -\frac{3}{4} \left(\frac{3}{\pi} \right)^{1/3}$

The main source of error in Thomas-Fermi approach was the kinetic energy term, followed by errors in exchange energy terms and also due to the complete neglect of electron correlations.

2.2.2 Hohenberg-Kohn theorems

Thomas-Fermi's theory was the footing point of the DFT, but the semi-classical expression of the energy was its only drawback. This density approach was further elaborated by the two theorems proposed by Hohenberg and Kohn (HK Theorems) [7], which are the key foundation of DFT.

Theorem I state that the external potential is a unique functional of the electron density $\rho(\vec{r})$, and hence the ground state energy is also a unique functional of electron density i.e., $E[\rho(\vec{r})]$.

Theorem II states that the electron density can be minimized with respect to energy using the variational principle. If and only if the input density is the real ground-state density ($\rho_o(\vec{r})$), the energy functional that yields the system's ground-state energy would have the lowest energy. Using the above two theorems, the Hamiltonian for many-electron system can be written as:

$$\hat{H} = -\frac{1}{2} \sum_i \nabla_i^2 - V_{ext}(\vec{r}_i) + \sum_{i \neq j} \frac{\rho(\vec{r}_i)\rho(\vec{r}_j)}{|\vec{r}_i - \vec{r}_j|} \quad (2.15)$$

Using the HK Theorems, Kohn and Sham considered a fictitious system of one electron that can replace the N-electrons system [10]. The methodology will be discussed in detail in the following sections.

2.2.3 Kohn-Sham approach

Kohn-Sham mapped the interacting N-electrons system on the non-interacting one electron system [10]. The total energy within the DFT formalism is written as:

$$E_{KS} = T[\rho(\vec{r})] + V_{ext}[\rho(\vec{r})] + V_H[\rho(\vec{r})] + E_{xc}[\rho(\vec{r})] \quad (2.16)$$

As per Kohn-Sham (KS) scheme, $T[\rho(\vec{r})]$ represents the non-interacting kinetic energy of electrons and is expressed in terms of the KS orbitals (ϕ_i) as:

$$T[\rho(\vec{r})] = -\frac{1}{2} \sum_{i=1} \phi_i^*(\vec{r}) \nabla^2 \phi_i(\vec{r}) \quad (2.17)$$

In a non-interacting homogeneous system, $T[\rho(\vec{r})]$ is the same as that given by Thomas-Fermi theory (equation 2.12). The energy derived from the external potential, V_{ext} , is denoted by $V_{ext}[\rho(\vec{r})]$ and is written as:

$$V_{ext}[\rho(\vec{r})] = \int \rho(\vec{r}) V_{ext}(\vec{r}) d\vec{r} \quad (2.18)$$

The square bracket indicates the functional term, implying that energy is a function of electron density, which is dependent on the electronic coordinate $\vec{r}(x, y, z)$. The Coulomb interaction between electrons gives rise to Hartree potential, V_H , which is given as equation 2.6. The Hartree energy corresponding to V_H is:

$$V_H[\rho(\vec{r})] = \frac{1}{2} \iint \frac{\rho(\vec{r})\rho(\vec{r}')}{|\vec{r} - \vec{r}'|} d\vec{r}d\vec{r}' \quad (2.19)$$

During the exchange of two particle's position, the wave function changes its sign due to their anti-symmetric nature. It is known as the exchange energy (E_x), and can be calculated as follows:

$$E_x = -\frac{1}{2} \sum_{ij} \iint \frac{\phi_i^*(\vec{r})\phi_i(\vec{r}')\phi_j^*(\vec{r})\phi_j(\vec{r}')}{|\vec{r} - \vec{r}'|} d\vec{r}d\vec{r}' \quad (2.20)$$

and the collective interaction of all the electrons of a system with one electron is called electronic correlation, and the corresponding energy is energy E_c . As there is no exact formulation for the correlation energy, the combination of the two ($E_x + E_c$) is together called exchange-correlation energy, E_{xc} . The exchange-correlation term, V_{xc} represented as a functional derivative of the exchange correlation energy, is the term that makes DFT efficient and beneficial over HF approximation:

$$V_{xc}(r) = \frac{\delta E_{xc}(\vec{r})}{\delta \rho(\vec{r})} \quad (2.21)$$

This approach is commonly misunderstood to describe the non-interacting electrons moving in a potential determined by the nuclei. In reality, electrons travel in an effective potential V_{eff} , which involves electronic interactions, although indirectly. In KS equations, the electron-electron interaction is substituted by the interaction of electrons with a medium, which take cares of electron-electron interactions. The KS equation in Schrödinger form is represented as:

$$\hat{H}_{KS}\phi(\vec{r}) = E_{KS}\phi_i(\vec{r}) \quad (2.22)$$

The corresponding Hamiltonian is:

$$\hat{H}_{KS} = -\frac{1}{2} \sum \nabla^2 + V_{eff} \quad (2.23)$$

V_{eff} is the effective potential, which includes three potential terms ($V_{ext} + V_H + V_{xc}$). It manipulates the non-interacting ground-state electron density to be similar to that of the real interacting system. To solve this Hamiltonian and find to the ground state energy and density of the system, an iterative technique is adopted which is known as the self-consistent method. A flow chart of self consistent field cycle is shown in Fig. 2.1. The trial density at which energy

is converged is then used to determine each potential term. The term, V_{xc} is still not adequately defined, leading to more approximations.

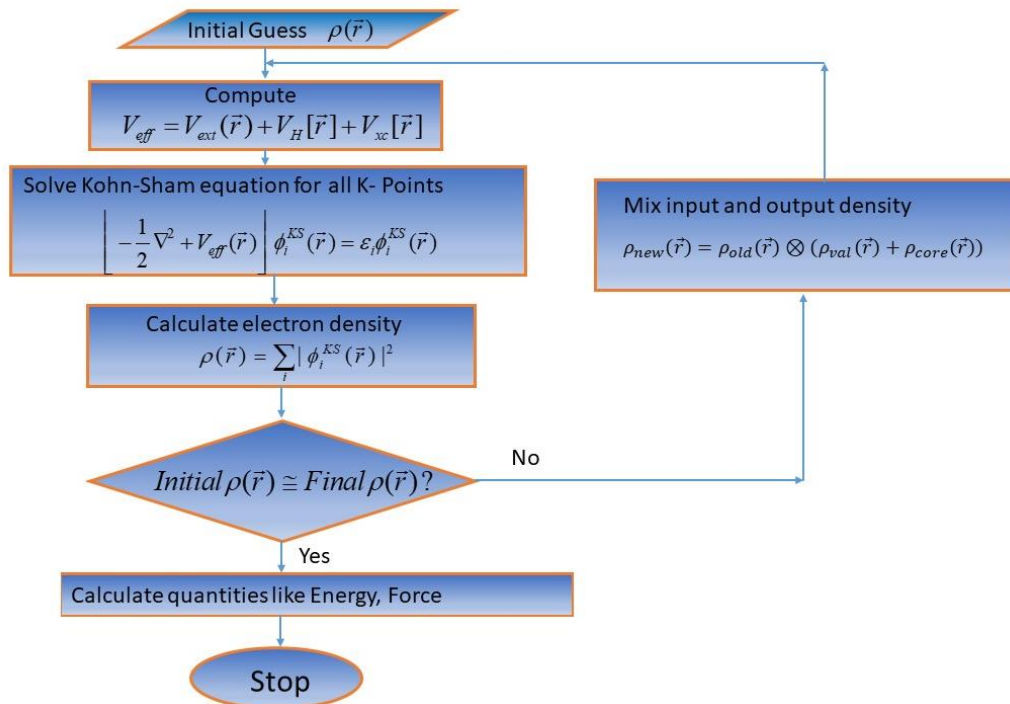


Fig. 2.1: Flow chart for self-consistent density functional calculations.

2.3 Exchange-Correlation functionals

We now have a workable framework for solving the electronic ground-state problem and, any required property may be computed using KS equations provided the electron density is known. Nevertheless, without knowing the precise form of the exchange correlation functional, E_{xc} , a fundamental parameter in DFT, the many-electron problem remains unsolved. Several approximations, such as LDA, GGA, HSE, meta-GGA, and others, have been introduced to describe the form, and some of them are presented here.

2.3.1 Local density approximation

In 1965, Kohn and Sham presented a simple approximation for the exchange correlation functional to achieve a meaningful solution to the many-electron problem, called local density approximation (LDA) [6]. The electron density in a system is assumed to vary slowly when compared to spatial coordinates, such that electrons see the entire system in a similar way as they see it locally. This is similar to the case of a homogeneous gas of free electrons. Under this approximation, exchange correlation has the following form:

$$E_{xc}^{LDA}[\rho(\vec{r})] = \int \rho(\vec{r}) \varepsilon_{xc}[\rho(\vec{r})] d^3\vec{r} \quad (2.24)$$

where, ε_{xc} denotes the exchange-correlation energy per particle of the interacting free electron gas having density $\rho(\vec{r})$. For metals with uniform electron density, LDA produces good results. Real systems, on the other hand, are not all homogeneous and have variable densities.

2.3.2 Generalized gradient approximation

The generalized gradient approximation technique (GGA) originated from Herman's (1969) proposition that electron density varies as a function of spatial coordinates and that the exchange-correlation energy may be represented as the gradient of electron density [11]. Having gradient density as an additional variable, GGA was considered more accurate functionals than LDA. Exchange-correlation functional as per this approximation is expressed as:

$$E_{xc}^{GGA}[\rho(\vec{r})] = \int \rho(\vec{r}) \varepsilon_{xc}[\rho(\vec{r}), \nabla(\rho(\vec{r}))] d^3\vec{r} \quad (2.25)$$

Since there is no simpler functional form that accurately captures GGA, E_{xc}^{GGA} is usually expressed by modifying the LDA functional with an additional term $F(s)$, which is nothing but the gradient correction term:

$$E_{xc}^{GGA}[\rho(\vec{r}), s] = \int \varepsilon_{xc}^{LDA}[\rho(\vec{r})] \rho(\vec{r}) F(s) d^3\vec{r} \quad (2.26)$$

Here, $s = C \frac{|\nabla\rho(\vec{r})|}{\rho^{4/3}(\vec{r})}$. The usual range of $s = 0-3$ in solids. The most widely used forms of

GGA are PW91 (Perdew and Wang, 1992) [12, 13] and PBE (Perdew, Burke, and Ernzerhof, 1996) [14]. As far as the structural properties are concerned, GGA outperforms LDA results, and it is also nearly accurate in determining the magnetic properties of the solids. Still, it somehow underestimates the band gap values resulting in a misleading prediction of band inversion. This urged the need to develop approximations leading to more accurate functionals.

2.3.3 Tran-Blaha modified Becke-Johnson potential (TB-mBJ)

Tran and Blaha (2009) introduced an effective exchange correlation functional that was subsequently evaluated in various solid materials, including wide band gap insulators, semiconductors, and a few strongly correlated 3d transition metal oxides. Their findings demonstrated the accurate prediction of band gap values, which were found to be in good

agreement with experimental results [15]. Several approaches, such as LDA +U and GW, have been presented as extensions to the traditional exchange correlation functionals LDA and GGA. The TB-mBJ functional has garnered increased attention due to its reduced computational cost. This approach represents a variation of the exchange correlation method first described by Becke and Johnson [16]. It can be mathematically expressed as.

$$v_{x,\sigma}^{MBJ}(\vec{r}) = cv_{x,\sigma}^{BR}(\vec{r}) + (3c - 2) \frac{1}{\pi} \sqrt{\frac{5}{12}} \sqrt{\frac{2t_{\sigma}(\vec{r})}{\rho_{\sigma}(\vec{r})}} \quad (2.27)$$

where $\rho_{\sigma} = \sum_{i,N} |\Psi_{i,\sigma}|^2$ and $t_{\sigma} = -\frac{1}{2} \sum_{i,N_{\sigma}} \nabla \Psi_{i,\sigma}^* \cdot \nabla \Psi_{i,\sigma}$ represents the electron density kinetic energy, respectively.

$$v_{x,\sigma}^{BR}(\vec{r}) = -\frac{1}{b_{\sigma}(\vec{r})} (1 - e^{-x_{\sigma}(\vec{r})}) - \frac{1}{2} x_{\sigma}(\vec{r}) e^{-x_{\sigma}(\vec{r})} \quad (2.28)$$

is the Becke-Roussel potential.

The factor ‘c’ was chosen as:

$$c = \alpha + \beta \sqrt{\frac{1}{V_{cell}} \int \frac{|\nabla \rho(\vec{r}')|}{\rho(\vec{r}')} d^3 \vec{r}'} \quad (2.29)$$

Where, α and β are the two free parameters and V_{cell} is the unit cell volume.

The TB-mBJ potential preferably considered in the present work. This potential has shown its applicability in determination of band gap of different oxides and other materials which is consistent with experimental reports.

2.4 Treating solids with DFT

In this section, we will discuss the practical approach to implement DFT for estimating the electronic structure of a real solid.

2.4.1. Electron-ion interactions

To solve the KS equations exactly, we need to find the remaining term, V_{ext} , which is the electron-ion interaction term. Since, we are dealing with solids having a large number of electrons, and significant electron oscillations near nuclei, defining V_{ext} , is difficult. Electrons behave differently depending about their location inside a solid (core or valence). Unlike valence electrons, the core electrons don't participate in bond formation and are mostly

inactive, rarely responsible for the physical properties of the material; therefore, they can be dealt differently in a solid using DFT. The basic approaches used to estimate the electron-ion interactions are all-electrons scheme and the pseudopotential techniques, which is discussed here.

2.4.1.1 Full potential and charge density

This scheme considers both the core and the valence electrons as spheres centered on atomic sites and interstitial regions, respectively. This approximation is also known as the Muffin-tin (MT) approximation (Figure 2.2). The potential is assumed to be spherically symmetric near the nuclei/core region, and flat in the interstitial regions. The core wave functions are described in terms of atomic orbitals, whereas valence electron wave-functions are represented as plane waves. The wavefunction is constructed by matching the solution of these two wavefunctions. The method is also known as the Full Potential Linear Augmented Plane wave method (FPLPAW). The MT approximation was frequently used in highly coordinated (metallic) systems, but for covalently bonded systems this approximation leads to inaccuracy in the results. In such cases, the full-potential treatment is essential.

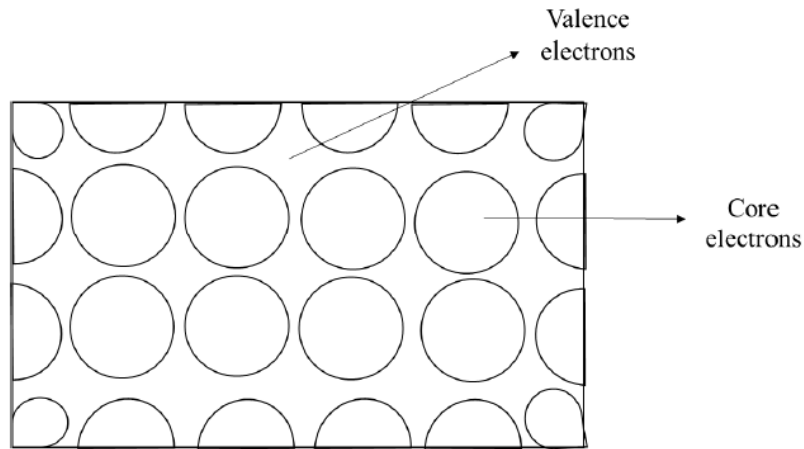


Fig. 2.2: Muffin-Tin approximation [17].

In the full potential approach, the potential and charge density are expanded into the atomic sphere and also in the interstitial region. Thus, they are completely general, so the scheme is treated as full potential calculations:

$$V(\vec{r}) = \begin{cases} \sum_{LM} V_{LM}(\vec{r}) Y_{LM}(\vec{r}) & \text{Inside sphere} \\ \sum_k V_k \exp(ik \cdot \vec{r}) & \text{Outside sphere} \end{cases} \quad (2.30)$$

2.4.1.2 Pseudopotential method

Using the pseudopotential (PP) [18, 19] method, we can narrow down the many-electron problem to a significant number of electrons that actually participate in bond formation, thus decreasing the computational cost. Since core electrons are basically localized near the nucleus, they rarely participate while forming solids. In this approach, the nucleus plus core can be considered frozen while only valence electrons are taken into consideration. This is called frozen-core approximation. The chosen wave function used to describe solids may not correspond to the true wave function within the core region, but the pseudo wave function, Ψ_i^{PP} , is on par with the true wave function after the cut-off region (\vec{r}_c). As per PP approach, KS equations can be rewritten as:

$$\left[-\frac{1}{2}\nabla^2 + V_{pp}[\rho(\vec{r})] \right] \Psi_i^{PP}(\vec{r}) = E_i \Psi_i^{PP}(\vec{r}) \quad (2.31)$$

Now the effective potential, V_{eff} , is replaced by pseudopotential, V_{pp} , leading to a different charge density, which have the form:

$$\rho(\vec{r}) = \sum_i |\Psi_i^{PP}(\vec{r})|^2 \quad (2.32)$$

2.4.1.3 Projected augmented wave (PAW) method

In 1994, E. Bloch proposed a generalized potential, which has both pseudopotential's efficiency and the accuracy of all-electron exact potential [20]. This approach was called the Projected Augmented Wave (PAW) method. The wave function associated with the PAW method has both core (Ψ_{core}) and valence contributions (Ψ_{val}) represented by radial and plane wave expansions, respectively. In addition, the overlapping wave function (Ψ_{net}) is trimmed off to get the final wave function (Ψ_{PAW}). Thus, are efficient in calculating exact all-electron properties.

$$\Psi_{PAW} = \Psi_{val} + \Psi_{core} - \Psi_{net} \quad (2.33)$$

For all electronic structure computations in this thesis, we employed the PAW technique.

2.4.2 Numerical and technical factors

Several numerical and technical factors are considered to reduce the computational effort in performing DFT calculations; a few of them are listed below:

2.4.2.1 Plane-wave expansions

In a solid, atoms are arranged periodically, and the particles move under a periodic potential which has the periodicity of the lattice.

$$V(\vec{r}) = V(\vec{r} + \vec{R}) \quad (2.34)$$

Here, \vec{R} is a translational lattice vector in real space. Bloch proposed a theorem, that says that the under the periodic potential wave function of such a periodic system can be expressed in terms of a function with the periodicity same as that of the lattice i.e.,

$$\Psi_k(\vec{r}) = u_k(\vec{r}) \exp(ik \cdot \vec{r}) \quad (2.35)$$

where, $u_k(\vec{r})$ is Bloch's periodic function: $u_k(\vec{r}) = u_k(\vec{r} + \vec{R})$

$$\Psi_k(\vec{r} + \vec{R}) = u_k(\vec{r} + \vec{R}) \exp[ik \cdot (\vec{r} + \vec{R})] = \Psi_k(\vec{r}) \exp(ik \cdot \vec{R}) \quad (2.36)$$

According to Bloch, the plane wave function under the periodic potential is of the same form as that of free electrons, but it differs only by a periodic phase factor, $\exp(ik \cdot \vec{R})$. Since any periodic function in real space can be expressed in reciprocal space using Fourier expansions, $u_k(\vec{r})$ can be expanded in terms of reciprocal lattice vector, G :

$$u_k(\vec{r}) = \sum_G C_k(G) \exp(iG \cdot \vec{r}) \quad (2.37)$$

Substituting this Fourier form of $u_k(\vec{r})$ in equation 2.35, we get:

$$\Psi_k(\vec{r}) = \sum_G C_k(G) \exp[i(k + G) \cdot \vec{r}] \quad (2.38)$$

The plane-wave function given by equation 2.37, which represents the motion of electrons in solids are known as plane wave basis sets. An infinite number of plane waves are required to completely map the whole solid, which is computationally not feasible. This can be avoided by limiting the number of plane waves by defining a cut-off energy parameter, as discussed in the next section.

2.4.2.2 Cut-off energy

The kinetic energy associated with the plane waves can be expressed in atomic units as:

$$E_{kin} = \frac{1}{2}|k + G|^2 \quad (2.39)$$

Since, the lower-energy solutions are more significant than those with higher energies, we can narrow down the infinite plane waves to a practical limit by introducing cut-off energy $E_{cut-off}$ [21, 22] i.e.,

$$\frac{1}{2}|k + G|^2 \leq E_{cut-off} \quad (2.40)$$

and the equation 2.36 becomes:

$$\Psi_k(\vec{r}) = \sum_{k+G_{cut}} C_{k+G} \exp[i(k + G) \cdot \vec{r}] \quad (2.41)$$

This $E_{cut-off}$ is used as an input parameter while optimizing a particular structure.

2.4.2.3 K-point sampling

A crystalline solid has a periodic arrangement of atoms and is made of unit cells. To deal with the entire solid, first, it is converted to a supercell containing multiple unit cells. The periodic boundary conditions are then used to expand the supercell to infinity, which is then converted into reciprocal space confined within the first Brillouin zone (BZ). The irreducible Brillouin zone (IBZ) can map the entire solid with the help of symmetry operations, which allows us to reduce the BZ further. The points in an IBZ can be represented by k-vectors, leading to an infinite number of wave functions. Every k-point carries information about the wave vector's magnitude, direction, and kinetic energy at that particular point. Considering every k-point is practically impossible; therefore, a handful set of k-points are used in DFT calculations using the following schemes:

- **Monkhorst-Pack method:** In 1976, Monkhorst and Pack proposed a scheme to generate a homogeneous mesh of k-points sampled over the whole IBZ to calculate the ground state energy, which is converged in DFT calculations for every system [21, 23].
- **Γ -point:** A single point is enough to completely describe a big supercell, and that point is Γ -point. It is the coinciding point of both real and reciprocal spaces, and thus the wave function used will be real [21].

2.5 Transport in a solid

In this section, semi-classical transport formalism is discussed to explain the transport behavior in solids. Since transport phenomena depend on the average behavior of the carriers, a statistical approach is required to deal with it.

2.5.1 Boltzmann transport theory

Transport of charge carriers may be thought of its response to external factors like temperature, electric field, etc. The transport theory describes all of the different ways that carriers might respond to these external factors or stimuli. One of the many transport theories is the Boltzmann transport theory [24], a semi-classical approach to study charge carrier transport. The main idea of the Boltzmann transport equation is to define the variation of the charge distribution function $f(\vec{r}, k, t)$ with time. The distribution function represents the distribution of charge carriers in real and momentum space over time. Considering the carriers are electrons here, the distribution function gives the number of electrons at point \vec{r} with wavenumber k . Integrating $f(\vec{r}, k, t)$ over k gives the electron density at point \vec{r} ; and further integrating over \vec{r} would give the total number of electrons. The change in electric field, temperature, and impurity effects carrier transport, which results in drift, diffusion, and scattering of charge carriers, respectively. The time evolution of $f(\vec{r}, k, t)$ is expressed in terms of these three effects:

$$\frac{\partial f(\vec{r}, k, t)}{\partial t} = \left(\frac{\partial f}{\partial t} \right)_{drift} + \left(\frac{\partial f}{\partial t} \right)_{diffusion} + \left(\frac{\partial f}{\partial t} \right)_{collision} \quad (2.42)$$

The drift term corresponds to the time variation of electron distribution function as a function of k and t at a fixed position \vec{r} . Now, $f(\vec{r}, k, t) = f(\vec{r}, k - \dot{k}dt, t - dt)$, i.e.,

$$\left(\frac{\partial f}{\partial t} \right)_{drift} = -\dot{k} \frac{\partial f(k)}{\partial k} \quad (2.43)$$

Likewise, at a fixed wavenumber, the change in $f(\vec{r}, k, t)$ would give the diffusion term. The carriers in a small volume ($d\vec{r}$) at position (\vec{r}), and time (t), are regarded to be the same as they were at the point $\vec{r} - v_k dt$ and at time $t - dt$, where v_k is the velocity of the carrier (here electrons). The diffusion-induced change in the distribution function over time may therefore be expressed as:

$$\left(\frac{\partial f}{\partial t} \right)_{diffusion} = -v_k \cdot \frac{\partial f(\vec{r})}{\partial \vec{r}} \quad (2.44)$$

The last term in equation 2.41 deals with the shifting of electrons from k to $k - k'$ state due to scattering mechanisms. If the scattering rate of moving from k state to an empty k' state is $W_{k-k'}$, the electron distribution function due to scattering can be expressed as:

$$\left(\frac{\partial f}{\partial t}\right)_{diffusion} = \int [f(k')(1-f(k))W_{k-k'} - f(k)(1-f(k'))W_{k-k'}] \frac{d^3k'}{(2\pi)^3} \quad (2.45)$$

In general, solving the above equation is not easy, so the collision term is assumed to be of the following form:

$$\left(\frac{\partial f}{\partial t}\right)_{collision} = -\frac{f(k) - f_o(k)}{\tau(k)} \quad (2.46)$$

And, this is known as *relaxation time approximation* (RTA). Here, $\tau(k)$ is the relaxation time, which is defined as the typical time for a system to return to its equilibrium state; and $f_o(k)$ is the electron distribution function at equilibrium. At steady-state, the distribution function will not change, and all the partial derivative terms will sum to zero.

$$\left(\frac{\partial f}{\partial t}\right)_{drift} + \left(\frac{\partial f}{\partial t}\right)_{diffusion} + \left(\frac{\partial f}{\partial t}\right)_{collision} = 0 \quad (2.47)$$

This electron distribution function may be used to calculate a number of transport characteristics, such as electron current density (J_e), and heat current density (J_Q):

$$J_e = \int 2ev_k f(k) \frac{d^3k}{(2\pi)^3} \quad (2.48)$$

$$J_Q = \frac{2}{8\pi^3} \int v_k [E_k - \mu] f(k) dk \quad (2.49)$$

Here, μ is the chemical potential. On substituting the distribution function expression, above integrals become:

$$J_Q = \frac{2e}{8\pi^3} \int v_k^2 \tau(k) \left(\frac{-\partial f_o}{\partial E_k}\right) \left[eE - \nabla\mu + \frac{E_k - \mu}{T} (-\nabla T) \right] dk = e^2 I_o E + e \frac{I_1}{T} (-\nabla T) \quad (2.50)$$

$$J_Q = \frac{2e}{8\pi^3} \int v_k^2 \tau(k) \left(\frac{-\partial f_o}{\partial E_k}\right) \left[eE - \nabla\mu + \frac{E_k - \mu}{T} (-\nabla T) \right] [E_k - \mu] dk = e^2 I_1 E + e \frac{I_2}{T} (-\nabla T) \quad (2.51)$$

where, I is the response function defined as:

$$I_n = \frac{1}{4\pi^3} \int v_k^2 \tau(k) \left(\frac{-\partial f_o}{\partial E_k} \right) [E_k - \mu]^n dk \quad (2.52)$$

This response function is used to determine different TE characteristics of the system, which are discussed in the next section.

2.5.2 Thermoelectric properties

Here, we will see how various TE parameters (S_α, σ, κ) are related to the above described response functions:

- **Thermal conductivity:** When no electric field is applied, i.e., $E_k = 0$ the thermal conductivity, κ can be defined by the relation between the heat current density and the thermal gradient: $J_Q = -\kappa \nabla T$. Thus, from equation 2.50 and 2.51, $\kappa = I_2 T$.
- **Electrical conductivity:** Under zero temperature gradient ($\nabla T = 0$) electrical conductivity is defined as the ratio of the electrical current density to the electric field generated due to the voltage gradient: $J_e = \sigma E$. Thus, from equations 2.50 and 2.52, we have $\sigma = e^2 I_o$.
- **Seebeck coefficient:** It is a measure of the open circuit voltage across the semiconductor that has temperature gradient. So, when, $J_e = 0$, $S_\alpha = -V_{oc} / \nabla T$. This gives $S_\alpha = I_1 / T I_o$. This becomes more prominent in materials having the asymmetric density of states around the Fermi level.

The Boltzmann transport theory is implemented in BoltzTraP code which we have used in the present thesis to calculate the above mentioned TE properties.

2.6 Computational software

To carry out the desired calculations, we used different packages, which are discussed in the following sections.

2.6.1 WIEN2k

In 1990, Peter Balaha and his team developed a code based on the full potential linearized augmented plane wave that was known as WIEN2k [17]. In this code, no shape approximations are made and the procedure is basically known as the full potential method. To calculate the material properties, first, we relax the crystal structure and optimize the lattice parameters. The RMT and cutoff energy are chosen as there is no charge leakage. The appropriate energy

convergence and cutoff energy of the core and valence were fixed before the SCF calculations. The SCF calculations contain all the necessary information regarding total energy, Fermi energy, the distance between the atoms, the charge on the atomic sphere, etc. The SCF cycle consists of the following steps:

LAPW0: generate potential from density

LAPW1: calculates valence bands

LAPW2: compute valence density from the eigen values

LCORE: computes core states and densities

MIXER: mixes input and output densities

2.6.2 VASP

In 1998, Prof. George Kresse and his team developed a DFT based package called the Vienna Ab initio Simulation Package (VASP) [25]. It uses plane-wave basis sets to represent KS orbitals and the PAW approach to account for the external interactions between electrons and nuclei. In the present thesis, VASP is used as a base for every calculation. For instance, to relax the crystal structures, optimize the lattice parameter, determine force constants required in Phonopy and Phono3py calculations, determine the energy-momentum relation, the density of state calculations, and many more. VASP is primarily comprised of four input files, which are as follows:

- INCAR: It is a basic “to-do” file, which defines what to do and how to do the desired run.
- POSCAR: It includes the geometric details of the crystal structure, such as the lattice vectors, types of atoms, and their atomic positions.
- KPOINTS: The k-points (Bloch vectors) required to sample the Brillouin zone for the computation are specified in the KPOINTS file. For band-structure calculations, it contains the high symmetry points along which bands are to be plotted.
- POTCAR: This file contains the pseudopotential information of every element of the compound. The POTCAR file of the compound is generated by concatenating the POTCARs of each atomic species which is different for different functionals.

2.6.3 BoltzTraP

Madsen et al. developed BoltzTraP package to calculate the Boltzmann Transport Properties [26]. It is based on a semi-classical approach to calculate the electronic transport coefficients such as σ , k_e , and S_α . It is used as an interface with DFT based codes such as WIEN2k [17], VASP [25]. In the present thesis, we have used BoltzTraP interfaced with WIEN2k. Since BoltzTraP was originally developed interfaced with WIEN2k, they share some common input files.

The required files are:

- Case.intrans: It contains the information of all the input parameters required to run the transport calculations, such as the temperature range, Fermi energy, energy cutoff, etc. Here, Case is the name of the directory.
- Case.struct: The crystal structure information is provided in Case.struct file.
- Case.energy: It includes the band structure information needed to run Boltz-TraP code.

2.6.4 Phonopy

Before computing any material property using DFT, one must ensure the proposed crystal structure's dynamical stability, which is carried out using the Phonopy package [27]. It deals with the atom's response with a thermal perturbation introduced in the system by the supercell approach. This software is based on harmonic and quasi-harmonic approximation included in the density functional perturbation theory (DFPT). The first and second-order force constants are determined using VASP and later are used as an input to find the phonon frequencies at the desired q-points using Phonopy as a post-processing tool.

2.6.4 Phono3py

The phonon-phonon coupling is realized using the Phono3py package [28], which is based on anharmonic lattice approximations. It uses the supercell approach to create displacements in the input structure and then can be used to determine different physical properties related to the phonon-phonon interactions. In our work, we used Phono3py to calculate the lattice thermal conductivity of the half Heusler compounds. The force constants for the supercells are calculated using VASP, which are then treated as inputs to calculate lattice thermal conductivity.

2.7 Experimental techniques

An experimental study relies on careful synthesis of samples followed by suitable characterizations, meeting the demand of chosen research topic. The present study is proposing the investigation of luminescence and local electronic structure of HfO₂ based nanophosphors. The sample preparation and relevant characterization techniques undertaken in this study are briefly discussed below:

2.7.1 Material synthesis

Researchers have explored various methods such as the chemical co-precipitation method, combustion route, sol-gel method, solid-state method, hydrothermal method, etc., to synthesize HfO₂ nanoparticles [29–32]. Among all the synthesis methods, the chemical co-precipitation method is chosen in this work considering the advantages such as cost-effectiveness, stabilization of metastable phases, good control on stoichiometry, nano-ranged crystallites, homogeneous particle distribution, time efficient, user-friendly and environment-friendly nature, offered by this method over others. This method has proven applicability to synthesize oxides NP's.

To synthesize nanometer sized HfO₂ through low temperature chemical co-precipitation method. Analytically graded reagents were used without further purification. Stoichiometric portion of all the reagents was weighted according to the reaction:



To synthesize NP's of HfO₂, initially stoichiometric HfCl₄ was dissolved in the DI water upon magnetic stirring. NH₄OH was poured dropwise and the pH value of the solution was maintained at 7.2 during the synthesis. The temperature was maintained at 120°C during the stirring to avoid intermediate Hf(OH)₄. After stirring for an hour on the hot plate the resulting precipitates were washed with distilled water with the help of a centrifuge. The excess salt was discarded and the yellow coloured precipitate was placed at the heating mantle overnight at 50°C. The dried powder was crushed and placed in the muffle furnace for further annealing at 1100°C.

2.7.2 Characterization techniques

Structural, morphological, and optical properties of synthesized nanocrystals are inspected in the present study, to accomplish the objectives. In doing so, various characterization techniques were utilized specifically XRD, X-ray absorption near edge structure (XANES) spectroscopy, Raman spectroscopy for structural characterization, and PL spectroscopy to study optical properties. The working principle and instrumental setup of the aforementioned techniques are discussed in the following subsections.

2.7.2.1 X-ray diffraction (XRD)

The XRD is a fundamental and non-invasive technique that offers significant insights into the phase composition, sample purity, crystallite dimensions, and shape of the specimen. In the case that the sample consists of a combination of multiple components, each component will manifest its distinct and characteristic diffraction peaks [33].

In 1895 Roentgen discovered the X-rays, after that in 1912 Laue predicted the possibility of diffraction of X-rays from regularly spaced atoms of crystals acting as scattering centers [34]. A monochromatic X-ray beam strikes the crystal system and constructive interference of scattered components generates the diffraction pattern. Every material is made up of a certain crystallographic arrangement of atoms, with unit cell representing the vital material specific structural and chemical information. These are arranged in a regular arrangement having atomic plane separation of the order of a few Å. The X-rays are scattered by crystal atoms and are reinforced to give diffraction patterns. This phenomenon of reinforcement is related to crystal plane spacing and incident angle, known as Bragg's law, given as follows:

$$n\lambda = 2d\sin\theta \quad (2.54)$$

where λ , θ , d , and n represent the wavelength of incident radiation, angle between the incident beam and lattice planes, interplanar spacing, and integer describing the order of diffraction, respectively.

The experimental station of a typical X-ray diffractometer mainly consists of X-ray source, sample, and X-ray detector, as shown in Fig. 2.3. In this geometry, X-ray source is fixed and the detector is moved through the desired range of angles. Apart from that, there is another geometry with the X-ray source and detector moving in opposite directions in a vertical plane. After diffraction, a suitable X-ray detector (proportional, scintillation or solid state detector) is employed to collect the diffracted signal, which accumulates the signal in the form of Laue's pattern. Between X-ray source and specimen, there are soller slits (closely spaced parallel metal

plates) to define and collimate incident X-ray beam and divergence slit to define the divergence of incident beam. After diffraction, in path between source and detector, there is antiscatter slit to reduce background radiation, and receiving slit to converge the diffracted beam before entering the detector [33–35].

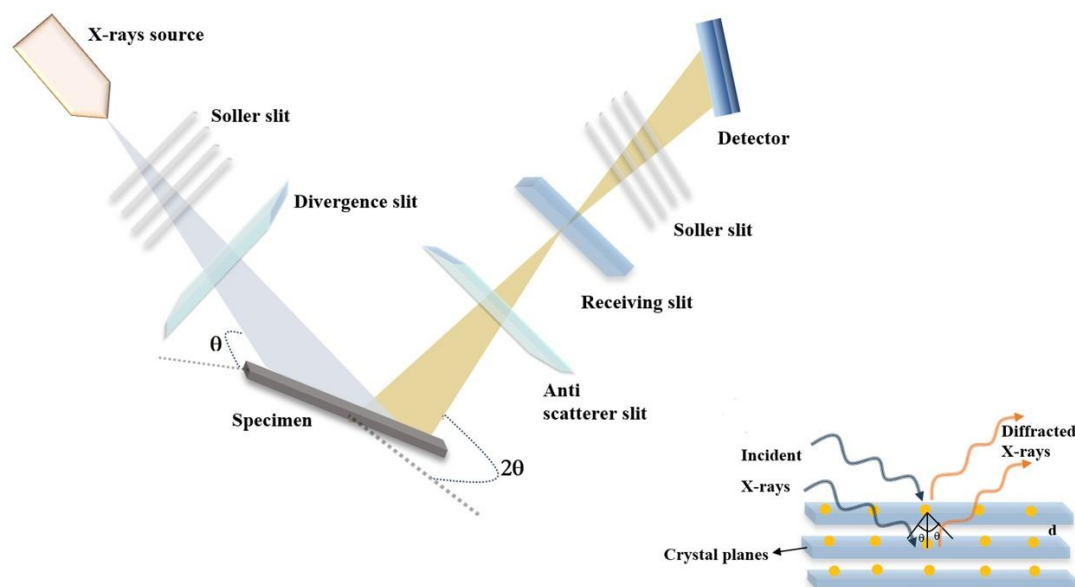


Fig. 2.3: A schematic instrumental arrangement for X-ray diffraction technique.

The peak width of XRD represents the information about crystal size, lattice distortion, and structural dislocation. Intensity is dependent upon: population of diffracting planes in the sample, concentration of species, particle size, chemical compositions, lattice plane orientation, crystal imperfections, and presence of amorphous constituents. The efficiency of XRD technique is dependent upon wavelength of radiation source and physical-chemical nature of the specimen. Due to difference in morphology of same material, it might exhibit XRD pattern with peaks having different relative intensities. This is due to preferred orientation of crystalline grains [34], Typical time taken to complete a particular scan is dependent upon two factors: step size and θ range. The analysis part is rather critical, which include determination of various parameters like cell parameters and angles of a particular crystal system. The analysis of XRD data is done by comparing the experimental data either with reference pattern from a crystallographic database or by simulated pattern, with former being the commonly practiced choice. To match the experimental data with reported references, some standard databases were established by the Joint Committee on Powder Diffraction standards (JCPDS) are commercially available. Apart from determining chemical composition and crystal structure information, XRD serves as an efficient technique to estimate the lattice strain, stress, and

crystallite size from various formulations. As the peak broadening is crucial factor in predicting the crystallite size, so Scherrer formula relates the broadening with crystallite size as following relationship [36]:

$$d = \frac{k\lambda}{\beta \cos \theta} \quad (2.55)$$

Where, d is crystallite size, β is full width at half maxima of diffraction peak, λ is wavelength of radiation, θ is diffraction angle, and k is Scherrer constant having a typical value of 0.9, though this value is dependent upon morphology of crystalline domains of the sample. However, another method to identify the crystallite size is the Williamson-Hall (W-H) plot which is given by:

$$\beta \cos \theta = \frac{k\lambda}{D} + 4\varepsilon \sin \theta \quad (2.56)$$

Where, ε is lattice strain. In W-H plotted between the $\beta \cos \theta$ and $\sin \theta$ in which intercept of graph give crystallite size and slope give strain in the system.

2.7.2.2 Raman spectroscopy

It is a non-destructive and versatile technique which provides information about chemical structure of material upon interaction with light [37]. It is a kind of finger-printing technique which offers both quantitative and qualitative analysis by measuring the intensity and frequency of scattered radiation, respectively [37]. Unlike IR spectroscopy, which deals with absorption of light by material, Raman spectroscopy relies upon examination of scattered light from the system. However, IR and Raman spectroscopy works complementary to each other. Moreover, the selection rules for IR and Raman spectroscopy differs by the fact that former requires change in dipole moment and later involves change in polarizability of the molecule [38]. Raman spectroscopy is based on the principle of inelastic scattering of radiation from the material. An essential condition to observe Raman spectrum is to have change in polarizability of material when incident upon by light. When light is incident on material, the interaction results in distortion of electron cloud around the nuclei and hence forms a virtual state of short lifetime. Most of the scattered radiation has same frequency as that of incident radiation and is termed as Rayleigh lines. Whereas, a small fraction of scattered radiation possesses the frequency smaller/larger than incident frequency, which are termed as Stokes/anti-Stokes lines. Stokes lines involve the transitions from lower vibrational level of virtual state to higher

vibrational level of ground state and are more intense compared to anti-Stokes lines. Hence, a typical Raman spectrum measures the Stokes lines. The relative intensities of Raman lines are dependent upon symmetry selection rules and population of various vibrational levels of ground state. Raman shift depends upon chemical composition of the scattering molecules and the intensity is governed by magnitude of variation in molecular polarization induced by incident light. This change in polarization governs the molecular vibrations [39]. A typical spectrometer consists of three main components: an excitation source (usually laser), sample, and detector system. The setup is garnished with suitable optics elements such as filter, monochromators etc. With advancement in this technique, laser sources are most popularly used as excitation source instead of lamps [39]. As, Raman intensity is 10^6 to 10^9 times less than Rayleigh scattering lines, so the laser sources are highly efficient in obtaining the otherwise frail Raman scattering lines. Some examples of laser sources are Argon ion laser (488.0 and 514.5 nm), Krypton ion laser (530.9 and 647.1 nm), He-Ne laser (632.8 nm), Nd:YAG laser (1064 and 532 nm), and near infra-red (NIR) excitation laser (785 and 830 nm) [40]. In present work, Nd:YAG laser (532 nm) was employed to obtain the Raman spectrum, as it is a long wavelength source and is known to cause no photodecomposition of samples as well as limits the fluorescence signal [38]. Generally, samples are analyzed after dispersion in some suitable solvents. However, in absence of appreciable dispersion of solid sample in any solvent, like in our case, the spectrum can be recorded by placing a small amount of powder sample on glass slide. Thus, upon irradiation, scattered light from the sample passes through various optics element (as is seen Fig. 2.4), which is finally fed to the detector. The data is obtained as intensity versus Raman shift (cm^{-1}). A general practice of analysis is matching the observed signals with literature database. However, in present case, there was no previous study on Raman spectrum of this system, which limited the analysis to quantitative stage.

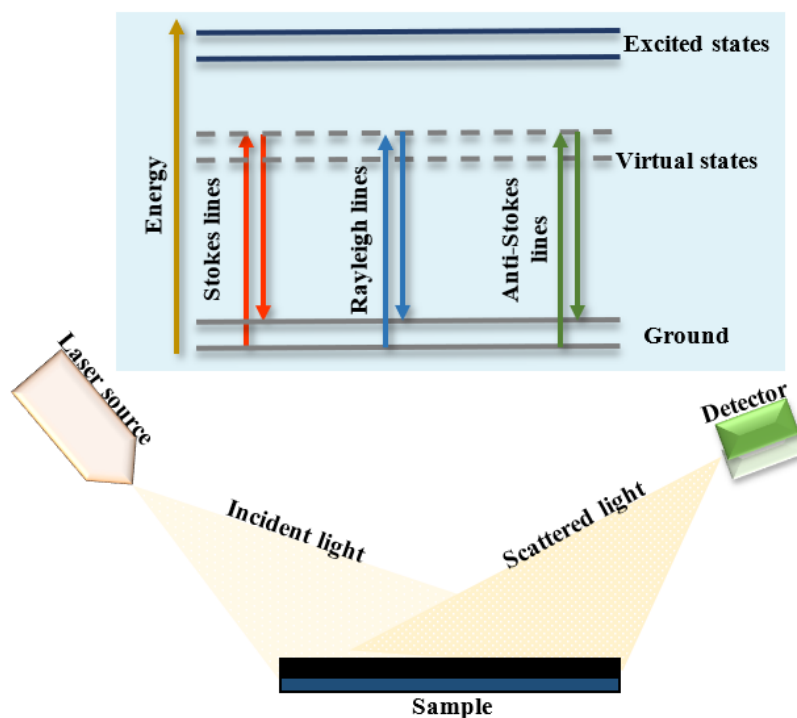


Fig. 2.4: A schematic illustration of energy level diagram for Raman spectroscopy.

2.7.2.3 X-ray absorption spectroscopy

XAS holds vital position in context to material characterization for examining the local electronic structure of the material. The quantum and physical state of absorbing atom is examined via transfer of energy from X-rays to core shell electrons, hence providing information about oxidation state, coordination number, symmetry of ligand environment, inter-atomic distances, and type of neighbouring atom [41, 42]. A typical XAS scan represents absorption coefficient versus incident X-ray energy, which exhibits some common features. XAS spectrum is divided in two parts: X-ray absorption near edge structure (XANES) and extended X-ray absorption fine structure (EXAFS). Principle of generation of XANES and EXAFS spectra is exemplified in Fig. 2.5. XANES is sensitive towards geometry and oxidation state and is less likely for quantitative analysis, while EXAFS exhibits radial distribution of electron density and yields quantitative analysis of bond length, coordination number and bond disorder [42].

2.7.2.3.1 Theory

When X-ray energy of order of electron binding energy for a particular shell (say K-shell) is provided, it results in maximum absorption with subsequent exhibition of sharp step like feature, called absorption edge (E_0). This absorption of energy is accompanied by transfer of

core shell electron to the highest unoccupied state (now called photoelectron) by creating a core hole or vacancy at its parent state, as governed by dipole and quadrupole selection rules. These core holes possess lifetime of order of 10^{-15} s, which decreases abruptly with an increase in atomic number of the element, hence causing broadening in XAS spectra as per relation $\Delta E = \hbar \times \tau^{-1}$, where τ and \hbar are core-hole lifetime and reduced Planck's constant, respectively [43, 44]. By increasing incident X-ray energy beyond absorption edge, the photoelectron gains kinetic energy and is scattered by neighbouring atoms before reaching the absorbing atom, which results in creation of spherical waves undergoing interference depending upon their phase difference. This interference of outgoing and scattered waves is origin behind imparting oscillatory profile to absorption coefficient named as EXAFS after normalization of oscillatory part, which is used to decrypt the information about neighbouring atoms. This region is dominated by single or multiple scattering from distant atoms and hence justifies the oscillatory nature of EXAFS region. However, many-body effect, i.e., inelastic effects experienced from extended valence orbitals of neighbouring atoms, destroys the coherence between photoelectron and core hole, which limits the probe length of EXAFS to 5-10 Å, and hence making it a short-range probing tool, suitable for crystalline as well as amorphous materials [44]. There are three modes in the XAS, which are transmission mode, electron yield mode, fluorescence yield mode.

Since, the physics behind XANES is that the probability of an electron to undergo transition from core level to empty levels depend upon energy of incident photon, thus energy of X-rays is scanned during data collection [44]. X-ray intensity after it has interacted with the sample is measured and analyzed. An important key point is the homogeneity of sample, since thickness variations reflected in data through introduction of non-linear response, can lead to wrong interpretation [45]. Transmission mode can be employed only for measurements utilizing hard X-rays, but not for soft X-rays due to less than 1 μm attenuation length. Figure 2.5: Left half of figure depicts the ways in which an incident X-ray beam can interact with matter and right half of figure illustrates the utilization of a particular interaction outcome as a X-ray absorption near edge structure (XANES) spectroscopy probe i.e. various modes of XANES measurement. Decay of core hole is accompanied by release of electrons, photons and ions being released from the surface of material. Detecting all the electrons emerging from sample surface in spite of their energy, one can obtain information about the current that flows to the sample owing to these emitted electrons [44]. Interaction cross section of electrons with matter is much higher than that of X-rays, thus the electrons that are detected must be originating from the surface or shallow depths beneath surface. So, probing depth of this mode lies in approximately 1-10 nm

range, influenced by edge strength and material properties. If the core-hole decays radiatively, then observation of fluorescence yield becomes the measurement basis. With the increase in incident energy, amount of fluorescent decay increases and can dominate Auger decay for hard X-ray measurements [44]. In that case, fluorescence intensity will be proportional to the absorption coefficient; however, for less dilute materials, peak features which could have been intense appear to be compressed characterized by a phenomenon of self-absorption.

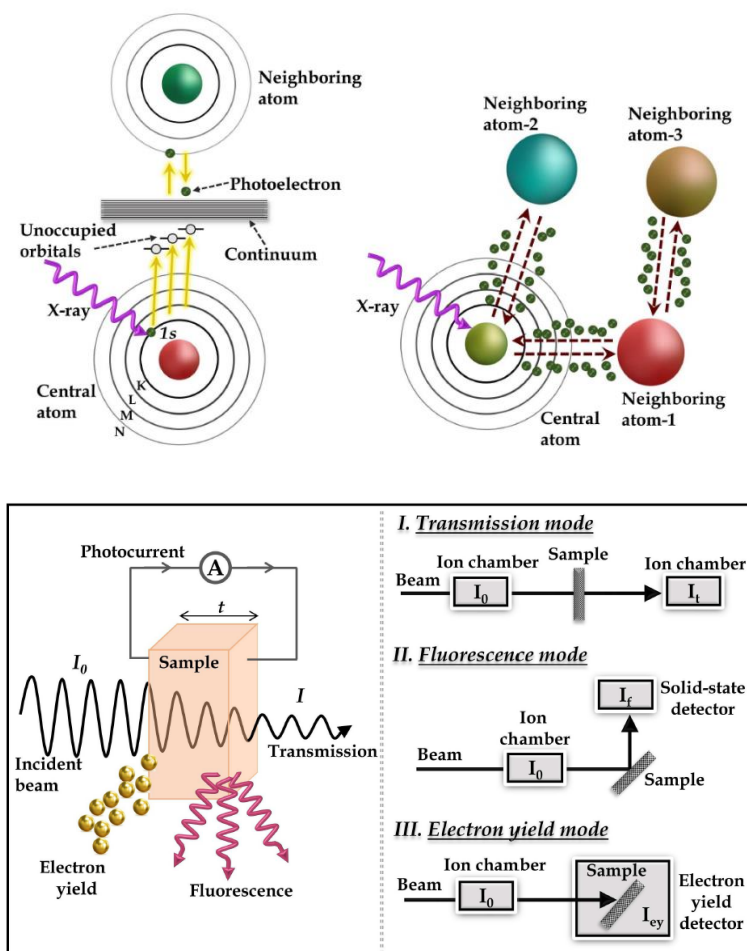


Fig. 2.5: A schematic representation of X-ray absorption spectra.

2.7.2.3.2 Data collection and analysis

The experiment is mainly concerned about recording the absorption coefficient μ , as per Beer-Lambert's law,

$$I_t = I_o e^{-\mu t} \quad (2.57)$$

where I_o , I_t and t are the incident intensity, transmitted intensity, and thickness of sample, respectively [46]. XAS requires broad energy range, where the broad bremsstrahlung region is useful. The X-rays emitted by these electrons in storage ring is fed to various beamlines, which

are dedicated for specific techniques by virtue of optics. Such a basic arrangement for XAS beamline is shown in Fig. 2.5, with demonstration of transmission and fluorescence mode of measurement. Due to such outstanding performance, synchrotron facilities are usually over-employed and one can get excess to experimental slot by submitting a proposal [41, 46]. The experimental plan starts with the choice of synchrotron facility, depending upon elements present in sample and absorption edges to be measured. With prior analysis of the sample status, it is decided whether to choose transmission or fluorescence mode. If the interest is to analyze chemical state (oxidation state and geometry), then XANES is focused and data collection is done till few hundred eV above absorption edge with slow scan rate.

2.7.2.4 Diffuse reflectance spectroscopy

Optical measurement constitutes the most important means of determining the band structure of materials and can be realized in three ways viz. UV-Vis absorption, transmission and diffuse reflectance measuring mode [47]. Optical reflections can be treated using Fresnel laws [48]. Highly opaque materials, which cannot be studied using UV-Vis electronic spectroscopy (both absorption and transmission), when exposed to electromagnetic radiation does show reflection whose angle of reflection is independent of angle of incidence termed as diffuse reflection [48]. In reality, diffuse reflection is a complex combination of reflection, refraction and scattering of incident radiation. When light is incident on an opaque powder sample, it gets reflected in all directions with one part undergoing specular reflection at surface, other part being refracted beneath the surface. It further undergoes internal reflection, reflection from powder grains' surfaces or repeated refraction and a part of this scattered light is received out of sample. This diffuse reflected light further weakens if it undergoes absorption by powder. Such materials exhibit absorption of light in certain energy range; thus, they act as absorbers as well as scatterers, simultaneously. This gives rise to a diffuse reflectance spectrum similar to a transmission spectrum. DRS is a technique for studying the spectral characteristics of opaque solid samples [49]. Thus, this complicated phenomenon is studied through careful consideration of absorbance and scattering characteristics of a material. Kubelka-Munk theory treats this phenomenon, to describe and analyze the diffuse reflectance spectrum, by obtaining an equivalent absorption spectrum of material [50]. It is considered that one can relate diffuse reflectance, R_∞ , from a layer of infinite thickness with absorption coefficient (K) and scattering coefficient (S) by the Kubelka-Munk remission function ($F(R_\infty)$) as:

$$F(R_\infty) = \frac{(1 - R_\infty)^2}{2R_\infty} = \frac{K}{S} \quad (2.58)$$

Infinite thickness for opaque samples is usually few mm. Optical band gap of such opaque materials can be calculated from Tauc plot by plotting a curve between $(h\nu(F(R)))^{1/n}$ versus $h\nu$ [51]. Here, n is power factor of transition mode and can have values 1/2, 3/2, 2 or 3 for direct allowed, direct forbidden, indirect allowed and indirect forbidden transitions, respectively. Extrapolation of the curve to x-axis gives the value of optical band gap of the material. A typical experimental set-up for DRS measurement is shown in Fig. 2.6. In order to reduce the specular reflection contribution, integrating sphere is used. Sample is placed in front of light source inside the integrating sphere and reflected light is concentrated on the detector through sphere coated with barium sulfate from inside. When angle of incidence of light is 0° , specularly reflected light exit from opening of sphere and does not interfere with diffuse reflectance measurement [52]. This type of set-up has increased the sensitivity of DRS manifold.

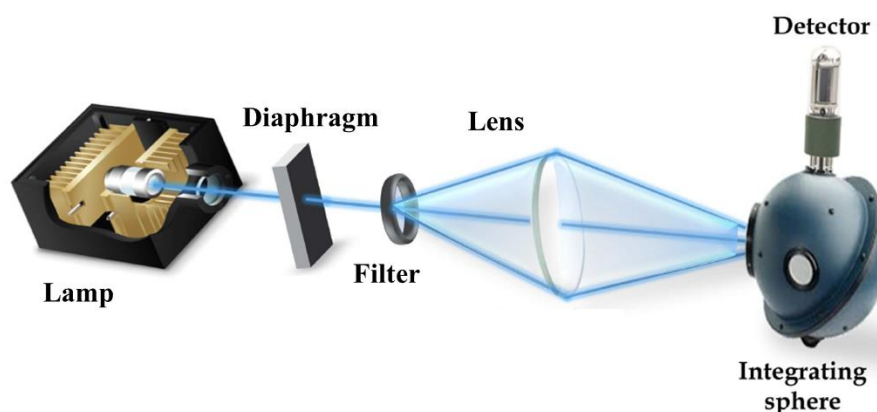


Fig 2.6: A typical experimental set up of diffuse reflectance spectra.

2.7.2.5 Photoluminescence:

A typical spectrometer is composed of three main components- light source, sample chamber, and photon detector. Apart from that, a dedicated optics section is employed to get information about characteristic features of sample. A schematic is presented in Fig. 2.7. The source can be high pressure mercury vapour lamp, laser or Xe lamp. The aim of experiment and wavelength range decides the type of excitation source. Among these, Xe lamp is popularly used due to its tendency to cover UV, visible, and NIR region. The sample holder cavity is at 45° with respect to the source, so as to align fluorescence emission towards detector. In between the sample holder and light source, an excitation monochromator is placed, which is usually a prism monochromator or diffraction grating. The sample holder cavity is attached to a transmission detector, which is usually a photomultiplier tube (PMT) to collect the transmitted signal. The

next section is analyzer monochromator, which is again a prism monochromator or diffraction grating to filter the stray light and to pass the emission of sample only to the detector. The last component is detector, which can be a PMT. The geometry is so arranged to have right angle between source and detector. Thus, the light from source excites the sample which undergoes electronic transitions to give fluorescence/phosphorescence signal, which is ultimately fed to the detector. The spectrometer is attached to a computer system, which collects the data and gives the output [53, 54]. The data is collected as intensity versus wavelength. There are usually two modes of data collection: emission and excitation spectrum. The former deals with scanning the emission over a range of excitation wavelengths, whereas later deals with monitoring the excitation when emission wavelength is fixed.

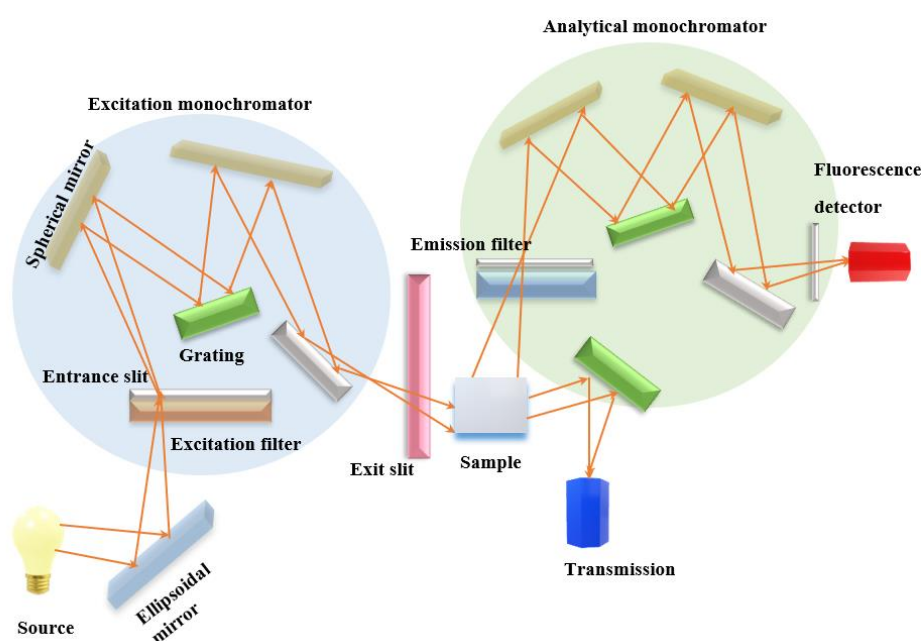


Fig. 2.7: A diagram representing the setup for photoluminescence measurements.

2.8 Summary

This chapter addresses the detailed computational methodology behind the present thesis, starting with introducing many-electron system. Following that, we discussed different approximate methods used to solve the many-electron Schrödinger equation using DFT. Furthermore, the essential explanation of exchange-correlation functionals is added to the discussion. The semi-classical Boltzmann transport theory used to calculate the transport properties is also discussed in brief. A brief overview of the computational software used to calculate the different material properties investigated in the thesis. After that experimental methodology and various characterization techniques are discussed.

References

- [1] N. Zettili, *Quantum mechanics: concepts and applications*, 2nd ed. Chichester, U.K.: Wiley, 2009.
- [2] I. N. Levine, *Quantum chemistry*, Seventh edition. Boston: Pearson, 2014.
- [3] M. Born and R. Oppenheimer, “Zur Quantentheorie der Molekeln,” *Annalen der Physik*, 389, 457–484, 1927, doi: 10.1002/andp.19273892002.
- [4] D. R. Hartree, “The Wave Mechanics of an Atom with a Non-Coulomb Central Field. Part I. Theory and Methods,” *Math. Proc. Camb. Phil. Soc.*, 24, 89–110, 1928, doi: 10.1017/S0305004100011919.
- [5] V. Fock, “Näherungsmethode zur Lösung des quantenmechanischen Mehrkörperproblems,” *Z. Physik*, 61, 126–148, 1930, doi: 10.1007/BF01340294.
- [6] M. C. Payne, M. P. Teter, D. C. Allan, T. A. Arias, and J. D. Joannopoulos, “Iterative minimization techniques for *ab initio* total-energy calculations: molecular dynamics and conjugate gradients,” *Rev. Mod. Phys.*, 64, 1045–1097, 1992, doi: 10.1103/RevModPhys.64.1045.
- [7] P. Hohenberg and W. Kohn, “Inhomogeneous Electron Gas,” *Phys. Rev.*, 136, B864–B871, 1964, doi: 10.1103/PhysRev.136.B864.
- [8] L. H. Thomas, “The calculation of atomic fields,” *Math. Proc. Camb. Phil. Soc.*, 23, 542–548, 1927, doi: 10.1017/S0305004100011683.
- [9] S. Seriy, “Modern Ab-Initio Calculations on Modified Tomas-Fermi-Dirac Theory,” *OJMSi*, 03, 96–103, 2015, doi: 10.4236/ojmsi.2015.33010.
- [10] W. Kohn and L. J. Sham, “Self-Consistent Equations Including Exchange and Correlation Effects,” *Phys. Rev.*, 140, A1133–A1138, 1965, doi: 10.1103/PhysRev.140.A1133.
- [11] F. Herman, J. P. Van Dyke, and I. B. Ortenburger, “Improved Statistical Exchange Approximation for Inhomogeneous Many-Electron Systems,” *Phys. Rev. Lett.*, 22, 807–811, 1969, doi: 10.1103/PhysRevLett.22.807.
- [12] J. P. Perdew and Y. Wang, “Accurate and simple analytic representation of the electron-gas correlation energy,” *Phys. Rev. B*, 45, 13244–13249, 1992, doi: 10.1103/PhysRevB.45.13244.
- [13] J. P. Perdew *et al.*, “Atoms, molecules, solids, and surfaces: Applications of the generalized gradient approximation for exchange and correlation,” *Phys. Rev. B*, 46, 6671–6687, 1992, doi: 10.1103/PhysRevB.46.6671.

- [14] J. P. Perdew, K. Burke, and M. Ernzerhof, “Generalized Gradient Approximation Made Simple [Phys. Rev. Lett. 77, 3865 (1996)],” *Phys. Rev. Lett.*, 78, 1396–1396, 1997, doi: 10.1103/PhysRevLett.78.1396.
- [15] P. Ondračka, D. Holec, D. Nečas, and L. Zajíčková, “Accurate prediction of band gaps and optical properties of HfO₂,” *J. Phys. D: Appl. Phys.*, 49, 395301, 2016, doi: 10.1088/0022-3727/49/39/395301.
- [16] A. D. Becke and E. R. Johnson, “A simple effective potential for exchange,” *The Journal of Chemical Physics*, 124, 221101, 2006, doi: 10.1063/1.2213970.
- [17] P. Blaha, “an Augment Plane Wave+ Local Orbitals Program for Calculating Crystal Properties, User’s Guide.” Vienna Austria.
- [18] P. Schwerdtfeger, “The Pseudopotential Approximation in Electronic Structure Theory,” *ChemPhysChem*, 12, 3143–3155, 2011, doi: 10.1002/cphc.201100387.
- [19] V. Heine, “The Pseudopotential Concept,” in *Solid State Physics*, 24, 1–36, 1970, doi: 10.1016/S0081-1947(08)60069-7.
- [20] P. E. Blöchl, “Projector augmented-wave method,” *Phys. Rev. B*, 50, 17953–17979, 1994, doi: 10.1103/PhysRevB.50.17953.
- [21] J. G. LEE, *COMPUTATIONAL MATERIALS SCIENCE: an introduction, second edition*. Place of publication not identified: CRC Press, 2023.
- [22] W. Kohn, “Nobel Lecture: Electronic structure of matter—wave functions and density functionals,” *Rev. Mod. Phys.*, 71, 1253–1266, 1999, doi: 10.1103/RevModPhys.71.1253.
- [23] H. J. Monkhorst and J. D. Pack, “Special points for Brillouin-zone integrations,” *Phys. Rev. B*, 13, 5188–5192, 1976, doi: 10.1103/PhysRevB.13.5188.
- [24] J. M. Ziman, *Electrons and Phonons*. Oxford University Press, 2001. doi: 10.1093/acprof:oso/9780198507796.001.0001.
- [25] G. Kresse and J. Furthmüller, “Efficient iterative schemes for *ab initio* total-energy calculations using a plane-wave basis set,” *Phys. Rev. B*, 54, 11169–11186, 1996, doi: 10.1103/PhysRevB.54.11169.
- [26] G. K. H. Madsen and D. J. Singh, “BoltzTraP. A code for calculating band-structure dependent quantities,” *Computer Physics Communications*, 175, 67–71, 2006, doi: 10.1016/j.cpc.2006.03.007.
- [27] A. Togo and I. Tanaka, “First principles phonon calculations in materials science,” *Scripta Materialia*, 108, 1–5, 2015, doi: 10.1016/j.scriptamat.2015.07.021.
- [28] A. Togo, L. Chaput, and I. Tanaka, “Distributions of phonon lifetimes in Brillouin zones,” *Phys. Rev. B*, 91, 094306, 2015, doi: 10.1103/PhysRevB.91.094306.

- [29] A. Sharma, M. Varshney, H.-J. Shin, K. Chae, and S. O. Won, "XANES, EXAFS and photoluminescence investigations on the amorphous Eu:HfO₂," *Spectrochimica Acta Part A: Molecular and Biomolecular Spectroscopy*, 173, 549–555, 2017, doi: 10.1016/j.saa.2016.10.006.
- [30] H. Padma Kumar, S. Vidya, S. Saravana Kumar, C. Vijayakumar, S. Solomon, and J. K. Thomas, "Optical properties of nanocrystalline HfO₂ synthesized by an auto-igniting combustion synthesis," *Journal of Asian Ceramic Societies*, 3, 64–69, 2015, doi: 10.1016/j.jascer.2014.10.009.
- [31] Y. Wan and X. Zhou, "Formation mechanism of hafnium oxide nanoparticles by a hydrothermal route," *RSC Adv.*, 7, 7763–7773, 2017, doi: 10.1039/C6RA26663K.
- [32] Z. J. Wang, T. Kumagai, H. Kokawa, M. Ichiki, and R. Maeda, "Preparation of hafnium oxide thin films by sol–gel method," *J Electroceram*, 21, 499–502, 2008, doi: 10.1007/s10832-007-9228-x.
- [33] B. D. Cullity and S. R. Stock, *Elements of X-ray diffraction*, 3. ed., new Internat. ed. Harlow: Pearson Education, 2014.
- [34] V. K. Pecharsky and P. Y. Zavalij, *Fundamentals of powder diffraction and structural characterization of materials*. New York: Springer, 2005.
- [35] Suryanarayana, C. and Norton, M. Grant, *X-ray Diffraction A Practical Approach*. Springer Verlag, 2014.
- [36] K. He, N. Chen, C. Wang, L. Wei, and J. Chen, "Method for Determining Crystal Grain Size by X-Ray Diffraction," *Crystal Research and Technology*, 53, 1700157, 2018, doi: 10.1002/crat.201700157.
- [37] X. Zhang, Q.-H. Tan, J.-B. Wu, W. Shi, and P.-H. Tan, "Review on the Raman spectroscopy of different types of layered materials," *Nanoscale*, 8, 6435–6450, 2016, doi: 10.1039/C5NR07205K.
- [38] N. B. Colthup, L. H. Daly, and S. E. Wiberley, *Introduction to infrared and Raman spectroscopy*, 3rd ed. Boston: Academic Press, 1990.
- [39] P. Vandenabeele, *Practical Raman Spectroscopy – An Introduction*, 1st ed. Wiley, 2013. doi: 10.1002/9781119961284.
- [40] G. S. Bumbrah and R. M. Sharma, "Raman spectroscopy – Basic principle, instrumentation and selected applications for the characterization of drugs of abuse," *Egyptian Journal of Forensic Sciences*, 6, 209–215, 2016, doi: 10.1016/j.ejfs.2015.06.001.

- [41] B. K. Teo, *EXAFS: Basic Principles and Data Analysis*, vol. 9. in *Inorganic Chemistry Concepts*, vol. 9. Berlin, Heidelberg: Springer Berlin Heidelberg, 1986. doi: 10.1007/978-3-642-50031-2.
- [42] Y. Iwasawa, K. Asakura, and M. Tada, Eds., *XAFS Techniques for Catalysts, Nanomaterials, and Surfaces*. Cham: Springer International Publishing, 2017. doi: 10.1007/978-3-319-43866-5.
- [43] F. M. F. de Groot, A. Kotani, and F. de Groot, *Core level spectroscopy of solids*. in *Advances in condensed matter science*, no. 6. Boca Raton, Fla.: CRC Press, 2008.
- [44] G. Bunker, *Introduction to XAFS: A Practical Guide to X-ray Absorption Fine Structure Spectroscopy*, 1st ed. Cambridge University Press, 2010. doi: 10.1017/CBO9780511809194.
- [45] M. Newville, “Fundamentals of XAFS,” *Reviews in Mineralogy and Geochemistry*, 78, 33–74, 2014, doi: 10.2138/rmg.2014.78.2.
- [46] S. K. Sharma, Ed., *Handbook of Materials Characterization*. Cham: Springer International Publishing, 2018. doi: 10.1007/978-3-319-92955-2.
- [47] F. Wooten, *Optical properties of solids*. New York NY: Academic Press, 1972.
- [48] K. Sakoda, *Optical properties of photonic crystals*. in *Springer series in optical sciences*, no. 80. Berlin Heidelberg New York: Springer, 2001.
- [49] W. Cao *et al.*, “Re-Visiting the Quantification of Hematite by Diffuse Reflectance Spectroscopy,” *Minerals*, 12, 872, 2022, doi: 10.3390/min12070872.
- [50] E. L. Simmons, “Reflectance spectroscopy: application of the Kubelka-Munk theory to the rates of photoprocesses of powders,” *Appl. Opt.*, 15, 951, 1976, doi: 10.1364/AO.15.000951.
- [51] M. Nowak, B. Kauch, and P. Szperlich, “Determination of energy band gap of nanocrystalline SbSI using diffuse reflectance spectroscopy,” *Review of Scientific Instruments*, 80, 046107, 2009, doi: 10.1063/1.3103603.
- [52] S. C. McClain, C. L. Bartlett, J. L. Pezzaniti, and R. A. Chipman, “Depolarization measurements of an integrating sphere,” *Appl. Opt.*, 34, 152, 1995, doi: 10.1364/AO.34.000152.
- [53] M. Anpo, S. Dzwigaj, and M. Che, “Chapter 1 Applications of Photoluminescence Spectroscopy to the Investigation of Oxide-Containing Catalysts in the Working State,” in *Advances in Catalysis*, 52, 1–42, 2009, doi: 10.1016/S0360-0564(08)00001-1.
- [54] J. R. Lakowicz, Ed., *Principles of Fluorescence Spectroscopy*. Boston, MA: Springer US, 2006. doi: 10.1007/978-0-387-46312-4.

Thermoelectric properties of pure and doped HfO₂

3.1 Introduction

The utilization of the TE energy harvesting technique can be a viable avenue for addressing the escalating demand for energy in a sustainable manner. The performance of a TE material is usually gauged by a dimensionless quantity known as the figure of merit i.e., $ZT = \sigma S_{\alpha}^2 T / \kappa_{total}$. To realize a high value of ZT , a TE material indeed has a low value of κ_{total} and a high value σ and S_{α} [1]. Augmentation in the TE performance of a material is significantly contributed by phonon and carrier transport [1, 2]. To achieve efficient TE performance at high temperatures, a variety of oxide-based materials, including some wide band gap semiconductors, have been theoretically predicted and experimentally realized [3–7].

The various existing polymorphs of HfO₂ and their applicability are discussed in Chapter 1. Although, the pure HfO₂ has a wide band gap of ~5.7 eV which is too large in the sense of TE applications but it naturally contains large concentrations of oxygen defects which can be generated during the sample growth and deposition. It has been observed that these oxygen vacancies play a key role in upsurging the carrier concentration of various polymorphs of HfO₂ and in reducing the band gap which makes it an excellent thermoelectric at high temperature. For instance, Hilderbrandt et al. have reported that *p*-type carrier concentration of the order $6 \times 10^{21} \text{ cm}^{-3}$ in HfO_{2-x} and reduction of band gap from 5.7 eV to 4.5 eV have been observed [8]. In a similar study, Kaiser et al. have found carrier concentration varies from $3.4 \times 10^{21} \text{ cm}^{-3}$ to $1.8 \times 10^{22} \text{ cm}^{-3}$ and Hadacek et al. have found 10^{22} cm^{-3} *p*-type charge carrier concentrations, in HfO₂ [9, 10]. Wu et al. have demonstrated the reduction in the band gap of *m*-HfO₂ owing to oxygen defects [11].

In addition to these studies, band engineering has been established as an effective technique to reduce the band gap and enhance carrier concentration. González et al. have reported that band engineering via Mn-doping in *m*-HfO₂ results in band gap reduction up to 2.1 eV [12]. Perevalov et al have realized the carrier concentration of $8.7 \times 10^{21} \text{ cm}^{-3}$ with the co-doping of Zr and La in HfO₂ [13]. In a theoretical investigation, Islamov et al. demonstrated the carrier concentration of the order 10^{21} cm^{-3} in Zr doped *o*-HfO₂ with oxygen defect [14]. Efforts have been made to improve its TE performance by doping, and it has been reported that C and V

doped *c*-HfO₂ could be a potential candidate for TE application [15, 16]. Besides enhancing carrier concentration and reducing band gap, the oxygen vacancies may also help in reducing the thermal conductivity in metal oxides [17, 18]. Various reports of relatively low κ_l for HfO₂ over other metal oxides have existed in the literature [19, 20]. These reports suggest that the naturally present oxygen vacancies are leading to higher carrier concentration and relatively low lattice thermal conductivity in HfO₂ which can make it an excellent thermoelectric energy harvesting material. Hence, it is vital to evaluate the effect of carrier concentration and doping for the true estimation of *ZT*.

Therefore, we explored the various polymorphs of HfO₂ in a broad temperature range (300 K -1200 K) at varying carrier concentrations to achieve optimum *ZT*. The detailed investigation of structural, electronic, phonon transport, and thermoelectric properties is carried out using the *first-principles* method and semi-classical Boltzmann transport theory. The phonon behavior is examined to check the dynamical stability of the studied systems and to evaluate the lattice thermal conductivities. We demonstrated how the optimized carrier concentration and doping can enhance the thermoelectric performance of HfO₂.

3.2 Computational Methodology

The electronic and transport properties were evaluated using the formalism of DFT as implemented in the WIEN2K code (a full potential linearized augmented plane wave method) [21]. The GGA scheme for XC potentials, given by Perdew-Burke-Ernzerhof (PBE), was used for structural optimization [22]. The approximations such as local density approximation and GGA underestimate the band gap [23]. Therefore, we have used TB-mBJ approximation [24] to comprehend exchange and correlation potentials which uses semilocal quantities to reproduce well step structures. For precise calculations, a K-mesh of 20× 20×20 with 256 K-points was used in the IBZ for all the polymorphs of HfO₂. The plane wave cutoff was decided by the $R_{MT}K_{max} = 7$, and the muffin tin sphere radii were chosen to be non-overlapping with RMT of 2.18 for Hf atom and 1.5 for O atom. The criterion for energy convergence was set to 0.0001 Ry/cell and the cut-off energy of the core and valence state was fixed at -6 Ry. The temperature dependent thermoelectric properties were obtained under constant relaxation time approximation using BoltzTraP code by solving semi-classical Boltzmann transport theory [25]. A denser K-mesh of 36×36×36 was employed for the calculation of various transport properties.

To check the dynamical stability of all polymorphs, we used Phonopy code [26]. We calculated the 2nd and 3rd order force constants using the Phono3py code [27] interfaced with the VASP [28] to estimate κ_l . The plane wave cut-off energy was set to 560 eV, and a $9 \times 9 \times 9$, $9 \times 9 \times 5$, $7 \times 7 \times 7$, $7 \times 7 \times 7$ Gamma-centred K-point mesh was used for the *c*-, *t*-, *m*-, and *o*- HfO₂, respectively. An optimized q-mesh of $25 \times 25 \times 25$ was used for the calculation of κ_l .

3.3 Results and discussion

3.3.1 Structural properties

The structural parameters are optimized for all the polymorphs of HfO₂ within the parameterization of GGA by fitting Birch-Murnaghan equation of states [29], and the corresponding volume optimization curves are shown in Fig. 3.1. Our optimized lattice parameters are in good agreement with the previously reported experimental results (listed in table 3.1) [30–33]. Therefore, we have not optimized the angles of the monoclinic structure but rather taken the experimental values from the literature.

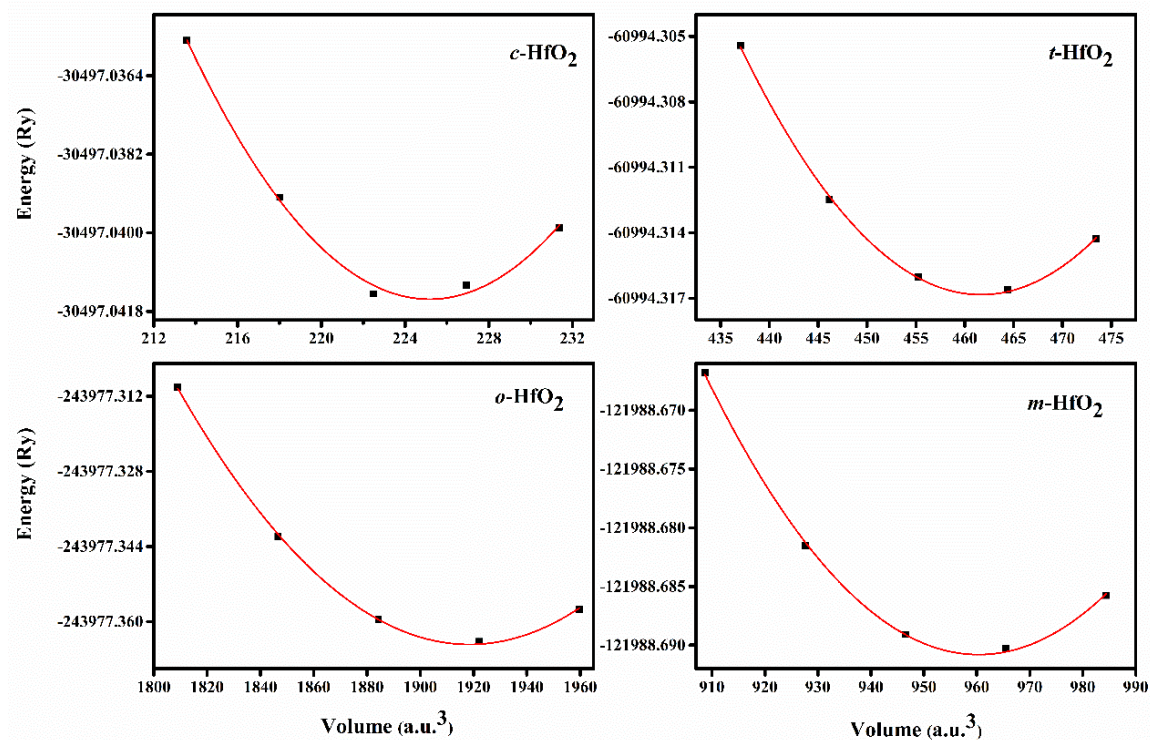


Fig. 3.1: Energy vs Volume optimization curve of all polymorphs of HfO₂.

Table 3.1. The optimized lattice parameters of all polymorphs of HfO₂.

Polymorphs of HfO ₂	Space group	Lattice parameters (in Å)	
		Theoretical	Experimental
Monoclinic	P2 ₁ /c	a = 5.14, b = 5.19, c = 5.33 $\alpha = 90^\circ, \beta = 99.19^\circ, \gamma = 90^\circ$	a = 5.11, b = 5.16, c = 5.29 [30]
Cubic	Fm $\bar{3}$ m	a = 5.09 $\alpha = \beta = \gamma = 90^\circ$	a = 5.09 [31]
Orthorhombic	Pbca	a = 5.18, b = 10.169, c = 5.29 $\alpha = \beta = \gamma = 90^\circ$	a = 5.107, b = 10.10, c = 5.270 [33]
Tetragonal	P4 ₂ /nmc	a = 3.54, c = 5.20 $\alpha = \beta = \gamma = 90^\circ$	a = 3.62, c = 5.28 [32]

To check the dynamical stability, we performed the phonon calculations on a $9 \times 9 \times 9$ k-mesh using the density functional perturbation theory implemented in the Phonopy code. A $2 \times 2 \times 2$ supercell is used for monoclinic and orthorhombic structures, whereas a $3 \times 3 \times 3$ supercell is employed for cubic and tetragonal structures to obtain force constants. The phonon band structure, as depicted in Fig. 3.2, shows no imaginary frequencies, indicating that all phases are dynamically stable. Moreover, the mechanical stability of all the polymorphs has already been established through elastic constants [34].

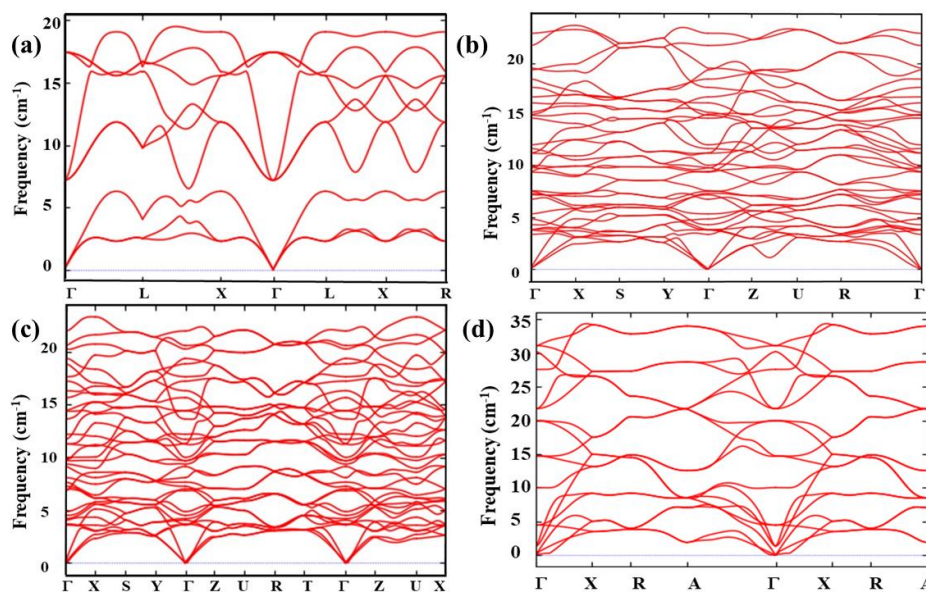


Fig. 3.2: The phonon band structure diagram for (a) *c*-HfO₂, (b) *m*-HfO₂, (c) *o*-HfO₂, and (d) *t*-HfO₂.

We doped HfO₂ with Ti at Hf sites and S at O sites, the resulting alloy formula is Hf_{1-x}Ti_xO₂ and HfO_{2-x}S_x where x= 0, 0.03, 0.06, 0.12, and 0.25. To simulate lower doping concentration (0.03, 0.06, 0.12), a 2x2x2 supercell has been used, whereas, for x= 0.25, a 1x1x1 supercell has been used. Since the Ti and S-doped *c*-HfO₂ have not been yet reported theoretically or experimentally, it is imperative to check the stability of the resulting alloys before doing any further calculations. Therefore, we have estimated the formation energy ($E_{formation}$) for all doping concentrations using the following relation:

$$E_{formation} = \frac{\{E_{Total} - n(E_{Hf\ atom} + E_{O\ atom} + E_{Ti\ or\ S\ atom})\}}{N} \quad (3.1)$$

where E_{Total} is the total energy of the pure or doped supercell, n is the number of atoms of the particular species, E_{Hf} , E_O , E_{Ti} , and E_S is the energy of the corresponding isolated atom, and N is the total number of atoms in the cell. The negative formation energy corresponding to all doping concentrations confirms their thermodynamic stabilities. Moreover, a convex hull is another reliable way to check the thermodynamic stability of materials [35]. The convex hull of formation energies referenced to the elemental standard states is shown in Fig. 3.3. It can be seen that Hf_{0.97}Ti_{0.03}O₂, Hf_{0.94}Ti_{0.06}O₂, Hf_{0.88}Ti_{0.12}O₂, HfO_{1.97}S_{0.03} and HfO_{1.94}S_{0.06} are lies on the convex hull line which shows that these doping concentrations are thermodynamically stable. We have also analyzed a few more hypothetical doping concentrations such as Hf_{0.75}Ti_{0.25}O₂, Hf_{0.50}Ti_{0.50}O₂, Hf_{0.25}Ti_{0.75}O₂, HfO_{1.88}S_{0.12}, HfO_{1.75}S_{0.25}, HfO_{1.50}S_{0.50}, HfO_{1.25}S_{0.75} and found that these are lying above the convex hull line which shows their instability. The decomposition energy, ΔE_d , is equal to the vertical distance in formation energy space between the particular material and the hull line [35] and $\Delta E_d = 0$ or negative is a signature of stability.

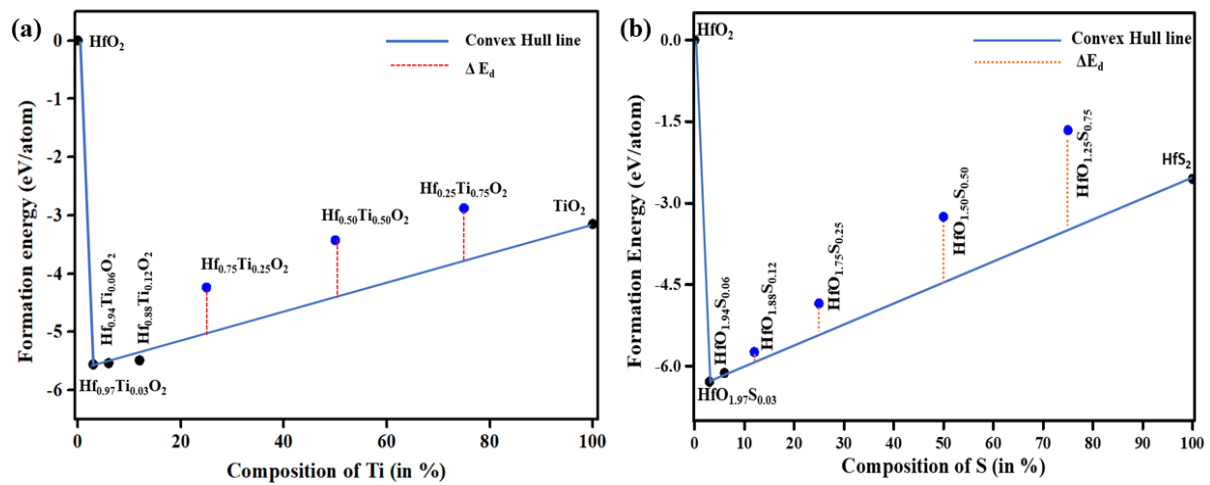


Fig. 3.3: A schematic convex hull of (a) $\text{Hf}_{1-x}\text{Ti}_x\text{O}_2$ and (b) $\text{HfO}_{2-x}\text{S}_x$ at different compositions (in %). ΔE_d is given by the vertical distance in formation energy space between the particular material and the hull line.

3.3.2 Electronic properties

The electronic band structure calculations are essential to understand the derived properties of polymorphic phases of HfO_2 . Fig. 3.4 shows the high symmetry points of c -, m -, o -, t - HfO_2 in the first Brillouin zone that is considered in the band structure calculations. The obtained band structure for various polymorphs along the high symmetry K-path is shown in Fig. 3.5. The estimated value of the band gap using GGA and TB-mBJ is listed in Table 3.2. The calculated band gaps using TB-mBJ potential are in good agreement with the previously available experimental and theoretical results [31], [36–38]. From the band structures, it can be seen that the top of the valence band for m -, o -, and t -phases are at Γ the point, and the c -phase is at X point. The bottom of the conduction band is at X for c - and m - HfO_2 and at Γ for o - and t - HfO_2 . The VBM of o - HfO_2 (inset Fig. 3.4) is shown in the inset for its better appearance. Hence the phases c -, o -, and t - HfO_2 show a direct band gap, whilst m - HfO_2 exhibits an indirect band gap.

Table 3.2. The band gaps (with GGA and TB-mBJ approach) and effective mass for all polymorphs of HfO_2 .

Polymorphs of HfO_2	Band gaps (in eV)				Effective Mass	
	Theoretical			Experim ental	CBM	VBM
	GGA	TB-mBJ	Others			
Monoclinic	4.11	5.76	TB-mBJ 5.76 [40]	5.71 [16]	$0.62m_e$	$2.49m_e$
Cubic	3.78	5.82	TB-mBJ 5.88 [40]	5.88 [35]	$0.73m_e$	$0.28m_e$
Orthorhombic	4.46	6.30	GGA 4.30 [41]	-----	$1.04m_e$	$2.92m_e$
Tetragonal	4.68	6.46	TB-mBJ 6.54 [40]	-----	$0.59m_e$	$4.85m_e$

For a better analysis of the band structure of all phases, we presented the partial density of states (PDOS) in Fig. 3.6. In the valence band (VB), the O-total atomic states are dominant over Hf-total atomic states and attain the maxima near the E_F . Whereas, in the conduction band (CB), Hf-total atomic states are dominant over O-atomic states in all studied energy regions. In the CB, the contribution of atomic states sharply increases ~ 6 eV, and after that, decreases at ~ 8 eV in all the phases except m - HfO_2 .

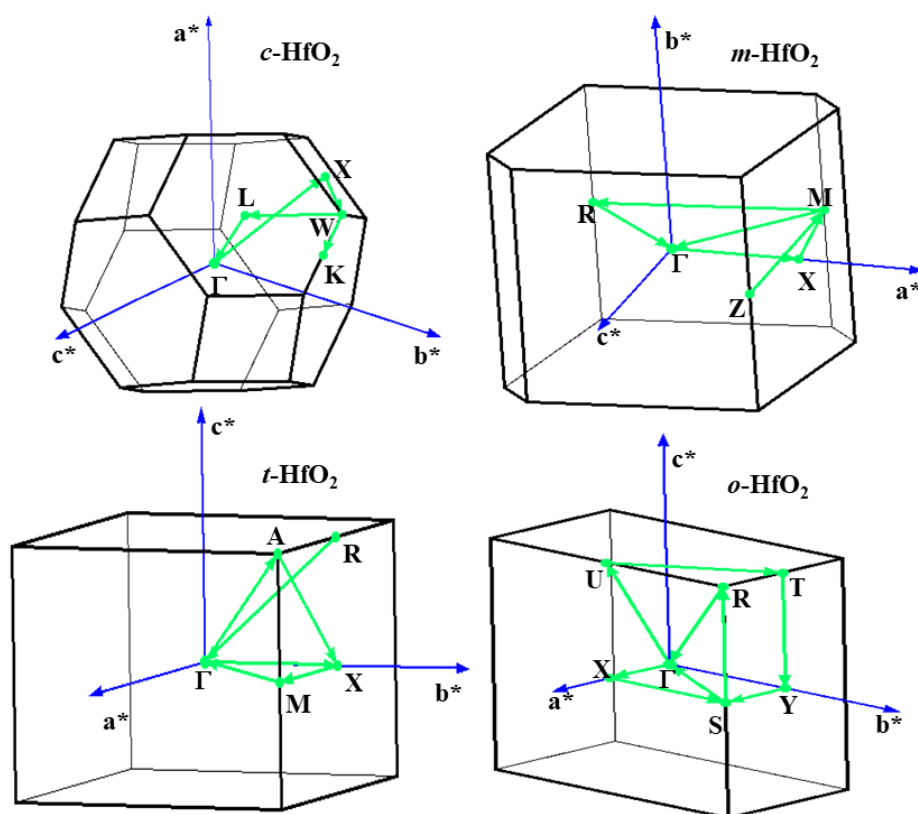


Fig. 3.4: The first Brillouin zone of all polymorphs of HfO₂ with high symmetry points.

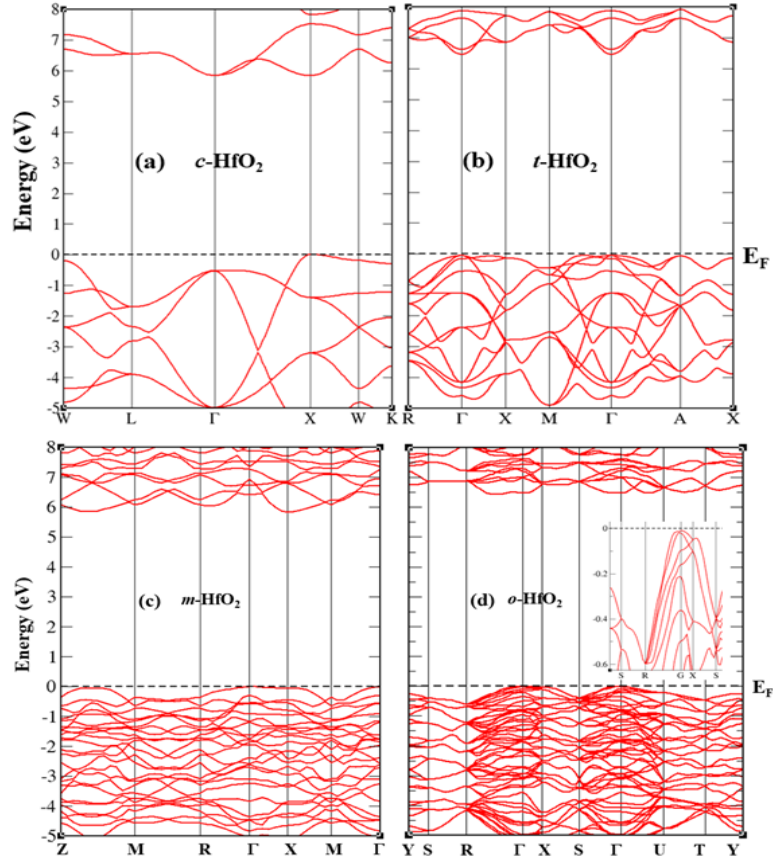


Fig. 3.5: The band structure diagram of all the polymorphs of HfO_2 (E_F is shifted to 0 eV) (Inset VBM of $o\text{-HfO}_2$).

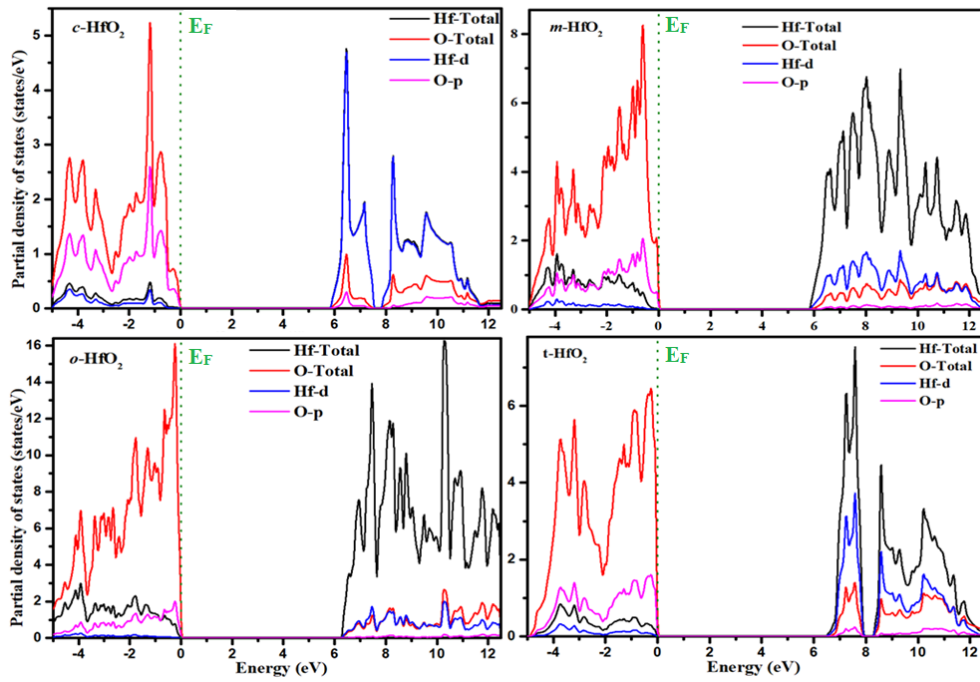


Fig. 3.6: The partial density of states of all the polymorphs of HfO_2 (E_F is shifted to 0 eV).

3.3.3 Effect of Ti doping on the electronic properties

In the case of $\text{Hf}_{1-x}\text{Ti}_x\text{O}_2$, it is observed that 25% doping radically shifted the band gap along Γ - Γ direction, and the magnitude of this band gap reduced to 2.16 eV with two-fold degeneracy (Fig. 3.7 (a)). This reduction in band gap may be attributed to the Ti states. For $x = 0.12$, 0.06, and 0.03 in $\text{Hf}_{1-x}\text{Ti}_x\text{O}_2$, we examined the band structures as shown in Fig. 3.7 (b)–(d). As discussed for $x = 0.25$, a similar band gap shift along the Γ - Γ direction is observed for all lower concentrations of Ti and the magnitude of the band gap increases monotonically as we move from $x = 0.25$ to lower doping concentrations. At $x = 0.03$, 0.06, 0.12, and 0.25 doping, the obtained value of band gap along Γ -H-N- Γ -P high symmetry K points is 2.68 eV, 2.61 eV, 2.48, and 2.16 eV, respectively. Further, it is observed that as we move towards lower doping values, the signature of flat bands starts to appear more vigorously. In $\text{Hf}_{1-x}\text{Ti}_x\text{O}_2$ ($x = 0.03$, 0.06, 0.12, 0.25), the band structures plotted along R- Γ -X-M- Γ high symmetry K points. To ascertain the effect of various atomic species on the electronic structures, we also analyzed the DOS for all values of x (Fig. 3.8 (a)–(d)). The contribution of various atoms in VBs of all doped structures is found to be the same as in the case of pure c - HfO_2 phase, whereas the induced Ti-states in lower CB occur in between 2 and 4 eV. Above ~ 6 eV, Hf-states dominant over Ti and O-states and shows the extent of hybridization. With the increase in the doping concentration of Ti in HfO_2 , the magnitude of DOS decreases as it is directly proportional to the number of atoms in the cell.

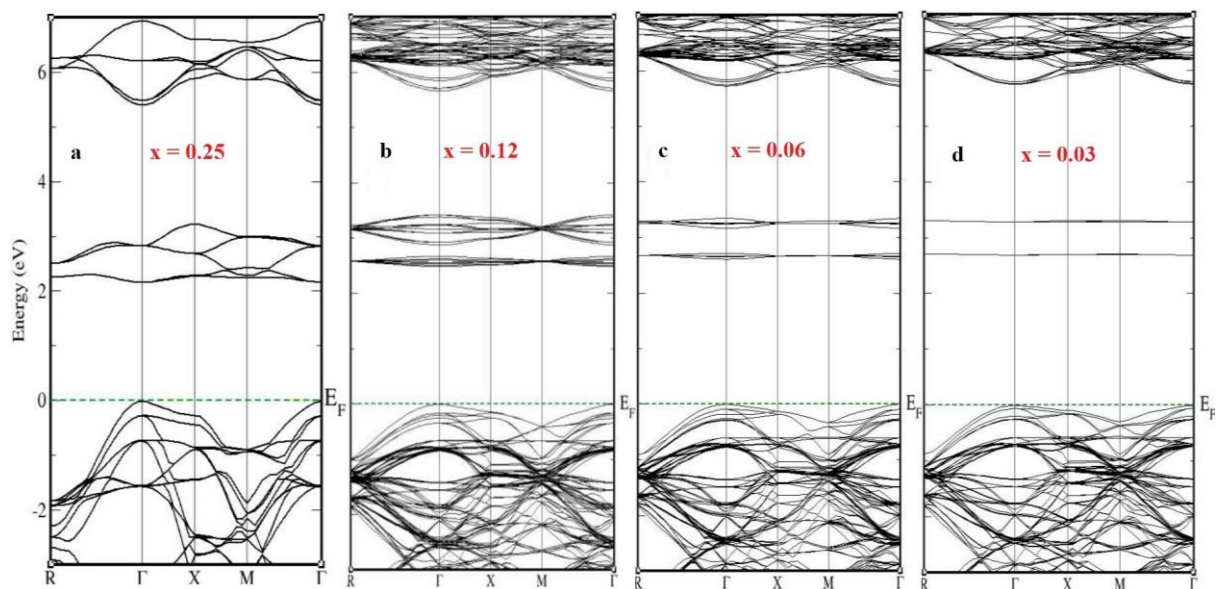


Figure 3.7: Band structure of $\text{Hf}_{1-x}\text{Ti}_x\text{O}_2$ (a) $x = 0.25$, (b) $x = 0.12$, (c) $x = 0.06$, (d) $x = 0.03$ (E_F is shifted to 0 eV).

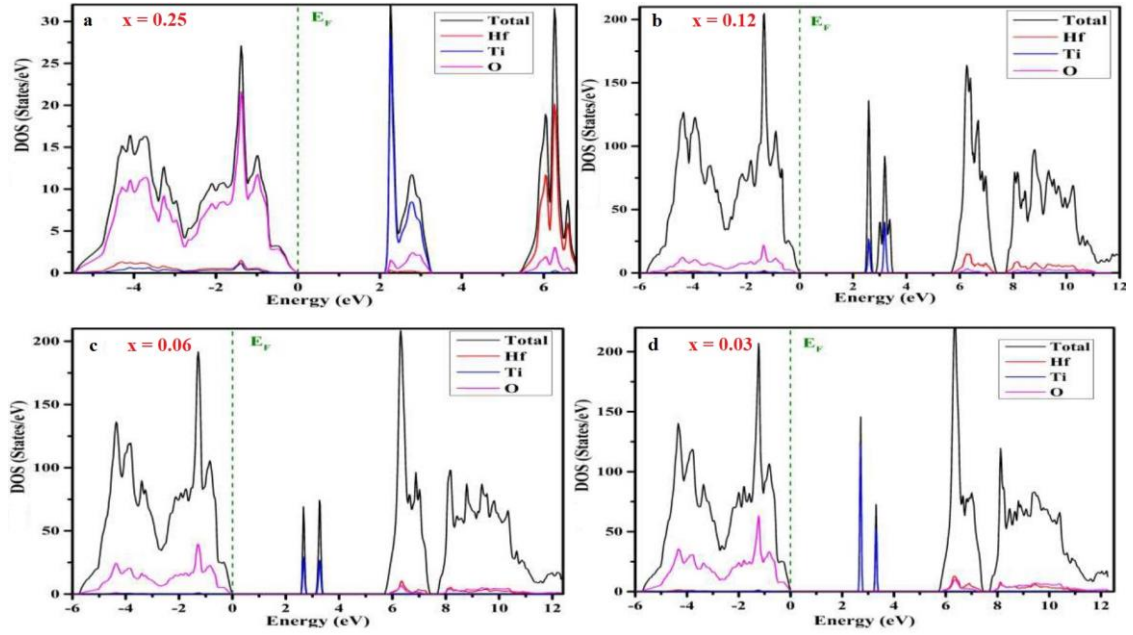


Figure 3.8. Density of states of $\text{Hf}_{1-x}\text{Ti}_x\text{O}_2$ (a) $x = 0.25$, (b) $x = 0.12$, (c) $x = 0.06$, (d) $x = 0.03$ (E_F is shifted to 0 eV).

3.3.4 Effect of S doping on the electronic properties

Next, we analyzed the electronic structure of S-doped $c\text{-HfO}_2$. At $x = 0.03$ and 0.06 doping, the obtained value of band gap along $\Gamma\text{-H-N-}\Gamma\text{-P}$ high symmetry points is 4.88 eV and 4.18 eV, respectively. Both doping concentrations show a direct band gap with flat band curvature along $\Gamma\text{-}\Gamma$ as represented in Fig. 3.9 (a, b). The reduction in band gap with doping can be ascribed to the fact that S ions have lower electronegativity than O ions, so the sulfurized oxides ($\text{HfO}_{2-x}\text{S}_x$) would tend to have lower energy which costs transferring an electron from the VB (S-3p or O-2p) to CB (Hf-5d) leading to the reduction in band gap. In Fig. 3.10 (a, b), the doping concentrations are examined to study the effect of various atomic species on the electronic structures. In VB, O-states dominate over the S-states and Hf-states, whereas S-states are induced in lower CB ($\sim 4\text{ eV}\text{-}6\text{ eV}$), and Hf-states dominate in higher energy regions. A good extent of hybridization is observed between Hf-, S-, and O-states.

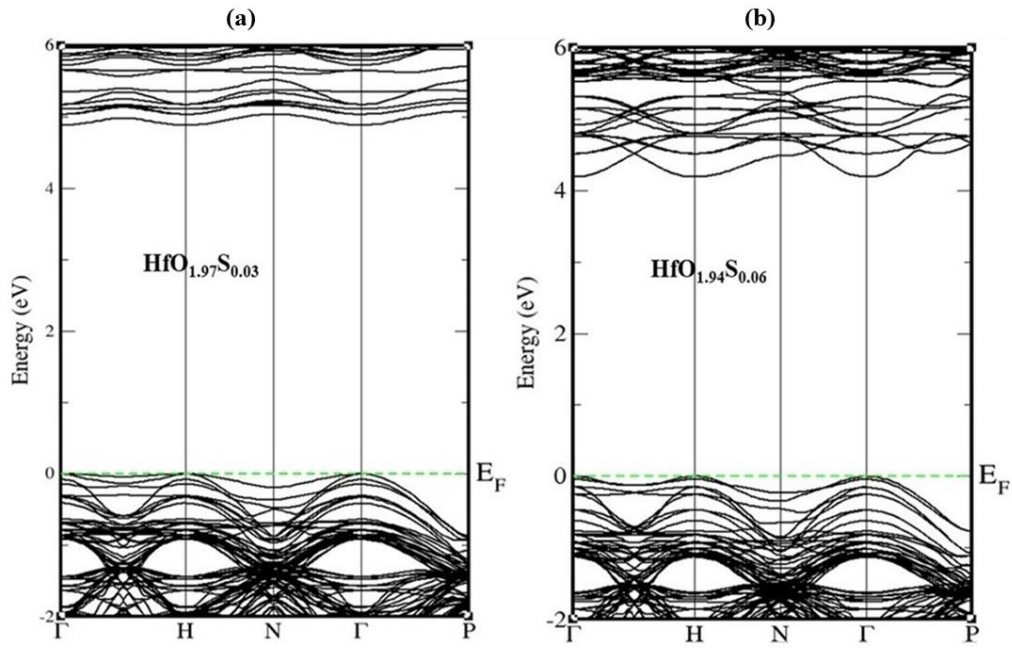


Figure 3.9: Band structures of $\text{HfO}_{2-x}\text{S}_x$ (a) $x = 0.03$, (b) $x = 0.06$ using TB-mBJ approach (E_F is shifted to 0 eV).

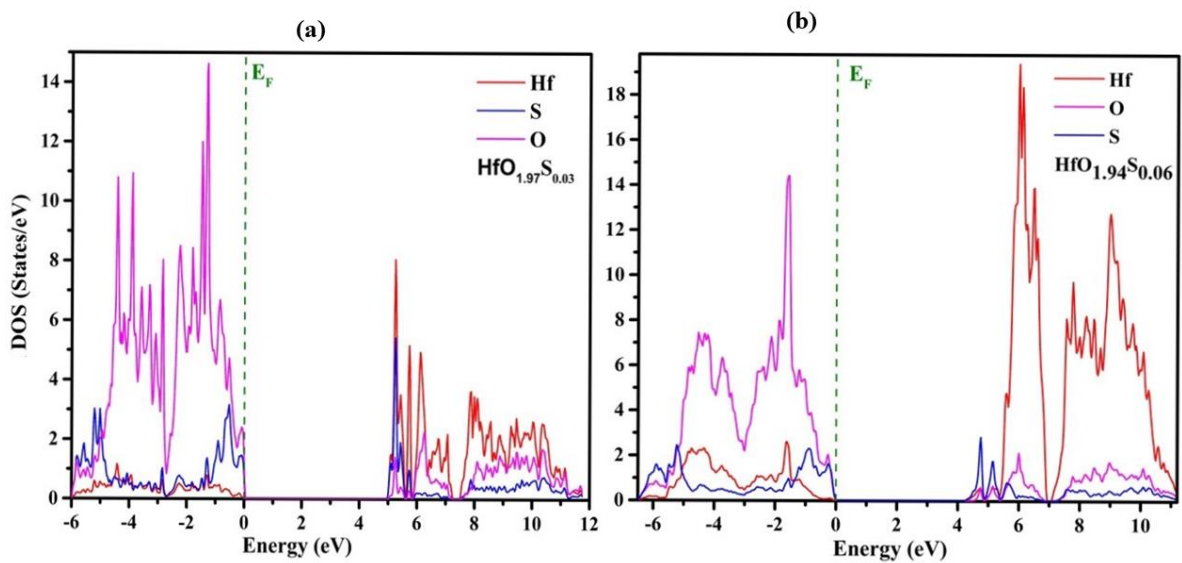


Figure 3.10: Density of states (DOS) of $\text{HfO}_{2-x}\text{S}_x$ (a) $x = 0.03$, (b) $x = 0.06$ (E_F is shifted to 0 eV).

3.3.5 Thermoelectric properties

For the accurate prediction of TE properties, the precise calculation of the band gap is required [37]. As our TB-mBJ calculation gives the highly accurate values of the band gap, we are highly optimistic to get a more realistic TE parameters to be compared with future experiments. The variation in the TE parameters such as S , σ/τ , κ_e/τ , PF , and ZT are analyzed with the varying carrier concentration at different temperatures under the constant relaxation time approximation of 10^{-14} s. We determined the value of τ using a methodology proposed by Kumar et al. [39] in which the experimental available value of electrical conductivity (σ) [29], and the theoretical calculated value of (σ/τ) is used in the relation, $\tau = \frac{\sigma_{exp.}}{\sigma/\tau}$. The obtained value of τ is of the order of $\sim 10^{-14}$ s at room temperature. We await more experimental results for electrical conductivity at higher temperature to find the τ at elevated temperatures.

The various TE parameters are obtained using the following expressions [25]:

$$S_{\alpha\beta}(\mu, T) = \frac{1}{eT\sigma_{\alpha\beta}(\mu, T)} \int \sigma_{\alpha\beta}(\varepsilon)(\varepsilon - \mu) \left(-\frac{\partial f(T, \varepsilon, \mu)}{\partial \varepsilon} \right) d\varepsilon \quad (3.2)$$

$$\kappa_{\alpha\beta}^e(\mu, T) = \frac{1}{e^2 T \Omega} \int \sigma_{\alpha\beta}(\varepsilon)(\varepsilon - \mu)^2 \left(-\frac{\partial f(T, \varepsilon, \mu)}{\partial \varepsilon} \right) d\varepsilon \quad (3.3)$$

$$\sigma_{\alpha\beta}(\mu, T) = \frac{1}{\Omega} \int \sigma_{\alpha\beta}(\varepsilon) \left(-\frac{\partial f(T, \varepsilon, \mu)}{\partial \varepsilon} \right) d\varepsilon \quad (3.4)$$

where Ω is the reciprocal space volume, f is the Fermi distribution function, e is the electron charge, and ε is the carrier energy. $\sigma_{\alpha\beta}(\varepsilon)$ is conductivity tensor can be expressed as:

$$\sigma_{\alpha\beta}(\varepsilon) = \frac{1}{N} \sum_{i,k} \sigma_{\alpha\beta}(i, k) \frac{\delta(\varepsilon - \varepsilon_{i,k})}{d\varepsilon} \quad (3.5)$$

where N is the number of k -points in the reciprocal space.

In light of the recent experiments indicating the possibility of high carrier concentration [8, 10, 13, 14] in various phases of HfO_2 , we analyzed the effect of carrier concentration on S_α in the range of $\sim 10^{18} - 10^{22} \text{ cm}^{-3}$ for different polymorphs of HfO_2 (Fig. 3.11). The variation of S_α is obtained for different temperatures with carrier concentrations. As expected, it decreases monotonically with increasing carrier concentrations for all studied phases. It is also important to know the effective mass (m^*) of all the phases to validate the obtained value of S_α , which is given as:

$$S_{\alpha} = \frac{8\pi^2 k_B^2}{3eh^2} m^* T \left(\frac{\pi}{3n} \right)^{2/3} \quad (3.6)$$

The m^* is evaluated by the fitting parabolic curve on the maxima of the VB and the minima of the CB, which are listed in Table 3.2. The variation in the values of m^* for different phases of HfO₂ is due to the orientation of their band curvature near the E_F, which leads to a significant contribution toward the value of S_{α} . As the m^* rises, the value of S_{α} increases. The maximum observed value of S_{α} for *c*-, *m*-, *o*-, and *t*- HfO₂ are found to be 830.81, 867.44, 922.62, and 945.27 $\mu\text{V/K}$, respectively, at 300 K for $1 \times 10^{18} \text{ cm}^{-3}$. We achieved a high value of S_{α} as compared to the previously reported doped (V, C) *c*-HfO₂ [15, 16] and other oxides Cu₂O and CuO [4].

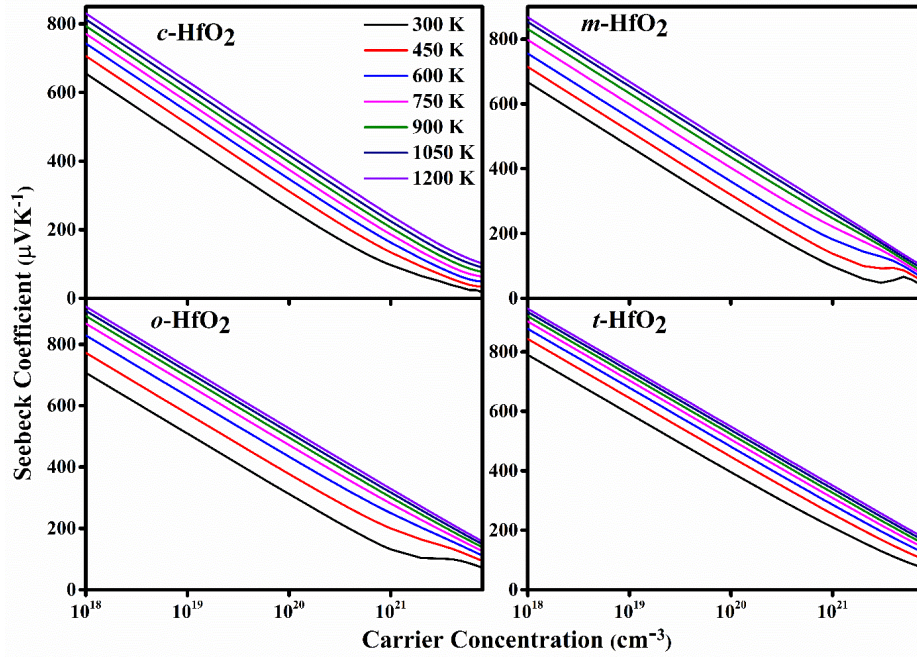


Fig. 3.11: The variation in Seebeck Coefficient with carrier concentrations at varying temperatures for all the polymorphs of HfO₂.

The behavior of electrical conductivity under the effect of carrier concentration at different temperatures is shown in Fig. 3.12. There is a slight variation in the value of σ/τ up to $1 \times 10^{20} \text{ cm}^{-3}$ after that; this increases monotonically. It is noted that the thermal excitation of carriers has a negligible effect on σ/τ . In the *c*-HfO₂, there is almost no effect of temperature; however, in all other phases, the values of σ/τ differ slightly at different temperatures. The highest observed value of σ/τ is 2.55×10^{20} , 0.66×10^{20} , 0.51×10^{20} , $0.97 \times 10^{20} \Omega^{-1} \text{m}^{-1} \text{s}^{-1}$ at room

temperature, whilst at 1200 K this slightly decreases to 2.34×10^{20} , 0.54×10^{20} , 0.40×10^{20} , $0.85 \times 10^{20} \text{ } \Omega^{-1} \text{m}^{-1} \text{s}^{-1}$ for *c*-, *m*-, *o*- and, *t*- HfO₂, respectively, at different carrier concentration.

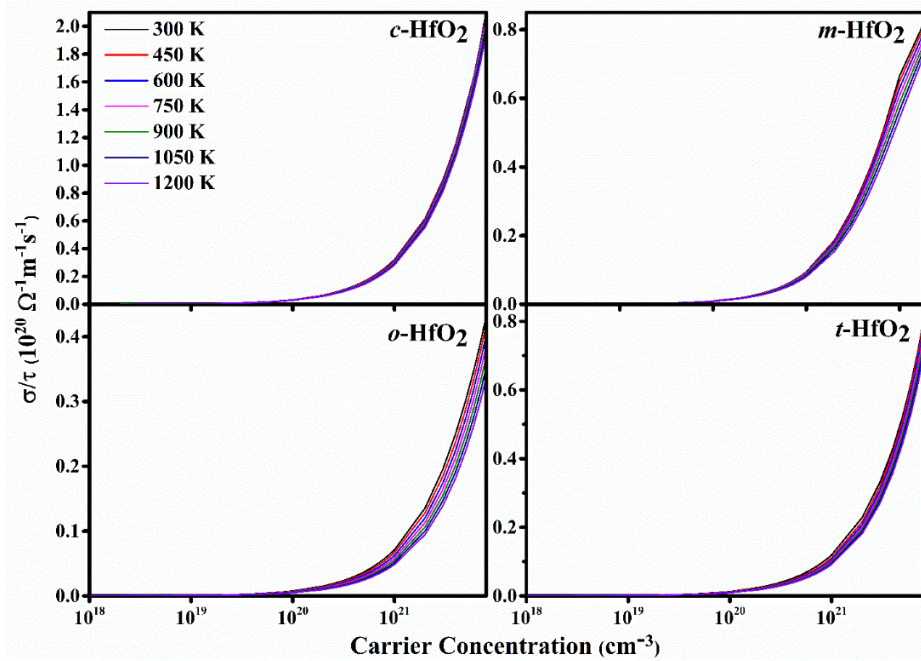


Fig. 3.12: The variation in electrical conductivity (σ/τ) with carrier concentrations at varying temperatures for all the polymorphs of HfO₂.

The variation in electronic thermal conductivity is directly proportional to the electrical conductivity, which validates the Wiedemann Franz law, i.e., $\kappa_e = L\sigma T$. Effect of carrier concentration at the different temperatures on κ_e/τ is shown in Fig. 3.13. At room temperature, the calculated value of κ_e/τ is 2.02×10^{15} , 0.48×10^{15} , 0.37×10^{15} , and $0.76 \times 10^{15} \text{ Wm}^{-1} \text{K}^{-1} \text{s}^{-1}$, whereas at the higher temperature, κ_e/τ increases to 8.33×10^{15} , 1.49×10^{15} , 1.40×10^{15} , and $3.95 \times 10^{15} \text{ Wm}^{-1} \text{K}^{-1} \text{s}^{-1}$ at 1200 K, for *c*-, *m*-, *o*- and, *t*-HfO₂, respectively at carrier concentration. The obtained values of σ/τ are significantly increased as compared to Cu₂O, NiO, and CuO [4].

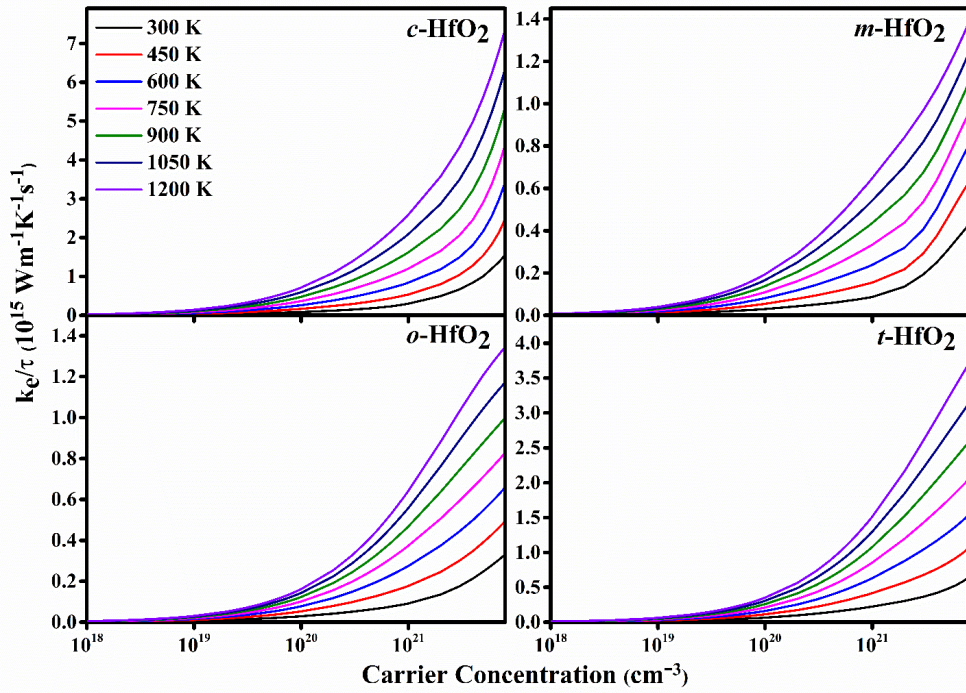


Fig. 3.13: The variation in electronic thermal conductivity with carrier concentrations at varying temperatures for all the polymorphs of HfO_2 .

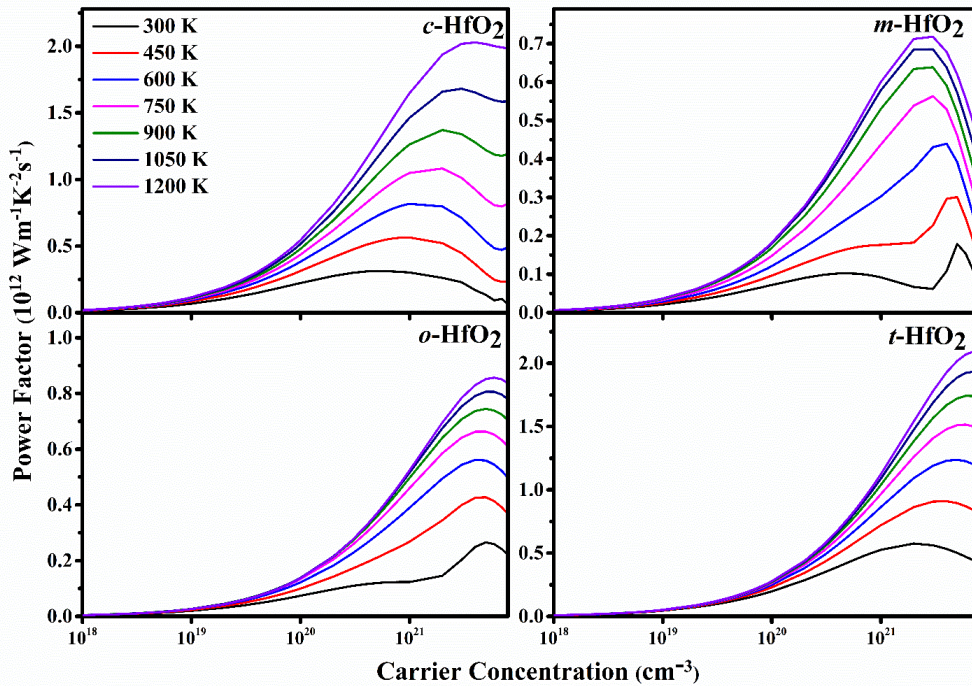


Fig. 3.14: The variation in power factor with carrier concentrations at varying temperatures for all the polymorphs of HfO_2 .

An increase in the value of PF is observed with the increasing carrier concentration, as shown in Fig. 3.14. The calculated value of PF is purely contributed by the S_α and σ . As we move

towards the higher temperature, the increment in PF is observed; the highest estimated value of PF is $2.020 \times 10^{12} \text{ Wm}^{-1}\text{K}^{-2}\text{s}^{-1}$ at $4 \times 10^{21} \text{ cm}^{-3}$, $0.71 \times 10^{12} \text{ Wm}^{-1}\text{K}^{-2}\text{s}^{-1}$ at $3 \times 10^{21} \text{ cm}^{-3}$, $0.85 \times 10^{12} \text{ Wm}^{-1}\text{K}^{-2}\text{s}^{-1}$ at $6 \times 10^{21} \text{ cm}^{-3}$, and $2.09 \times 10^{12} \text{ Wm}^{-1}\text{K}^{-2}\text{s}^{-1}$ at $8 \times 10^{21} \text{ cm}^{-3}$, for c -, m -, o - and t - HfO₂, respectively. Therefore, it can be seen that the optimized carrier concentration for the PF is of the order of 10^{21} cm^{-3} .

The lattice part of the thermal conductivity plays a major role in maximizing the TE performance as it can be tuned independently, unlike S_{α} , σ/τ , κ_e/τ , which are interdependent on each other. The κ_l decreases with the increase in temperature, as shown in Fig. 3.15. The room temperature κ_l for c -, m -, o -, and t -HfO₂ are obtained as 5.56, 2.87, 4.32, and 1.75 $\text{Wm}^{-1}\text{K}^{-1}$, respectively, and this decreases to 1.58, 0.92, 1.12, and 0.53 $\text{Wm}^{-1}\text{K}^{-1}$, respectively at 1200 K. The high value of κ_l of the c -HfO₂ phase as compared to others may be due to its isotopic nature and less overlapping between its acoustic and optical modes. A significant extent of overlapping in m -, o -, and t -HfO₂ is observed as visible in the phonon band structure diagram. The low value of κ_l indicates that HfO₂ polymorphs can be promising TE materials at elevated temperature.

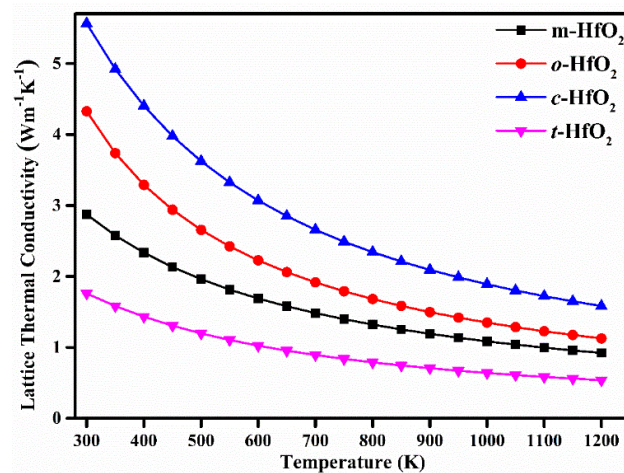


Fig. 3.15: The behavior of lattice thermal conductivity with varying temperatures for all the polymorphs of HfO₂.

Based upon the values of PF and k_{total} , the carrier concentration dependent ZT is determined for polymorphs at different fixed temperatures, as shown in Fig. 3.16. As the temperature rises, the ZT rises with it. It is observed that the ZT increases with an increase in carrier concentration up to 10^{21} cm^{-3} and after that decreases. The peak value of ZT is 0.77 at $3 \times 10^{20} \text{ cm}^{-3}$, 0.97 at $1 \times 10^{21} \text{ cm}^{-3}$, 0.83 at $2 \times 10^{21} \text{ cm}^{-3}$, 0.87 at $5 \times 10^{21} \text{ cm}^{-3}$ at the 1200 K for c -, m -, o - and t - HfO₂,

respectively. The highest value of ZT of the m -HfO₂ phase is mainly governed by its low κ_{total} among all polymorphs.

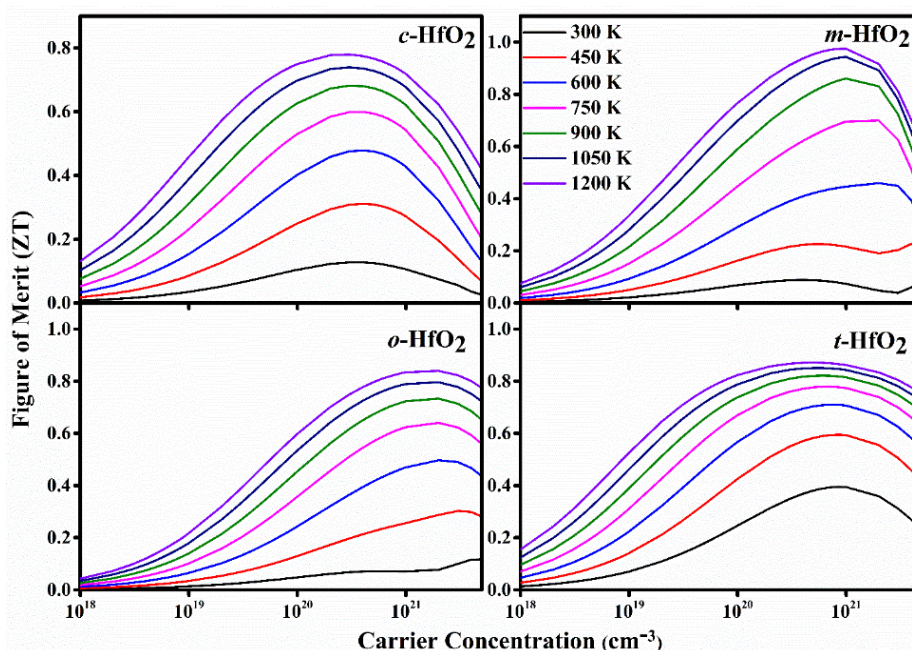


Fig. 3.16: The variation in the figure of merit with carrier concentrations at varying temperatures for all the polymorphs of HfO₂.

After obtaining the optimized carrier concentrations ($3 \times 10^{20} \text{ cm}^{-3}$, $1 \times 10^{21} \text{ cm}^{-3}$, $2 \times 10^{21} \text{ cm}^{-3}$, and $5 \times 10^{20} \text{ cm}^{-3}$ for c -, m -, o -, and t -HfO₂, respectively), we investigated the effect of temperature on ZT at these optimized carrier concentrations (Fig. 3.17). It is observed that ZT increases with increasing temperature. At room temperature, the calculated values of ZT are 0.12, 0.07, 0.07, 0.39 and a sharp increment is observed as we move towards high temperatures; at 1200 K, these values increase to 0.77, 0.97, 0.83, 0.87 for c -, m -, o - and, t -HfO₂, respectively. At 750 K, the reported value of ZT in m - and t -HfO₂ is nearly equal. It is to be noted that we got high figure of merit at the optimized carrier concentration in HfO₂ as compare to BiCuSeO ($ZT \sim 0.70$) [40], Ag-doped Ca₃Co₄O₉ ($ZT = 0.50$) [41], La-doped SrTiO₃ ($ZT = 0.27$) [42], Al-doped ZnO ($ZT = 0.44$) [43], Al and Ga co-doped ZnO ($ZT = 0.65$) [44]. The various studied polymorphs of HfO₂ were found suitable for high temperature TE energy harvesting applications. The carrier concentration mediated high ZT for HfO₂ is experimentally viable due to its high temperature stability [1200 °C – 2500 °C] and an attainable carrier concentration ($\sim 10^{21} \text{ cm}^{-3}$) with naturally occurring oxygen defects [8], [10], [13], [14].

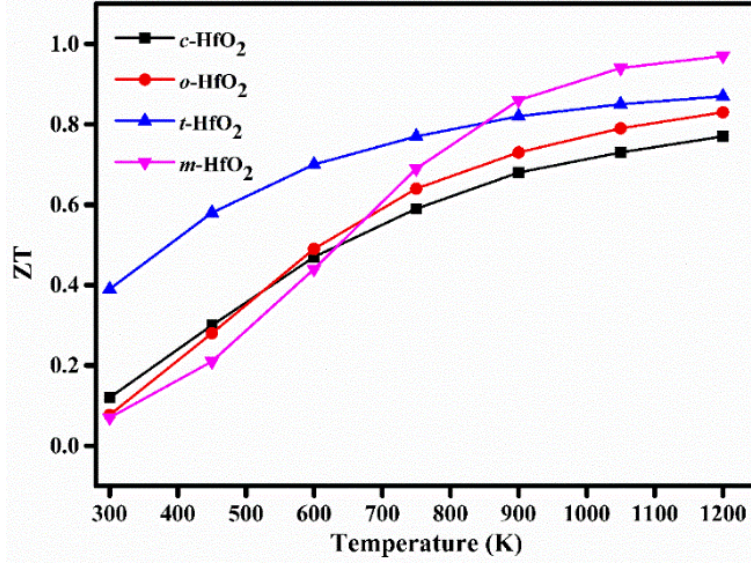


Fig. 3.17: The variation in figure of merit with temperature at the optimized carrier concentrations ($3 \times 10^{20} \text{ cm}^{-3}$, $1 \times 10^{21} \text{ cm}^{-3}$, $2 \times 10^{21} \text{ cm}^{-3}$, $5 \times 10^{20} \text{ cm}^{-3}$ for *c*-, *m*-, *o*- and *t*-phases, respectively).

3.3.6 Effect of doping on TE properties

For pure *c*-HfO₂, an increase in the value of S_{α} (Fig. 3.18) is observed with a rise in temperature from 300 K to 1200 K. The value of S_{α} at room temperature is found to be 214.48 $\mu\text{V/K}$ and 230.03 $\mu\text{V/K}$ at 1200 K, which is in good agreement with previous studies [15], [16].

With Ti-doping, an enhancement in S_{α} with temperature has been observed. For $x = 0.25$, we noticed almost 20% increase in its value both at room temperature and 1200 K relative to its value in pure *c*-HfO₂. For lower concentrations of Ti, the value of S_{α} further increased at room temperature whilst it decreased for higher temperatures. The maximum values of S_{α} at $x = 0.03$, 0.06, 0.12, and 0.25 are estimated as 320.31, 305.20, 299.77, and 306.13 $\mu\text{V/K}$ at 300 K, 450 K, 700 K, and 1050 K, respectively (Fig. 3.18 (a)). The calculated value of S_{α} for sulfur doping at 300 K is found to be 248.79, 292.10 $\mu\text{V/K}$, whereas, for 1200 K, the value is 223.32, 237.66 $\mu\text{V/K}$ for $x = 0.03$, 0.06 concentrations, respectively (Fig. 3.18 (b)). We obtained a higher value of S_{α} using Ti-doping as compared to S doping and V-doped HfO₂ [16]. Increase in the value of S_{α} with doping may be attributed to the reduction in the band gap and increment in the density of states above the fermi level. Further, as discussed earlier, with doping the flat bands appeared in lower CBs, which produced high S_{α} values and low mobility and hence resulted in low conductivity. To further verify this, we also calculated the effective mass (m^*) as listed in

Table 3.3. It is observed that in the entire temperature range, the positive value of S_α shows the p -type behavior for pure and doped structures.

Table 3.3: The variation of effective mass with $\text{Hf}_{1-x}\text{Ti}_x\text{O}_2$ and $\text{HfO}_{2-x}\text{S}_x$.

	$\text{Hf}_{1-x}\text{Ti}_x\text{O}_2$					$\text{HfO}_{2-x}\text{S}_x$	
	x = 0	x = 0.03	x = 0.06	x = 0.12	x = 0.25	x = 0.03	x = 0.06
m^* (at CBM)	0.73 m_e	14.96 m_e	3.47 m_e	3.26 m_e	2.84 m_e	3.03 m_e	1.11 m_e
m^* (at VBM)	0.28 m_e	0.54 m_e	0.55 m_e	0.55 m_e	0.51 m_e	2.01 m_e	1.70 m_e

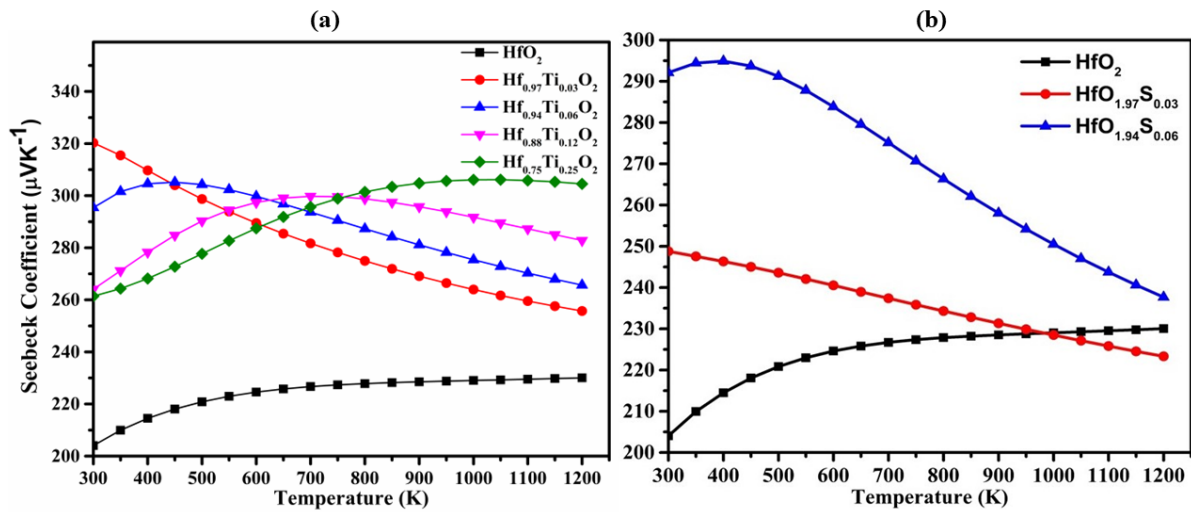


Figure 3.18: The variation of Seebeck coefficient of (a) $\text{Hf}_{1-x}\text{Ti}_x\text{O}_2$ ($x= 0, 0.03, 0.06, 0.12, 0.25$) and (b) $\text{HfO}_{2-x}\text{S}_x$ ($x= 0, 0.03, 0.06$).

The variation of electrical conductivity (σ/τ) with a temperature of pure c - HfO_2 is shown in Fig. 3.19. It showed an almost linearly increasing trend. The value of σ/τ at 300 K and 1200 K is found to be $0.058 \times 10^{20} \Omega^{-1}\text{m}^{-1}\text{s}^{-1}$ and $0.32 \times 10^{20} \Omega^{-1}\text{m}^{-1}\text{s}^{-1}$, respectively.

We observed a monotonous decrease in σ/τ with the increase in temperature for all doping concentrations. For $x = 0.03, 0.06, 0.12,$ and 0.25 the observed values of σ/τ at room temperature and at 1200 K have found to be $0.008 \times 10^{20}, 0.006 \times 10^{20}, 0.0054 \times 10^{20}, 0.004 \times 10^{20} \Omega^{-1}\text{m}^{-1}\text{s}^{-1}$ and $0.144 \times 10^{20}, 0.1132 \times 10^{20}, 0.09381 \times 10^{20}, 0.068 \times 10^{20} \Omega^{-1}\text{m}^{-1}\text{s}^{-1}$, respectively (Fig. 3.19 (a)). The decrease in mobility with enhancing Ti concentration, from $\text{Ti} = 0.03$ to 0.25 , may be accounted for such behavior. A similar behavior of σ/τ is observed with S doping. The

calculated value of σ/τ at 300 K is found to be 0.017×10^{20} , $0.006 \times 10^{20} \Omega^{-1}\text{m}^{-1}\text{s}^{-1}$, whilst for 1200 K the values are 0.129×10^{20} , $0.089 \times 10^{20} \Omega^{-1}\text{m}^{-1}\text{s}^{-1}$, for $x = 0.03, 0.06$ concentrations, respectively (Fig. 3.19 (b)).

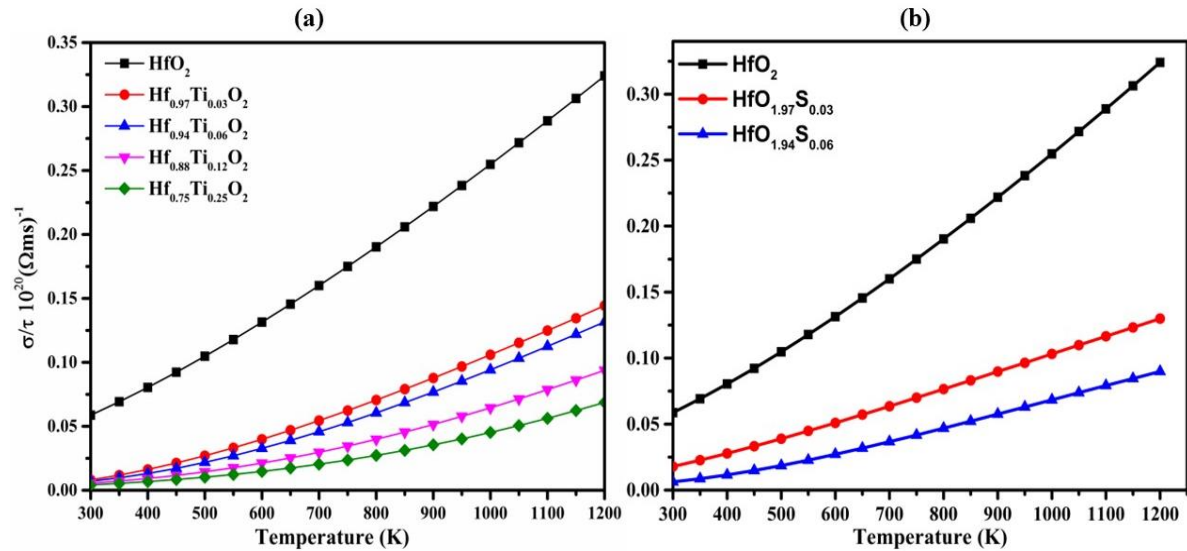


Figure 3.19: The variation of electrical conductivity of (a) $\text{Hf}_{1-x}\text{Ti}_x\text{O}_2$ ($x = 0, 0.03, 0.06, 0.12, 0.25$) and (b) $\text{HfO}_{2-x}\text{S}_x$ ($x = 0, 0.03, 0.06$).

The electronic thermal conductivity (κ_e) follows a similar trend as electrical conductivity (Fig. 3.20). The observed results of κ_e are in accordance with the Wiedemann-Franz law, which states that the thermal conductivity is proportional to electrical conductivity i.e., $\kappa = L\sigma T$ where L is Lorentz number. The calculated value of κ_e/τ for pure c - HfO_2 at 300 K is $0.10 \times 10^{15} \text{ Wm}^{-1}\text{K}^{-1}\text{s}^{-1}$ and $2.78 \times 10^{15} \text{ Wm}^{-1}\text{K}^{-1}\text{s}^{-1}$ at 1200 K.

At $x = 0.03, 0.06, 0.12$ and 0.25 doping concentrations, observed values of κ_e/τ at room temperature are 0.030×10^{15} , 0.023×10^{15} , 0.05×10^{15} and $0.011 \times 10^{15} \text{ Wm}^{-1}\text{K}^{-1}\text{s}^{-1}$, whereas at 1200 K, the values of κ_e/τ are 0.94×10^{15} , 0.80×10^{15} , 1.10×10^{15} and $0.63 \times 10^{15} \text{ Wm}^{-1}\text{K}^{-1}\text{s}^{-1}$, respectively (Fig. 3.20 (a)). With the S doping the calculated value of κ_e/τ at 300 K is found to be 0.043×10^{15} , $0.020 \times 10^{15} \text{ Wm}^{-1}\text{K}^{-1}\text{s}^{-1}$, and for 1200 K, 0.64×10^{15} , and $0.53 \times 10^{15} \text{ Wm}^{-1}\text{K}^{-1}\text{s}^{-1}$, for $x = 0.03, 0.06$ concentrations, respectively (Fig. 3.20 (b)). It is evident that doping of sulfur is more significant in obtaining lower κ_e/τ as compared to Ti-doping and C-doping [15].

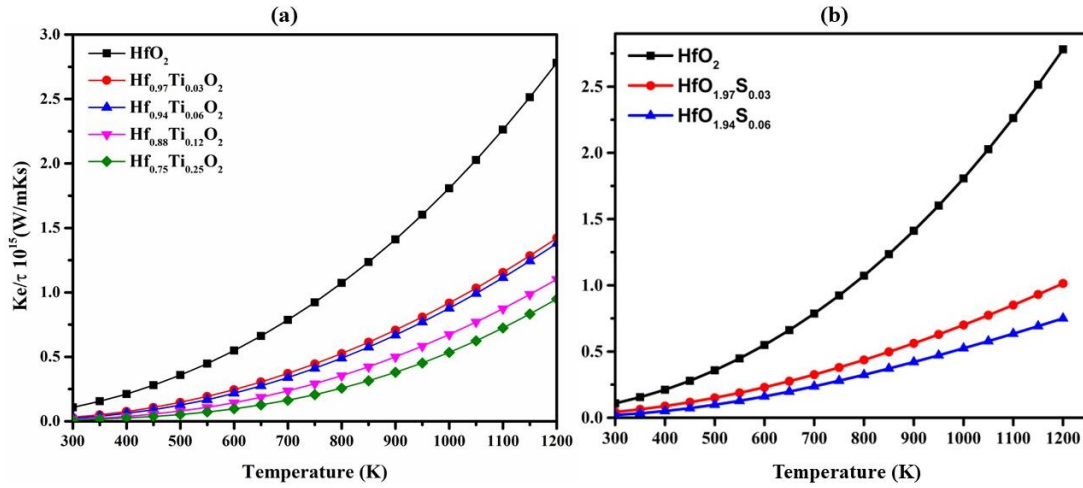


Figure 3.13: The variation of electronic thermal conductivity of (a) $Hf_{1-x}Ti_xO_2$ ($x = 0, 0.03, 0.06, 0.12, 0.25$) and (b) $HfO_{2-x}S_x$ ($x = 0, 0.03, 0.06$).

The calculated value of PF at 300 K is $0.24 \times 10^{12} \text{ Wm}^{-1}\text{K}^{-2}\text{s}^{-1}$ and increases to $1.71 \times 10^{12} \text{ Wm}^{-1}\text{K}^{-2}\text{s}^{-1}$ at 1200 K, which is in good agreement with the previous study of Cao et al. [15]. In the case Ti-doping at $x = 0.03, 0.06, 0.12,$ and 0.25 doping concentration structures the observed value of PF at room temperature are $0.08295 \times 10^{12}, 0.06919 \times 10^{12}, 0.037 \times 10^{12}$ and $0.0279 \times 10^{12} \text{ Wm}^{-1}\text{K}^{-2}\text{s}^{-1}$, respectively (Fig. 3.21 (a)). The observed value of PF at 1200K is $0.9443 \times 10^{12}, 0.8089 \times 10^{12}, 0.750 \times 10^{12},$ and $0.63667 \times 10^{12} \text{ Wm}^{-1}\text{K}^{-2}\text{s}^{-1}$. The observed value of PF in the case S-doping at $x = 0.03$ and 0.06 doped structures are 0.11×10^{12} and $0.053 \times 10^{12} \text{ Wm}^{-1}\text{K}^{-2}\text{s}^{-1}$, whilst at 1200 K values are 0.64×10^{12} and $0.53 \times 10^{12} \text{ Wm}^{-1}\text{K}^{-2}\text{s}^{-1}$, respectively (Fig. 3.21 (b)). The variation of PF clearly signifies that it depends on the S_α and σ/τ .

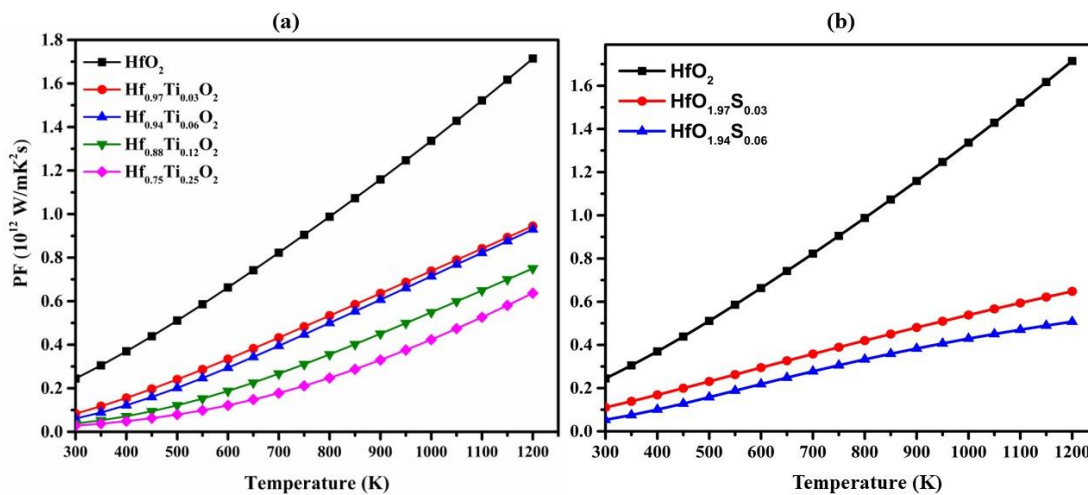


Figure 3.21: The variation of power factor of (a) $Hf_{1-x}Ti_xO_2$ ($x = 0, 0.03, 0.06, 0.12, 0.25$) and (b) $HfO_{2-x}S_x$ ($x = 0, 0.03, 0.06$).

Benefitting from increase in S_α and decrease in electronic thermal conductivity, the TE figure of merit of $\text{Hf}_{1-x}\text{Ti}_x\text{O}_2$ can be significantly improved with Ti concentration. In pure $c\text{-HfO}_2$, the observed value of ZT at 300 K is 0.67 and increased to 0.73 at 1200 K (Fig. 3.22). The maximum value of ZT amongst all doping concentrations is found ~ 0.82 for $x = 0.03$ at 400 K. The approximately same value of ZT is observed for $x = 0.06$, at 800 K and 1200 K, respectively (Fig. 3.22 (a)). In the case of S-doping the ZT values are 0.76 and 0.77 for $x = 0.03$ and 0.06, respectively at room temperature. At 1200 K, these values are 0.76, and 0.81, for $x = 0.03$ and 0.06, respectively (Fig. 3.22 (b)). The maximum value of ZT (0.82) is observed at 800 K for $x = 0.06$. This due to the lowest value of κ_e/τ at this concentration among all structures. We obtained a relatively higher value of ZT for doped structures (*this is the upper most limit of figure of merit*).

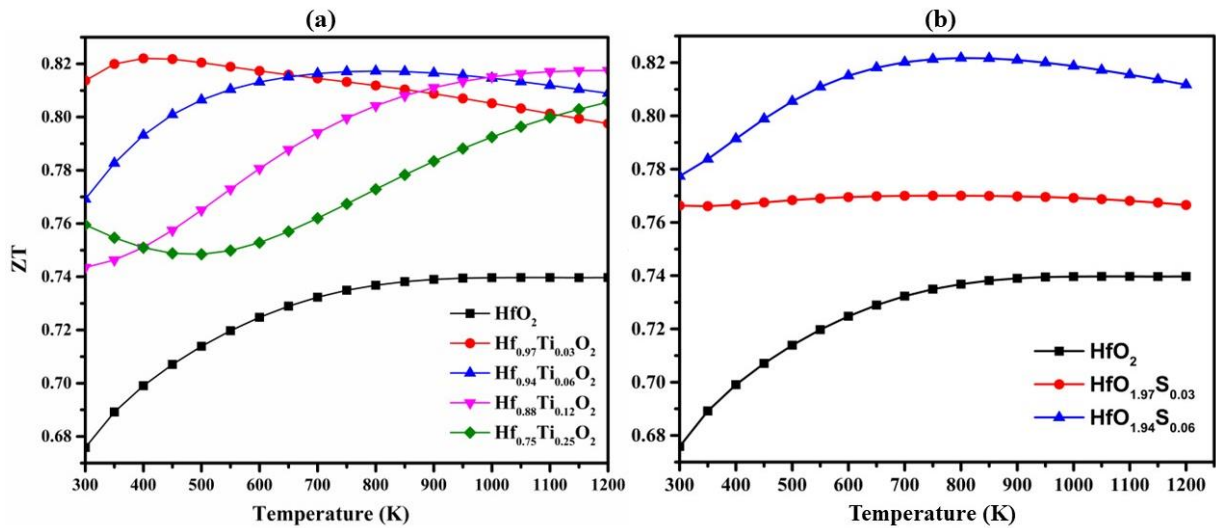


Figure 3.22: The variation of ZT of (a) $\text{Hf}_{1-x}\text{Ti}_x\text{O}_2$ ($x = 0, 0.03, 0.06, 0.12, 0.25$) and (b) $\text{HfO}_{2-x}\text{S}_x$ ($x = 0, 0.03, 0.06$).

The previous highest value reported is 0.79 at 75% doping of V-doped HfO_2 [16]. The similar Ti-doping has also been shown to enhance the figure of merit in various other materials such as $\text{ZrO}_{0.97}\text{Ti}_{0.03}$ (0.81) [45], $\text{Ti}_{0.07}\text{Cu}_{1.73}\text{S}$ (0.54) [46], and $\text{V}_{0.855}\text{Ti}_{0.1}\text{CoSb}$ (0.70) [47]. A similar enhancement has been observed in the figure of merit in $\text{Cu}_2\text{SnSe}_{3-x}\text{S}_x$ (0.66) [48], and BiOCuSe (0.30) [52] with S-doping. Our results may open a new avenue for $c\text{-HfO}_2$ as a versatile material for TE application in a wide temperature range.

3.4 Conclusion:

In this chapter, we discussed the structural, electronic, phonon dynamics, and transport properties of HfO₂ polymorphs i.e., cubic (*c*), monoclinic (*m*), tetragonal (*t*), and orthorhombic (*o*) and doped *c*-HfO₂ for their possible application in high temperature thermoelectric energy harvesting. This study is inspired by few recent experimental reports which have established the possibility of getting high carrier concentration in some of these polymorphs. The dynamical stability of all the polymorphs was assessed by phonon dispersion calculations. The thermodynamical stability of the Ti and S doping concentrations in *c*-HfO₂ was confirmed using formation energy and convex hull formalism. The electronic band structure and transport properties were calculated using the highly accurate TB-mBJ potentials. Our calculations have revealed that the *c*-, *o*-, and *t*- phases have a direct band gap, and the *m*-phase has an indirect band gap. The doping of Ti and S leads to a reduction in the band gap of *c*-HfO₂. These findings are in good agreement with the available experimental results. The high *m** of the tetragonal phase leads to its large *S*_α, among other phases. Among all the studied polymorphs, the *t*-HfO₂ shows the lowest value of lattice thermal conductivity 1.75 W/mK at 300 K which reduces to 0.53 W/mK at 1200 K. Owing to their large power factor and low lattice thermal conductivity, the high figure of merit, i.e., 0.97, 0.87, 0.83, and 0.77, has observed at 1200 K for the optimized carrier concentration $1 \times 10^{21} \text{ cm}^{-3}$, $2 \times 10^{21} \text{ cm}^{-3}$, $5 \times 10^{20} \text{ cm}^{-3}$, and $3 \times 10^{20} \text{ cm}^{-3}$ in the *m*-, *o*-, *t*-, and, *c*-polymorphs of HfO₂, respectively. In all the studied phases, the least observed value of *ZT* was in *c*-HfO₂. The doping of Ti and S at the Hf and O sites on *c*-HfO₂ was analyzed, respectively, to enhance its *ZT*. Doping leads to create new trap states in the band gap. It was observed that Ti doping has a lower band gap as compared to S doping. The magnitude of the Seebeck coefficient is high in Ti doping as compared to S doping. Further, the effective mass calculation was done to understand the behavior of the Seebeck coefficient. The maximum value of *ZT* (~ 0.82) was observed at 800 K for *x* = 0.06 doping concentration. The optimized carrier concentration is in close agreement with the available experimental reports. Our results have demonstrated that the TE parameters can be manipulated in a favourable way at selected carrier concentration and doping to get enhanced TE performance at a higher temperature.

References

- [1] Y. Sun, Y. Liu, R. Li, Y. Li, and S. Bai, "Strategies to Improve the Thermoelectric Figure of Merit in Thermoelectric Functional Materials," *Front. Chem.*, 10, 865281, 2022, doi: 10.3389/fchem.2022.865281.
- [2] Z. Chen, X. Zhang, and Y. Pei, "Manipulation of Phonon Transport in Thermoelectrics," *Adv. Mater.*, 30, 1705617, 2018, doi: 10.1002/adma.201705617.
- [3] Y. Yin, B. Tudu, and A. Tiwari, "Recent advances in oxide thermoelectric materials and modules," *Vacuum*, 146, 356–374, 2017, doi: 10.1016/j.vacuum.2017.04.015.
- [4] J. Linnera, G. Sansone, L. Maschio, and A. J. Karttunen, "Thermoelectric Properties of p-Type Cu₂O, CuO, and NiO from Hybrid Density Functional Theory," *J. Phys. Chem. C*, 122, 15180–15189, 2018, doi: 10.1021/acs.jpcc.8b04281.
- [5] L. Peng, N. Miao, G. Wang, J. Zhou, S. R. Elliott, and Z. Sun, "Novel metal oxides with promising high-temperature thermoelectric performance," *J. Mater. Chem. C*, 9, 12884–12894, 2021, doi: 10.1039/D1TC02404C.
- [6] R. Akram, J. Khan, S. Rafique, M. Hussain, A. Maqsood, and A. Ali Naz, "Enhanced thermoelectric properties of single phase Na doped Na_xCoO₂ thermoelectric material," *Mater. Lett.*, 300, 130180, 2021, doi: 10.1016/j.matlet.2021.130180.
- [7] A. V. Pashkevich *et al.*, "Structure, electric and thermoelectric properties of binary ZnO-based ceramics doped with Fe and Co," *J. Alloys Compd.*, 895, 162621, 2022, doi: 10.1016/j.jallcom.2021.162621.
- [8] E. Hildebrandt, J. Kurian, M. M. Müller, T. Schroeder, H.-J. Kleebe, and L. Alff, "Controlled oxygen vacancy induced *p*-type conductivity in HfO_{2-x} thin films," *Appl. Phys. Lett.*, 99, 112902, 2011, doi: 10.1063/1.3637603.
- [9] N. Kaiser *et al.*, "Defect-Stabilized Substoichiometric Polymorphs of Hafnium Oxide with Semiconducting Properties," *ACS Appl. Mater. Interfaces*, 14, 1290–1303, 2022, doi: 10.1021/acsami.1c09451.
- [10] N. Hadacek, A. Nosov, L. Ranno, P. Strobel, and R.-M. Galéra, "Magnetic properties of HfO₂ thin films," *J. Phys. Condens. Matter*, 19, 486206, 2007, doi: 10.1088/0953-8984/19/48/486206.
- [11] J. Wu, "Impact of oxygen vacancies on monoclinic hafnium oxide and band alignment with semiconductors," *Mater. Today Commun.*, 25, 101482, 2020, doi: 10.1016/j.mtcomm.2020.101482.

- [12] L. A. González, S. Gálvez-Barboza, E. Vento-Lujano, J. L. Rodríguez-Galicia, and L. A. García-Cerda, “Mn-modified HfO₂ nanoparticles with enhanced photocatalytic activity,” *Ceram. Int.*, 46, 13466–13473, 2020, doi: 10.1016/j.ceramint.2020.02.130.
- [13] T. V. Perevalov *et al.*, “The atomic and electronic structure of Hf_{0.5}Zr_{0.5}O₂ and Hf_{0.5}Zr_{0.5}O₂:La films,” *J. Sci. Adv. Mater. Devices*, 6, 595–600, 2021, doi: 10.1016/j.jsamd.2021.08.001.
- [14] D. R. Islamov and T. V. Perevalov, “Effect of oxygen vacancies on the ferroelectric Hf_{0.5}Zr_{0.5}O₂ stabilization: DFT simulation,” *Microelectron. Eng.*, 216, 111041, 2019, doi: 10.1016/j.mee.2019.111041.
- [15] Z. Cao, T. Fan, X. Hou, J. Niu, R. Sharma, and S. A. Dar, “Evaluation of structural, electronic, thermoelectric, and optical results of C-doped HfO₂ by first-principle’s investigation,” *Int. J. Energy Res.*, 44, 144–157, 2020, doi: 10.1002/er.4878.
- [16] R. Sharma, S. A. Dar, and V. Srivastava, “Half-metallic ferromagnetism and thermoelectric properties of vanadium doped Hf_{1-x}V_xO₂ (x = 0, 0.25, 0.50, 0.75) alloys by first principles perspective,” *Phys. Lett. A*, 411, 127559, 2021, doi: 10.1016/j.physleta.2021.127559.
- [17] B. Duan *et al.*, “Regulation of oxygen vacancy and reduction of lattice thermal conductivity in ZnO ceramic by high temperature and high pressure method,” *Ceram. Int.*, 46, 26176–26181, 2020, doi: 10.1016/j.ceramint.2020.07.115.
- [18] G.-K. Ren, J.-L. Lan, K. J. Ventura, X. Tan, Y.-H. Lin, and C.-W. Nan, “Contribution of point defects and nano-grains to thermal transport behaviours of oxide-based thermoelectrics,” *Npj Comput. Mater.*, 2, 16023, 2016, doi: 10.1038/npjcompumats.2016.23.
- [19] E. A. Scott, J. T. Gaskins, S. W. King, and P. E. Hopkins, “Thermal conductivity and thermal boundary resistance of atomic layer deposited high-*k* dielectric aluminum oxide, hafnium oxide, and titanium oxide thin films on silicon,” *APL Mater.*, 6, 058302, 2018, doi: 10.1063/1.5021044.
- [20] M. A. Panzer *et al.*, “Thermal Properties of Ultrathin Hafnium Oxide Gate Dielectric Films,” *IEEE Electron Device Lett.*, 30, 1269–1271, 2009, doi: 10.1109/LED.2009.2032937.
- [21] P. Blaha, “an Augment Plane Wave+ Local Orbitals Program for Calculating Crystal Properties, User’s Guide.” Vienna Austria.
- [22] J. P. Perdew, K. Burke, and M. Ernzerhof, “Generalized Gradient Approximation Made Simple [Phys. Rev. Lett. 77, 3865 (1996)],” *Phys. Rev. Lett.*, 78, 1396–1396, 1997, doi: 10.1103/PhysRevLett.78.1396.

- [23] P. Borlido, J. Schmidt, A. W. Huran, F. Tran, M. A. L. Marques, and S. Botti, “Exchange-correlation functionals for band gaps of solids: benchmark, reparametrization and machine learning,” *Npj Comput. Mater.*, 6, 96, 2020, doi: 10.1038/s41524-020-00360-0.
- [24] F. Tran and P. Blaha, “Accurate Band Gaps of Semiconductors and Insulators with a Semilocal Exchange-Correlation Potential,” *Phys. Rev. Lett.*, 102, 22, 226401, 2009, doi: 10.1103/PhysRevLett.102.226401.
- [25] G. K. H. Madsen and D. J. Singh, “BoltzTraP. A code for calculating band-structure dependent quantities,” *Comput. Phys. Commun.*, 175, 67–71, 2006, doi: 10.1016/j.cpc.2006.03.007.
- [26] A. Togo and I. Tanaka, “First principles phonon calculations in materials science,” *Scr. Mater.*, 108, 1–5, 2015, doi: 10.1016/j.scriptamat.2015.07.021.
- [27] A. Togo, L. Chaput, and I. Tanaka, “Distributions of phonon lifetimes in Brillouin zones,” *Phys. Rev. B*, 91, 094306, 2015, doi: 10.1103/PhysRevB.91.094306.
- [28] G. Kresse and D. Joubert, “From ultrasoft pseudopotentials to the projector augmented-wave method,” *Phys. Rev. B*, 59, 1758–1775, 1999, doi: 10.1103/PhysRevB.59.1758.
- [29] F. Birch, “Finite Elastic Strain of Cubic Crystals,” *Phys. Rev.*, 71, 809–824, 1947, doi: 10.1103/PhysRev.71.809.
- [30] S. Pathak, G. Mandal, P. Das, and A. B. Dey, “Structural characteristics of HfO₂ under extreme conditions,” *Mater. Chem. Phys.*, 255, 123633, 2020, doi: 10.1016/j.matchemphys.2020.123633.
- [31] N. Kumar, B. P. A. George, H. Abrahamse, V. Parashar, S. S. Ray, and J. C. Ngila, “A novel approach to low-temperature synthesis of cubic HfO₂ nanostructures and their cytotoxicity,” *Sci. Rep.*, 7, 9351, 2017, doi: 10.1038/s41598-017-07753-0.
- [32] T. Tobase *et al.*, “Pre-Transitional Behavior in Tetragonal to Cubic Phase Transition in HfO₂ Revealed by High Temperature Diffraction Experiments,” *Phys. Status Solidi B*, 255, 1800090, 2018, doi: 10.1002/pssb.201800090.
- [33] D. Banerjee, R. Sewak, C. C. Dey, D. Toprek, and P. K. Pujari, “Orthorhombic phases in bulk pure HfO₂: Experimental observation from perturbed angular correlation spectroscopy,” *Mater. Today Commun.*, 26, 101827, 2021, doi: 10.1016/j.mtcomm.2020.101827.
- [34] R. Wu *et al.*, “Elastic and vibrational properties of monoclinic HfO₂ from first-principles study,” *J. Phys. Appl. Phys.*, 45, 125304, 2012, doi: 10.1088/0022-3727/45/12/125304.

- [35] C. J. Bartel, “Review of computational approaches to predict the thermodynamic stability of inorganic solids,” *J. Mater. Sci.*, 57, 10475–10498, 2022, doi: 10.1007/s10853-022-06915-4.
- [36] R. Kumar, A. Vij, and M. Singh, “Defects assisted luminescence in *m*-HfO₂ nanocrystals: An experimental and theoretical study,” *Optik*, 248, 168121, 2021, doi: 10.1016/j.ijleo.2021.168121.
- [37] P. Ondračka, D. Holec, D. Nečas, and L. Zajíčková, “Accurate prediction of band gaps and optical properties of HfO₂,” *J. Phys. Appl. Phys.*, 49, 395301, 2016, doi: 10.1088/0022-3727/49/39/395301.
- [38] J. E. Jaffe, R. A. Bachorz, and M. Gutowski, “Low-temperature polymorphs of ZrO₂ and HfO₂: A density-functional theory study,” *Phys. Rev. B*, 72, 144107, 2005, doi: 10.1103/PhysRevB.72.144107.
- [39] V. Kumar Gudelli, V. Kanchana, G. Vaitheeswaran, A. Svane, and N. E. Christensen, “Thermoelectric properties of chalcopyrite type CuGaTe₂ and chalcostibite CuSbS₂,” *J. Appl. Phys.*, 114, 223707, 2013, doi: 10.1063/1.4842095.
- [40] F. Li *et al.*, “Polycrystalline BiCuSeO oxide as a potential thermoelectric material,” *Energy Environ. Sci.*, 5, 7188, 2012, doi: 10.1039/c2ee21274a.
- [41] Y. Wang, Y. Sui, J. Cheng, X. Wang, and W. Su, “Comparison of the high temperature thermoelectric properties for Ag-doped and Ag-added Ca₃Co₄O₉,” *J. Alloys Compd.*, 477, 817–821, 2009, doi: 10.1016/j.jallcom.2008.10.162.
- [42] S. Ohta, T. Nomura, H. Ohta, and K. Koumoto, “High-temperature carrier transport and thermoelectric properties of heavily La- or Nb-doped SrTiO₃ single crystals,” *J. Appl. Phys.*, 97, 034106, 2005, doi: 10.1063/1.1847723.
- [43] P. Jood *et al.*, “Al-Doped Zinc Oxide Nanocomposites with Enhanced Thermoelectric Properties,” *Nano Lett.*, 11, 4337–4342, 2011, doi: 10.1021/nl202439h.
- [44] M. Ohtaki, K. Araki, and K. Yamamoto, “High Thermoelectric Performance of Dually Doped ZnO Ceramics,” *J. Electron. Mater.*, 38, 1234–1238, 2009, doi: 10.1007/s11664-009-0816-1.
- [45] N. Jain, R. Kumar, R. Kumar, and M. Singh, “Enhancement of thermoelectric performance of ZrO₂ via Titanium doping,” *Mater. Today Proc.*, 51, 699–702, 2022, doi: 10.1016/j.matpr.2021.06.211.
- [46] D.-D. Liang, B.-P. Zhang, and L. Zou, “Enhanced thermoelectric properties of Cu_{1.8}S by Ti-doping induced secondary phase,” *J. Alloys Compd.*, 731, 577–583, 2018, doi: 10.1016/j.jallcom.2017.09.305.

- [47] S. Li *et al.*, “Titanium Doping to Enhance Thermoelectric Performance of 19-Electron VCoSb Half-Heusler Compounds with Vanadium Vacancies,” *Ann. Phys.*, 532, 1900440, 2020, doi: 10.1002/andp.201900440.
- [48] R. Ma *et al.*, “Thermoelectric properties of S and Te-doped Cu₂SnSe₃ prepared by combustion synthesis,” *J. Asian Ceram. Soc.*, 6, 13–19, 2018, doi: 10.1080/21870764.2018.1439609.

Pressure induced structural phase transition in monoclinic-HfO₂

4.1 Introduction

HfO₂, generally, possesses diverse properties, e.g., optical, thermoelectric, ferroelectric, piezoelectric, etc. which are highly phase dependent [1–4]. Various strategies such as external pressure, temperature, doping, and electric field have been explored for phase transition in HfO₂ [5–8]. The aliovalent dopants (Pr and Cr) have been reported to convert monoclinic (*m*)-HfO₂ from an indirect to a direct band gap material cubic (*c*)-HfO₂, in addition to lowering its band gap, which improves its optical behavior [9, 10]. The isovalent doping of Si in HfO₂, under thermal treatment up to 1100 °C, has resulted in the orthorhombic (*o*)-HfO₂ (*Pca2₁*) phase in the thin film as well as bulk samples [11, 12]. High pressure (~33.5 GPa) can also lead to *m*- to *o*-HfO₂ [6] but this transition pressure can be lowered significantly (~7 GPa) with Si doping [12]. The high dielectric constant and wide band gap of HfO₂ over SiO₂ make it a full complementary metal oxide semiconductor, which Intel launched in 2007 for its production process [13]. It is evident from the literature that the effect of Si dopant interactions and strain results in an asymmetric distortion in the O sublattice of Si–HfO₂ crystal structure that leads to a ferroelectric ordered state because of further crystal splitting [14]. Si doped HfO₂ provides remarkable stability in the subloop switching behavior and access to intermediate polarisation states [15]. This also lowers the coercive field and improves the polarization retention which improves its ferroelectric behaviour [15, 16]. It has also been observed that *o*-HfO₂ (*Pca2₁*) acts as a good ferroelectric material [17], and in another study, these ferroelectric materials were reported to have a strong optical response over *m*-HfO₂ [18]. Therefore, it can be anticipated that Si doping might lead to phase transformation, enhancing its applicability area.

The aim of this study is to understand the pressure-induced *m*- to *o*-phase transition in HfO₂ with Si doping vis-à-vis the available experimental observations [12]. So, in pursuit of this motive, in the present study, we examined the effect of pressure on phase transitions from monoclinic to orthorhombic in Si-doped and pure HfO₂. Thermal stability analysis was carried out using ab initio molecular dynamics (AIMD). We studied the structural, and electronic

properties of o -Hf_{1-x}Si_xO₂ ($x = 0, 0.03, 0.06, 0.09$) under various applied pressure using a *first-principles* approach.

4.2 Computational Details

The structural optimization of Hf_{1-x}Si_xO₂ ($x = 0, 0.03, 0.06, 0.09$) in m - and o - phases with and without pressure were obtained using the *first-principles* method as implemented in VASP [19]. The relaxation was carried out within the parametrization of GGA of PBE [20]. The convergence criteria for self-consistent field energy were set to 10^{-7} eV and the force relaxation was carried out till 0.01 eV/Å. The plane wave cutoff energy of 500 eV and a gamma centered k-mesh of $7 \times 7 \times 5$ was used for the calculations. To check the thermal stability, the AIMD simulations were carried out in a canonical ensemble at temperatures 1673 K (it is the temperature at which o -HfSiO₂ has been obtained [12]) using a time step of 1 fs, which lasted for 5000 fs. The phonon dispersions were obtained using the Phonopy code [21].

The electronic properties were calculated using the WIEN2k package which is based on the FPLAPW method [22]. The TB-mBJ was used as exchange and correlation potential for accurate determination of the band gap of HfO₂ [23]. To achieve more realistic results a good energy convergence of 0.0001 Ry/cell, and the non overlapping muffin tin radii with $R_{\text{MT}k_{\text{max}}} = 7$ were employed. The k-mesh of $15 \times 15 \times 14$ and $12 \times 12 \times 12$ was used, resulting in 518 and 412 k-points in the irreducible Brillouin Zone (IBZ) of m - and o -HfO₂, respectively. A $2 \times 2 \times 2$ supercell with 96 atoms was constructed to obtain the various Si doping concentrations i.e., 0.03, 0.06, 0.09.

4.3 Results and Discussion

4.3.1 Structural Properties

Generally, the threshold transition pressure for m - to o -transitions in centrosymmetric phases ($Pbca$ and $Pnma$) of HfO₂ lies in the range of 2.7 – 27.0 GPa whereas the pure orthorhombic phase has been obtained at ~33.5 GPa [6]. It has also been reported that the Si doping in m -HfO₂ can lead to a non-centrosymmetric o -phase ($Pca2_1$) at a relatively lower pressure [12]. To understand the reason behind this, we have performed systematic DFT calculations. From now on, we will refer non-centrosymmetric o -HfO₂ ($Pca2_1$) as o -HfO₂ in all further discussions. The optimized lattice constants for o -Hf_{1-x}Si_xO₂ ($x = 0, 0.03, 0.06, 0.09$) under the effect of applied pressure are listed in Table 4.1.

Table 4.1: Lattice constant (in units of Å) of $o\text{-Hf}_{1-x}\text{Si}_x\text{O}_2$ ($x = 0, 0.03, 0.06, \text{ and } 0.09$) under pressure (in units of GPa).

	x = 0				x = 0.03		x = 0.06		x = 0.09	
Pressure	0	8	14	15	0	14	0	8	0	8
<i>a</i>	5.26	5.20	5.17	5.16	5.28	5.16	5.38	5.20	5.40	5.20
<i>b</i>	5.04	4.99	4.95	4.95	5.13	4.94	5.06	4.99	5.03	4.97
<i>c</i>	5.07	5.01	4.96	4.95	5.17	4.95	5.08	4.97	5.09	4.97

The enthalpy vs pressure variation (Fig. 4.1) depicts that on increasing pressure the enthalpy also increases and a crossover is observed at 15 GPa, 14 GPa, 8 GPa, and 8 GPa for $x=0, 0.03, 0.06, \text{ and } 0.09$, respectively, which is called as transition pressure (P_T) and these pressure values agree well with available experimental data [12]. Fig. 4.2 shows the pressure versus volume curve for m - to $o\text{-HfO}_2$ transition at 15 GPa. The increase in pressure leads to a change in the volume of the unit cell, which is again in good agreement with experimental results [12]. This change in the volume from $m \rightarrow o\text{-HfO}_2$ at 15 GPa indicates a first order phase transition. A relatively lower volume in $o\text{-HfO}_2$, as compared to $m\text{-HfO}_2$, is due to the reorientation of oxygen atoms in the cell.

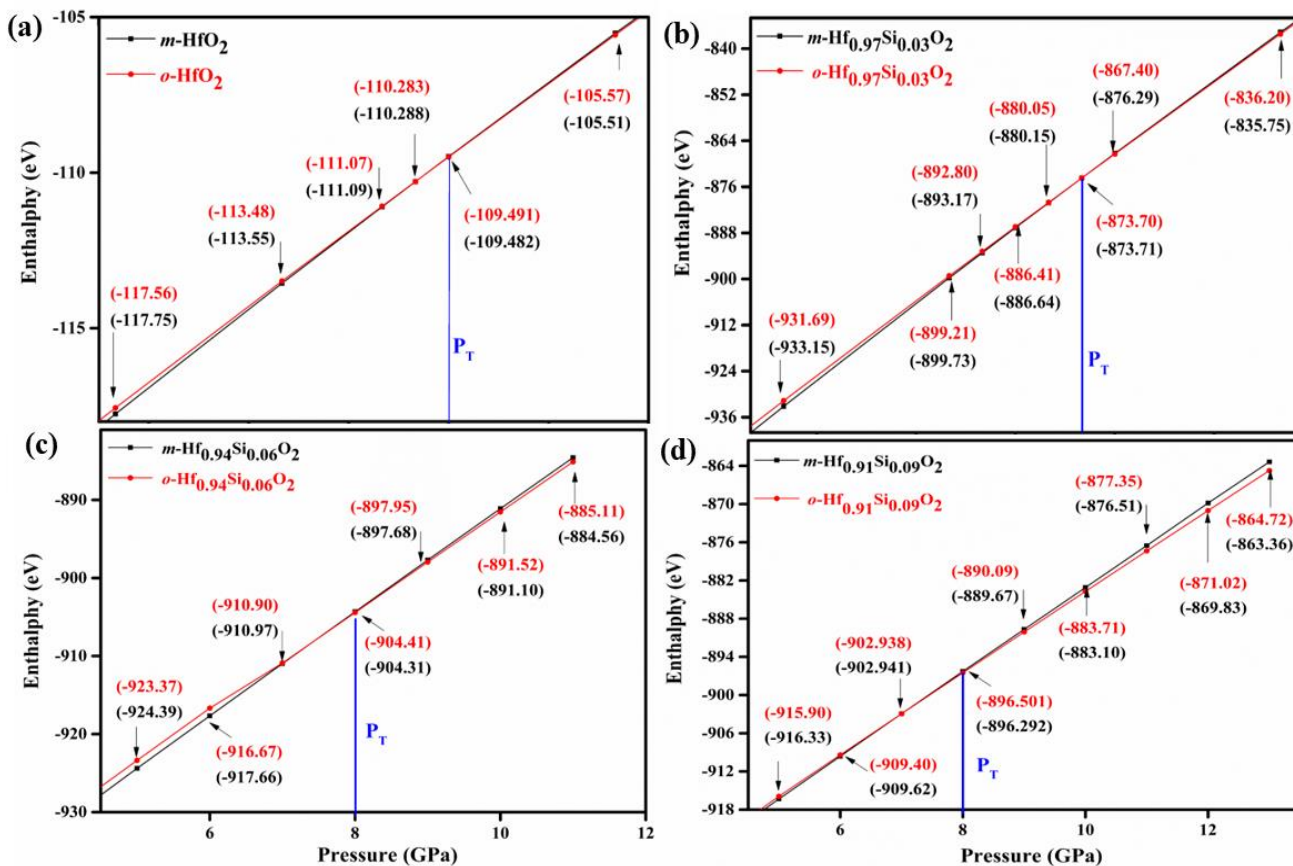


Fig. 4.1: The structural phase transition of m - and o - $\text{Hf}_{1-x}\text{Si}_x\text{O}_2$ for (a) $x = 0$, (b) $x = 0.03$, (c) $x = 0.06$, and (d) $x = 0.09$ (values written in black and red colours represent the enthalpy of monoclinic and orthorhombic phases, respectively).

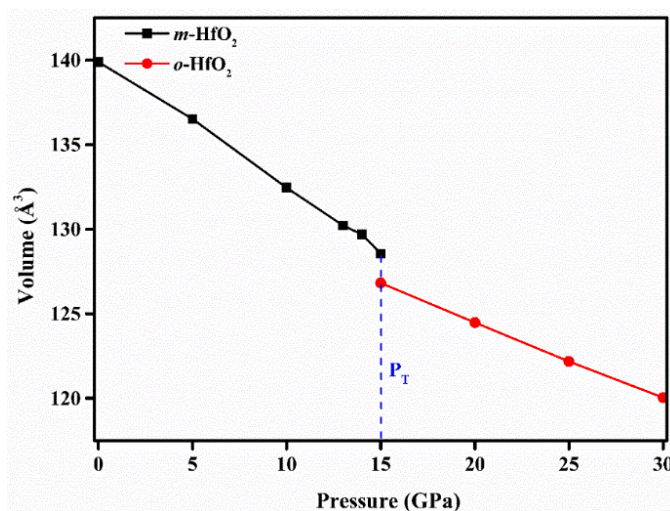


Fig. 4.2: Change in volume as a function of pressure in m - to o - HfO_2 .

The P_T decreases with an increase in doping concentration as the bond length of Hf-O increases, whereas the Si-O bond length decreases (Fig. 4.3 (a)). The reduction in P_T can also be attributed to charge transfer between Si and α -HfO₂. It is evident, from Fig. 4.3 (b), that the magnitude of DOS of isolated Si atom decreases when it is doped in α -HfO₂.

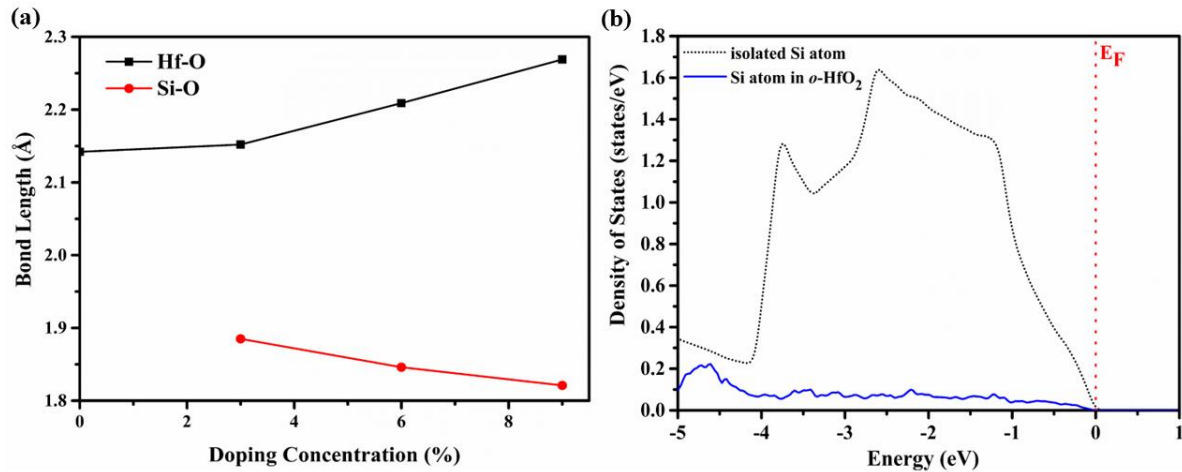


Fig. 4.3: (a) Variation in bond length of α -Hf_{1-x}Si_xO₂ ($x = 0, 0.03, 0.06,$ and 0.09) at 0 GPa (b) Density of states of isolated and Si-doped HfO₂ at 0 GPa.

To gain further insights into the charge transfer from Si to α -HfO₂, we have carried out the Bader charge analysis. The Bader charge of the isolated Si atom is +3.92035. In pure SiO₂, it reduces to +3.20978 and O has a charge of magnitude -1.62048. As shown in Table 4.2, the charge on the Si dopant in α -HfSiO₂ reduces in comparison to isolated Si atom as well as Si in SiO₂, which indicates the charge transfer from Si to α -HfO₂. This charge transfer can also be visualized in the isosurface plot of pure and doped HfO₂ as shown in Fig. 4.4 (a)–(d). The Bader charge transfer is consistent with the DOS of isolated Si and Si-doped HfO₂ (Fig. 4.3 (b)). This shows that the Si atom fully oxidized with the localization of charges on the Hf atom. As shown in Fig. 4.3 (a), the bond length of Hf-O increases, whereas the Si-O bond length decreases with doping. This indicates that α -HfSiO₂ is relatively more stable than α -HfO₂. Moreover, the decrease in Si-O bond length with doping enhances the charge transfer between Si and α -HfO₂, which further leads to the lowering of transition barrier of Si in α -HfO₂. This decrease in transition barrier may also account for the reduction in P_T [24, 25].

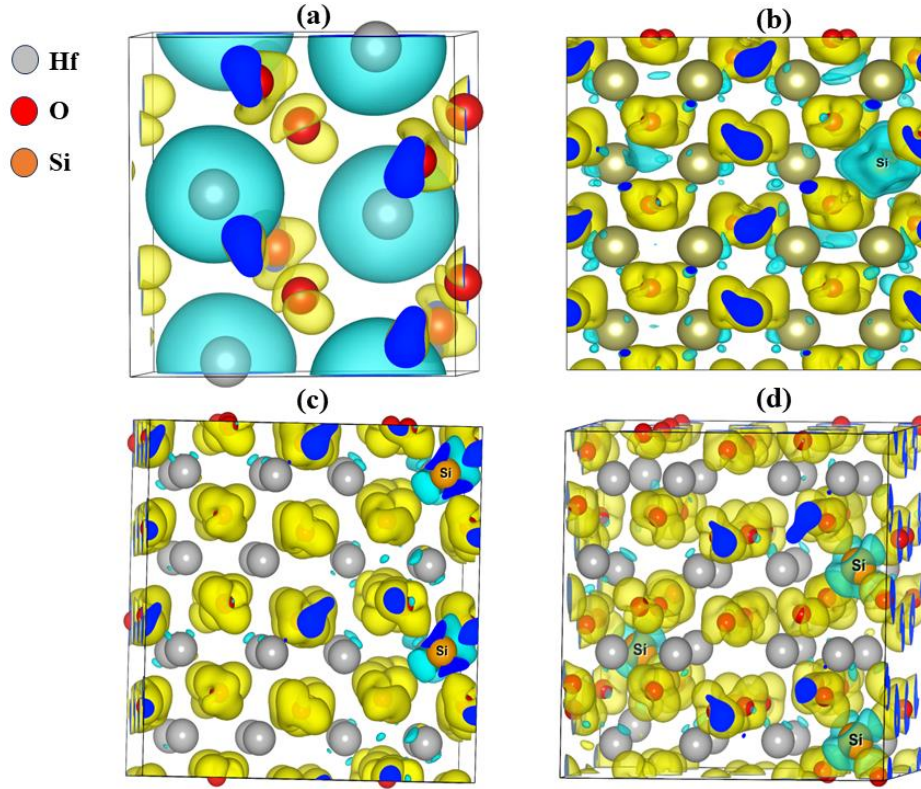


Fig. 4.4: Isosurface plot of partial charge density (a) *o*-HfO₂ (b) Hf_{0.97}Si_{0.03}O₂ (c) Hf_{0.94}Si_{0.06}O₂ (d) Hf_{0.91}Si_{0.09}O₂. (In the units of e/Å³ with isosurface level 0.015).

Table 4.2: The Bader charges of *o*-Hf_{1-x}Si_xO₂ (x = 0, 0.03, 0.06 and 0.09).

	Hf	O	Si
HfO₂	+2.36758	-1.19100	-
Hf_{0.97}Si_{0.03}O₂	+2.57081	-1.29239	+2.61049
Hf_{0.94}Si_{0.06}O₂	+2.56793	-1.28940	+2.62349
Hf_{0.91}Si_{0.09}O₂	+2.54281	-1.26813	+2.64150

4.3.2 Stability analysis

Prior to proceed for band structure calculations, we examined the thermal stability of the orthorhombic phases for all Si concentrations. The formation energy for *o*-Hf_{1-x}Si_xO₂ (x = 0, 0.03, 0.06, and 0.09) was estimated using the undermentioned relation:

$$E_{formation} = \frac{\{E_{Total} - n(E_{Hf_{atom}} + E_{O_{atom}} + E_{Si_{atom}})\}}{N} \quad (4.1)$$

where E_{Total} is the total energy of pristine or doped supercell, N is the total number of atoms in the cell, E_{Hf} , E_{Si} , and E_O is the energy of corresponding individual Hafnium, Silicon, and Oxygen atom, n is the number of atoms of a particular species in the cell. The obtained value of formation energies under the effect of applied pressure for o -Hf $_{1-x}$ Si $_x$ O $_2$ ($x = 0, 0.03, 0.06,$ and 0.09) are -3.7586 eV/atom, -5.7857 eV/atom, -5.7509 eV/atom, and -5.7267 eV/atom, respectively. Whilst for m -Hf $_{1-x}$ Si $_x$ O $_2$ ($x = 0, 0.03, 0.06,$ and 0.09) the value of formation energies is -3.7579 eV/atom, -5.7796 eV/atom, -5.7435 eV/atom, and -5.7183 eV/atom, respectively. The slightly more negative formation energies for all studied doping concentrations confirm the thermodynamic stability of o -Hf $_{1-x}$ Si $_x$ O $_2$ over m -Hf $_{1-x}$ Si $_x$ O $_2$. The dynamical stability has also been assessed for the pristine o -HfO $_2$ and m -HfO $_2$ at 15 GPa, as shown in Fig. 4.5. The absence of negative frequencies in phonon dispersion curves verifies that the systems are dynamically stable.

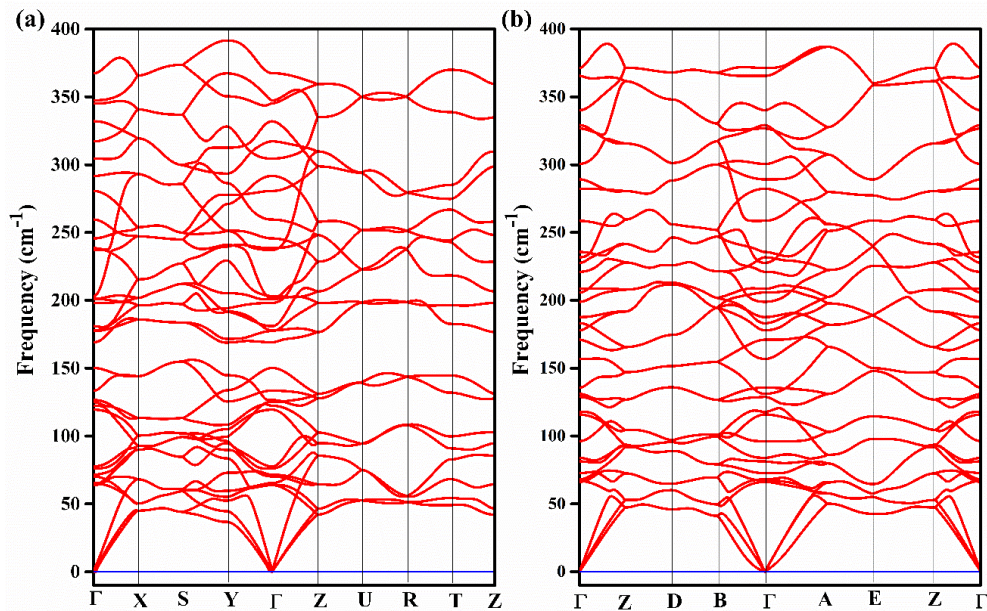


Fig. 4.5: The phonon dispersion curve of (a) m -HfO $_2$ (b) o -HfO $_2$ at 15 GPa.

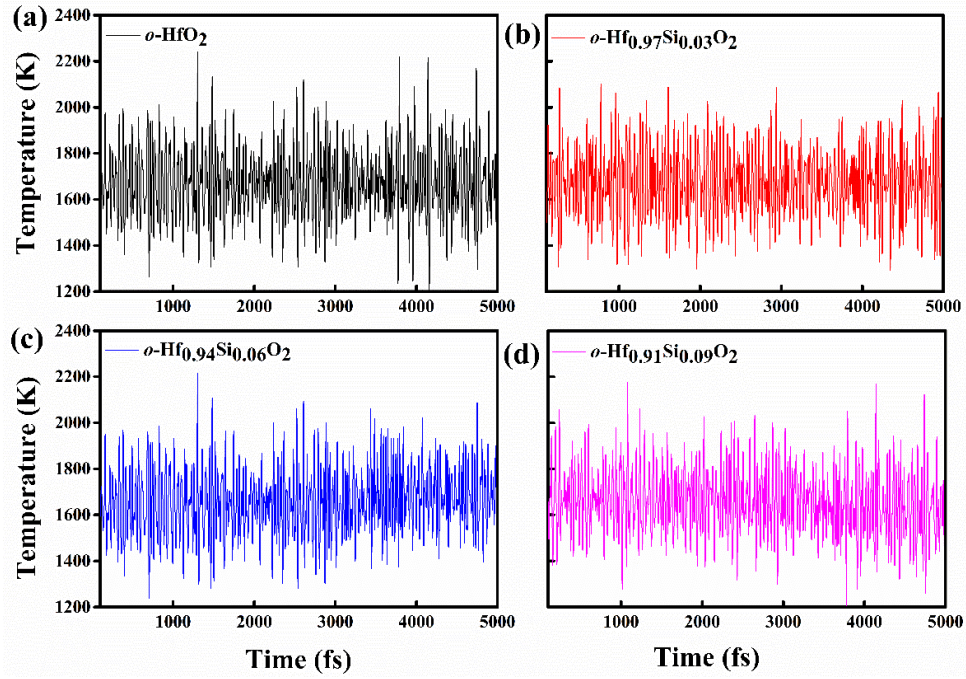


Fig. 4.6: The AIMD simulations of temperature fluctuations versus time of $o\text{-Hf}_{1-x}\text{Si}_x\text{O}_2$ ($x = 0, 0.03, 0.06, \text{ and } 0.09$).

The AIMD simulations have been performed up to the time step of 5000 fs in the canonical ensemble (NVT) to verify the stability of the proposed material (Fig. 4.6). The results AIMD simulation and the formation energy are consistent which confirms the stability of the $o\text{-Hf}_{1-x}\text{Si}_x\text{O}_2$. The rate of Si diffusion in $o\text{-HfO}_2$ (Fig. 4.7), calculated from AIMD results, decreases with an increase in doping concentration i.e., $0.56 \times 10^{-6} \text{ cm}^2/\text{s}$, $0.45 \times 10^{-6} \text{ cm}^2/\text{s}$, and $0.35 \times 10^{-6} \text{ cm}^2/\text{s}$ for $x = 0.03, 0.06, \text{ and } 0.09$, respectively.

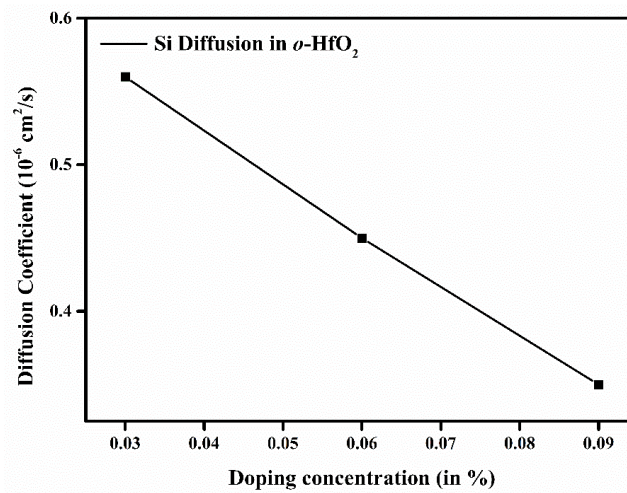


Fig. 4.7: The variation in diffusion coefficient with doping concentration for $o\text{-Hf}_{1-x}\text{Si}_x\text{O}_2$ ($x = 0, 0.03, 0.06, \text{ and } 0.09$).

4.3.3 Electronic Properties

The electronic band structure calculations for *o*-HfO₂ have been analyzed at the optimized values of P_T i.e., 8 GPa, 14 GPa, and 15 GPa. An indirect band gap, Fig. 4.8, with magnitude 6.18 eV at 0 GPa, along high symmetry path Γ -X-S-Y- Γ -Z-U-R-T-Z, is obtained using TB-mBJ potential which shows a reasonable agreement with a prior report [26]. The magnitude of the band gap increases slightly with increasing pressure as listed in Table 4.3. The Si-doping creates new energy states between the conduction band (CB) and the valence band (VB). It further leads to a change in band gap from indirect (Γ -Y) to direct one along Γ - Γ (**Fig. 4.9 (a)-(c)**). For more clarity (Fig. 4.10), we compared the band structure of Hf_{0.91}Si_{0.09}O₂ with pure HfO₂ at 8GPa. As shown in Table 4.3, the magnitude of the band gap decreases to 4.55 eV, 4.13 eV, and 4.06 eV for *o*-Hf_{1-x}Si_xO₂ ($x = 0.03, 0.06, 0.09$). This reduction may be attributed to a decrease in the rate of Si diffusion coefficient in HfO₂ with increasing doping concentration [27] as shown in Fig. 4.7. The similar reduction in band gap with Si doping has also been experimentally observed in other oxides e.g., ZrO₂, and ZnO [28, 29]. The decrease in band gap with diffusion coefficient has also been reported in Y-doped ZrO₂ [30, 31].

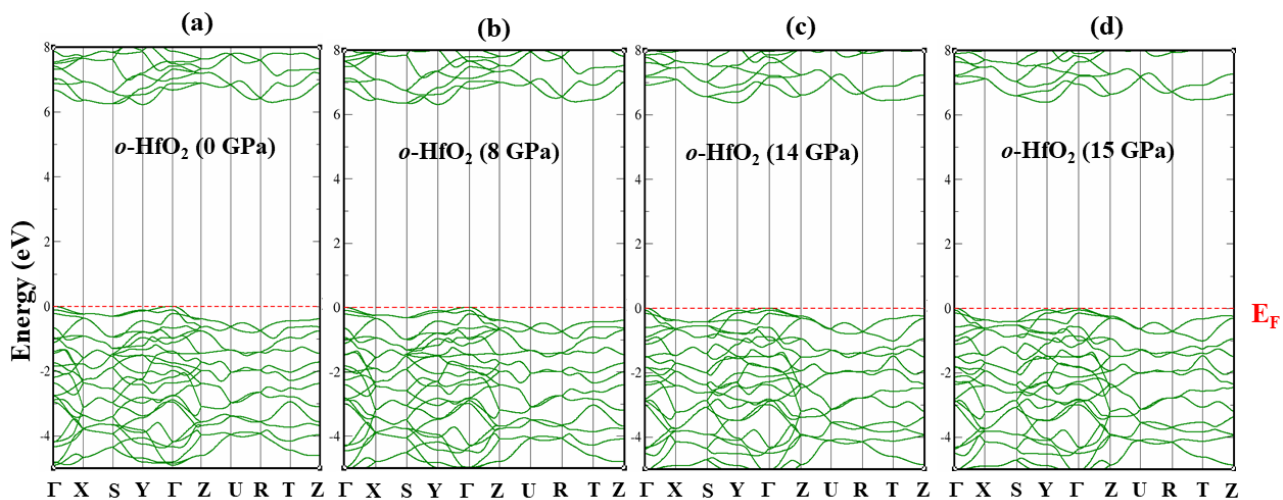


Fig. 4.8: Band structure of *o*-HfO₂ (a) 0 GPa (b) 8 GPa (c) 14 GPa (d) 15 GPa at phase transition pressures within TB-mBJ approach (E_F is shifted to 0 eV).

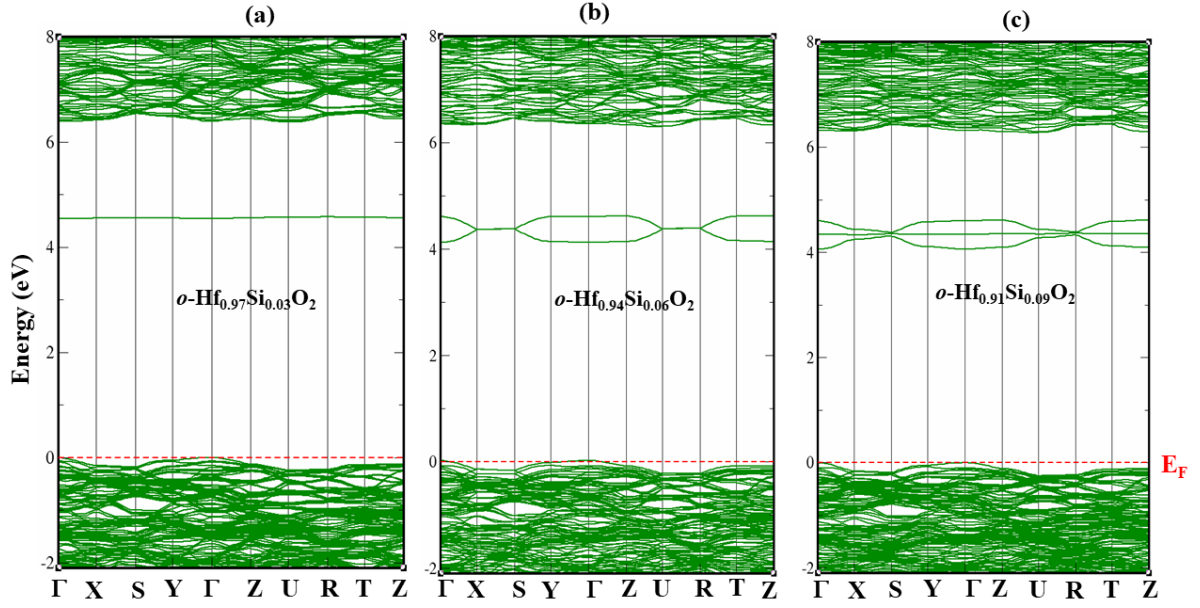


Fig. 4.9: Band structure of (a) $o\text{-Hf}_{0.97}\text{Si}_{0.03}\text{O}_2$ at 14 GPa, (b) $o\text{-Hf}_{0.94}\text{Si}_{0.06}\text{O}_2$ at 8 GPa (a) $o\text{-Hf}_{0.91}\text{Si}_{0.09}\text{O}_2$ at 8 GPa calculated within TB-mBJ approach (E_F is shifted to 0 eV).

Table 4.3: The calculated band gap of $o\text{-Hf}_{1-x}\text{Si}_x\text{O}_2$ ($x = 0, 0.03, 0.06, \text{ and } 0.09$) (within GGA and TB-mBJ potentials)

		x=0				x= 0.03	x= 0.06	x= 0.09
Pressure		0 GPa	8 GPa	14 GPa	15 GPa	14 GPa	8 GPa	8 GPa
Band Gap (eV)	GGA	4.41	4.47	4.56	4.60	2.89	2.45	2.43
	mBJ	6.38	6.45	6.52	6.58	4.55	4.13	4.06
		6.45 [#]						

[#]calculated using B3LYP functional [26].

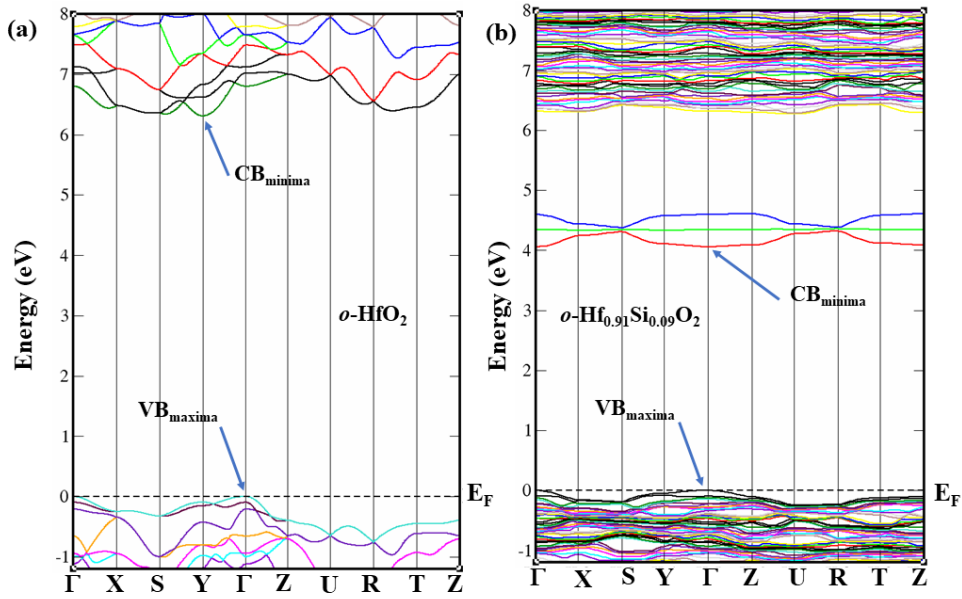


Fig. 4.10: Band structure of (a) $o\text{-HfO}_2$ and (b) $o\text{-Hf}_{0.91}\text{Si}_{0.09}\text{O}_2$ at transition pressure of 8 GPa (E_F is shifted to 0 eV).

We have analyzed the DOS to understand the contribution of various atomic species in band structure as shown in Fig. 4.11 (a)-(d). For $x = 0$, Hf-states dominate over O-states in the CB, whilst in the VB O-states dominate over Hf-states. In the case of Si-doped structures, near the Fermi level, the O-2p states are pre-dominant; however, in the deep VB (~ 8 eV) the Si-2p states show significant contribution over Hf-5d and O-2p states. It is worth mentioning that Si doping results in the formation of new energy states near the minima of CB, in which $x = 0.03$ has the highest magnitude as compared to other doping concentrations. At higher energies, the significant intermixing of Hf-5d, Si-2p, and O-2p states increases in the extent of hybridization in $\text{Hf}_{1-x}\text{Si}_x\text{O}_2$.

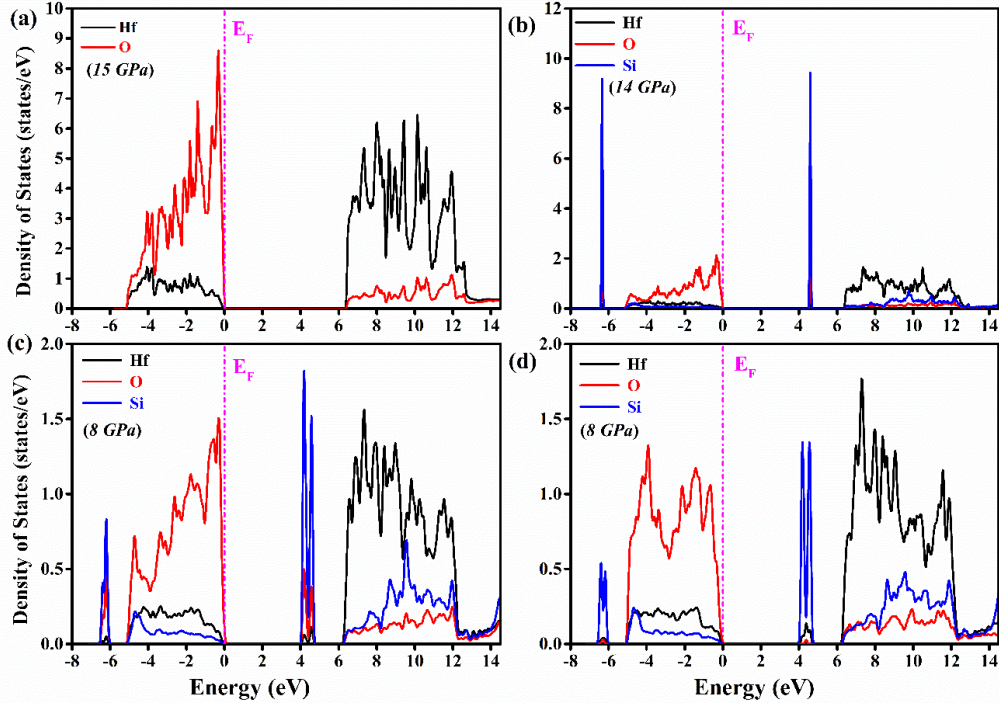


Fig. 4.11: Density of States (DOS) of (a) o -HfO₂ (b) o -Hf_{0.97}Si_{0.03}O₂ (c) o -Hf_{0.94}Si_{0.06}O₂ (d) o -Hf_{0.91}Si_{0.09}O₂ (E_F is shifted to 0 eV).

4.4 Conclusion

We have presented a systematic study of the pressure induced structural phase transitions from centrosymmetric m -HfO₂ to non-centrosymmetric o -HfO₂ with Si-doping. The phase transition for pure $m \rightarrow o$ -HfO₂ has occurred at the transition pressure of 15 GPa. With an increase in Si-doping, the transition pressure has reduced to 14 GPa, 8 GPa, and 8 GPa for $x=0.03, 0.06,$ and 0.09 respectively. The obtained results are in excellent agreement with experimental observations. This reduction in pressure with Si doping has been attributed to a reduction in bond length and charge transfer from Si to o -HfO₂. The thermal stability of o -HfO₂ has been assessed via *ab initio* molecular dynamics and negative value of formation energy. The doping has led to the transformation of the indirect band gap centrosymmetric m -HfO₂ to direct band gap non-centrosymmetric o -HfO₂ and creates new energy levels near the CB minima which results in the reduction of band gap. Our proposed study has accurately predicted the phase transition pressures and stability of Si-doped non-centrosymmetric o -HfO₂. This might be a suitable choice for optoelectronic, ferroelectric device applications.

References

- [1] M. Kumar, R. P. Singh, and A. Kumar, "Opto-electronic properties of HfO₂: A first principle-based spin-polarized calculations," *Optik*, 226, 165937, 2021, doi: 10.1016/j.ijleo.2020.165937.
- [2] R. Sharma, S. A. Dar, and V. Srivastava, "Half-metallic ferromagnetism and thermoelectric properties of vanadium doped Hf_{1-x}V_xO₂ (x = 0, 0.25, 0.50, 0.75) alloys by first principles perspective," *Phys. Lett. A*, 411, 127559, 2021, doi: 10.1016/j.physleta.2021.127559.
- [3] J. Liu, S. Liu, L. H. Liu, B. Hanrahan, and S. T. Pantelides, "Origin of Pyroelectricity in Ferroelectric HfO₂," *Phys. Rev. Appl.*, 12, 034032, 2019, doi: 10.1103/PhysRevApplied.12.034032.
- [4] S. Dutta *et al.*, "Piezoelectricity in hafnia," *Nat. Commun.*, 12, 7301, 2021, doi: 10.1038/s41467-021-27480-5.
- [5] O. Ohtaka *et al.*, "Phase Relations and Volume Changes of Hafnia under High Pressure and High Temperature," *J. Am. Ceram. Soc.*, 84, 1369–1373, 2004, doi: 10.1111/j.1151-2916.2001.tb00843.x.
- [6] W. Zhang *et al.*, "Pressure-Induced Phase Transition and Compression Properties of HfO₂ Nanocrystals," *Inorg. Chem.*, 61, 3498–3507, 2022, doi: 10.1021/acs.inorgchem.1c03450.
- [7] B. Lai *et al.*, "Study on the phase transition dynamics of HfO₂-based ferroelectric films under ultrafast electric pulse," *J. Phys. Condens. Matter*, 33, 405402, 2021, doi: 10.1088/1361-648X/ac14f9.
- [8] Q.-J. Hong *et al.*, "Combined computational and experimental investigation of high temperature thermodynamics and structure of cubic ZrO₂ and HfO₂," *Sci. Rep.*, 8, 14962, 2018, doi: 10.1038/s41598-018-32848-7.
- [9] T. Dehury, S. Kumar, and C. Rath, "Structural transformation and bandgap engineering by doping Pr in HfO₂ nanoparticles," *Mater. Lett.*, 302, 130413, 2021, doi: 10.1016/j.matlet.2021.130413.
- [10] S. Gálvez-Barboza, Luis. A. García-Cerda, and Luis. A. González, "Effect of Ce doping on the structure and optical properties of HfO₂ films by the Pechini-type sol–gel method," *J. Sol-Gel Sci. Technol.*, 88, 371–378, 2018, doi: 10.1007/s10971-018-4829-1.
- [11] T. S. Böske *et al.*, "Phase transitions in ferroelectric silicon doped hafnium oxide," *Appl. Phys. Lett.*, 99, 112904, 2011, doi: 10.1063/1.3636434.

- [12] C. M. Fancher, L. Zhao, M. Nelson, L. Bai, G. Shen, and J. L. Jones, “Pressure-induced structures of Si-doped HfO₂,” *J. Appl. Phys.*, 117, 234102, 2015, doi: 10.1063/1.4922717.
- [13] M. Bohr, R. Chau, T. Ghani, and K. Mistry, “The High-k Solution,” *IEEE Spectr.*, 44, 29–35, 2007, doi: 10.1109/MSPEC.2007.4337663.
- [14] T. Li *et al.*, “Origin of Ferroelectricity in Epitaxial Si-Doped HfO₂ Films,” *ACS Appl. Mater. Interfaces*, 11, 4139–4144, 2019, doi: 10.1021/acsami.8b19558.
- [15] M. C. Chun *et al.*, “Effect of wake-up on the polarization switching dynamics of Si doped HfO₂ thin films with imprint,” *J. Alloys Compd.*, 823, 153777, 2020, doi: 10.1016/j.jallcom.2020.153777.
- [16] K. Lee *et al.*, “Stable Subloop Behavior in Ferroelectric Si-Doped HfO₂,” *ACS Appl. Mater. Interfaces*, 11, 38929–38936, 2019, doi: 10.1021/acsami.9b12878.
- [17] R. Materlik, C. Künneth, M. Falkowski, T. Mikolajick, and A. Kersch, “Al-, Y-, and La-doping effects favoring intrinsic and field induced ferroelectricity in HfO₂: A first principles study,” *J. Appl. Phys.*, 123, 164101, 2018, doi: 10.1063/1.5021746.
- [18] S.-S. Lin, C.-S. Liao, and S.-Y. Fan, “Effects of substrate temperature on properties of HfO₂, HfO₂:Al and HfO₂:W films,” *Surf. Coat. Technol.*, 271, 269–275, 2015, doi: 10.1016/j.surfcoat.2014.10.057.
- [19] G. Kresse and D. Joubert, “From ultrasoft pseudopotentials to the projector augmented-wave method,” *Phys. Rev. B*, 59, 1758–1775, 1999, doi: 10.1103/PhysRevB.59.1758.
- [20] J. P. Perdew, K. Burke, and M. Ernzerhof, “Generalized Gradient Approximation Made Simple [Phys. Rev. Lett. 77, 3865 (1996)],” *Phys. Rev. Lett.*, 78, 1396–1396, 1997, doi: 10.1103/PhysRevLett.78.1396.
- [21] A. Togo, L. Chaput, and I. Tanaka, “Distributions of phonon lifetimes in Brillouin zones,” *Phys. Rev. B*, 91, 094306, 2015, doi: 10.1103/PhysRevB.91.094306.
- [22] P. Blaha, “an Augment Plane Wave+ Local Orbitals Program for Calculating Crystal Properties, User’s Guide.” Vienna Austria.
- [23] F. Tran and P. Blaha, “Accurate Band Gaps of Semiconductors and Insulators with a Semilocal Exchange-Correlation Potential,” *Phys. Rev. Lett.*, 102, 226401, 2009, doi: 10.1103/PhysRevLett.102.226401.
- [24] B. B. Sharma, B. Chakraborty, S. Gohil, and N. Garg, “Engineering ZnO with Cu doping to lower the transition pressure: Experimental and theoretical investigations,” *AIP Adv.*, 13, 015022, 2023, doi: 10.1063/5.0132933.

- [25] Y. Wang, T. Hou, S. Tian, S.-T. Lee, and Y. Li, "Influence of Doping Effect on Zinc Oxide by First-Principles Studies," *J. Phys. Chem. C*, 115, 7706–7716, 2011, doi: 10.1021/jp111203e.
- [26] A. El Boutaybi *et al.*, "Electro-optic properties of ZrO₂, HfO₂, and LiNbO₃ ferroelectric phases: A comparative density functional study," *Phys. Rev. B*, 107, 045140, 2023, doi: 10.1103/PhysRevB.107.045140.
- [27] H. Chen *et al.*, "Thickness Dependence of Optical Transmittance of Transparent Wood: Chemical Modification Effects," *ACS Appl. Mater. Interfaces*, 11, 35451–35457, 2019, doi: 10.1021/acsami.9b11816.
- [28] K. Lee *et al.*, "Leakage current suppression in spatially controlled Si-doped ZrO₂ for capacitors using atomic layer deposition," *Thin Solid Films*, 657, 1–7, 2018, doi: 10.1016/j.tsf.2018.04.033.
- [29] C. Hong *et al.*, "Structural, electrical, and optical properties of Si-doped ZnO thin films prepared via supercycled atomic layer deposition," *Mater. Sci. Eng. B*, 273, 115401, 2021, doi: 10.1016/j.mseb.2021.115401.
- [30] T. Arima, K. Fukuyo, K. Idemitsu, and Y. Inagaki, "Molecular dynamics simulation of yttria-stabilized zirconia between 300 and 2000 K," *J. Mol. Liq.*, 113, 67–73, 2004, doi: 10.1016/j.molliq.2004.02.038.
- [31] C. V. Reddy, I. N. Reddy, J. Shim, D. Kim, and K. Yoo, "Synthesis and structural, optical, photocatalytic, and electrochemical properties of undoped and yttrium-doped tetragonal ZrO₂ nanoparticles," *Ceram. Int.*, 44, 12329–12339, 2018, doi: 10.1016/j.ceramint.2018.04.020.

Effects of various dopants on optical properties of HfO₂

5.1 Introduction

In recent years, the oxide based materials have captivated the attention of scientific society due to their inimitable properties in the allied area of optoelectronics [1, 2]. HfO₂ has been considered the most appropriate host for optoelectronic applications due to its unique characteristics such as high permittivity, low leakage current, and good thermal and interface stability [3, 4]. Various existing polymorphs of HfO₂ were discussed in the Chapter 1. HfO₂ is extensively used as a coating material due to its hardness and widespread spectral transparency range i.e., from infrared (IR) to ultraviolet (UV) [5–7]. The applicability of HfO₂ is identified in industrial applications like laser mirrors [8], and optical coatings [9, 10]. Recently, HfO₂ thin film on a double-sided Si substrate (HfO₂/Si/HfO₂) has proven its applicability as an anti-reflection coating by reducing the IR reflection [11]. The antireflective coating of HfO₂ reduces the Fresnel loss that can be used in night vision devices [7, 12]. S-Parramon et al. have shown experimentally that Ti doping in HfO₂ thin films leads to improved optical properties like refractive index, and extinction coefficient [13]. Using *first-principles calculations*, Tan et al. have also shown that Ti doping in *m*-HfO₂ modifies its various optical properties [14]. Recently, it has been revealed by Khera et al. that doping of transition metals (Co, Ni, Zn) in *c*-HfO₂ may lead to better optical properties [15]. Besides the transition metals, anionic (S, N, F, and C) doping has also been highly studied in the recent past to enhance various physical and chemical properties of metal oxides [16, 17]. It has been shown that doping of S in HfO₂ thin film leads to improved durability and optical response [18–20]. Zhang et al. have reported that the effect of co-doping of C and F can improve the optical properties of *c*-HfO₂ [21].

In the present chapter, we explored the optical properties of *c*-HfO₂, a non centrosymmetric *o*-HfO₂, and how the doping at anionic and cationic sites can enhance its optical performance.

5.2 Computational details

The optical properties calculations were performed using the optic program as built in the WIEN2K package [22, 23]. The GGA scheme for XC) potentials, given by PBE, was used for structural optimization [24]. The approximations such as local density approximation and GGA

underestimate the band gap. Therefore, we have used TB-mBJ approximation [25] to comprehend exchange and correlation potentials which uses semilocal quantities to reproduce well step structures.

For precise calculations, a K-mesh of $20 \times 20 \times 20$ was used in the IBZ for all the studied cases of HfO₂. The plane wave cutoff was decided by the $R_{\text{MTKmax}} = 7$, and the muffin tin sphere radii were chosen to be non-overlapping with RMT of 2.18 for the Hf atom and 1.5 for O atom. The criterion for energy convergence was set to 0.0001 Ry/cell and the cut-off energy of the core and valence state was fixed at -6 Ry.

5.3 Results and discussion

The structure optimization, thermodynamical stability, and variation in band structure under different doping were discussed in chapters 3 and 4. Here, we studied the linear optical response of *c*-HfO₂ and a non centrosymmetric *o*-HfO₂. The effect of Ti, and Si doping on Hf sites in *c*- and *o*-HfO₂, respectively, and S-doping O sites in *c*-HfO₂ is examined.

To analyze how electromagnetic (EM) radiations interact with a material, it is necessary to analyze the dielectric function:

$$\varepsilon(\omega) = \varepsilon_1(\omega) + i\varepsilon_2(\omega) \quad (5.1)$$

where the symbol $\varepsilon_1(\omega)$ and $\varepsilon_2(\omega)$ are real and imaginary components of the dielectric function.

The $\varepsilon_1(\omega)$ and $\varepsilon_2(\omega)$ components are associated with intraband transitions and interband transitions for a metallic and a semiconductor material, respectively.

The Kramers-Kronig transformation is used to obtain the real component, $\varepsilon_1(\omega)$, which is given by:

$$\varepsilon_1(\omega) = 1 + \frac{2p}{\pi} \int \frac{\omega' \varepsilon_2(\omega')}{(\omega'^2 - \omega^2)} d\omega' \quad (5.2)$$

where p denotes the momentum matrix.

The imaginary component $\varepsilon_2(\omega)$ can be calculated from transitions between VB to CB states and related to electronic structure and the absorption of the incident EM wave as:

$$\varepsilon_2(\omega) = \frac{2\pi e^2}{\Omega \varepsilon_0} \sum |\Psi_k^c| u \cdot r |\Psi_k^v|^2 \delta(E_k^c - E_k^v - E) \quad (5.3)$$

where Ψ_k^c and Ψ_k^v are the wave function related with the CB and VB at k point, u represents the electric field component, Ω represents the unit cell volume, and e represents the charge.

The real and imaginary part of the dielectric constant gives the information about refractive index and extinction coefficient, respectively. Refractive index $n(\omega)$ and extinction coefficient $k(\omega)$ are given by:

$$n(\omega) = \sqrt{\frac{|\varepsilon(\omega)| + \varepsilon_1(\omega)}{2}} \quad (5.4)$$

$$k(\omega) = \sqrt{\frac{|\varepsilon(\omega)| - \varepsilon_1(\omega)}{2}} \quad (5.5)$$

The Reflectivity of a material depends on the refractive index and extinction coefficient of a material which is given by:

$$R(\omega) = \frac{(n-1)^2 + k^2}{(n+1)^2 + k^2} \quad (5.6)$$

The optical conductivity is dependent on the imaginary component and can be expressed as:

$$\sigma(\omega) = \frac{\omega}{4\pi} \text{Im } \varepsilon(\omega) \quad (5.7)$$

The value of absorption coefficient $\alpha(\omega)$ depends on $k(\omega)$ which can be expressed as:

$$\alpha(\omega) = \frac{2\omega k}{c} \quad (5.8)$$

5.3.1 Ti and S doping in *c*-HfO₂

We obtained a response of $\varepsilon_1(\omega)$ of Hf_{1-x}Ti_xO₂ and HfO_{2-x}S_x using equation 5.2, which is shown in **Fig. 5.1(a, b)**. The calculated value of static dielectric constant $\varepsilon_1(0)$ is 3.86 for pristine *c*-HfO₂. The calculated values of static dielectric constant $\varepsilon_1(0)$ for Hf_{1-x}Ti_xO₂ is 4.12, 3.65, 4.16, and 5.24 at $x = 0.03, 0.06, 0.12,$ and $0.25,$ respectively. In the case of HfO_{2-x}S_x this value reduced as compared to pure and Ti doped HfO₂.

With the increase in photonic energy, the graph shows decreasing behavior, which may be ascribed to Maxwell-Wagner interfacial polarization [26, 27]. At low energy, the real component lies at a higher value, indicating more polarization ability and showing a higher refractive index. Real part $\varepsilon_1(\omega)$, for $x = 0$, exhibits the maximum value at 7.06 eV, which is in good agreement with previous studies [2, 21, 28], and for Hf_{1-x}Ti_xO₂ at $x = 0.03, 0.06, 0.12,$ and $0.25,$ the maximum values obtained at 3.27, 3.25, 3.12 and 2.9 eV, respectively. Whereas for HfO_{2-x}S_x the maximum obtained values are 8.04 eV, and 7.94 eV for $x = 0.03$ and 0.06 doping concentrations, respectively.

As the incident photon energy increases, the real component starts to decrease and attain a negative value in the range 11.88–14 eV for $x = 0$, 10.73–11.56 eV for $x = 0.03$, 10.69–14.86 eV for $x = 0.06$, 10.63–14.74 eV for $x = 0.12$, and 10.29–10.95 eV and 11.61–11.94 eV for $x =$

0.25. In the case of $\text{HfO}_{2-x}\text{S}_x$, the real component attains the negative value in the range 10.63–14.79 eV for $x = 0.03$, and 10.57–14.62 eV for $x = 0.06$. Negative values of $\epsilon_1(\omega)$ in these particular energy, ranges suggest the metallic behavior of $\text{Hf}_{1-x}\text{Ti}_x\text{O}_2$ and $\text{HfO}_{2-x}\text{S}_x$. This signifies that electromagnetic radiation will be reflected by the material due to the phenomenon of an anomalous dispersion [29].

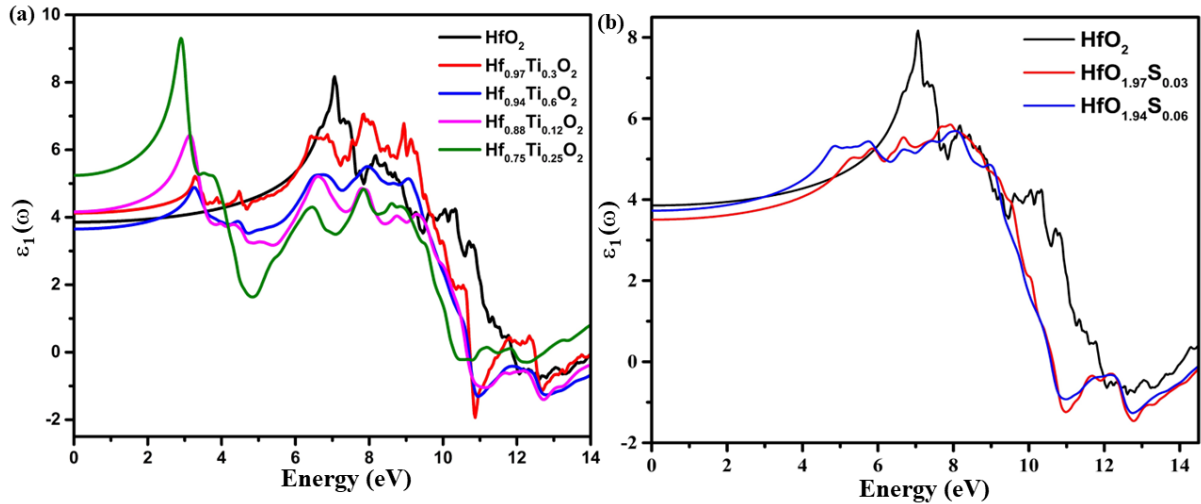


Fig. 5.1 Real part of dielectric function (a) $\text{Hf}_{1-x}\text{Ti}_x\text{O}_2$ ($x = 0, 0.03, 0.06, 0.12$ and 0.25) (b) $\text{HfO}_{2-x}\text{S}_x$ ($x = 0, 0.03$, and 0.06).

We obtained the response of $\epsilon_2(\omega)$ of $\text{Hf}_{1-x}\text{Ti}_x\text{O}_2$ and $\text{HfO}_{2-x}\text{S}_x$ using equation 5.3, which is shown in **Fig. 5.2 (a, b)**. An increase in the value of $\epsilon_2(\omega)$ is observed onwards the optical band gap and reaches a maximum at 11 eV for $x = 0$, which shows the transition of electrons between the VB $\text{O}-p$ states to CB $\text{Hf}-d$ states. For $\text{Hf}_{1-x}\text{Ti}_x\text{O}_2$, at $x = 0.03, 0.06, 0.12$, and 0.25 , the maximum observed values are at 10.69 eV, 10.67 eV, 10.56 eV, and 9.66 eV, respectively. In the case of $\text{HfO}_{2-x}\text{S}_x$, at $x = 0.03$, the observed values of highest absorption peak lie in the range of 9.71–10.19 eV, and for $x = 0.06$ lies at 9.83 eV. This shift in the transition peaks is in good agreement with our result of DOS (Fig. 3.8, 3.10) as shown in Chapter 3. These peaks reflect the interaction among various atoms in the VB and CB. In the higher photon energy region, the decrease in $\epsilon_2(\omega)$ corresponds to the low probability of transitions between unoccupied and occupied orbitals.

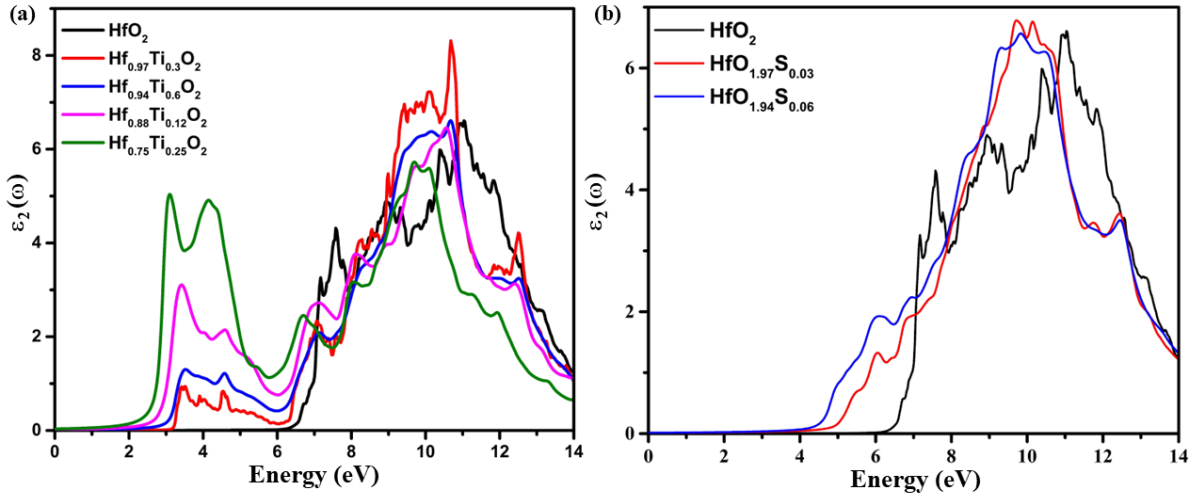


Fig. 5.2 Imaginary part of dielectric function of (a) $\text{Hf}_{1-x}\text{Ti}_x\text{O}_2$ ($x = 0, 0.03, 0.06, 0.12$ and 0.25) (b) $\text{HfO}_{2-x}\text{S}_x$ ($x = 0, 0.03$, and 0.06).

The nature of $n(\omega)$ of $\text{Hf}_{1-x}\text{Ti}_x\text{O}_2$ and $\text{HfO}_{2-x}\text{S}_x$ with incident photon energy, obtained using equation 5.4, which is shown in Fig. 5.3 (a, b). It can be visualized that the static value of refractive index $n(0)$ for $c\text{-HfO}_2$ is 1.96. With the Ti doping the $n(0)$ changes to 2.03, 1.91, 2.04, and 2.29 for $x = 0.03, 0.06, 0.12$, and 0.25 doping concentration, respectively. In the case of $\text{HfO}_{2-x}\text{S}_x$, the value of $n(0)$ becomes 1.87, 1.93 for $x = 0.03$ and 0.06 doping concentration, respectively. The decrement in the refractive index after a particular wavelength is due to optical dispersion [29]. Refractive index below unity is due to the fact that group velocity of incident radiation is greater than c means that the group velocity shift in the -ve region and the behaviour of medium changes from linear to non-linear.

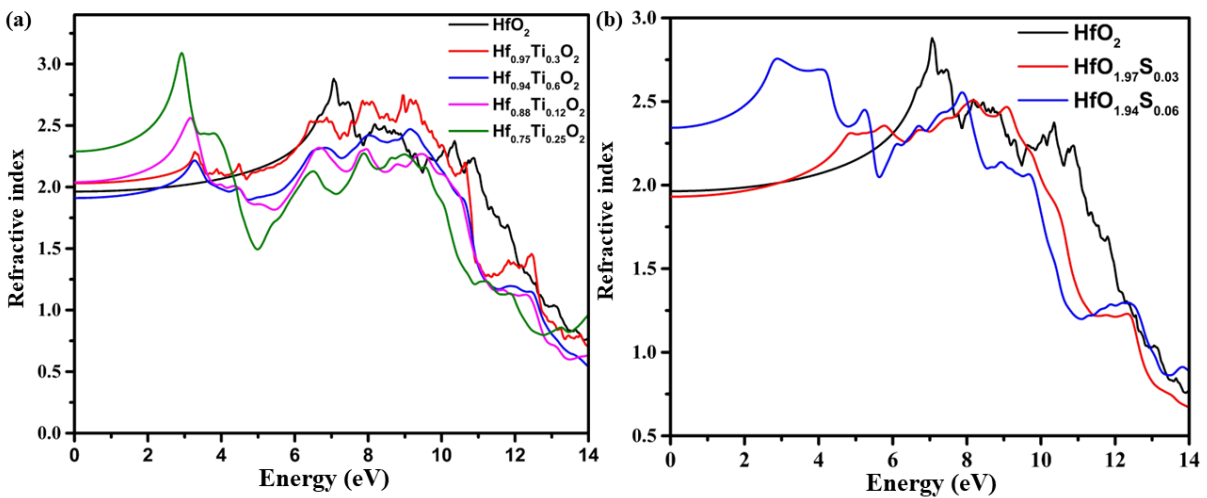


Fig. 5.3 Refractive index of (a) $\text{Hf}_{1-x}\text{Ti}_x\text{O}_2$ ($x = 0, 0.03, 0.06, 0.12$ and 0.25) (b) $\text{HfO}_{2-x}\text{S}_x$ ($x = 0, 0.03$, and 0.06).

We obtained the extinction coefficient of $\text{Hf}_{1-x}\text{Ti}_x\text{O}_2$ and $\text{HfO}_{2-x}\text{S}_x$ using equation 5.5, which is shown in Fig. 5.4 (a, b). The value of the extinction coefficient follows the same trend as the imaginary part of the dielectric function. The highest value of $k(\omega)$ was observed at 11.80 eV for pure and doped structures its value lies between 10.09 to 10.83 eV. In the high energy region, $k(\omega)$ shows large fluctuations this may be due to different rates of excitation of the electron.

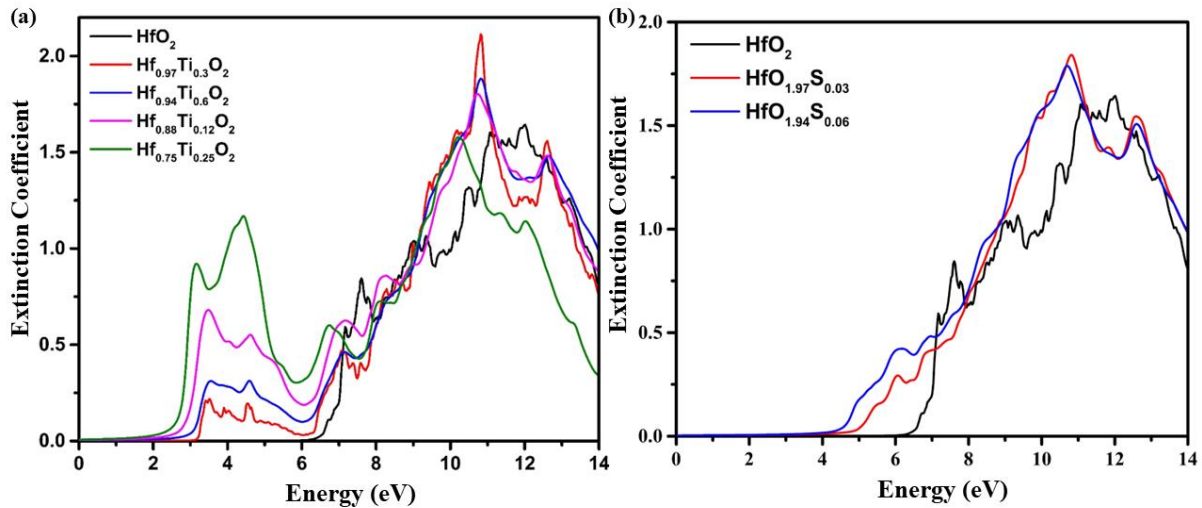


Fig. 5.4 Extinction coefficient of (a) $\text{Hf}_{1-x}\text{Ti}_x\text{O}_2$ ($x = 0, 0.03, 0.06, 0.12$ and 0.25) (b) $\text{HfO}_{2-x}\text{S}_x$ ($x = 0, 0.03$, and 0.06).

The Reflectivity (Figure 5.5) defines the material's ability to reflect the incident photons from its surface, which is calculated using equation 6. The calculated value of $R(0)$ is 0.105 for pristine $c\text{-HfO}_2$ showing fair agreement with previous reported results [29, 30]. In $\text{Hf}_{1-x}\text{Ti}_x\text{O}_2$ doped structures the calculated value of $R(0)$ is 0.115, 0.097, 0.117 and 0.15 for $x = 0.03, 0.06, 0.12$, and 0.25 , respectively (Figure 5.5 a). Whilst, in $\text{HfO}_{2-x}\text{S}_x$ the value become 0.092, 0.10 for $x = 0.03$ and 0.06 doping concentrations, respectively (Figure 5.5 b). It is observed that in the visible region, Ti-doped HfO_2 shows improved results over Mn, Fe, Co, and Ni doping [30]. Hence suggested doping can work as a better antireflective coating material.

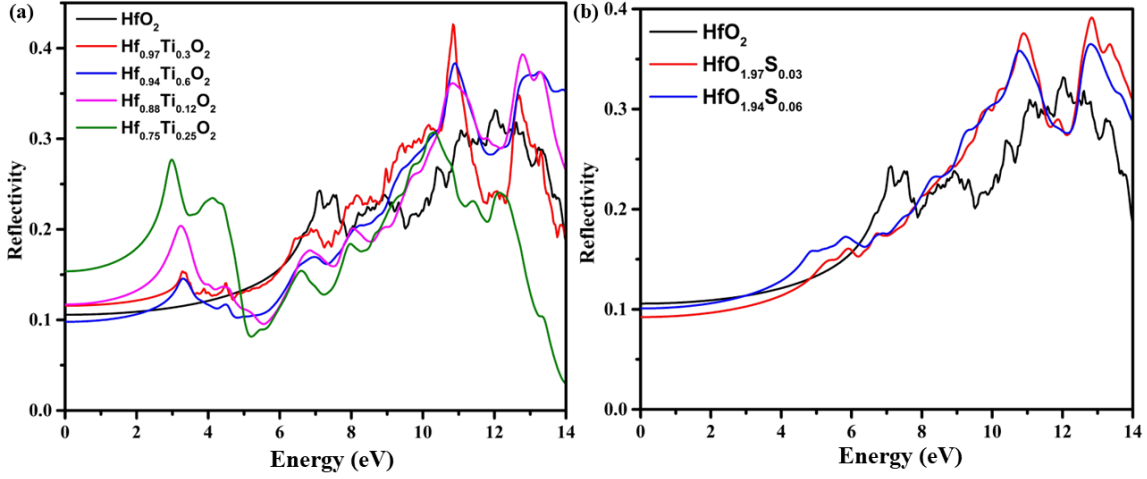


Fig. 5.5 Reflectivity of (a) $\text{Hf}_{1-x}\text{Ti}_x\text{O}_2$ ($x = 0, 0.03, 0.06, 0.12$ and 0.25) (b) $\text{HfO}_{2-x}\text{S}_x$ ($x = 0, 0.03$, and 0.06).

The response of optical conductivity of the $\text{Hf}_{1-x}\text{Ti}_x\text{O}_2$, and $\text{HfO}_{2-x}\text{S}_x$ is the same as the response of absorption and extinction coefficient, which is obtained through equation 5.7 and depicted in Figure 5.6 (a, b). The highest peaks of optical conductivity are observed in the range of 9 eV to 11eV for Ti and S-doping in *c*- HfO_2 . The highest observed value is in the range where the value of $\epsilon_1(\omega)$ is negative, which indicates that optical conductivity is high in the metallic region.

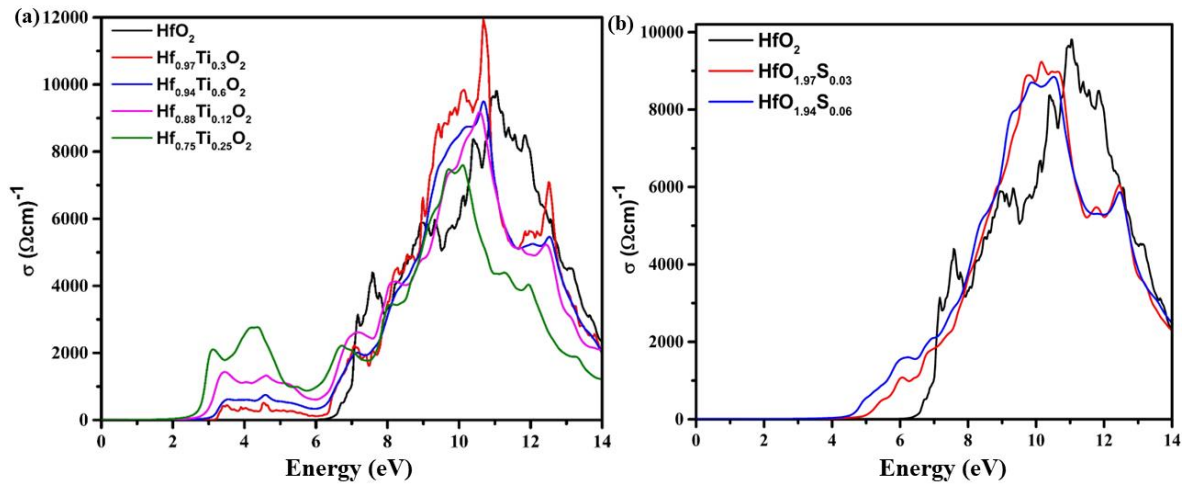


Fig. 5.6 Optical conductivity of (a) $\text{Hf}_{1-x}\text{Ti}_x\text{O}_2$ ($x = 0, 0.03, 0.06, 0.12$ and 0.25) (b) $\text{HfO}_{2-x}\text{S}_x$ ($x = 0, 0.03$, and 0.06).

The behaviour of the absorption coefficient $\alpha(\omega)$ of $\text{Hf}_{1-x}\text{Ti}_x\text{O}_2$ and $\text{HfO}_{2-x}\text{S}_x$, is obtained using equation 5.8 and shown in Fig. 5.7 (a, b).

This is an important parameter that indicates how much distance is covered by the beam of definite energy as it passes through any material before the absorption. In pure *c*- HfO_2 the

observed value of $\alpha(\omega)$ is 6.09 which is in good agreement with the previous study [29] whilst in the Ti doped structures this decreases to 3.18, 2.94, 2.48, and 2.29 eV for $x = 0.03, 0.06, 0.12$ and 0.25 , respectively (Fig. 5.7 (a)). In $\text{HfO}_{2-x}\text{S}_x$ the observed value of $\alpha(\omega)$ is 4.88, 4.36 for $x = 0.03$, and 0.06 , respectively (Fig. 5.7 (b)).

The fluctuation in the values is due to different rates of excitation of electrons. The value of the absorption coefficient signifies low absorption in the visible region, while high absorption is achieved in the UV region and no absorption in the IR region. High absorption in the UV region makes it a suitable candidate for optoelectronic memristors and other optical devices.

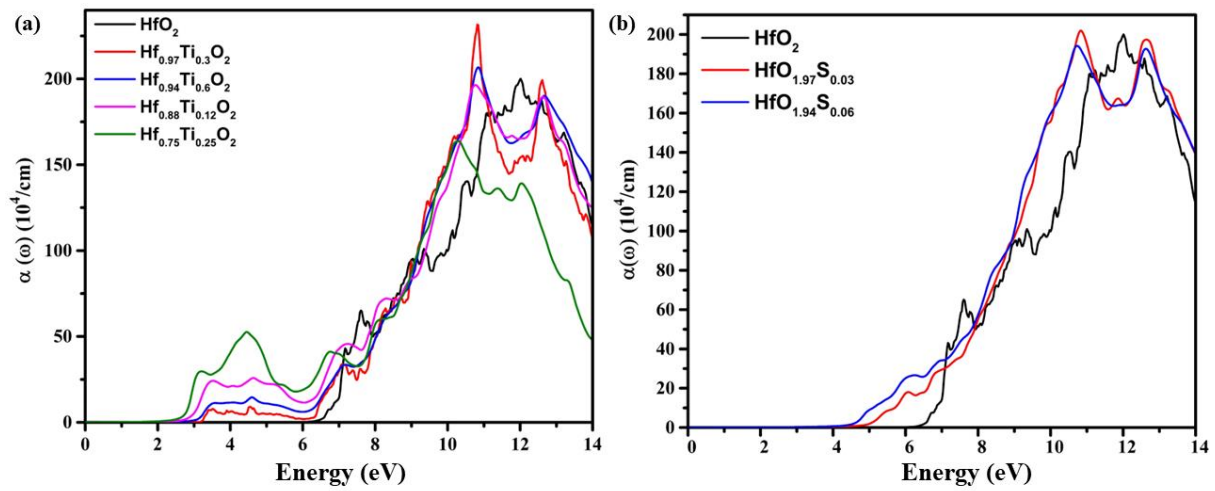


Fig. 5.7 Absorption Coefficient of (a) $\text{Hf}_{1-x}\text{Ti}_x\text{O}_2$ ($x = 0, 0.03, 0.06, 0.12$ and 0.25) (b) $\text{HfO}_{2-x}\text{S}_x$ ($x = 0, 0.03$, and 0.06).

5.3.2 Si doping in $o\text{-HfO}_2$

Now, we discuss the effect of pressure on the linear optical properties of non-centrosymmetric $o\text{-Hf}_{1-x}\text{Si}_x\text{O}_2$ ($x = 0, 0.03, 0.06$, and 0.09).

The real and imaginary components of the dielectric function of the $o\text{-Hf}_{1-x}\text{Si}_x\text{O}_2$ are obtained using equations 5.2 and 5.3, and shown in Fig. 5.8 (a and b). The variation in the value of $\epsilon_1(0)$ is 3.31, 3.35, 3.34, and 3.38 for $x = 0, 0.03, 0.06$, and 0.09 , respectively. In the range of $\sim 4\text{--}11$ eV, a large number of peaks are observed, and the magnitude of $\epsilon_1(\omega)$ is high for $\text{Hf}_{0.91}\text{Si}_{0.09}\text{O}_2$ up to 7.23 eV as shown in Fig. 5.8 (a). At 11.79 eV, $o\text{-Hf}_{0.91}\text{Si}_{0.09}\text{O}_2$ and $o\text{-Hf}_{0.94}\text{Si}_{0.06}\text{O}_2$ become metallic whereas $o\text{-Hf}_{0.97}\text{Si}_{0.03}\text{O}_2$ and pristine $o\text{-HfO}_2$ show metallic behaviour at 12.02 eV of photon energy.

The observed values of $\epsilon_2(\omega)$ are 6.32 eV, 4.49 eV, 4.10 eV, 4.01 eV for $x = 0, 0.03, 0.06$ and 0.09 , respectively. It is clear from Fig. 5.8 (b) that the dielectric function is closely related to

the band gap. We observed that threshold energy shifted to lower photon energy with an increase in Si concentration. There appear four sharp peaks of $\varepsilon_2(\omega)$, at 7.73 eV, 8.30 eV, 9.29 eV, and a maximum value at 10.94 eV. These peaks reflect the interaction among various atoms in the VB and CB. The lower lying peaks are mainly contributed by the O-2p and Hf-5d states and high energy peaks are associated with the Si-2p and Hf-5d atomic states.

The refractive index of $\text{Hf}_{1-x}\text{Si}_x\text{O}_2$ is obtained using equation 4. The observed value of static refractive index $n(\omega)$ is ~ 1.82 and 1.83 for pure and Si-doped o - HfO_2 (Fig. 5.8 (c)). The o - $\text{Hf}_{0.91}\text{Si}_{0.09}\text{O}_2$ has the lower value of $n(\omega)$ as compared to other studied concentrations of o - HfO_2 , this will accelerate the EM radiations as they pass through this material. The value of $n(\omega)$ becomes less than unity as the incident photon energy reaches 12.3 eV which means, that after this, the behavior of the system changes from linear to non-linear. A decrease in the value of the refractive index after 7.29 eV is due to the optical dispersion behavior of the material [2].

The extinction coefficient of $\text{Hf}_{1-x}\text{Si}_x\text{O}_2$ is obtained using equation 5. The $k(\omega)$, as shown in Fig. 5.8 (d), follows a similar pattern as the imaginary part of the dielectric constant. The highest value of $k(\omega)$ observed at 10.94 eV for pristine o - HfO_2 and after that, it decreases as doping increases.

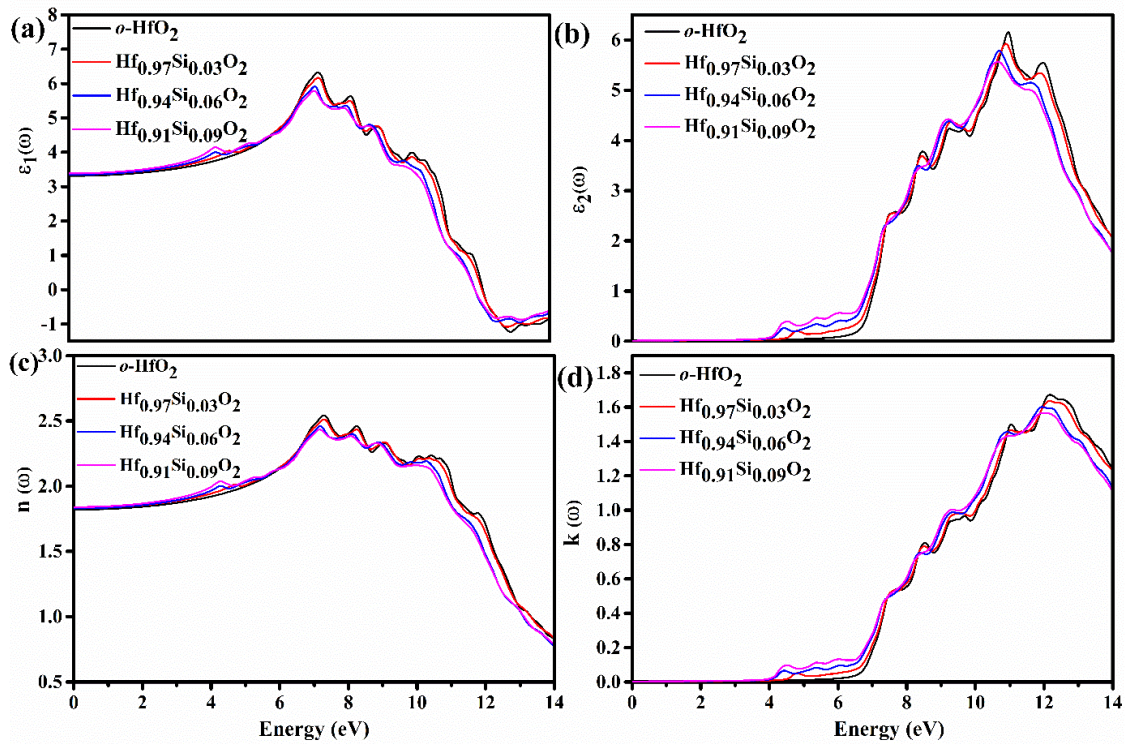


Fig. 5.8: (a) Real part (b) Imaginary part (c) Refractive index (d) Extinction coefficient of o - $\text{Hf}_{1-x}\text{Si}_x\text{O}_2$ ($x = 0, 0.03, 0.06,$ and 0.09).

The reflectivity of $\text{Hf}_{1-x}\text{Si}_x\text{O}_2$ is obtained using equation 5.6. The measured static value reflectivity $R(0)$ is ~ 0.084 and augmented at the high photon energy up to 12 eV and then starts to decline as shown in Fig. 5.9 (a). In the lower photon energy region, the material shows an optically transparent nature. $R(\omega)$ slightly increases in the infra-red region and UV region it shows maximum reflectivity (0.35).

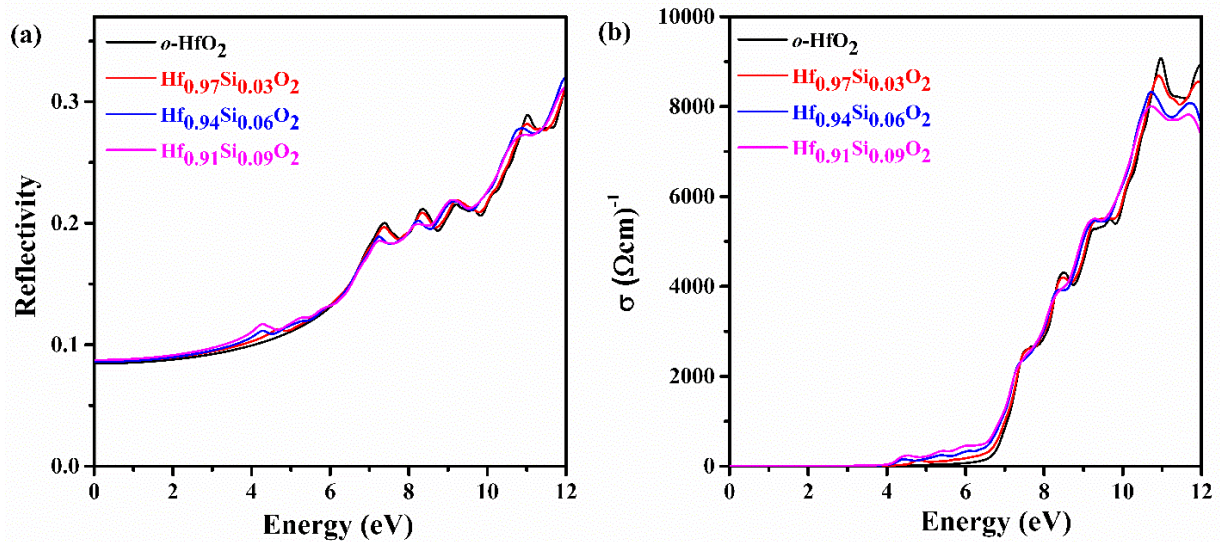


Fig. 5.9: (a) Reflectivity (b) Conductivity of $o\text{-Hf}_{1-x}\text{Si}_x\text{O}_2$ ($x = 0, 0.03, 0.06, \text{ and } 0.09$).

The Conductivity of $\text{Hf}_{1-x}\text{Si}_x\text{O}_2$ is obtained using equation 5.7. It can be seen, from Fig. 5.9 (b), that the $\sigma(\omega)$ follows the same behavior as $\epsilon_2(\omega)$, and attain the maximum value at 10.96 eV, 10.89 eV, 10.72 eV, and 10.69 eV with a magnitude of $9044.11 \Omega^{-1}\text{cm}^{-1}$, $8661.76 \Omega^{-1}\text{cm}^{-1}$, $8317.64 \Omega^{-1}\text{cm}^{-1}$, $7973.52 \Omega^{-1}\text{cm}^{-1}$, for $x=0, 0.03, 0.06, 0.09$, respectively.

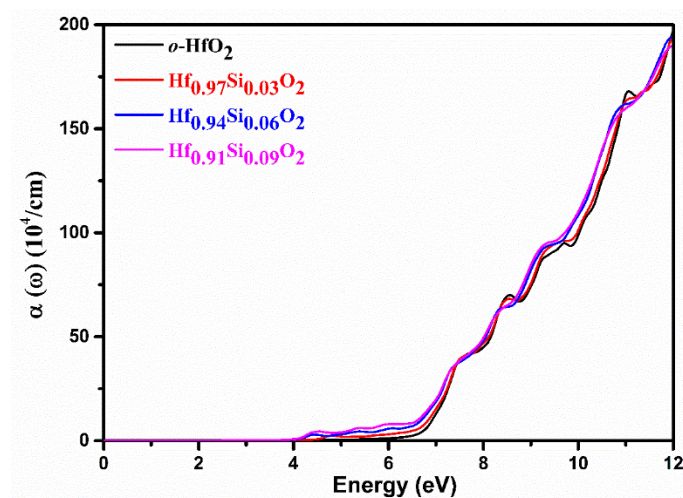


Fig. 5.10: Absorption Coefficient of $o\text{-Hf}_{1-x}\text{Si}_x\text{O}_2$ ($x = 0, 0.03, 0.06, \text{ and } 0.09$).

The absorption Coefficient of $\text{Hf}_{1-x}\text{Si}_x\text{O}_2$ is obtained using equation 5.8. The value of $\alpha(\omega)$ decreases from 6.23 eV to 4.01 eV due to the incorporation of dopants as shown in **Fig. 5.10**. In the high photon energy range, the fluctuation in the value of $\alpha(\omega)$ is due to a different rate of excitation of the electron. Doping leads to a redshift in absorption and reduces the forbidden band width. This decrease in the $\alpha(\omega)$ for high doping concentration may be due to the low diffusion coefficient value of the doped structure, see Fig. 4.7 Chapter 4 [31]. As a result, the Si-doped *o*- HfO_2 would be suggested as an efficient material for UV absorption.

5.4 Conclusion

Optical parameters such as dielectric constant, and refractive index have been calculated to foresee the use of HfO_2 for optoelectronic applications. We predicted that Ti doping at $x = 0.03$ and S doping at $x = 0.06$, have the lowest value of static dielectric constant which may make it suitable for electron transport. The calculated decrease in reflectivity also suggests the utility of Ti and S-doped HfO_2 for the anti-reflective coating material. In the case of Si doped HfO_2 it is analyzed that doping leads to enhancing the UV absorption area but no significant changes were observed in the refractive index. The high absorption in the UV region makes HfO_2 a suitable candidate for optical devices. The suggested doping mechanism can be used to improve the required optical properties and make HfO_2 as a suitable candidate in optoelectronic applications.

References

- [1] C. S. Hwang and B. Dieny, “Advanced memory—Materials for a new era of information technology,” *MRS Bull.*, 43, 330–333, 2018, doi: 10.1557/mrs.2018.96.
- [2] M. Kumar, R. P. Singh, and A. Kumar, “Opto-electronic properties of HfO₂: A first principle-based spin-polarized calculations,” *Optik*, 226, 165937, 2021, doi: 10.1016/j.ijleo.2020.165937.
- [3] L. Khomenkova, X. Portier, J. Cardin, and F. Gourbilleau, “Thermal stability of high-*k* Si-rich HfO₂ layers grown by RF magnetron sputtering,” *Nanotechnology*, 21, 285707, 2010, doi: 10.1088/0957-4484/21/28/285707.
- [4] C. H. Fu *et al.*, “A low gate leakage current and small equivalent oxide thickness MOSFET with Ti/HfO₂ high-*k* gate dielectric,” *Microelectron. Eng.*, 88, 1309–1311, 2011, doi: 10.1016/j.mee.2011.03.073.
- [5] S. Lange, V. Kiisk, V. Reedo, M. Kirm, J. Aarik, and I. Sildos, “Luminescence of RE-ions in HfO₂ thin films and some possible applications,” *Opt. Mater.*, 28, 1238–1242, 2006, doi: 10.1016/j.optmat.2006.02.011.
- [6] S. B. Khan, Z. Zhang, and S. L. Lee, “Annealing influence on optical performance of HfO₂ thin films,” *J. Alloys Compd.*, 816, 152552, 2020, doi: 10.1016/j.jallcom.2019.152552.
- [7] J. Ni, Y. Zhu, S. Wang, Z. Li, Z. Zhang, and B. Wei, “Nanostructuring HfO₂ Thin Films as Antireflection Coatings,” *J. Am. Ceram. Soc.*, 92, 3077–3080, 2009, doi: 10.1111/j.1551-2916.2009.03306.x.
- [8] H. Jiao *et al.*, “Study of HfO₂ /SiO₂ dichroic laser mirrors with refractive index inhomogeneity,” *Appl. Opt.*, 53, A56, 2014, doi: 10.1364/AO.53.000A56.
- [9] A. Lauria, I. Villa, M. Fasoli, M. Niederberger, and A. Vedda, “Multifunctional Role of Rare Earth Doping in Optical Materials: Nonaqueous Sol–Gel Synthesis of Stabilized Cubic HfO₂ Luminescent Nanoparticles,” *ACS Nano*, 7, 7041–7052, 2013, doi: 10.1021/nn402357s.
- [10] S. Li *et al.*, “Structure and optical properties of HfO₂ films on Si (100) substrates prepared by ALD at different temperatures,” *Phys. B Condens. Matter*, 584, 412065, 2020, doi: 10.1016/j.physb.2020.412065.

- [11] J. Gu *et al.*, “Fabrication and performances of double-sided HfO₂ anti-reflection films with ultra-high infrared transmittance,” *J. Alloys Compd.*, 858, 158337, 2021, doi: 10.1016/j.jallcom.2020.158337.
- [12] Y. Wang, Z. Lin, X. Cheng, H. Xiao, F. Zhang, and S. Zou, “Study of HfO₂ thin films prepared by electron beam evaporation,” *Appl. Surf. Sci.*, 228, 93–99, 2004, doi: 10.1016/j.apsusc.2003.12.028.
- [13] J. Sancho-Parramon, M. Modreanu, S. Bosch, and M. Stchakovsky, “Optical characterization of HfO₂ by spectroscopic ellipsometry: Dispersion models and direct data inversion,” *Thin Solid Films*, 516, 7990–7995, 2008, doi: 10.1016/j.tsf.2008.04.007.
- [14] T. Tan, Z. Liu, and Y. Li, “First-principles calculations of electronic and optical properties of Ti-doped monoclinic HfO₂,” *J. Alloys Compd.*, 510, 78–82, 2012, doi: 10.1016/j.jallcom.2011.08.084.
- [15] E. A. Khera *et al.*, “Structural, electronic and optical properties of transition metal doped Hf_{1-x}TM_xO₂ (TM = Co, Ni and Zn) using modified TB-mBJ potential for optoelectronic memristors devices,” *Optik*, 212, 164677, 2020, doi: 10.1016/j.ijleo.2020.164677.
- [16] Y. Zhu *et al.*, “Anionic defect engineering of transition metal oxides for oxygen reduction and evolution reactions,” *J. Mater. Chem. A*, 7, 5875–5897, 2019, doi: 10.1039/C8TA12477A.
- [17] Y. Liu, W. Wang, X. Xu, J.-P. Marcel Veder, and Z. Shao, “Recent advances in anion-doped metal oxides for catalytic applications,” *J. Mater. Chem. A*, 7, 7280–7300, 2019, doi: 10.1039/C8TA09913H.
- [18] H. S. Jin, T. J. Seok, D.-Y. Cho, and T. J. Park, “Dependence of electrical properties on sulfur distribution in atomic-layer-deposited HfO₂ thin film on an InP substrate,” *Appl. Surf. Sci.*, 491, 83–87, 2019, doi: 10.1016/j.apsusc.2019.06.100.
- [19] Z. Zhang *et al.*, “Improvement of Resistive Switching Performance in Sulfur-Doped HfO_x-Based RRAM,” *Materials*, 14, 3330, 2021, doi: 10.3390/ma14123330.
- [20] H.-K. Kang *et al.*, “Improving Electrical Properties by Effective Sulfur Passivation via Modifying the Surface State of Substrate in HfO₂/InP Systems,” *J. Phys. Chem. C*, 122, 7226–7235, 2018, doi: 10.1021/acs.jpcc.8b00524.
- [21] Y.-F. Zhang, H. Ren, and Z.-T. Hou, “First-principles calculations of electronic and optical properties of F, C-codoped cubic HfO₂,” *J. Magn. Magn. Mater.*, 375, 61–64, 2015, doi: 10.1016/j.jmmm.2014.09.043.

- [22] P. Blaha, “an Augment Plane Wave+ Local Orbitals Program for Calculating Crystal Properties, User’s Guide.” Vienna Austria.
- [23] C. Ambrosch-Draxl and J. O. Sofo, “Linear optical properties of solids within the full-potential linearized augmented planewave method,” *Comput. Phys. Commun.*, 175, 1–14, 2006, doi: 10.1016/j.cpc.2006.03.005.
- [24] J. P. Perdew, K. Burke, and M. Ernzerhof, “Generalized Gradient Approximation Made Simple [Phys. Rev. Lett. 77, 3865 (1996)],” *Phys. Rev. Lett.*, 78, 1396–1396, 1997, doi: 10.1103/PhysRevLett.78.1396.
- [25] F. Tran and P. Blaha, “Accurate Band Gaps of Semiconductors and Insulators with a Semilocal Exchange-Correlation Potential,” *Phys. Rev. Lett.*, 102, 226401, 2009, doi: 10.1103/PhysRevLett.102.226401.
- [26] M. Saeed *et al.*, “First-principles prediction of the ground-state crystal structure of double-perovskite halides $\text{Cs}_2\text{AgCrX}_6$ ($X = \text{Cl, Br, and I}$),” *J. Phys. Chem. Solids*, 160, 110302, 2022, doi: 10.1016/j.jpcs.2021.110302.
- [27] A. Singh, R. Chatterjee, S. K. Mishra, P. S. R. Krishna, and S. L. Chaplot, “Origin of large dielectric constant in La modified $\text{BiFeO}_3\text{-PbTiO}_3$ multiferroic,” *J. Appl. Phys.*, 111, 014113, 2012, doi: 10.1063/1.3675279.
- [28] Z. Cao, T. Fan, X. Hou, J. Niu, R. Sharma, and S. A. Dar, “Evaluation of structural, electronic, thermoelectric, and optical results of C-doped HfO_2 by first-principle’s investigation,” *Int. J. Energy Res.*, 44, 144–157, 2020, doi: 10.1002/er.4878.
- [29] J. T. Mazumder, R. Mayengbam, and S. K. Tripathy, “Theoretical investigation on structural, electronic, optical and elastic properties of TiO_2 , SnO_2 , ZrO_2 and HfO_2 using SCAN meta-GGA functional: A DFT study,” *Mater. Chem. Phys.*, 254, 123474, 2020, doi: 10.1016/j.matchemphys.2020.123474.
- [30] R. Sharma, S. A. Dar, and A. K. Mishra, “Structure, electronic, magnetic and optical properties of cubic $\text{Hf}_{1-x}(\text{TM})_x\text{O}_2$ ($X = 0, 0.25$, $\text{TM} = \text{Mn, Fe, Co, Ni}$): A first principle investigation,” *J. Alloys Compd.*, 791, 983–993, 2019, doi: 10.1016/j.jallcom.2019.03.361.
- [31] H. Chen *et al.*, “Thickness Dependence of Optical Transmittance of Transparent Wood: Chemical Modification Effects,” *ACS Appl. Mater. Interfaces*, 11, 35451–35457, 2019, doi: 10.1021/acsami.9b11816.

Photoluminescence and local electronic structure analysis of pure and Eu^{3+} doped HfO_2

6.1 Introduction

The technological areas of the phosphor-based materials have gathered great attention due to numerous enthralling potential applications such as solid state lighting. The contemporary light emitting diodes (LEDs) have received much attention over the conventional light sources due to their exclusive properties, such as low operating voltage, longer lifetime, compactness, high efficiency, and diverse applicability makes it next generation illumination sources [1, 2]. Researchers also particularly drawn to RE doped luminous materials because of their notable qualities including, high color rendering index (CRI), good color purity, great chemical stability and high luminescence efficiency [3, 4]. The RE doping has the ability to improve electron transport between $4f$ levels and their wavelength ranges from ultraviolet (UV) to infrared (IR) [4]. Numerous oxide-based materials such as TiO_2 , ZrO_2 , HfO_2 have been exploited with the RE doping to enrich the field of luminescence [3, 5, 6].

Along with the development of high-performance devices of this material, the HfO_2 also drawn much research attention for its structural re-adjustments. The HfO_2 exists in the different polymorphs as discussed in Chapter 1. At a higher temperature ($\sim 2600^\circ\text{C}$), the tetragonal phase can also be transformed into cubic phase [7]. Instead of high temperature annealing based phase transformation studies, the monoclinic to cubic phase transformation of HfO_2 has been achieved through yttrium doping at moderate temperatures [8]. Likewise, doping of other aliovalent ions such as Dy^{3+} and Sm^{3+} and isovalent ions such as Ti^{4+} and Zr^{4+} have been reported for stabilizing the cubic or tetragonal phases at lower annealing temperatures ($500^\circ\text{C} - 800^\circ\text{C}$) [6, 9, 10]. It has been observed that formation of oxygen ion vacancies and their coordination with Hf^{4+} cations helped to stabilize the tetragonal and cubic phases when the oversized aliovalent rare earth cations were incorporated in HfO_2 [11]. Eu^{3+} doping effect on the structure modification of HfO_2 have been observed under the temperature variation and a tetragonal phase appears at high temperature [12]. Density functional theory calculations have shown that oversized trivalent ions preferentially stabilize the cubic phase and not the tetragonal phase [13]. Experimental studies have shown mixed results on the formation of

tetragonal and cubic phases with the doping of lanthanides in HfO₂. For example, based on X-ray diffraction (XRD) results, 20% Tb could stabilize the tetragonal phase in HfO₂ thin films [14]. A few studies have been reported on the local bonding arrangement and modification in the crystal system [15, 16]. X-ray absorption spectroscopy (XAS) is commonly used to identify the defect type and formal valence states and local symmetry of dopant ions using X-ray absorption near edge structure (XANES). Intrinsic luminescence has been reported in undoped HfO₂ which ascribed to the oxygen vacancy which acts as luminescence centres in the crystal lattice [17]. The wide band gap and low phonon frequency makes it promising host for doping of RE activator ions [13]. Efforts have been intensified for the PL properties of HfO₂ via doping of RE activator ions such as Sm³⁺, Dy³⁺, Gd³⁺, Pr³⁺, and Er³⁺ which leads to energy transfer between different energy level of host and activator [6, 11, 14, 15, 18]. The RE doped HfO₂ nanocrystals have been found to alter in size and exhibit phase-dependent luminous characteristics at varying temperatures and pH levels [19]. Under the suitable doping condition Eu³⁺ doped amorphous HfO₂ leads to PL due to defects which reside in the crystal sites with inversion centres [16]. It is demonstrated that doping of Sm³⁺ ions in HfO₂ leads to phase transformation and shows the emission in near green and red region [20], whereas Dy³⁺ and Sm³⁺ binary doped HfO₂ nanophosphors shows PL emission in blue, yellow and red region and used as latent finger print imaging application [6].

The present study demonstrates the structure, morphological, XANES, PL response of HfO₂ with varying Eu³⁺ concentration. The phase transformation of HfO₂ powder at lower temperature obtained by chemical co-precipitation method. The effect of phase transition on electronic and optical properties have investigated by XANES and PL. Moreover, a detailed discussion has been provided for the oxygen vacancies and structural phase transition using *first-principles calculations*.

6.2 Experimental and theoretical details

6.2.1 Material synthesis

HfO₂ nanocrystals were synthesised through low temperature chemical co-precipitation method [16]. To synthesis NP's of HfO₂, initially stoichiometric HfCl₄ was dissolved in the DI water upon magnetic stirring. NH₄OH was poured dropwise and pH value of solution was maintained at 7.2 during the synthesis. For the doped samples, Eu³⁺ doping ratio was defined as molar ratio of HfO₂. The stoichiometric proportion of HfCl₄.5H₂O and Eu(CH₃COO)₃.H₂O were weighted and separately dissolved into de-ionized (DI) water with the help of magnetic

stirring for 2 hrs. The temperature was maintained at 120°C during the stirring to avoid intermediate states. After stirring for an hour on hot plate the resulting precipitates were washed with distilled water with the help of centrifuge. The excess salt was discarded and yellow colored precipitate was placed at the heating mantle overnight at 50°C. The dried powder was crushed and placed in the muffle furnace for further annealing at 600°C and 1100°C.

6.2.2 Characterization

Powder X-ray diffraction pattern was obtained using Rigaku Ultima-IV X-Ray diffractometer (Cu-K α , $\lambda = 1.5417 \text{ \AA}$) operated at 8.04 KeV. Photoluminescence and Raman spectra were performed on inVia confocal Raman microscope using 325 nm line of He-Cd laser and 514 nm line of Ar laser respectively in this work. UV-Vis absorption spectroscopy was performed on Indian make RIMS (RIII India) set-up. XANES spectra for the synthesized samples were collected at the soft X-ray beam line of Pohang Accelerator laboratory (PLS-II). Hf L₁-edge XANES were collected at 1 D XRS KIST-PAL beamline, and O K-edge and Eu M_{5,4}-edge XANES spectra were collected at the soft X-ray beam line (10D). PLE and PL spectra for Eu doped HfO₂ samples were measured via employing Horiba spectrophotometer.

6.2.3 Theoretical methodology

The electronic structure calculations of *m*-HfO₂ were performed using DFT based FPLAPW method as implemented in WIEN2k program package [21]. The GGA of PBE [22] and TB-mBJ were used for XC potentials [23]. The GGA approximation underestimate the band gap whereas TB-mBJ potential use semilocal quantities to reproduce well step structures. The muffin tin radii were chosen to be non-overlapping to get better convergence of energy eigen values. Plane wave cutoff was decided by $R_{\text{mt}}K_{\text{max}} = 7$ and convergence criteria for energy and charge was set to 0.0001 Ry/cell. A $17 \times 17 \times 16$ k-points mesh was used which results in 518 k-points in the IBZ. The oxygen vacancies were simulated using a $2 \times 2 \times 2$ supercell of 92 atoms with $10 \times 9 \times 9$ k-points mesh.

The structural optimization of Hf_{1-x}Eu_xO₂ ($x = 0, 0.03, 0.06, 0.07$) in monoclinic and cubic phases were obtained using first-principles method as implemented in VASP [24]. The relaxation was carried out within the parametrization of GGA of PBE [22]. The convergence criteria for self-consistent field energy were set to 10^{-7} eV and the atomic force relaxation was carried out till 0.01 eV/Å. The plane wave cutoff energy of 550 eV and a gamma centered k-mesh of $9 \times 9 \times 7$ was used for the calculations. A $2 \times 2 \times 2$ and $1 \times 1 \times 7$ supercell with 96

and 84 atoms, respectively was constructed to obtain the Eu doping concentrations i.e., 0.03, 0.06, 0.07.

6.3 Results and discussion

6.3.1 Structure analysis

XRD pattern of synthesized HfO₂ at 1100°C, shown in Fig. 6.1. All diffracted peaks resembled with standard reference JCPDS card No. 78–0049, no extra peaks were observed which indicates the high purity of HfO₂. Rietveld refinement of crystal structure was done using the FullProf suite using pseudo Voigt shape function [25]. Rietveld refinement confirmed the monoclinic phase of annealed HfO₂ with space group P2₁/c. The unit cell parameters were found to be a=5.06 Å, b=5.11 Å, c=5.23 Å, β=99.19°. Cell volume for monoclinic phase was found to be 133.85 Å³. Reliability factor which confirms the quality of fit such as weighted profile R factor (R_{wp}), profile R factor (R_p), expected R factor (R_{exp}) are listed in Table 6.1. Average crystallite size is calculated using the Scherrer relation [6]:

$$D = \frac{0.9\lambda}{\beta \cos \theta} \quad (6.1)$$

Where λ is the wavelength of the X-rays, D is the crystallite size, β is the full width at half maximum of the diffraction peak).

The average crystallite size was calculated to be ~ 32.85 nm which confirms the nanometer size particles. Normalised occupancy indicates the presence of Hf and O vacancy.

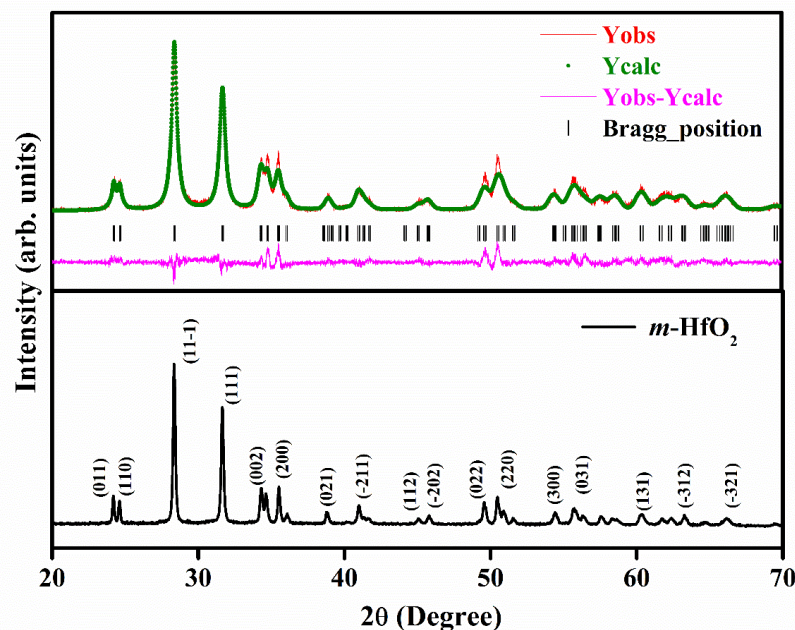


Fig. 6.1: XRD and Rietveld refinement of *m*-HfO₂.

Table 6.1. Refined parameters, convergence indicator (chi square), phase for HfO₂ at 1100°C.

Sample	R _p	R _{wp}	R _{exp}	χ ²	GOF	Phase (in %)	Normalized Occupancy
HfO ₂	15.5	14.0	13.5	1.07	2.09	<i>m</i> – 100	Hf – 0.92 O1 – 0.97 O2 – 1.00

Fig. 6.2 shows the XRD data of HfO₂ samples at 600°C. Fig. 6.2 (a) shows the XRD patterns from HfO₂ sample at 1100°C. Fig. 6.2 (b)-(e) show the XRD patterns of undoped HfO₂, HfO₂:3.0 mol% Eu, HfO₂:5.0 mol% Eu, and HfO₂:7.0 mol% Eu samples, respectively. It was noticeable that the XRD patterns of HfO₂ at 600°C matches with the standard profile of HfO₂ (JCPDS card no. 78-0049) with a monoclinic structured unit cell (space group P2₁/c) with lattice parameters; a = 5.12 Å, b = 5.17 Å, c = 5.29 Å, α = γ = 90° and β = 99.19°. This strengthened the formation of monoclinic phase of HfO₂ at 600 °C. Noticeable changes were seen in the XRD patterns of Eu doped samples. The evolution of a few new peaks at ~ 30.2°, 35.1°, 50.3° and 60° in the HfO₂:3.0 mol% Eu along with the peaks of monoclinic structured HfO₂. The intensity of newly evolved XRD peaks is improved in the HfO₂: 5.0 mol% Eu sample and the intensity of XRD peaks of monoclinic structured HfO₂ was significantly diminished. Eventually, the XRD peaks of monoclinic structured HfO₂ were eradicated and the intensity of peaks at ~ 30.2°, 35.1°, 50.3° and 60° was dominated in the XRD patterns of HfO₂:7.0 mol% Eu sample. The peak position of these newly evolved peaks (~ 30.2°, 35.1°, 50.3° and 60°) was fairly matched with the previously reported XRD patterns of cubic phase of HfO₂ nanoparticles. Likewise, the JCDPF card no. 53-0560 also match with the XRD findings of HfO₂:7.0 mol% Eu sample and convey cubic phase of HfO₂ (space group Fm $\bar{3}$ m a = b = c = 5.105 Å, α = β = γ = 90 °).

For the analysis of the content of phases and more information regarding the XRD pattern of HfO₂ samples. The rietveld refinement analysis was performed using the Fullprof suite with pseudo-Voigt shape function [25]. The rietveld refinement peaks fitted well with the XRD pattern as shown in Fig. 6.3. With increase in the Eu concentration the peaks become more dominant and intense. The rietveld refinement parameters were summarised in Table 6.2.

The calculated crystallite size from HfO₂, HfO₂:3.0 mol% Eu, HfO₂:5.0 mol% Eu, and HfO₂:7.0 mol% Eu samples were observed 32.99 nm, 11.32 nm, 12.69 nm and 13.60 nm, respectively. The slope of W-H plot was used to measure the strain of the all studied samples. The strain for the synthesized HfO₂, 3.0, 5.0 and 7.0 mol% Eu doped HfO₂ samples were found to be 2.76, 8.34, 7.39, 4.52, respectively. The strain was reduced in the samples are having single phase (or nearly the single-phase nature) and leads higher XRD peak intensity. The dislocation density was correlated with the crystallite size as follows:

$$\delta = \frac{1}{D^2} \quad (6.2)$$

where δ is dislocation density and D is the crystallite size. The measured values of δ for HfO₂, 3.0, 5.0 and 7.0 mol% Eu doped HfO₂ samples are 0.0009, 0.007, 0.006, and 0.005, respectively. The structural transformation, monoclinic to cubic phase, may arise due to the substitution of Hf⁴⁺ (ionic radii = 0.078 nm) by the larger sized Eu³⁺ ions (ionic radii = 0.106 nm), which promotes the formation of oxygen vacancies. The strain produced in the lattice, due to larger sized Eu³⁺ ions, may push O²⁻ ions towards the Hf ions leading to Hf-O8 kind of polyhedron formation in the HfO₂:Eu³⁺ compound and leading to alteration in the lattice parameters of the resultant unit cell, which cause the arrangement of ions in the cubic structure [5].

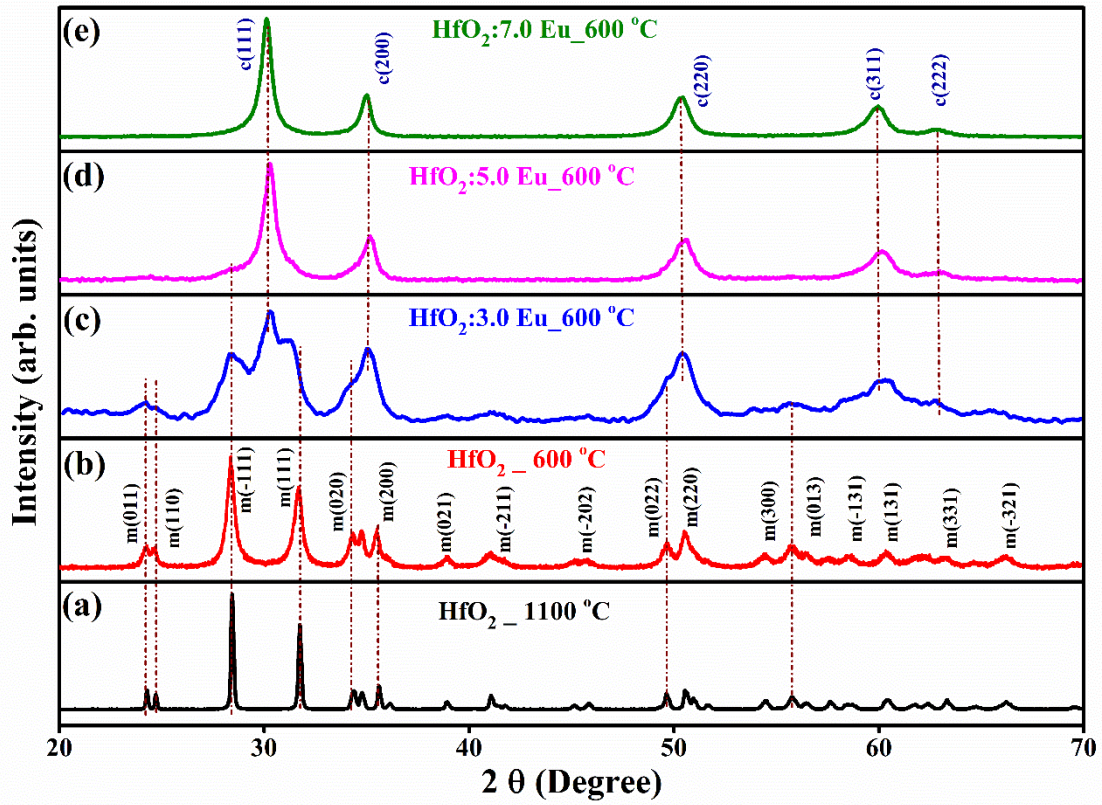


Fig. 6.2: XRD patterns of pure and Eu doped HfO_2 (at 3.0, 5.0 and 7.0 mol%).

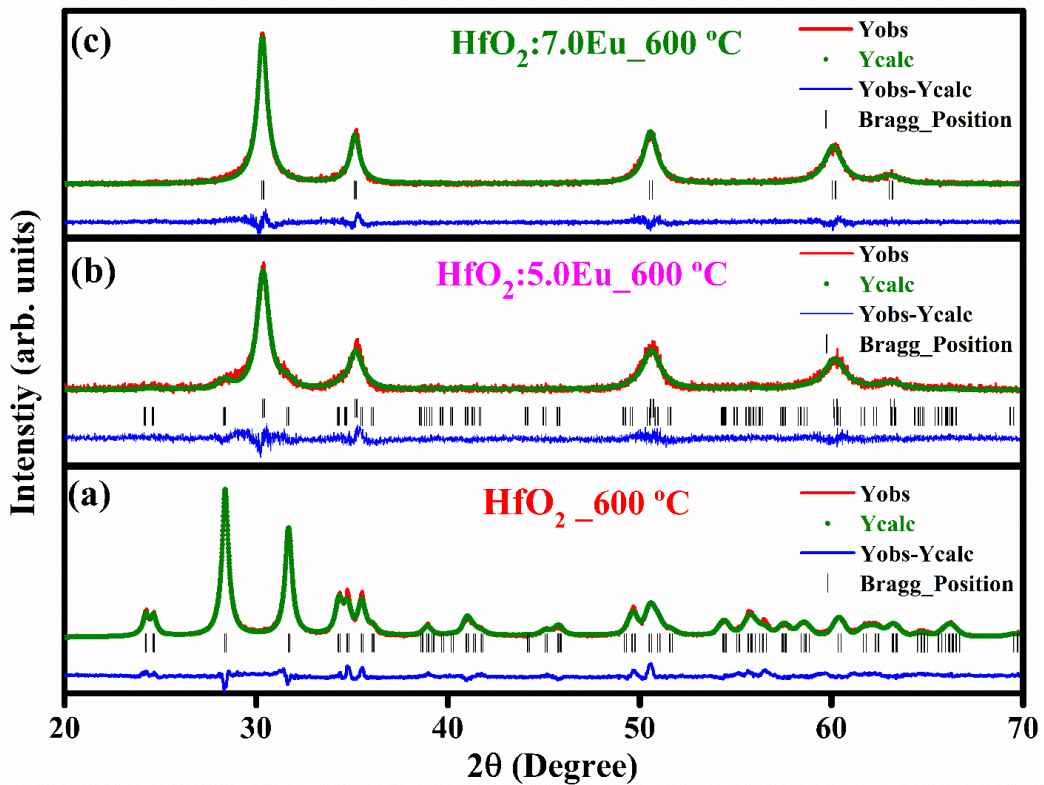


Fig. 6.3: Rietveld refinement of pure and Eu doped HfO_2 (at 5.0 and 7.0 mol%).

Table 6.2. Refined parameters, convergence indicator (chi square) and phase for pure and doped HfO₂.

Sample	R _p	R _{wp}	R _{exp}	χ^2	GOF	Phase (in %)	Normalized Occupancy
HfO ₂	16.0	17.5	16.2	1.26	1.08	<i>m</i> – 100	Hf – 1.04 O1 – 1.22 O2 – 0.98
HfO ₂ : 5.0 Eu	24.6	28.7	26.60	1.17	1.07	<i>c</i> – 96.58 <i>m</i> – 3.42	Hf – 0.95 O1 – 0.97 O2 – 1.12 Eu – 0.05
HfO ₂ : 7.0 Eu	20.1	20.9	18.33	1.29	1.14	<i>c</i> – 100	Hf – 0.93 O1 – 0.92 O2 – 1.07 Eu – 0.07

6.3.2 First-principles study of structural phase transition

The *first-principles* calculations have been used to analyse the effect of doping on the structural phase transition in HfO₂. The calculated atomic positions and cell parameters of monoclinic as well as cubic phases are in good agreement with the experimental findings (Table 6.3). The variation of the total energy vs doping concentration is shown in Fig. 6.4. The crossover point in the energy vs doping concentration is called as transition point (P_T). It clearly shows that Eu doping concentrations up to P_T i.e., 5.11% (close to experimental result of 5%) acquire minimum amount of energy for the *m*-HfO₂ resulting in a stable structure. After P_T , the cubic structure is more stable than monoclinic one. The difference in the energies of monoclinic and cubic phases increases with higher doping concentration. Hence, we theoretically validate the phase transition and stability of cubic phase after P_T which is in excellent agreement with our experimental results.

Table 6.3. Theoretical and experimental lattice parameters of HfO₂.

HfO ₂ phases	Space group	Lattice parameters (in Å)	
		Theoretical	Experimental
Monoclinic	P2 ₁ /c	a = 5.14, b = 5.19, c = 5.33	a = 5.12, b = 5.17, c = 5.29
Cubic	Fm $\bar{3}$ m	a = 5.09	a = 5.104

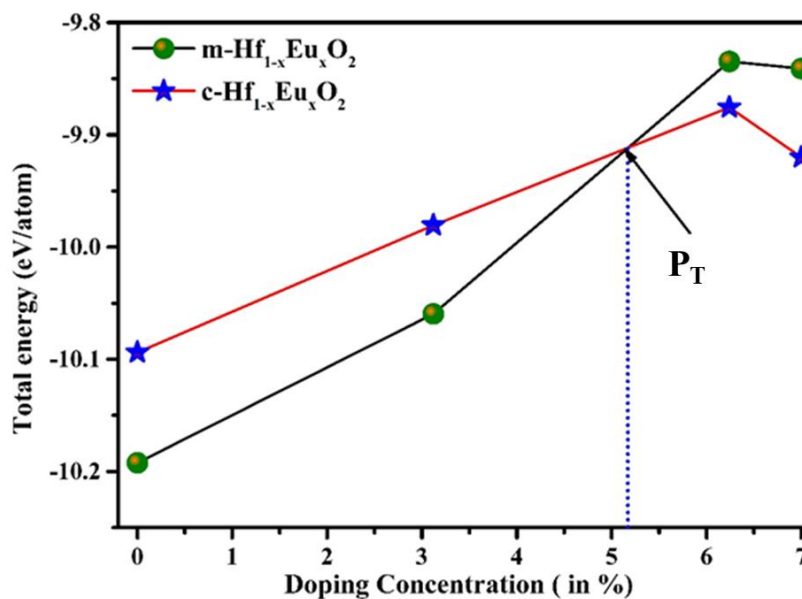


Fig. 6.4: The total energy vs doping concentration of Hf_{1-x}Eu_xO₂ (at 0, 3%, 6% and 7%)

6.3.3 Raman spectroscopy

Vibrational modes of HfO₂ nanoparticles were investigated using Raman spectrum as shown in Fig. 6.5. We observed Raman modes at wavenumbers 108, 136, 149, 164, 244, 258, 324, 335, 381, 398, 498, 522, 550, 582, 642, 673, and 779 cm⁻¹ with most intense peaks at 149cm⁻¹ and 498cm⁻¹. Except the small variation in peak width all the modes have good resemblance with previous reports of monoclinic HfO₂ phase [26–28]. Raman modes from 108 to 324 cm⁻¹ are purely dominant by Hf-Hf bond vibration and remaining modes involves the vibration of oxygen atom with O-Hf and O-O stretching bond [27]. The slight variation occurring in the peak intensity and peak position towards high wave number may be ascribed to the formation of nanostructures leading to phonon confinement. The Raman shift at peak positions 136, 149, 244, 381, 398, 498, 642 and 673 cm⁻¹ show Hf dominant mode which has minimal peak shift and peak broadening, while remaining peak are associated with oxygen atom. Hafnium shows approximately quasiharmonic and oxygen shows anharmonic behaviour [27].

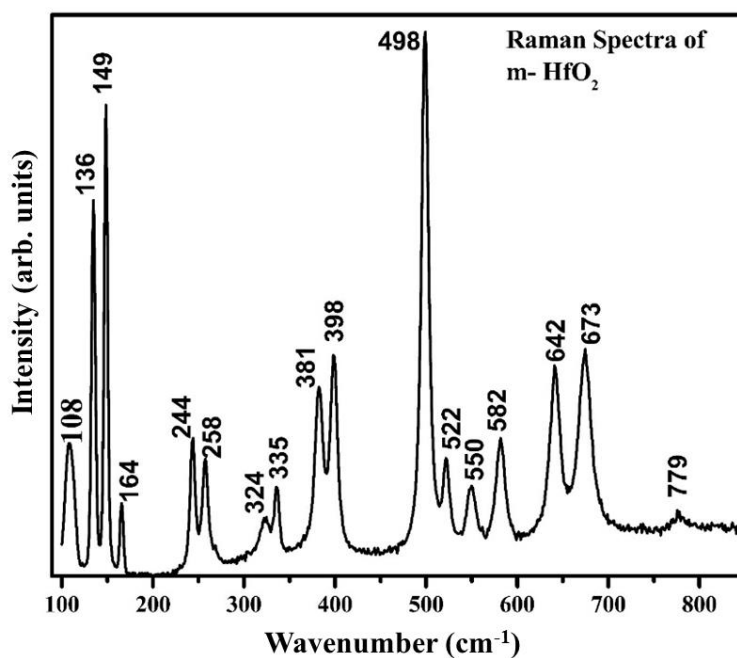


Fig. 6.5: Raman spectra of *m*-HfO₂.

6.3.4 X-ray absorption spectroscopy

Fig. 6.6 shows the O K-edge spectra of HfO₂ and HfO₂:7.0 mol% Eu samples. In previous reports, it has been reported that the cubic phasic CeO₂ and pseudo-cubic HfO₂ and ZrO₂ compounds experience vivid crystal field effects [29, 30]. The dx^2-y^2 and dz^2 orbitals (i.e., e_g orbitals) of metal elements align between the O ligand fields and experience weak interaction on the other hand metal's d_{xy} , d_{xz} , and d_{yz} orbitals (i.e., t_{2g} orbitals) directed towards the oxygen ligands, and experience strong interaction. The ligand field interaction impulses the t_{2g} orbitals at higher energy and the e_g orbitals are placed at lower energy [31]. It is noticeable from the Fig. 6.6 that both of the samples have exhibited two sharp features at 533.8 eV and 538.2 eV for e_g and t_{2g} orbitals, respectively. O K edge spectra of HfO₂ is quite similar to the spectra of bulk HfO₂ with monoclinic crystal structure [30, 32]. In case of monoclinic unit cell of HfO₂, there is no centre of symmetry in M-O₇ (M is metal and O is Oxygen atoms) polyhedra and the different d orbitals interact, uncommonly, with the crystal field of O ligands. In case of monoclinic structured ZrO₂, the orbital degeneracy was uninvolved and resulted complex splitting of d orbitals [30]. The monoclinic phase of HfO₂ has been reported with fragmented e_g and sharp t_{2g} spectral features in the O K-edge XANES spectra. On the other hand, the tetragonal phase of HfO₂ has reported with sharp e_g and splitted t_{2g} features in the O K-edge XANES spectra [32]. The M-O₈ polyhedra also exists in cubic phasic HfO₂ and the crystal field splitting values (i.e., energy separation between e_g and t_{2g} spectral features) remains the

same for both cubic and tetragonal phase of HfO_2 [32, 33]. In the present case the O K-edge of HfO_2 :7.0 mol% Eu sample exhibited the splitting/broadening in the e_g peak (marked by *) and better symmetric t_{2g} spectral feature (within the spectral resolution of used beam line). On the other hand, the HfO_2 :7.0 mol% Eu sample shows the sharp or less splitted e_g spectral feature and broadened t_{2g} feature. This strengthened the monoclinic phase in HfO_2 :7.0 mol% Eu sample and cubic phase in HfO_2 :7.0 mol% Eu sample. XRD results have confirmed the formation of monoclinic phase in HfO_2 :7.0 mol% Eu sample and stabilization of cubic phase in HfO_2 :7.0 mol% Eu sample. Therefore, a difference has been observed in the O K-edge XANES of both of the samples which arises due to the distinct hybridization of frontier orbitals of Hf and O atoms in metal-oxygen polyhedra.

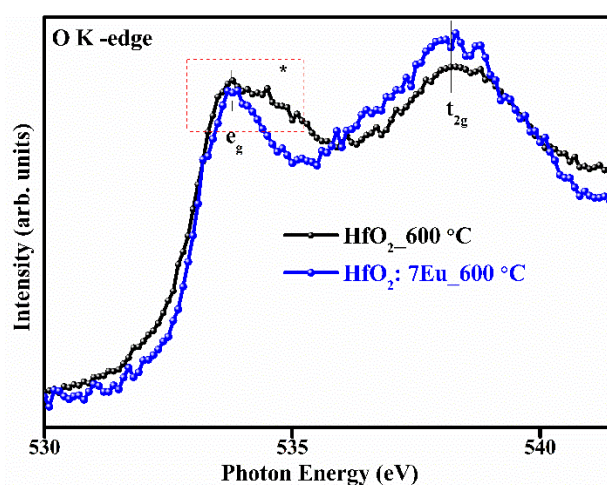


Fig. 6.6: O K-edge XANES spectra of HfO_2 and HfO_2 :7.0 mol% Eu.

The Hf L-edge XANES spectra of HfO_2 , HfO_2 :3.0 mol% Eu, HfO_2 :5.0 mol% Eu, HfO_2 :7.0 mol% Eu samples (Fig. 6.7). The Hf L_1 -edge XANES spectrum arises due to the $2s$ core level transitions to the p -type unoccupied states. In the Fig. 6.7, there is no measurable change in the pre-edge, main edge and post edge features of Eu doped samples. This indicates oxidation state of Hf^{4+} ions and local coordination of Hf and O atoms is not affected under the Eu doping conditions in HfO_2 lattice.

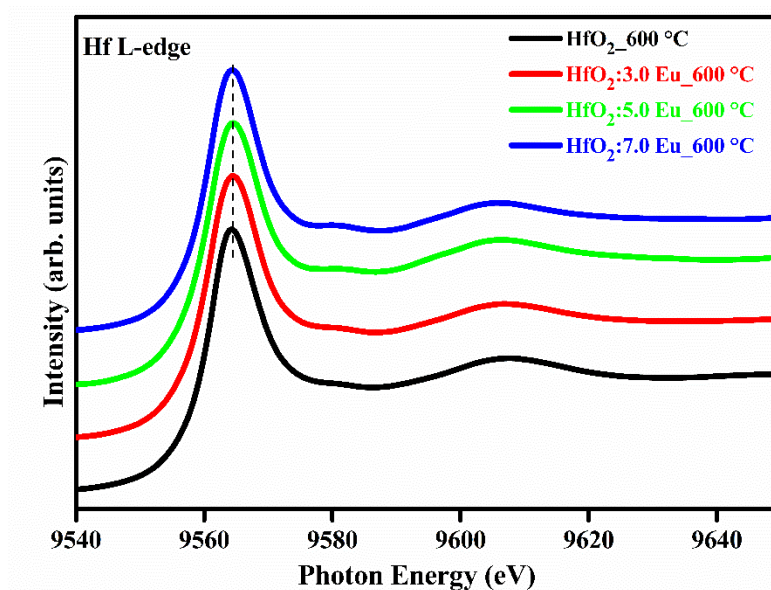


Fig. 6.7: Hf L-edge XANES spectra of HfO₂ and HfO₂: 3.0, 5.0 and 7.0 mol% Eu.

To understand the valence state of Eu ions in HfO₂, the Eu M_{5,4} edge XANES measurements are performed as presented in Fig. 6.8. Reference Eu₂O₃ sample was also scanned under the same conditions for collecting the Eu M_{5,4} edge XANES spectrum. It is noticeable that main spectral features of reference Eu₂O₃ and Eu doped HfO₂ samples are quite similar and showing two intense peaks at ~ 1136 eV and ~ 1164 eV, which are corresponding to the M₅ and M₄ edges, respectively. The M₅ and M₄ edges originate from the Eu 3d_{5/2} and 3d_{3/2} electronic transitions to the 4f states, respectively, and their intensities are proportional to the density of unoccupied 4f states [16]. The energy difference between M₅ and M₄ edges is ~ 28 eV and is consistent with previous reports of Eu³⁺ ions containing sample [16]. A closer view of Fig. 6.8 conveys that the lower Eu concentration doped HfO₂ samples are showing M_{5,4} edge features at lower energy. This indicates that, at lower Eu doping concentrations, the Eu ions may coordinate with oxygen atom with EuO kind of geometry with +2 valence state. However, we have not seen distinct EuO crystalline phases in the XRD data. Therefore, it is anticipated that EuO kind of clusters, if formed, are very diluted in HfO₂ lattice or present in the amorphous form. The M_{5,4} peaks of higher concentration Eu doped HfO₂ sample are fairly matched with the spectral features of reference Eu₂O₃ sample and confirm the dominant Eu³⁺ ions in HfO₂:7 mol% Eu sample.

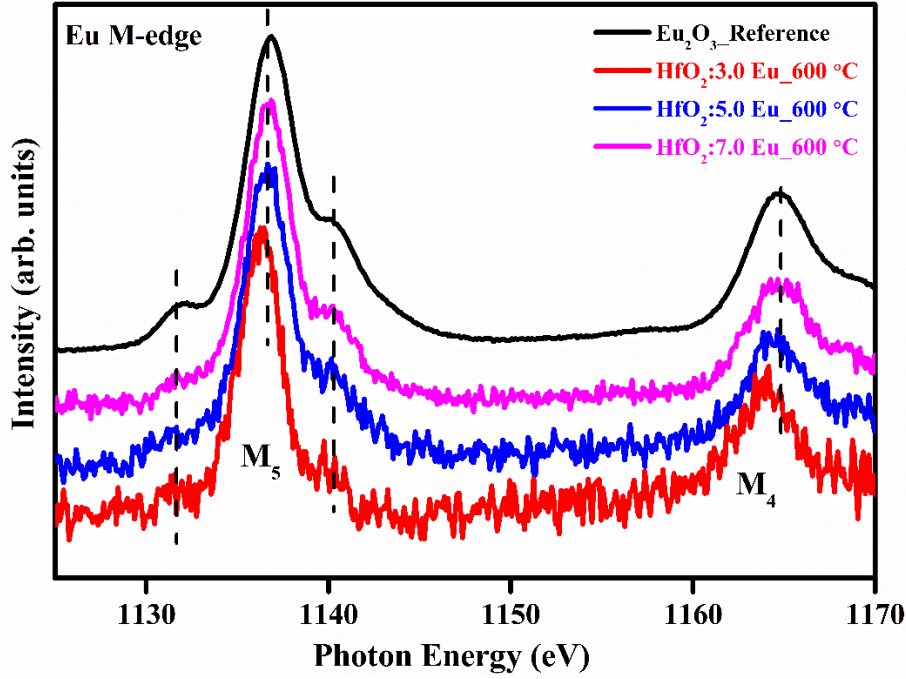


Fig. 6.8: Eu $M_{5,4}$ -edge XANES spectra of 3.0, 5.0 and 7.0 mol% Eu doped HfO_2 .

6.3.5 Band gap analysis

The experimental band gap of HfO_2 nano particles was estimated using UV-Vis absorption spectroscopy. The optical absorption is mainly attributed to the transmission of the electrons from valance band to the conduction band. Fig. 6.9 (a) shows the absorption spectrum of $m\text{-HfO}_2$ which shows the fundamental absorption edge in the short UV region. According to Wood and Tauc, the E_g associated with the absorbance and photon energy is given by:

$$(\alpha h\nu) = \beta (h\nu - E_g)^m \quad (6.3)$$

where α is absorbance, h is Planck's constant, ν is the frequency, E_g is the optical band gap, m is a constant assign to the different electronic transitions as $m=1/2, 2, 3, 2/3$ for direct allowed, indirect allowed, indirect forbidden, direct forbidden transitions, respectively. The band gap can be obtained from the extrapolation of the straight line portion of $(\alpha h\nu)^m$ vs $h\nu$ plot to $h\nu=0$. Monoclinic HfO_2 being indirect band gap material and thus band gap was calculated using $m=2$ and extrapolating the linear portion of the curve tail as shown in Fig. 6.9 (b). Estimated band gap in $m\text{-HfO}_2$ is 5.71eV which is moderately higher and also in close agreement with previous studies [34–36]. In $m\text{-HfO}_2$ a small shoulder like structure also appears near the band edge of band gap. The shoulder feature may be ascribed to oxygen vacancy in the crystal lattice or shifting of Hf-O bond length. Without affecting the lattice structure, the small variation of Hf-

O bond length may create a perturbed potential and influence the optical and electronic band properties, resulting in shoulder formation [37].

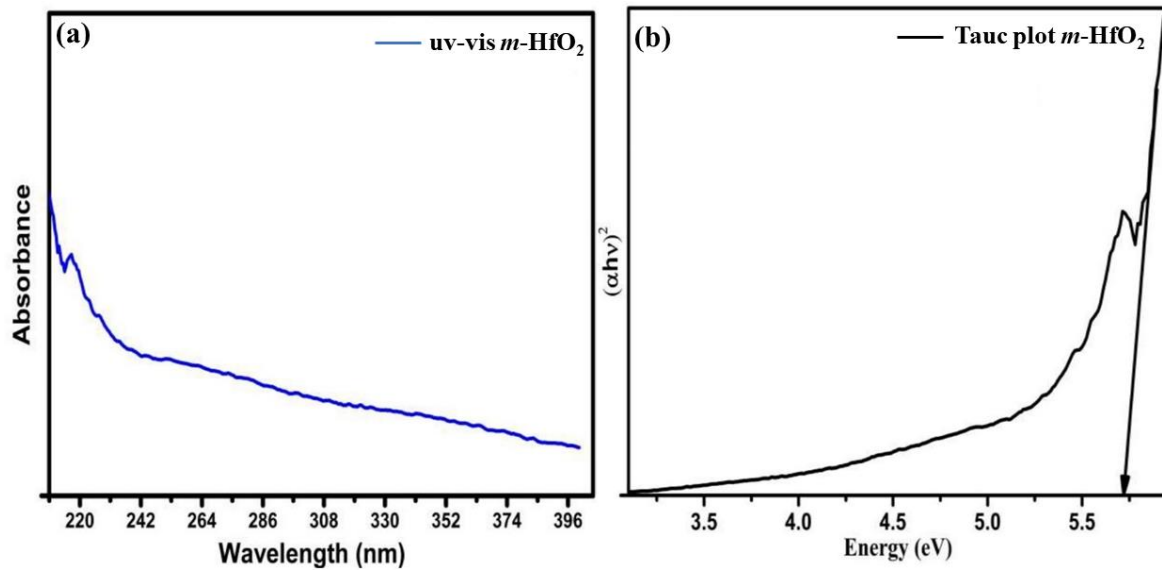


Fig. 6.9: (a) Absorbance spectrum and (b) Tauc plot for *m*-HfO₂.

6.3.5.1 Theoretical analysis of band gap

For theoretical insights of band gap, study, we performed DFT calculations using the experimentally determined unit cell parameters. The band structures and DOS of the pristine *m*-HfO₂ calculated with GGA and TB-mBJ are shown in Fig. 6.10 (a, b). It is evident that the both the approximations predict maxima of valance band E_v lying at the high symmetry Gamma point (Γ) of the Brillouin zone and conduction band minima E_c lying at the high symmetry X point of Brillouin zone which results in an indirect band gap along Γ -X direction. The value of band gaps is listed in Table 6.4. As mentioned earlier, the value of band gap (4.1 eV) predicted with GGA approximation is quite smaller in comparison to the experimental determined value (5.71 eV), whilst the TB-mBJ predicted band gap (5.78 eV) is in excellent agreement with the experimental value, however with slight overestimation.

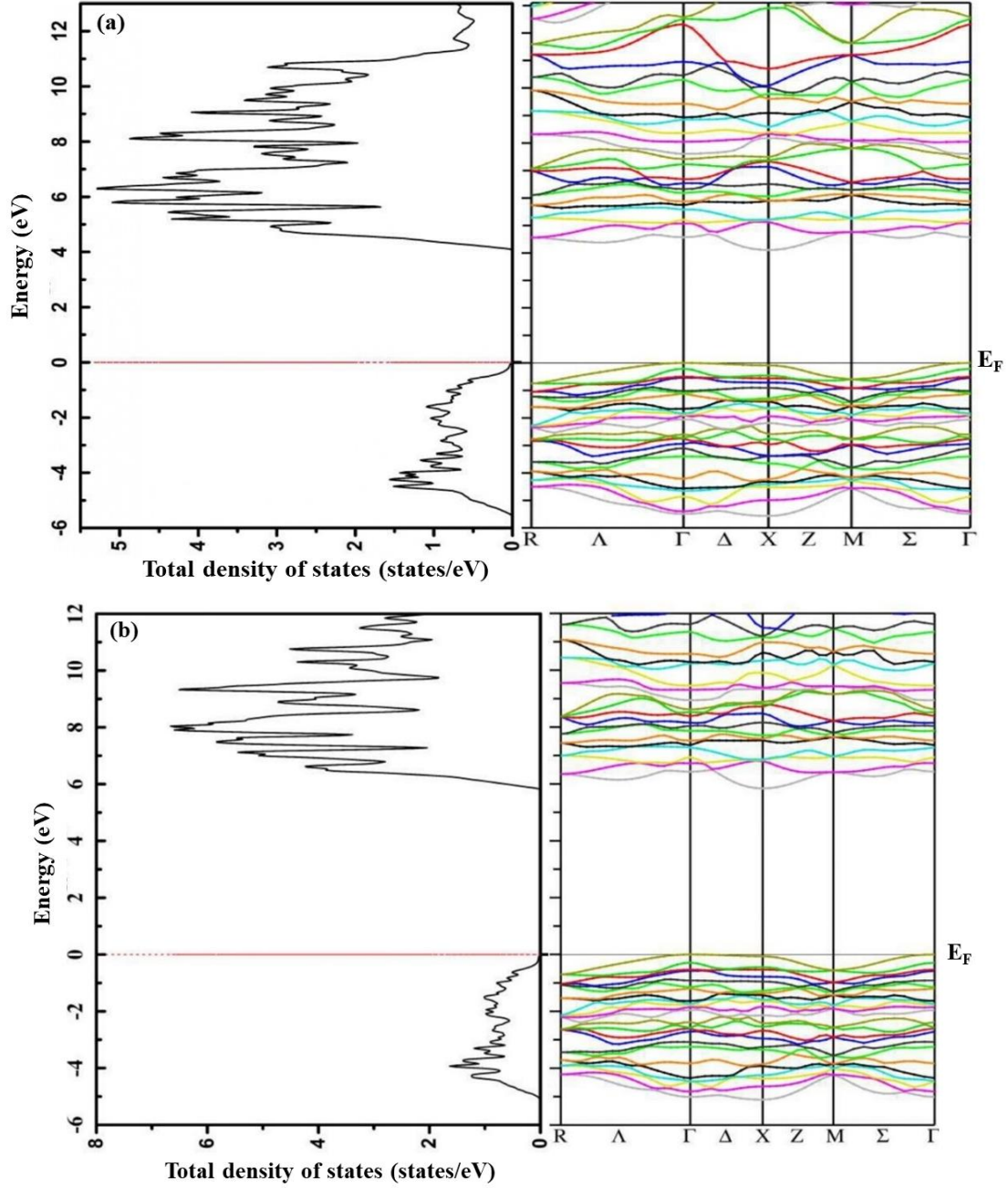


Fig. 6.10: Band structure of $m\text{-HfO}_2$ using (a) GGA and (b) TB-mBJ approach (E_F is shifted to 0 eV).

To gain the more insight of electronic structure of $m\text{-HfO}_2$ we explored the partial density of state of $m\text{-HfO}_2$, using GGA and TB-mBJ potentials, as shown in Figure 6.11 (a, b). The qualitative features of DOS calculated using both the approaches are quite similar. Therefore, here we are presenting the details analysis using TB-mBJ only. The low-lying states are mainly composed of $O\text{-}p$ states with a very feeble contribution from $Hf\text{-}d$ states. Except a small peak at around -10 eV, a high-density valence band gages from ~ -5.0 eV to 0 eV (which

corresponds to Fermi energy here). The conduction band, on the other hand, is dominated by *Hf-d* states with a weak presence of *O-p* states which shows a hybridization between *Hf-d* states and *O-p* states.

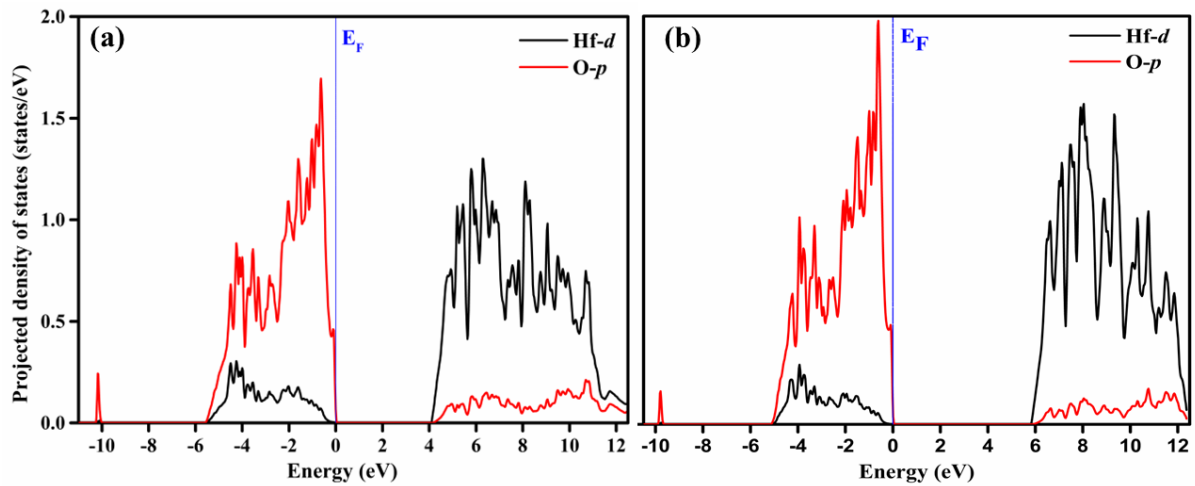


Fig. 6.11: Projected density of states of *m*-HfO₂ using (a) GGA approach and (b) TB-mBJ approach (E_F is shifted to 0 eV).

6.3.6 Photoluminescence

6.3.6.1 Photoluminescence study of pure HfO₂:

The effect of defect states observed from the above discussed results, are also observed in PL spectrum. Upon excitation of pristine HfO₂ at 325 nm, the broad PL spanning in the range 350-700 nm is observed, as shown in Fig 6.12. The overall emission is fall in the warm white region, as seen from the Commission International de l'Éclairage (CIE) coordinate diagram (inset fig. 6.12). In this phase the dominant emission appears at 450 nm (2.75 eV), 536 nm (2.31 eV) and 562 nm (2.20 eV) corresponding to blue, green and yellow regions respectively. The emission is indicating towards active role of defect states in imparting the broad luminescence. Researchers have earlier experimentally shown the presence of oxygen vacancy related radiative defect states in HfO₂ thin film [17]. The electrons are captured in these oxygen vacancies and lead to the formation of ionized oxygen vacancy centers. Single and doubly charged vacancy leads to trap extra electron which is polaronic in nature. On the vacancy site, the trapped electron doesn't fit in vacancy space rather they distributed over nearest Hf atom [38], leading to the broad PL spectrum. It is seen that two types of oxygen vacancies exist in *m*-HfO₂ named as 3-fold (O3) and 4-fold (O4) because each oxygen atom is surrounded by 3 Hf atoms and 4 Hf atom, respectively. The removal of oxygen atoms leads to the structural

relaxations of the nearest-neighbour Hf ions surrounding the vacancy which leads to the lower energy configuration corresponding to defect states which is verified by our calculations. As the doubly O-vacancy lowers the band gap up to 0.60 eV and 0.39 eV in case of O3 and O4, respectively, the observed PL spectra in *m*-HfO₂ cannot be explained using doubly O-vacancy as discussed in following text. So, here we only concentrate on single O-vacancies. It has been found that the defect states corresponding to O4 vacancy is more stable than the O3 vacancy. The total density of states corresponding to these vacancies is depicted in Fig. 6.13 (a). The conduction band minima, in case of O3 single vacancy, is red-shifted at 2.27 eV and at 2.18 eV in case of O4 single vacancy which results in decrease of energy band gap. As the TB-mBJ approach predicts the accurate band gap, near to experimental value, this probably increases the accuracy with which it envisages the defect states. According to our calculations the PL peaks (shown in Fig. 6.12) corresponding to 562 nm, 536 nm and 450 nm wavelength are attributed to O4 single vacancy. These peaks are correlated with total density of states as shown in Fig. 6.13 (b). First peak arises at 563 nm, second at 534 nm, and third at 476 nm which are in close agreement with our experimental observation.

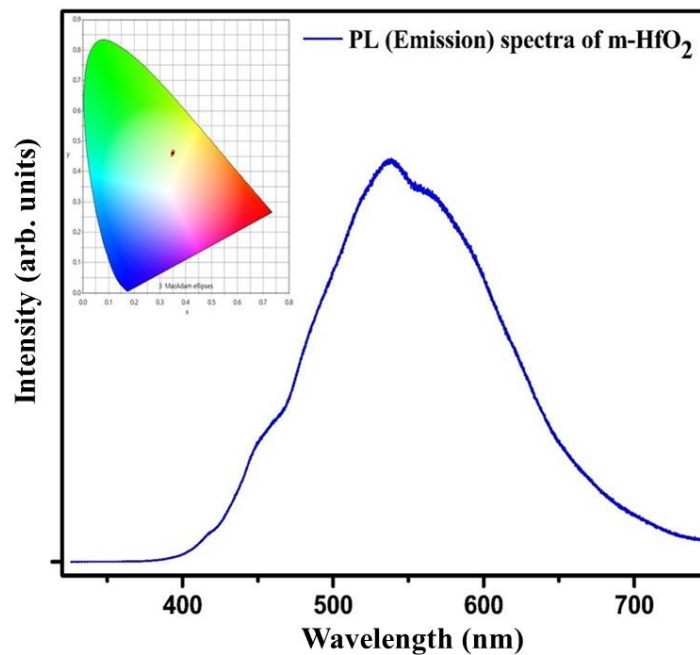


Fig. 6.12: PL emission spectrum and CIE plot (inset) of *m*-HfO₂.

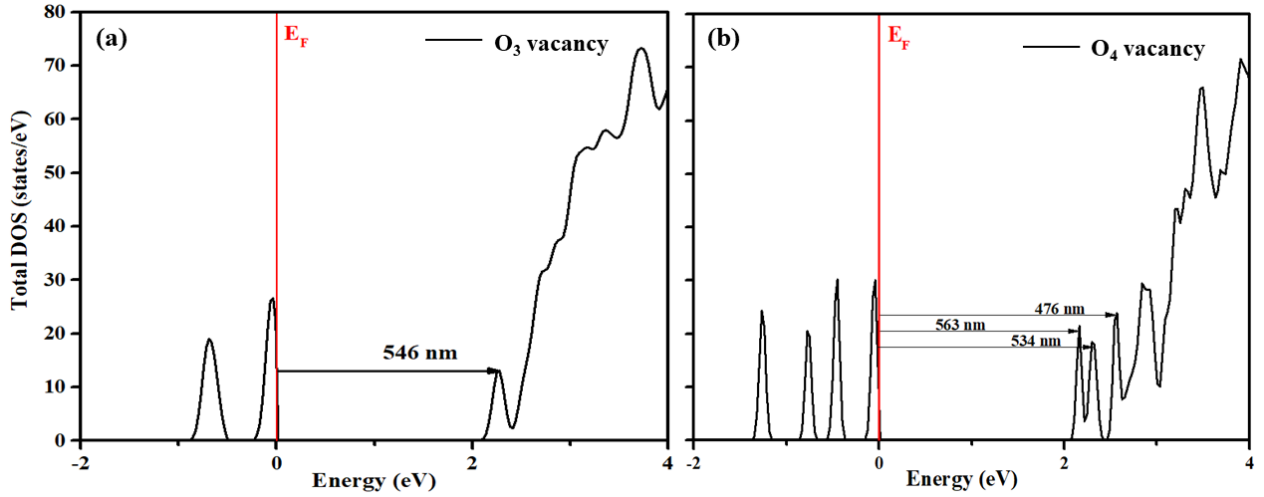


Fig. 6.13: Total density of states of *m*-HfO₂ with (a) three and (b) four-fold single oxygen vacancy using TB-mBJ (E_F is shifted to 0 eV).

6.3.6.2 Photoluminescence study of Eu^{3+} doped HfO_2

The photoluminescence excitation (PLE) spectra for HfO₂ doped with varying Eu^{3+} ion concentrations were measured at room temperature in the spectral wavelength range from 325 to 550 nm by monitoring 611 nm emission wavelength as demonstrated in Fig. 6.14. The PLE spectra consists of several excitation peaks related to f-f electronic transitions located at 331, 361, 383, 394, 414, 465 and 532 nm initiating from ground energy level (7F_0) to various excited energy levels such as 5H_3 , 5D_4 , 5G_2 , 5L_6 , 5D_3 , 5D_2 and 5D_1 of Eu^{3+} ions, respectively. Among all these excitation peaks, the sharp intense excitation peak was observed at 394 nm corresponds to $^7F_0 \rightarrow ^5L_6$ transition, which well matches the emission profile of the n-UV LED chip. The various excitation peaks, including 361, 383, 394 and 465 nm were opted to record the emission spectral profiles of Eu^{3+} doped HfO₂ samples.

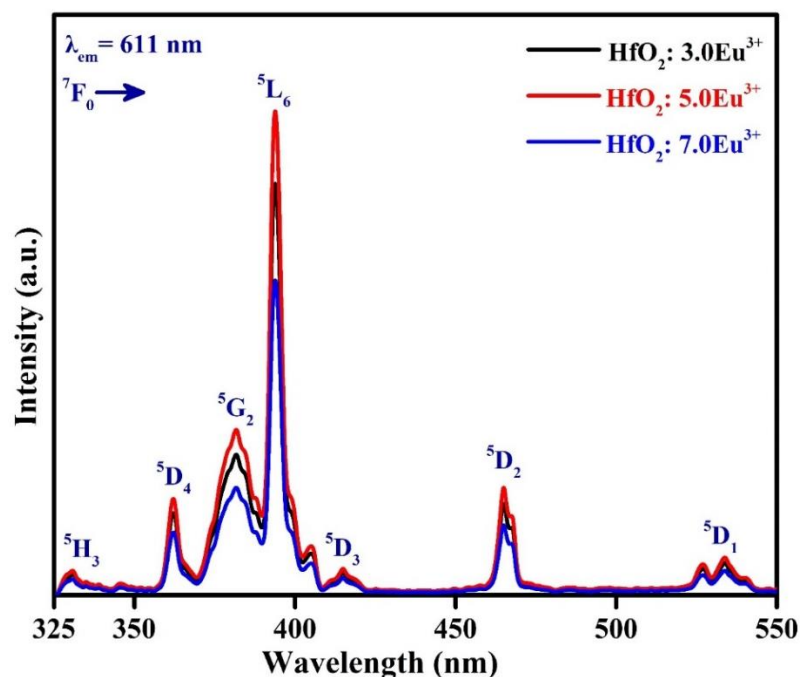


Fig. 6.14: Photoluminescence excitation spectra for HfO₂ doped with varying Eu³⁺ ion concentrations under 611 nm emission wavelength.

The emission spectra of HfO₂ with varying Eu³⁺ ion concentrations were observed in the 375-750 nm spectral range by monitoring the excitation wavelength of 275 nm presented in Fig. 6.15. Also, the emission spectra for HfO₂ doped with differing Eu³⁺ ion concentrations were measured in the wavelength region from 550 to 750 nm at room temperature under various excitation wavelengths, including 361, 383, 394 and 465 nm, respectively as shown in Fig. 6.16 (a)-(d). Using above mentioned different excitations, the emission spectra of Eu³⁺ doped HfO₂ samples reveal that several emission peaks starting from higher energy excited level (⁵D₀) to various lower energy levels such as ⁷F_J (where J = 0, 1, 2, 3 and 4), which represents the emission peak observed at 578, 587, 611, 654 and 710 nm, respectively. A minute variation in the emission peak intensity with varying the different excitation wavelengths was noticed. The emission peak observed at 611 nm corresponds to the ⁵D₀ → ⁷F₂ transition and was highly intense as compared to other emission peaks, which ascribed to forced electric dipole (ED) transition. The forced ED transition is hypersensitive in behaviour and obeys the following selection rule such as ΔJ = 2 [32, 33]. Furthermore, the emission intensity of the ⁵D₀ → ⁷F₂ transition remains dominant through the crystal field strength of the local environment [39, 40]. The emission peak located at 587 nm corresponds to the ⁵D₀ → ⁷F₁ transition was a magnetic dipole (MD) transition in behaviour and following the Laporte selection rule such as ΔJ = 1, which ascribed to the insensitive to the crystal field environment of the Eu³⁺ ions in the

synthesized samples [40]. The emission intensity ratio of ED ($^5D_0 \rightarrow ^7F_2$) to MD ($^5D_0 \rightarrow ^7F_1$) is referred to as the asymmetric fraction, which explains the degree of distortion concerning the inversion symmetry of the Eu^{3+} ions. In the present work, the emission intensity of ED transition was greater than the emission intensity of MD transition, which indicates the presence of Eu^{3+} ions at sites without inversion symmetry. The emission intensity varies with Eu^{3+} ion concentrations in the synthesized samples as shown in inset Fig. 6.16 (a)-(d). As increasing the Eu^{3+} concentration in the synthesized samples from 3.0 mol% to 5.0 mol%, the emission intensity increases and beyond that the emission intensity decreases with an increase in the concentration of Eu^{3+} ions up to 7.0 mol%. This behaviour occurs because of concentration quenching phenomena. The quenching phenomena can be taken place owing to a decrease in the distance between the dopant (Eu^{3+}) ions, which increases the non-radiative energy transfer (NRET) and multipolar interaction or resonant energy transfer (RET). The optimal dopant ion concentration in Eu^{3+} doped HfO_2 samples was discovered to be 5.0 mol%.

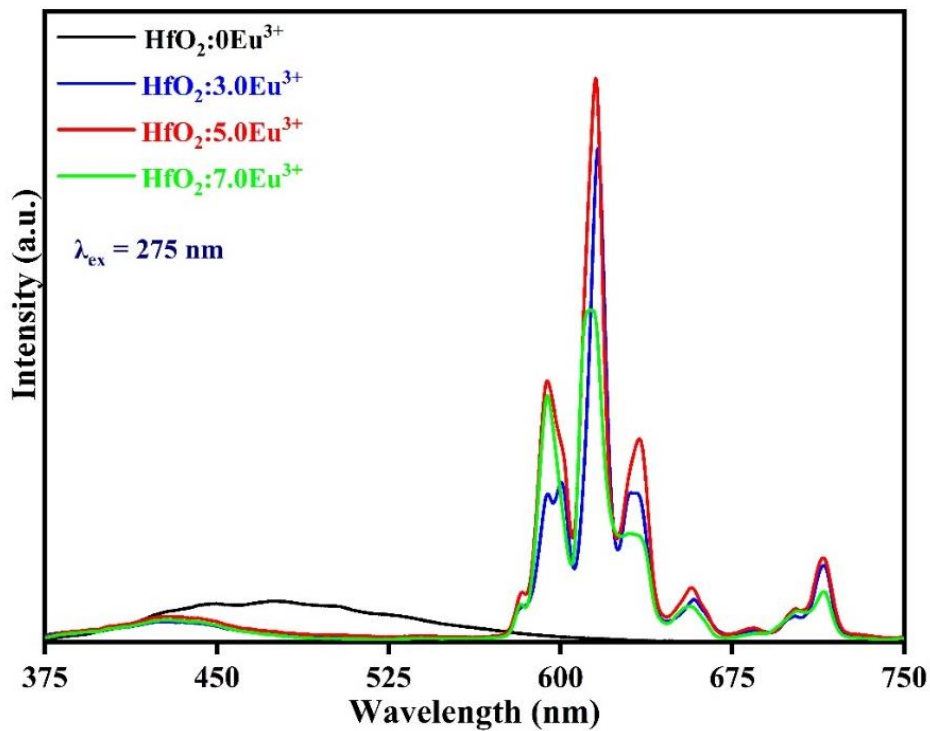


Fig. 6.15: Emission spectra of Eu^{3+} doped HfO_2 samples pumping under excitation wavelength of 275 nm.

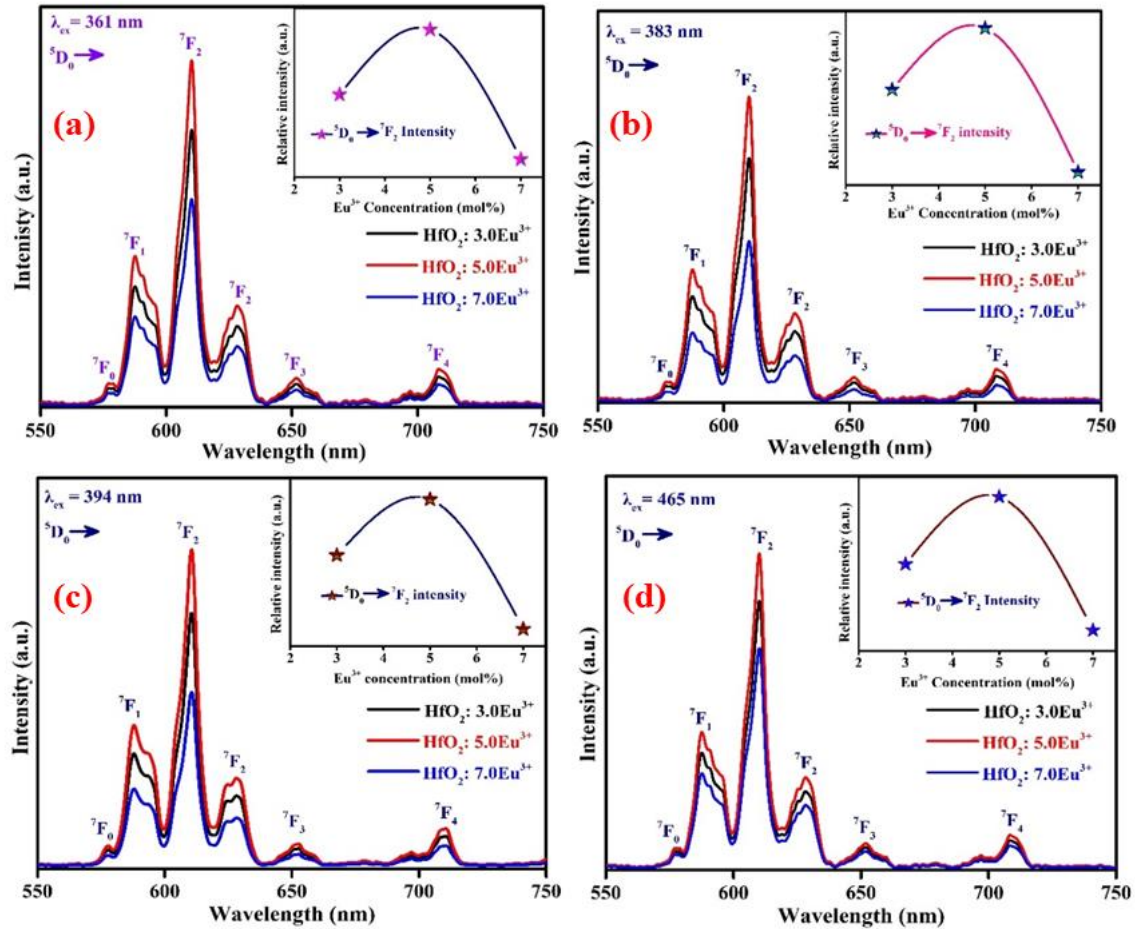


Fig. 6.16: Emission spectra of Eu^{3+} doped HfO_2 samples pumping under various excitation wavelengths, including 361 nm, 383 nm, 394 nm and 465 nm.

Furthermore, the partial energy level diagram that includes excitation and emission as well as possible some other type of non-radiative transition (NRT) of Eu^{3+} doped HfO_2 sample are presented in Fig. 6.17. By absorbing the specific photon energy, the Eu^{3+} ions at ground energy level (${}^7\text{F}_0$) were excited to the higher energy level (${}^5\text{L}_6$) of Eu^{3+} ions. The excited Eu^{3+} ions have been de-excited by emitting the phonon or photon via NRT before carrying out the downward radiative transitions, including ${}^5\text{D}_0 \rightarrow {}^7\text{F}_J$ ($J = 0, 1, 2, 3$ and 4) of Eu^{3+} ions.

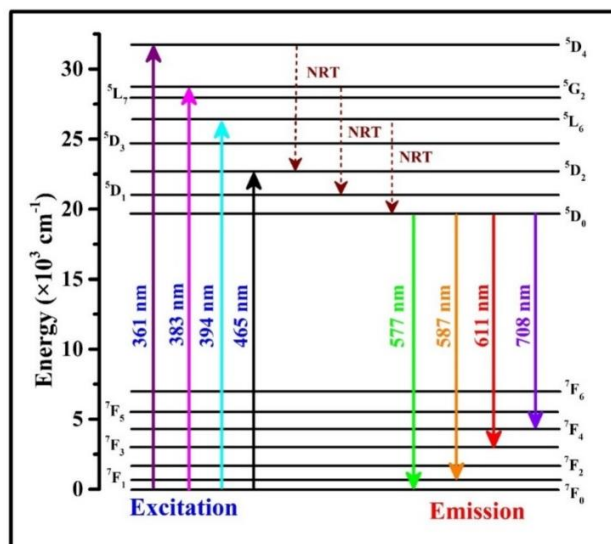


Fig. 6.17: Partial energy level diagram of Eu^{3+} doped HfO_2 samples.

6.3.6.3 Estimation of CIE coordinates, correlated color temperature (CCT) and color purity

The Commission International de l'Éclairage (CIE) 1931 parameters like (x, y) color coordinates, CCT values may be calculated via employing the emission data to understand the colorimetric features of the prepared samples. To reveal the color tone of the emission, the calculated color coordinates were represented on the CIE 1931 graph. The calculated color coordinates shown in the CIE chromaticity graph for 5.0 mol% Eu^{3+} doped HfO_2 sample (i.e., optimized 5.0 mol% doped) excited along with different wavelengths, including 361 nm, 383 nm, 393 nm and 465 nm situated in the reddish region (shown in Fig. 6.18).

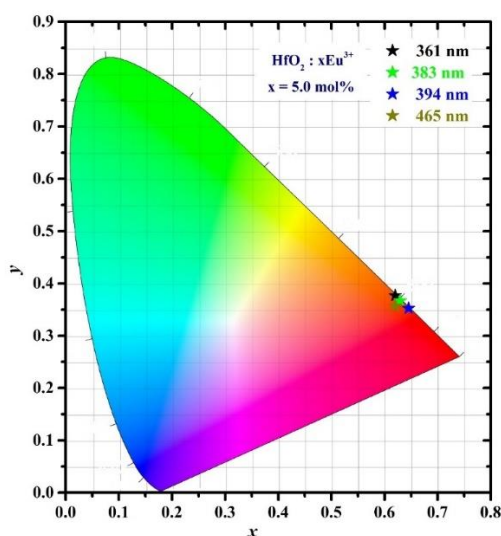


Fig. 6.18: CIE chromaticity diagram for optimized $\text{HfO}_2:5.0 \text{ mol}\% \text{Eu}^{3+}$ sample under various excitation wavelengths, including 361 nm, 383 nm, 394 nm and 465 nm.

The estimated color coordinates for optimized HfO₂:5.0 mol% Eu³⁺ were found close to the standard National television Standard Committee (NTSC) and the red-emitting commercial phosphors. Furthermore, the CCT is a crucial parameter that reveals the distinct color of the light emitted by the luminous components and estimated in kelvin (K). The McCamy empirical relation has been used to compute the CCT values for HfO₂: xEu³⁺ samples [41];

$$CCT = -449n^3 + 3525n^2 - 6823n + 5520.3 \quad (6.4)$$

in above relation $n = \frac{x-X_e}{Y-Y_e}$; $X_e = 0.332$ and $Y_e = 0.186$ is the epicentre, respectively. The estimated CCT for optimized 5.0 mol% Eu³⁺ doped HfO₂ sample was found to be 1221 K, 1225 K, 1232 K and 1224 K under different excitation wavelengths. The estimated CCT values for the optimized HfO₂: xEu³⁺ (x = 5.0 mol%) samples are below 4000 K signifying the aptness of HfO₂: 5.0 mol% Eu³⁺ sample for warm lighting applications. The CP of the as-synthesized HfO₂: xEu³⁺ samples have been evaluated from the given relation below [41]:

$$CP = \frac{\sqrt{(x-x_{ee})^2+(y-y_{ee})^2}}{\sqrt{(x_d-x_{ee})^2+(y_d-y_{ee})^2}} \quad (6.5)$$

in the above relation, (x, y) (x_{ee}, y_{ee}) and (x_d, y_d) shows the chromaticity coordinates, equal energy point and dominant wavelength of as-synthesized samples, respectively. The CP for the optimized 5.0 mol% Eu³⁺ doped HfO₂ sample was found to 97.2 %, 97.8 %, 98.5 % and 98.1% under different excitation wavelengths. Hence, the aforementioned results show that the direct utility of Eu³⁺ doped HfO₂ samples may be a suitable candidate for the red emitting element for photonic device applications.

6.4 Conclusion

Single phase monoclinic and cubic HfO₂ nanocrystals successfully synthesized using the chemical co-precipitation method. XRD analysis confirms the pure monoclinic phase formation at 600 °C and 1100 °C. At low temperature the XRD results revealed a mixed phase formation at lower concentration and a dominant cubic phase achieved at 5 mol% doping of Eu³⁺ in HfO₂. The phase transition was also confirmed by theoretical study which revealed the transition ~ 5.11 mol% doping concentration. X-Ray absorption spectra was used to identify the oxidation state of Eu ions in the HfO₂. The Eu³⁺ ions are dominantly present in the Eu-doped HfO₂ samples. The magnitude of band gap estimated by experimental and *first-principles calculations* was in good agreement. The *m*-HfO₂ shows broad photoluminescence

in warm white towards yellowish region upon 325 nm excitation, which may be assigned to 4-fold (O_4) vacancies as predicted by *first principles calculations*.

The PL study of $Hf_{1-x}O_2: xEu^{3+}$ demonstrates the emission in red region with high color purity under different excitation wavelengths from near UV to blue light. PL emission spectra show four emission bands at 594 nm, 609 nm, 650 nm, and 716 nm corresponding to $4f \rightarrow 4f$ transitions of Eu^{3+} under excitation wavelengths of 361 nm, 383 nm, 394 nm and 465 nm. The reddish PL emission with high color purity under different excitation wavelengths from near-UV to blue region may be exploited in solid state lighting-based applications.

References

- [1] J. Sun, X. Zhang, Z. Xia, and H. Du, "Luminescent properties of $LiBaPO_4:RE$ ($RE = Eu^{2+}$, Tb^{3+} , Sm^{3+}) phosphors for white light-emitting diodes," *J. Appl. Phys.*, vol. 111, 013101, 2012, doi: 10.1063/1.3673331.
- [2] Z. Wang, J. Ha, Y. H. Kim, W. B. Im, J. McKittrick, and S. P. Ong, "Mining Unexplored Chemistries for Phosphors for High-Color-Quality White-Light-Emitting Diodes," *Joule*, 2, 914–926, 2018, doi: 10.1016/j.joule.2018.01.015.
- [3] K. R. V. Babu, C. G. Renuka, R. B. Basavaraj, G. P. Darshan, and H. Nagabhushana, "One pot synthesis of $TiO_2:Eu^{3+}$ hierarchical structures as a highly specific luminescent sensing probe for the visualization of latent fingerprints," *J. Rare Earths*, 37, 134–144, 2019, doi: 10.1016/j.jre.2018.05.019.
- [4] Manju *et al.*, "Charge transfer-induced fast blue emission in $SrZnO_2:Ce$," *Appl. Phys. Lett.*, 119, 121108, 2021, doi: 10.1063/5.0064383.
- [5] L. X. Lovisa *et al.*, "White photoluminescence emission from ZrO_2 co-doped with Eu^{3+} , Tb^{3+} and Tm^{3+} ," *J. Alloys Compd.*, 674, 245–251, 2016, doi: 10.1016/j.jallcom.2016.03.037.
- [6] S. Kumar, T. Dehury, and C. Rath, "Stabilization of Cubic Phase at Room Temperature and Photoluminescence Properties of Dy and Sm Co-Doped HfO_2 Nanoparticles," *ECS J. Solid State Sci. Technol.*, 10, 081009, 2021, doi: 10.1149/2162-8777/ac1c54.
- [7] T. Tobase *et al.*, "Pre-Transitional Behavior in Tetragonal to Cubic Phase Transition in HfO_2 Revealed by High Temperature Diffraction Experiments," *Phys. Status Solidi B*, 255, 1800090, 2018, doi: 10.1002/pssb.201800090.

- [8] N. Kumar, B. P. A. George, H. Abrahamse, V. Parashar, S. S. Ray, and J. C. Ngila, “A novel approach to low-temperature synthesis of cubic HfO₂ nanostructures and their cytotoxicity,” *Sci. Rep.*, 7, 9351, 2017, doi: 10.1038/s41598-017-07753-0.
- [9] T. Song *et al.*, “Stabilization of the Ferroelectric Phase in Epitaxial Hf_{1-x}Zr_xO₂ Enabling Coexistence of Ferroelectric and Enhanced Piezoelectric Properties,” *ACS Appl. Electron. Mater.*, 3, 2106–2113, 2021, doi: 10.1021/acsaelm.1c00122.
- [10] S. Pokhriyal and S. Biswas, “Tuning of dielectric properties in Ti-Doped granular HfO₂ nanoparticles for high-k applications,” *Ceram. Int.*, 48, 11199–11208, 2022, doi: 10.1016/j.ceramint.2021.12.340.
- [11] F. H. Borges, D. S. Da Hora Oliveira, G. P. Hernandez, S. J. Lima Ribeiro, and R. R. Gonçalves, “Highly red luminescent stabilized tetragonal rare earth-doped HfO₂ crystalline ceramics prepared by sol-gel,” *Opt. Mater. X*, 16, 100206, 2022, doi: 10.1016/j.omx.2022.100206.
- [12] E. R. Andrievskaya, “Phase equilibria in the refractory oxide systems of zirconia, hafnia and yttria with rare-earth oxides,” *J. Eur. Ceram. Soc.*, 28, 2363–2388, 2008, doi: 10.1016/j.jeurceramsoc.2008.01.009.
- [13] C.-K. Lee, E. Cho, H.-S. Lee, C. S. Hwang, and S. Han, “First-principles study on doping and phase stability of HfO₂,” *Phys. Rev. B*, 78, 012102, 2008, doi: 10.1103/PhysRevB.78.012102.
- [14] E. Montes *et al.*, “Thermoluminescent characterization of HfO₂:Tb³⁺ synthesized by hydrothermal route,” *Appl. Radiat. Isot.*, 83, 196–199, 2014, doi: 10.1016/j.apradiso.2013.06.008.
- [15] M. Nand *et al.*, “Different polymorphs of Y doped HfO₂ epitaxial thin films: Insights into structural, electronic and optical properties,” *J. Alloys Compd.*, 928, 167099, 2022, doi: 10.1016/j.jallcom.2022.167099.
- [16] A. Sharma, M. Varshney, H.-J. Shin, K. Chae, and S. O. Won, “XANES, EXAFS and photoluminescence investigations on the amorphous Eu:HfO₂,” *Spectrochim. Acta. A. Mol. Biomol. Spectrosc.*, 173, 549–555, 2017, doi: 10.1016/j.saa.2016.10.006.
- [17] T. V. Perevalov, V. Sh. Aliev, V. A. Gritsenko, A. A. Saraev, and V. V. Kaichev, “Electronic structure of oxygen vacancies in hafnium oxide,” *Microelectron. Eng.*, 109, 21–23, 2013, doi: 10.1016/j.mee.2013.03.005.

- [18] T. Dehury, S. Kumar, and C. Rath, “Structural transformation and bandgap engineering by doping Pr in HfO₂ nanoparticles,” *Mater. Lett.*, 302, 130413, 2021, doi: 10.1016/j.matlet.2021.130413.
- [19] E. Montes *et al.*, “Effect of pH on the optical and structural properties of HfO₂:Ln³⁺, synthesized by hydrothermal route,” *J. Lumin.*, 175, 243–248, 2016, doi: 10.1016/j.jlumin.2016.03.009.
- [20] S. Kumar, S. B. Rai, and C. Rath, “Monoclinic to cubic phase transformation and photoluminescence properties in Hf_{1-x}Sm_xO₂ (x = 0–0.12) nanoparticles,” *J. Appl. Phys.*, 123, 055108, 2018, doi: 10.1063/1.5016377.
- [21] P. Blaha, “an Augment Plane Wave+ Local Orbitals Program for Calculating Crystal Properties, User’s Guide.” Vienna Austria.
- [22] J. P. Perdew, K. Burke, and M. Ernzerhof, “Generalized Gradient Approximation Made Simple [Phys. Rev. Lett. 77, 3865 (1996)],” *Phys. Rev. Lett.*, 78, 1396–1396, 1997, doi: 10.1103/PhysRevLett.78.1396.
- [23] F. Tran and P. Blaha, “Accurate Band Gaps of Semiconductors and Insulators with a Semilocal Exchange-Correlation Potential,” *Phys. Rev. Lett.*, 102, 226401, 2009, doi: 10.1103/PhysRevLett.102.226401.
- [24] G. Kresse and D. Joubert, “From ultrasoft pseudopotentials to the projector augmented-wave method,” *Phys. Rev. B*, 59, 1758–1775, Jan. 1999, doi: 10.1103/PhysRevB.59.1758.
- [25] J. Rodriguez-Carvajal, “‘FULLPROF: A Program for Rietveld Refinement and Pattern Matching Analysis’, Abstracts of the Satellite Meeting on Powder Diffraction of the XV Congress of the IUCr.” Toulouse, France, 1990.
- [26] B.-K. Kim and H. Hamaguchi, “Raman spectrum of 18O-labelled Hafnia,” *Mater. Res. Bull.*, 32, 1367–1370, 1997, doi: 10.1016/S0025-5408(97)00114-1.
- [27] C. W. Li, M. M. McKerns, and B. Fultz, “Raman spectrometry study of phonon anharmonicity of hafnia at elevated temperatures,” *Phys. Rev. B*, 80, 054304, 2009, doi: 10.1103/PhysRevB.80.054304.
- [28] P. E. Quintard, P. Barbéris, A. P. Mirgorodsky, and T. Merle-Méjean, “Comparative Lattice-Dynamical Study of the Raman Spectra of Monoclinic and Tetragonal Phases of Zirconia and Hafnia,” *J. Am. Ceram. Soc.*, 85, 1745–1749, 2004, doi: 10.1111/j.1151-2916.2002.tb00346.x.

- [29] V. R. Mastelaro, V. Briois, D. P. F. De Souza, and C. L. Silva, “Structural studies of a ZrO_2 – CeO_2 doped system,” *J. Eur. Ceram. Soc.*, 23, 273–282, 2003, doi: 10.1016/S0955-2219(02)00188-7.
- [30] C.-H. Lu, J. M. Raitano, S. Khalid, L. Zhang, and S.-W. Chan, “Cubic phase stabilization in nanoparticles of hafnia-zirconia oxides: Particle-size and annealing environment effects,” *J. Appl. Phys.*, 103, 124303, 2008, doi: 10.1063/1.2936983.
- [31] S. Chaudhary, D. Hsieh, and G. Refael, “Orbital Floquet engineering of exchange interactions in magnetic materials,” *Phys. Rev. B*, 100, 220403, 2019, doi: 10.1103/PhysRevB.100.220403.
- [32] D.-Y. Cho, H.-S. Jung, and C. S. Hwang, “Structural properties and electronic structure of HfO_2 - ZrO_2 composite films,” *Phys. Rev. B*, 82, 094104, 2010, doi: 10.1103/PhysRevB.82.094104.
- [33] J. I. Beltrán, M. C. Muñoz, and J. Hafner, “Structural, electronic and magnetic properties of the surfaces of tetragonal and cubic HfO_2 ,” *New J. Phys.*, 10, 063031, 2008, doi: 10.1088/1367-2630/10/6/063031.
- [34] H. Padma Kumar, S. Vidya, S. Saravana Kumar, C. Vijayakumar, S. Solomon, and J. K. Thomas, “Optical properties of nanocrystalline HfO_2 synthesized by an auto-igniting combustion synthesis,” *J. Asian Ceram. Soc.*, 3, 64–69, 2015, doi: 10.1016/j.jascer.2014.10.009.
- [35] J. Manikantan, H. B. Ramalingam, B. C. Shekar, B. Murugan, R. R. Kumar, and J. S. Santhoshi, “Physical and optical properties of HfO_2 NPs – Synthesis and characterization in finding its feasibility in opto-electronic devices,” *Adv. Powder Technol.*, 28, 1636–1646, 2017, doi: 10.1016/j.appt.2017.03.022.
- [36] M. S. Ghamsari, M. R. Gaeni, W. Han, and H.-H. Park, “Efficient blue luminescence from HfO_2 colloidal nanocrystals,” *Mater. Express*, 7, 72–78, 2017, doi: 10.1166/mex.2017.1347.
- [37] L. Qin, J. Li, S. Meng, H. Lu, and T. Tohyama, “A small shoulder of optical absorption in polycrystalline HfO_2 by LDA+U approach,” *Solid State Commun.*, 244, 28–32, 2016, doi: 10.1016/j.ssc.2016.06.015.
- [38] Z. Gangqiang, T. Sanqi, and T. Tingting, “Electronic Structure and Optical Properties of Monoclinic HfO_2 with Oxygen Vacancy,” *Rare Met. Mater. Eng.*, 42, 1576–1580, 2013, doi: 10.1016/S1875-5372(13)60093-4.

- [39] N. F. Santos *et al.*, “Luminescence studies on SnO₂ and SnO₂:Eu nanocrystals grown by laser assisted flow deposition,” *Phys. Chem. Chem. Phys.*, 17, 13512–13519, 2015, doi: 10.1039/C4CP06114D.
- [40] K. Smits *et al.*, “Europium doped zirconia luminescence,” *Opt. Mater.*, 32, 827–831, 2010, doi: 10.1016/j.optmat.2010.03.002.
- [41] Vikas and M. Jayasimhadri, “Thermally stable red luminescence from Eu³⁺-activated telluro zinc phosphate glass under near-ultraviolet light excitation for photonic applications,” *Luminescence*, 37, 2059–2066, 2022, doi: 10.1002/bio.4391.

Summary and the future outlooks

In this chapter, we summarize our research entitled “*Study of HfO₂ based Structures for Optical and Thermoelectric Applications*” by discussing the outcomes of every finding. We have examined the optical and TE properties of HfO₂ using experiment and DFT investigations for future efficient lighting and green energy harvesting. The summary of the work done is presented as follows:

Chapter 1 describes the introduction of the problem and the technological advancement of the solid state lighting and TE application. A brief discussion on transport parameters and the strategies to enhance the performance of TE materials is presented. This chapter explains the basic concept of luminescence and spectroscopic features of rare earth ions. The importance selected host, the objective of the present thesis, and the scope of thesis were included.

Chapter 2 DFT was used to examine the structural, electronic, optical, and thermoelectric properties of pure and doped HfO₂. The present chapter briefly discusses the methodology of the entire calculations performed to fulfil the existing study. The discussion starts with the physical interpretation of many-body problem. Subsequently, we discuss the emergence of DFT, one of the prominent methods for solving many particle system. In addition to that, the necessary explanation of exchange correlation functionals were included. The semi-classical Boltzmann transport theory was discussed to study the transport parameters.

Along with this, we focused on the method to prepare the HfO₂ and HfO₂: xEu³⁺ with varying concentrations. It also explains the experimental tools that were used in the structural and optical properties of HfO₂. The structural properties were investigated by the X-ray Diffractometer, and Raman spectroscopy. The oxidation state of rare earth ions was examined via X-ray absorption spectroscopy and the PL properties of HfO₂ were also discussed in this chapter.

Chapter 3 examines the thermoelectric properties of pure and doped HfO₂. The optimization of the figure of merit by tuning carrier concentrations was an effective way to realize efficient thermoelectrics. Using the *first-principles* calculation combined with the semi-classical Boltzmann transport theory and phonon dynamics, we realized the high thermoelectric

performance in various polymorphs of HfO₂. The phonon dispersion calculations confirm the dynamical stability of all polymorphs of HfO₂. The thermodynamical stability of the Ti and S doping concentrations was confirmed using formation energy and convex hull formalism. The electronic and thermoelectric properties were found using TB-mBJ potential. The observed values of the Seebeck coefficient are 945.27 $\mu\text{V/K}$, 922.62 $\mu\text{V/K}$, 867.44 $\mu\text{V/K}$, and 830.81 $\mu\text{V/K}$ for tetragonal (*t*), orthorhombic (*o*), monoclinic (*m*), and cubic (*c*) phases of HfO₂, respectively, at 300 K. The highest value of electrical conductivity was observed in *c*-HfO₂ at 1200 K, and the lowest value of electronic thermal conductivity was observed in *o*-HfO₂ at 300 K. The lattice thermal conductivity was decreased at higher temperatures. The peak value of ZT was 0.77 at $3 \times 10^{20} \text{ cm}^{-3}$, 0.97 at $1 \times 10^{21} \text{ cm}^{-3}$, 0.83 at $2 \times 10^{21} \text{ cm}^{-3}$, 0.87 at $5 \times 10^{21} \text{ cm}^{-3}$ at the 1200 K for *c*-, *m*-, *o*- and *t*- HfO₂, respectively. The low lattice thermal conductivity leads to the high values of the figure of merit at the optimized carrier concentrations ($\sim 10^{21} \text{ cm}^{-3}$). In all the studied phases, least observed value of ZT was in *c*-HfO₂. The doping of Ti and S at the Hf and O sites on *c*-HfO₂ was analyzed, respectively, to enhance its ZT . Doping leads to create new trap states in the band gap. It was observed that Ti doping has a lower band gap as compared to S doping. The magnitude of the Seebeck coefficient is high in Ti doping as compared to S doping. Further, the effective mass calculation was done to understand the behavior of the Seebeck coefficient. The maximum value of ZT (~ 0.82) was observed at 800 K for $x = 0.06$ doping concentration. The estimated high figure of merit can make HfO₂ a potential material for thermoelectric energy harvesting applications at elevated temperatures.

Chapter 4 describes the structural phase transition in the HfO₂ under the effect of doping and pressure. Here, we discuss the phase transition from a centrosymmetric *m*-HfO₂ to a non-centrosymmetric *o*-HfO₂ with Si doping. The reported phase transition pressures i.e., 15GPa, 14 GPa, 8 GPa, and 8GPa for $x = 0, 0.03, 0.06, \text{ and } 0.09$, respectively for Hf_{1-x}Si_xO₂ are in excellent agreement with available experimental results. It was observed that with increasing Si concentrations the transition pressures reduce significantly which was understood in terms of bond length and charge transfer. The thermal stability of the obtained *o*-HfO₂ phase was examined via ab initio molecular dynamics up to its synthesis temperature. The negative formation energy also confirms its thermodynamical stability. The band gap and density of states were analyzed using Tb-mBJ potential. The density of states indicates the noticeable appearance of Si states in the lower conduction band and an increase in the extent of hybridization.

Chapter 5 illustrates the optical properties of pure and doped HfO₂. The effect of Ti, Si, and S was investigated on the optical properties of HfO₂ using dielectric and refractive index calculations. The refractive index of *c*-HfO₂ slightly enhanced with Ti and S doping. The absorption coefficient and optical conductivity enhanced from visible to UV region in Ti doped *c*-HfO₂. The effect of Si doping on *o*-HfO₂ also broader the UV absorption range but no significant enhancement in refractive index was observed. The observations revealed that at a lower pressure i.e., 8GPa; similar optical response of non-centrosymmetric HfO₂ can be observed. The optical properties can be augmented via the suggested doping mechanism. The optical response of HfO₂ under different doping makes it a viable candidate in optoelectronic applications.

Chapter 6 explains the defect states analysis in the pristine HfO₂ and a low temperature synthesis of cubic HfO₂. The samples were synthesized via the chemical co-precipitation method. The crystal structure and phase analysis of the prepared sample was carried out by XRD and Rietveld refinement studies. The UV-visible spectroscopy used to analyze the band gap of HfO₂. Theoretical observed band gap using the TB-mBJ approach was in good agreement with the experimental results. The PL peaks corresponding to 562 nm, 536 nm, and 450 nm wavelength are attributed to oxygen vacancy. To analyze the vacancy, we have calculated the density of states of O₃ and O₄ vacancy using DFT. The peaks are correlated with the total density of states of O₄ single vacancy and are in close agreement with our experimental observation.

A low temperature synthesis of HfO₂:xEu³⁺ (x = 0, 3, 5, and 7 mol%) at 600 °C. The XRD results revealed the monoclinic phase in undoped HfO₂ and showed mixed phase formation at lower concentrations and a dominant cubic phase achieved at 5 mol% doping of Eu in HfO₂. Further, the phase transition was also calculated using density function theory which shows the transition point at ~5.11% doping concentration. X-ray absorption spectra identify the +3 oxidation state of Eu ions in the HfO₂. PL study demonstrates the emission in the red region with high color purity under different excitation wavelengths from near UV to blue light. The reddish PL emission with high color purity under different excitation wavelengths from n-UV to blue region may be exploited in solid state lighting-based applications.

Future outlooks:

- To explore various methods to improve the thermoelectric performance of HfO₂.
- To extend the theoretical work for understanding of various defect mechanism and doping in HfO₂.
- To improve the optical response of non-centrosymmetric phase HfO₂.
- To extend the utility of HfO₂ as a future spintronic material.
- To investigate novel thermoelectric materials using machine learning.

CURRICULUM VITÆ

Rajesh Kumar



Contact Information Khera, Mahendergarh –123 034
Haryana, India
Email – kumarr394@gmail.com
Phone – +91 8059997406

Date of Birth 18th February, 1994

Designation Research Scholar
Department of Applied Physics
Delhi Technological University (DTU), India

Education Ph.D. (Since January 2019)
Thesis Title: Study of HfO₂ based materials for thermoelectric and optical applications
Department of Applied Physics
Delhi Technological University (DTU), India

Master of Science (M.Sc.) Physics (2015)
Department of Physics
Kurukshetra University Kurukshetra (KUK), Haryana, India
Aggregate Percentage: **67.85**

Bachelor of Science (B.Sc.) (2013)
Dronacharya Govt. P.G. College, Gurugram
Maharshi Dayanand University (MDU), Haryana, India
Aggregate Percentage: **70.68**

Senior Secondary (12th) (2010)
Suraj Sr. Sec. School affiliated to CBSE, Mahendergarh, Haryana, India
Aggregate Percentage: **76.16**

Matriculation (10th) (2008)
Suraj Sr. Sec. School affiliated to CBSE, Mahendergarh, Haryana, India
Aggregate Percentage: **76.50**

Research Interests	<p>First principles calculation using Density Functional Theory</p> <p>Thermoelectric materials: Bulk, Hetrostructures</p> <p>Defect and magnetic study on two-dimensional materials</p> <p>Luminescence study</p>
Awards	<p>CSIR-NET AIR-108 (2018)</p> <p>GATE AIR-833 (2018)</p> <p>Research excellence award in 2022 and 2021</p>
Skills	<p>Operating systems: Linux, Windows</p> <p>Software Packages: WIEN2k, Vienna ab-initio simulation package, Quantum espresso, Phonopy, Phono3py, BoltzTraP</p> <p>Experience of working on High-Performance computers (HPC)</p> <p>Graphical software: Xmgrace, origin, Vesta, Xcrysden</p> <p>Experimental: X-ray Diffraction, Photoluminescence</p>

Publications in International and National journals

1. **Rajesh Kumar**, Mukhtiyar Singh, Ankush Vij, “*Unraveling the effect of pressure on structural phase transition, electronic and optical properties of $Hf_{1-x}Si_xO_2$ ($x = 0, 0.03, 0.06, 0.09$): A first-principles investigation*”, **J. Phys. Chem. Solids** 185, 111773 (2024).
2. **Rajesh Kumar**, Jitender Kumar, Ramesh Kumar, Akshay Kumar, Aditya Sharma, S.O. Won, K.H. Chae, Mukhtiyar Singh, Ankush Vij, “*Monoclinic to cubic structural transformation, local electronic structure, and luminescence properties of Eu-doped HfO_2* ”, **Appl. Phys. A** 129, 712 (2023).
3. **Rajesh Kumar**, Sangeeta, Ramesh Kumar, Ramesh Kumar Bibiyan, Mukhtiyar Singh, Ankush Vij, “*An ab-initio study of induced half metallic ferromagnetism in $Hf-Nb$ alloy oxides*”, **Eur. Phys. J. Plus** 138, 561 (2023).
4. **Rajesh Kumar**, Ramesh Kumar, Sangeeta, Kulwinder Kumar, Mukhtiyar Singh, “*Insights in to structural, electronic and thermoelectric properties of $ZnTMN_2$ ($TM= Zr$ and Hf)*”, **Indian J. Pure Appl. Phys.** 61, 910-914 (2023).
5. Sangeeta, **Rajesh Kumar**, Ramesh Kumar, Kulwinder Kumar, Mukhtiyar Singh, “*Unravelling the Ultralow Thermal Conductivity of Ternary Antimonide Zintl Phase $RbGaSb_2$: A First-principles Study*”, **Indian J. Pure Appl. Phys** 61, 731-734 (2023).

6. Ramesh Kumar, **Rajesh Kumar**, Sangeeta, Mukhtiyar Singh, “*Pressure Induced Surface States and Wannier Charge Centers in Ytterbium Monoarsenide*”, **Indian J. Pure Appl. Phys** 61, 735-738 (2023).
7. **Rajesh Kumar**, Ramesh Kumar, Mukhtiyar Singh, Deshraj Meena, Ankush Vij, “*Carrier concentration mediated enhancement in thermoelectric performance of various polymorphs of hafnium oxide: a plausible material for high temperature thermoelectric energy harvesting application*”, **J. Phys. D: Appl. Phys.** 55, 495302 (2022).
8. **Rajesh Kumar**, Ramesh Kumar, Mukhtiyar Singh, Ankush Vij, “*A first-principle study of electronic, thermoelectric, and optical properties of sulfur doped c-HfO₂*”, **Phys. Scr.** 97, 075813 (2022).
9. **Rajesh Kumar**, Mukhtiyar Singh, Ankush Vij, “*Electronic, thermoelectric, and optical studies of cubic Hf_{1-x}Ti_xO₂: An attempt to enhance the key parameters*”, **J. Solid State Chem.** 307, 122829 (2022).
10. Nimit Jain, **Rajesh Kumar**, Ramesh Kumar, Mukhtiyar Singh, “*Enhancement of thermoelectric performance of ZrO₂ via Titanium doping*”, **materials today: proceedings** 51, 699-702 (2022).
11. **Rajesh Kumar**, Mukhtiyar Singh, Ankush Vij, “*Defects Assisted Luminescence in m-HfO₂ Nanocrystals: An Experimental and Theoretical Study*”, **Optik** 248, 168121 (2021).
12. Jitender Kumar, **Rajesh Kumar**, Mukhtiyar Singh, Shalendra Kumar, Ravi Kumar, Sung Ok Won, Ranjeet Brajpuriya, Sourabh Dwivedi, Ram K. Sharma, Ankush Vij, “*Structural, diffuse reflectance and luminescence study of t-Mg₂BO₅ nanostructures*”. **Appl. Phys. A** 127, 617 (2021).

Conferences and Workshops

1. Participated and presented paper at the national workshop on material design and processing (8-10 May, 2023), Jawaharlal Nehru University, Delhi, India.
2. Participated and presented Poster at the 33rd IUPAP conference on computational physics (1-4 August, 2022), TEXAS, Austin, TX USA (Virtual).
3. Participated and presented Poster at the IUMRS-ICA (19-23 December, 2022), Indian Institute of Technology Jodhpur, Rajasthan, India.
4. Participated and presented Poster in the national webinar on Advances in Physics (25-26 June, 2020), Guru Jambheshwar University of Science and Technology, Hisar, India.

Declaration: I hereby declare that the above information is correct to the best of my knowledge.

Rajesh Kumar